

# **The energy spectrum of primary cosmic rays measured with the KASCADE-Grande experiment**

DISSERTATION

zur Erlangung des akademischen Grades eines  
Doktors der Naturwissenschaften,

vorgelegt von

**Diplom-Physiker Dirk Kickelbick**

geboren am 18. Juni 1974 in Stollberg

genehmigt vom Fachbereich Physik  
der Universität Siegen.

Siegen  
Juni 2008

Gutachter der Dissertation: Univ.-Prof. Dr. P. Buchholz  
Univ.-Prof. Dr. C. Grupen

Datum der Disputation: 11. Juli 2008

gedruckt auf alterungsbeständigem holz- und säurefreiem Papier

## Abstract

The measurement of the energy spectrum of cosmic rays is an important tool to reveal the nature of cosmic rays. In order to measure the cosmic rays up to an energy of  $10^{18}$  eV, the KASCADE experiment was extended to KASCADE-Grande. It is a ground based detector to measure extensive air showers, which are initiated by the primary particles of the cosmic radiation. In order to obtain the energy spectrum, data from December 2003 to September 2007 are analyzed by using the method of constant intensity. This method is applied to the number of charged particles in an air shower and leads to a zenith angle independent number of charged particles, which is a measure of the shower size. Simulations of air showers are then used to calibrate the shower size to the primary energy. Thus, the primary energy spectrum in the energy range of  $10^{16}$  eV to  $10^{18}$  eV is determined. In the energy region from  $10^{16}$  eV to  $10^{17}$  eV the resulting spectrum and the spectrum measured with KASCADE overlap. Both measurements are in good agreement in this energy range. Due to the extended energy range, the energy spectrum of KASCADE-Grande connects the KASCADE spectrum with the measurements of experiments like AGASA, Auger and HiRes, which measure up to the highest energies of cosmic rays.

## Zusammenfassung

Die Messung des Energiespektrums der geladenen kosmischen Strahlung ist ein wichtiges Hilfsmittel, um die Natur der kosmischen Strahlung aufzudecken. Das KASCADE-Grande-Experiment ist eine Erweiterung des KASCADE-Experiments, um den messbaren Energiebereich auf  $10^{18}$  eV zu erweitern. Es ist ein Experiment zur Messung ausgedehnter Luftschauer am Boden. Ausgedehnte Luftschauer werden durch die Primärteilchen der kosmischen Strahlung in der Atmosphäre erzeugt. Für die Analyse werden Messdaten von Dezember 2003 bis September 2007 ausgewertet. Um das Energiespektrum zu bestimmen, wird die Methode der konstanten Intensität auf die Anzahl der geladenen Teilchen des Luftschauers angewendet. Diese Methode liefert eine zenitwinkelunabhängige Anzahl der geladenen Teilchen, welche ein Maß für die Schauergröße ist. Simulationen von Luftschauern werden verwendet, um die Schauergröße mit der Primärenergie zu kalibrieren. Damit kann das Energiespektrum im Bereich von  $10^{16}$  eV bis  $10^{18}$  eV bestimmt werden. Dieses überlappt im Energiebereich von  $10^{16}$  eV bis  $10^{17}$  eV mit den Messungen von KASCADE. Beide Messungen stimmen in diesem Energiebereich gut überein. Durch die Vergrößerung des messbaren Energiebereiches wird eine Verbindung zwischen dem gemessenen Spektrum von KASCADE und den Messungen von Experimenten wie AGASA, Auger oder HiRes hergestellt, die bis zu den höchsten Energien der kosmischen Strahlung messen.



# Contents

<b>1</b>	<b>Introduction</b>	<b>1</b>
<b>2</b>	<b>Cosmic rays</b>	<b>3</b>
2.1	Energy spectrum of the cosmic rays . . . . .	3
2.2	The composition of cosmic rays . . . . .	5
2.3	Acceleration and propagation of cosmic rays . . . . .	6
2.4	The origin of the knee . . . . .	7
2.5	Extensive air showers . . . . .	8
<b>3</b>	<b>The KASCADE-Grande experiment</b>	<b>15</b>
3.1	The KASCADE detector array . . . . .	16
3.1.1	The $e/\gamma$ detector . . . . .	17
3.1.2	The $\mu$ detector . . . . .	17
3.1.3	The FADC system . . . . .	18
3.1.4	Data acquisition . . . . .	18
3.2	The central detector . . . . .	19
3.2.1	Hadron calorimeter . . . . .	20
3.2.2	The muon chamber system and trigger plane . . . . .	20
3.2.3	Top cluster and top layer . . . . .	20
3.3	The muon tracking detector . . . . .	21
3.4	The Grande array . . . . .	22
3.5	The Piccolo array . . . . .	22
3.6	Central data acquisition . . . . .	23
<b>4</b>	<b>Reconstruction and simulation of extensive air showers</b>	<b>25</b>
4.1	Reconstruction of extensive air showers in KASCADE-Grande . . . . .	25
4.2	Simulation of extensive air showers for KASCADE-Grande . . . . .	28
<b>5</b>	<b>Data sample selection</b>	<b>31</b>
5.1	Quality cuts . . . . .	31
5.2	Trigger and reconstruction efficiency . . . . .	35
5.3	Summary . . . . .	39

<b>6</b>	<b>Constant intensity method and corrected shower size spectra</b>	<b>41</b>
6.1	Constant intensity method . . . . .	42
6.1.1	Shower size spectra . . . . .	42
6.1.2	Constant intensity cuts . . . . .	45
6.1.3	Attenuation curves . . . . .	46
6.2	Corrected shower size spectra . . . . .	48
6.3	Summary . . . . .	51
<b>7</b>	<b>Subsample selection and energy conversion</b>	<b>53</b>
7.1	Shower fluctuations and composition dependence . . . . .	53
7.2	Subsample cuts . . . . .	56
7.3	Energy conversion . . . . .	59
7.4	Summary . . . . .	63
<b>8</b>	<b>All particle primary energy spectrum</b>	<b>65</b>
8.1	Energy calibration function . . . . .	65
8.2	Study of systematic uncertainties . . . . .	68
8.2.1	Influence of the uncertainty in the shower core position reconstruction . . . . .	68
8.2.2	Influence of the precision in the arrival direction reconstruction . . . . .	71
8.2.3	Influence of the precision of the reconstructed number of charged particles . . . . .	71
8.2.4	Influence of the uncertainties of the various applied fits . . . . .	75
8.2.5	Influence of the primary composition . . . . .	79
8.2.6	Influence of the shower fluctuations . . . . .	79
8.2.7	Overall systematic error . . . . .	84
8.3	Summary . . . . .	86
<b>9</b>	<b>Summary and conclusions</b>	<b>87</b>
<b>A</b>	<b>Number of charged particles determined by applying the constant intensity method</b>	<b>91</b>
<b>B</b>	<b>Error propagation when using the constant intensity method</b>	<b>93</b>
<b>C</b>	<b>Result of the application of the constant intensity method</b>	<b>97</b>
C.1	Results of the attenuation curve fits . . . . .	98
C.2	Resulting shower size spectra using reference angle $0^\circ$ . . . . .	99
C.3	Comparing the corrected shower size spectra for the reference angles $0^\circ$ and $21^\circ$ . . . . .	100
C.4	Corrected shower size spectra . . . . .	101
<b>D</b>	<b>Examination of the shower fluctuations</b>	<b>103</b>
D.1	Fluctuations of the number of charged particles for hydrogen induced showers . . . . .	104

---

D.2	Fluctuations of the number of charged particles for iron induced showers	110
D.3	Fluctuations of the number of muons for hydrogen induced showers . . .	116
D.4	Fluctuations of the number of muons for iron induced showers . . . . .	122
D.5	Summary of the fluctuations for hydrogen induced showers . . . . .	128
<b>E</b>	<b>Examination of the energy conversion</b>	<b>131</b>
E.1	Influence of standard quality cuts on the event distribution over the KAS- CADE-Grande array . . . . .	132
E.2	Distributions of the muon number as a function of the primary energy .	133
E.3	Profile plots for the energy conversion using standard cuts . . . . .	136
E.4	Comparing results using subsample cuts with results using standard quality cuts . . . . .	137
<b>F</b>	<b>Energy spectrum with systematics</b>	<b>139</b>
	<b>List of Figures</b>	<b>144</b>
	<b>List of Tables</b>	<b>145</b>
	<b>List of Acronyms</b>	<b>147</b>
	<b>Bibliography</b>	<b>149</b>
	<b>Danksagung</b>	<b>157</b>





---

## Introduction

---

Since their discovery in 1912, the interest in studying cosmic rays has grown steadily. The cosmic radiation connects astrophysics with particle physics. In astrophysics, the cosmic radiation provides information about astrophysical processes of objects in outer space. In particle physics, it can provide insights into particle interactions at very high energies, which can not be provided by particle accelerators. Although the cosmic radiation was discovered almost one century ago, fundamental questions are not answered yet. For example, the origin and the acceleration mechanisms of cosmic rays are not yet known.

The investigation of the energy spectrum of the cosmic rays gives a handle to answer these questions. The energy spectrum follows a power law with several features. One prominent feature is the so-called knee. At an energy of several PeV, the spectral index of the energy spectrum changes from about 2.7 to about 3.1. The various models about the origin and the acceleration of the cosmic rays lead to different predictions of the position and the shape of the knee. Therefore, the study of the energy spectrum can help to exclude different models and, finally, helps to reveal the nature of the cosmic rays.

Due to the steep decrease of the intensity of the cosmic rays with the energy of the primary particle, the cosmic radiation can not be studied directly for energies higher than about  $10^{14}$  eV. For higher energies, the cosmic rays are measured indirectly by detecting extensive air showers at ground level. These extensive air showers are initiated by the interaction of primary cosmic ray particles with air nuclei. A drawback of this method compared to the direct measurement is, that the primary energy has to be reconstructed from measured properties of the extensive air showers. In this thesis, the energy spectrum is reconstructed for data measured with the KASCADE-Grande experiment.

After a short overview of the theory of cosmic rays and extensive air showers in Chap. 2, the KASCADE-Grande experiment is introduced in Chap. 3. In Chap. 4, the reconstruction of the measured data and the simulation of extensive air showers are explained. The available data and the necessary cuts on these data are presented and explained in Chap. 5. This chapter is followed by three chapters describing the analysis of the data. In Chap. 6, the method of constant intensity is introduced. This method provides a zenith angle independent measure of the shower size. In order to reconstruct

the primary energy from the shower size, a conversion relation is determined in Chap. 7. In Chap. 8, the energy spectrum is calculated. This chapter is completed by the study of the systematic uncertainties. Finally, in Chap. 9, the results are summarized and conclusions are drawn.

---

# Cosmic rays

---

Highly energetic charged particles coming from outer space, that are hitting the earth's atmosphere are called cosmic rays or cosmic radiation. In 1912, V. Hess discovered the cosmic radiation by measuring the discharging effect of electroscopes during balloon flights [Hes12]. In 1939, P. Auger discovered extensive air showers (EAS) using spatially separated detectors. He observed coincident events and concluded, that the primary particles interact with the atoms and molecules in the atmosphere initiating the extensive air showers. Many aspects of the cosmic rays have been examined and discovered since then. It is clear now, that the cosmic radiation consists of different types of charged particles, like electrons, protons, and fully ionized atomic nuclei. The energies of the primary particles cover an energy range of 11 orders of magnitude from  $10^9$  eV up to  $10^{20}$  eV. But there are still essential questions, which could not be answered yet, like the type of sources the cosmic rays are coming from, or which mechanisms are accelerating the cosmic rays to such high energies.

In this chapter, a brief overview of the observed properties of the cosmic radiation and a brief introduction of the theoretical models explaining the origin and the acceleration mechanisms of the cosmic rays are given.

### 2.1 Energy spectrum of the cosmic rays

Since the discovery of cosmic rays, their energy spectrum has been measured by many experiments. It covers an energy range of about 11 orders of magnitude and about 30 orders of magnitude in the flux of the cosmic rays. In Fig. 2.1, the energy spectrum measured by different experiments is shown. In order to see the structures of the spectrum in more detail, the flux is multiplied by a factor of  $E^{2.5}$ .

The energy spectrum can be described by a power law:

$$\frac{dN}{dE} \propto E^{-\gamma}, \quad (2.1)$$

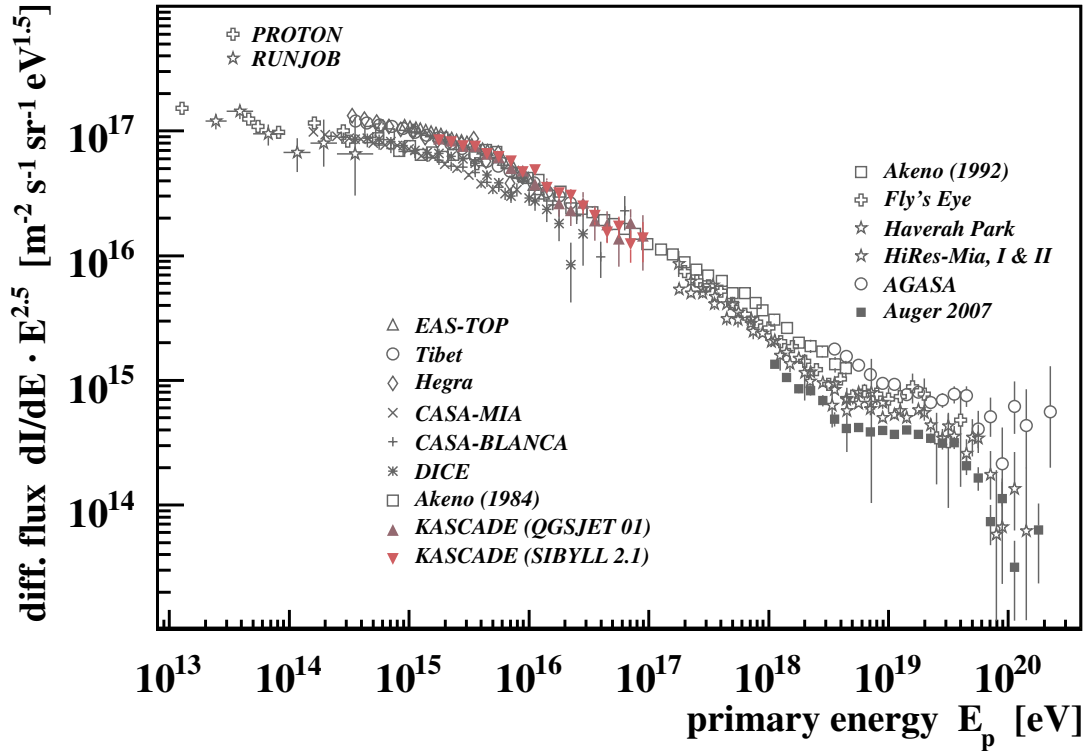


**Figure 2.1:** Energy spectrum of the cosmic radiation. The experiments PROTON [Gri70] and RUNJOB [Apa01] are direct measurements. Whereas, EAS-TOP [Agl99], Tibet [Ame95], Hegera [Arq00], CASA-MIA [Gla99], CASA-BLANCA [Fow01], DICE [Swo00], KASCADE [Ant05], Akeno [Nag84, Nag92], Fly’s Eye [Bir94], Haverah Park [Ave03], HiRes [AZ01, Abb08], AGASA [Tak03], and Auger [Rot07, Per07, FSL07] are air shower experiments, which measure the cosmic rays indirectly.

with a spectral index  $\gamma$  in the range of 2.5 – 3.2. Particles up to an energy of about 100 TeV can be measured directly by experiments on balloons or satellites, but for higher energies the flux is too small to measure cosmic rays directly, because their sensitive detection area in the order of 1 m<sup>2</sup> is too small. Therefore, experiments have to observe the cosmic radiation indirectly by measuring extensive air showers. These ground based experiments use the atmosphere above them as detection medium, and hence, the detection area can be increased considerably compared to balloon or satellite experiments.

The energy spectrum shows some features, where the spectral index is changing. The first of these features is the so-called “knee” and it was discovered in 1958 [Kul58]. At about 4 PeV the spectral index changes from about 2.7 to 3.1. The presence of a second knee at about  $4 \cdot 10^{17}$  eV is suggested by the measurements of Yakutsk [Knu06], Haverah Park [Ave03], Fly’s Eye [Bir94], and HiRes-MIA [AZ01]; these experiments see a change of the spectral index from about 3.0 to about 3.3. On the other hand, the

experiments Akeno [Nag92] and AGASA [Tak03] do not see the presence of a second knee. Hence, the existence of this feature is not yet proven.

Another feature of the energy spectrum is the so-called "ankle". At an energy of about  $5 \cdot 10^{18}$  eV, the spectral index changes from about 3.1 to 2.75. The origin of this change of the spectral index can be explained by a transition of the origin of the cosmic radiation from galactic to extragalactic sources.

Finally, another feature of the energy spectrum was predicted by Greisen, Zatsepin and Kuzmin [Gre66, Zat66]. For energies above  $5 \cdot 10^{19}$  eV, the energy of the photons of the cosmic microwave background radiation in the rest frame of the proton is in the order of 200 MeV and more, which exceeds the threshold energy for inelastic pion-production. Hence, the ultra-high energy particles lose energy in these processes as long as their energy is above the threshold energy. It is assumed, that the sources of these ultra-high energetic cosmic rays are extragalactic, and therefore, the cutoff in the energy spectrum should be seen. This cutoff is referred to as GZK-cutoff. It is still not clear, if the GZK-cutoff is present in the energy spectrum. Measurements by AGASA [Tak03, Hay99] show no decrease of the flux for primary energies above  $10^{20}$  eV indicating no GZK-cutoff, whereas, the results from HiRes [Abb08] are in agreement with the predicted cutoff energy at about  $5 \cdot 10^{19}$  eV. This is also supported by the first results of Auger [Rot07, Per07, FSL07].

## 2.2 The composition of cosmic rays

The study of the chemical composition of cosmic rays can help to reveal their origin and their acceleration mechanisms. Only for energies up to  $10^{14}$  eV, the chemical composition is known precisely due to balloon and satellite experiments. Here, the cosmic radiation consists of about 98 % of hadrons and 2 % of electrons and photons. 86 % of the hadronic component are protons and 12 % are helium nuclei. The rest are fully ionized nuclei of heavier elements up to iron. In Fig. 2.2, the relative elemental abun-

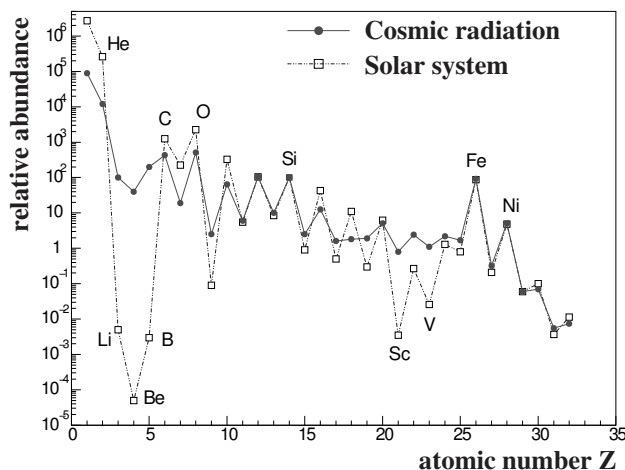


**Figure 2.2:** Comparison of the relative elemental abundance in the solar system and the cosmic radiation [Wef91].

dance in the solar system is compared with the relative abundance of the cosmic radiation [Sim83, Wef91, WS98]. The abundance is normalized to the abundance of silicon. The abundances in the solar system and in the cosmic radiation are in good agreement,

which suggests, that the sources of the cosmic radiation are comparable to the sun in the sense, that the elements are produced by nucleosynthesis. But there are also disagreements. Firstly, two groups of elements, Li, Be, B at low masses and Sc, Ti, V, Cr, Mn at higher masses, are much more abundant in the cosmic rays than in the solar system. In nucleosynthesis, these elements are only produced to a small amount. They are spallation products of the collision of the CNO group for the lighter elements and the iron group for the heavier elements with the interstellar medium. Secondly, the abundance of hydrogen and helium is lower in the cosmic rays compared to the abundance in the solar system. In a group of acceleration models (see the following section), only charged particles can be accelerated efficiently. The ionization energies of hydrogen and helium are relatively high. Therefore, a sufficient amount of these elements are not ionized, and hence, not accelerated. Therefore, the abundance of these elements is decreased in the cosmic rays compared to their abundance in the solar system. But, whatever the reasons are for these disagreements, the theories describing the sources and mechanisms of the cosmic radiation have to explain these discrepancies. Therefore, air shower experiments try to measure the elemental composition of the cosmic radiation at energies above  $10^{14}$  eV.

## 2.3 Acceleration and propagation of cosmic rays

Models, which should explain the acceleration and the propagation of the cosmic radiation have to describe the characteristics of the cosmic rays, like the power law of the energy spectrum with a spectral index of  $\gamma \approx 2.7$ , or their observed energy density of  $\varepsilon \approx 1 \text{ eV/cm}^3$ . Contemporary models of the acceleration mechanisms belong to one of three categories, stochastic acceleration models, direct acceleration models, or top-down models.

In stochastic models, the cosmic ray particles gain their final energy by many interactions each with a small increase of the energy. The fundamental process of the stochastic acceleration is called Fermi acceleration of first order [Fer49]. In this model, particles gain energy by diffusive acceleration at shock waves. In a shock front, two different regions with different characteristics of the magnetic field are generated. A particle traverses a shock wave several times and it is reflected on either side by a diffusive scattering. At each reflection, the particle gains energy proportional to the speed of the shock wave. The energy that a particle can achieve depends on the number of crossings in the wave before it escapes. Therefore, the maximum energy such a process can attain is limited by the lifetime of the shock front. One advantage of this model is, that it results in a power law for the energy spectrum with a spectral index of  $\gamma \approx 2.0$ , almost independent of the configuration of the shock wave front [Dru83]. There are several astrophysical objects, which could produce such shock waves.

Supernova explosions are one of the most promising candidates. In the galaxy there are three supernova explosions per century on average, which results in a power of about  $3 \cdot 10^{35} \text{ J/s}$ . In order to generate an energy density of  $1 \text{ eV/cm}^3$  for the cosmic rays, a power of  $5 \cdot 10^{33} \text{ J/s}$  is necessary. This means, that in order to obtain the observed energy density of cosmic rays, the energy emitted by supernova explosions has to be transformed into acceleration of the particles with an efficiency of only a few

percent. Measurements of TeV gamma rays [Eno02, Aha04, Uch07], which can be created by the collisions of accelerated protons with the interstellar medium, showed, that hadrons can be accelerated in shock wave fronts. Other sources of shock waves could be the termination shock of a stellar wind [Ces83], the termination shock of a galactic wind [Jok87], or the atmosphere of a neighboring star of a pulsar, which is hit by the pulsar wind [Har90]. All these galactic candidates are able to accelerate cosmic rays to a maximum energy in the order of  $10^{16}$  eV.

Secondly, in direct acceleration models the cosmic ray particles are accelerated very efficiently in a few steps or even in one single step. These models require strong magnetic and electric fields in order to accelerate particles. Possible objects are polar caps of rapidly rotating pulsars [Che86], relativistic jets from Active Galactic Nuclei (AGN), or supernovae, that emit highly relativistic jets, which accelerate the cosmic ray particles [Rac93]. The models for this category are describing sources of the cosmic radiation, which can be also extragalactic.

Finally, in top-down models, the origin of the ultra high cosmic radiation is explained by yet undiscovered phenomena. Most prominently, this could be an unknown ultra-heavy particle, which decays into high energetic particles. An overview about top-down models is given in [Sig03].

The two latter categories of models, the direct acceleration and the top-down scenarios, predict primary energies of the cosmic radiation above  $10^{16}$  eV.

The origin of the cosmic rays up to approximately  $10^{16}$  eV are probably of galactic origin. The time, that the cosmic ray particles need to cross the thickness of the disk of the galaxy, is small compared to their lifetimes. The measured distribution of these particles is isotropic. Therefore, it is suggested, that the cosmic ray particles propagate diffusively from their sources to the earth. The particles are deflected by the magnetic and electric fields of the galaxy, losing the information of the direction of their sources. On their travel, the particles lose energy by collisions, decay and ionization processes. Furthermore, particles can escape the galaxy and get lost. All these effects are causing a change in the spectral index of the energy spectrum from about  $\gamma \approx 2.0$  to  $\gamma \approx 2.7$ . The change in the composition is due to the decay and spallation of the cosmic ray particles.

## 2.4 The origin of the knee

The origin of the knee is still an unsolved problem. Various models try to explain the existence of the knee in different ways. In the following, an overview about the various models is given. These models can be categorized.

Firstly, there are models, which explain the knee structure as an effect of the underlying acceleration mechanisms. This class of models is strongly connected with the models of diffusive shock acceleration. In these models, the knee in the spectrum is caused by the maximum attainable energy of the cosmic ray particles and it is also assumed, that the particles are originating from the galaxy. The maximum energy, which can be achieved in these models is a few PeV. The energy a particle receives, depends on the number of crossings of the shock front, which increases with a decrease of the time the particle needs to cross the front. This time is proportional to the Larmor radius  $\propto 1/Z$  of the particle. Therefore, the maximum achievable energy depends on the

charge  $Z$  of the particle. Hence, the knee position depends on the type of the cosmic ray particles, i.e. the knee position for the various elements vary with the charge  $Z$  of the primary particle. More details can be found in [Ber99, Sta93, Kob02].

Secondly, there are models, which explain the knee as an effect of the propagation of the cosmic rays. Particles, that transverse the galaxy, have a certain probability to escape from it. This probability depends on the galactic magnetic field, which confines the cosmic rays. Irregular magnetic fields, which superimpose the regular magnetic field, lead to an additional drift component of the cosmic ray particles. This drift increases with the energy of the particle and leads to a leakage of particles for energies above approximately 3 PeV. This results in a steeper energy spectrum, and hence, in the knee structure. In these models, the position of the knee for different elements is proportional to the charge  $Z$ , because the drift depends on the energy per unit charge  $E/Z$  [Ptu93, Can02].

Thirdly, there are so-called “single source scenarios” [Erl97]. In these models, the knee is a signature of a single, near, and relatively young supernova remnant. Particles are accelerated by the shock wave of this object. This particle radiation is superimposed with a featureless background cosmic radiation. The knee in the total spectrum is mainly caused by the knee structure of the CNO group, which marks the end of the acceleration of the local supernova remnant.

Finally, there are so-called “exotic” models. One of these theories assumes massive neutrinos. In this case, protons can be destroyed by the process  $p + \bar{\nu}_e \rightarrow n + e^+$ . For a neutrino mass of  $m_\nu = 0.40 \text{ eV}$  the threshold energy of this process is about 3 PeV, which leads to the knee. This model predicts also a second knee at about  $3 \cdot 10^{17} \text{ eV}$  due to the same reaction for helium nuclei [Wig00].

Other exotic models involve new particle physics. In these models, the knee in the energy spectrum is not caused by the sources or the propagation of the cosmic ray particles, but due to effects in the development of the extensive air showers in the atmosphere. The interaction of the primary particles with air nuclei produce so far undetected heavy particles [Kaz01]. These new particles can not be measured by the detectors, and hence, the primary energy is underestimated, which causes the knee structure in the energy spectrum. These models depend on the corresponding interaction cross-sections. These cross-sections depend on the energy per nucleon  $E/A$ . Therefore, the position of the knee with respect to the type of the primary particle is proportional to the atomic mass  $A$  rather than to the atomic number  $Z$ . The measurements of KASCADE [Ant05] show, that the knee position changes with the type of the primary particle and, that the knee starts with the hydrogen component. Due to insufficient statistics the dependence could not be resolved.

## 2.5 Extensive air showers

In order to study the cosmic rays above a primary energy of  $10^{14} \text{ eV}$ , the secondary particles of extensive air showers are measured. These secondary particles are generated by the interaction of primary particles with nuclei in the upper atmosphere, which leads to an extensive air shower (EAS). In 1939, the existence of air showers was discovered by



P. Auger [Aug39]. In the following, an overview about the characteristics of extensive air showers is given.

For a hadronic extensive air shower, which is initiated by a hadronic interaction of the primary particle with an air nucleus, the inelastic cross-section of the primary particle-air nucleus reaction defines the mean free path length of the primary particle in the atmosphere. This cross-section depends on the energy of the primary particle. The probability of an interaction of a primary particle with an atmospheric nucleus depends on the cross-section and the density of the atmosphere. Therefore, for a certain primary energy, the height of the first interaction above ground level is not fixed and varies due to the probability distribution of the interaction process. This leads to fluctuations in the shower development.

The development of extensive air showers is characterized by two processes, the production of particles by interaction, and the decay of particles. Basically, an air shower comprises of three different classes of secondary particles, the hadronic, the electromagnetic, and the muonic component, see Fig. 2.3.

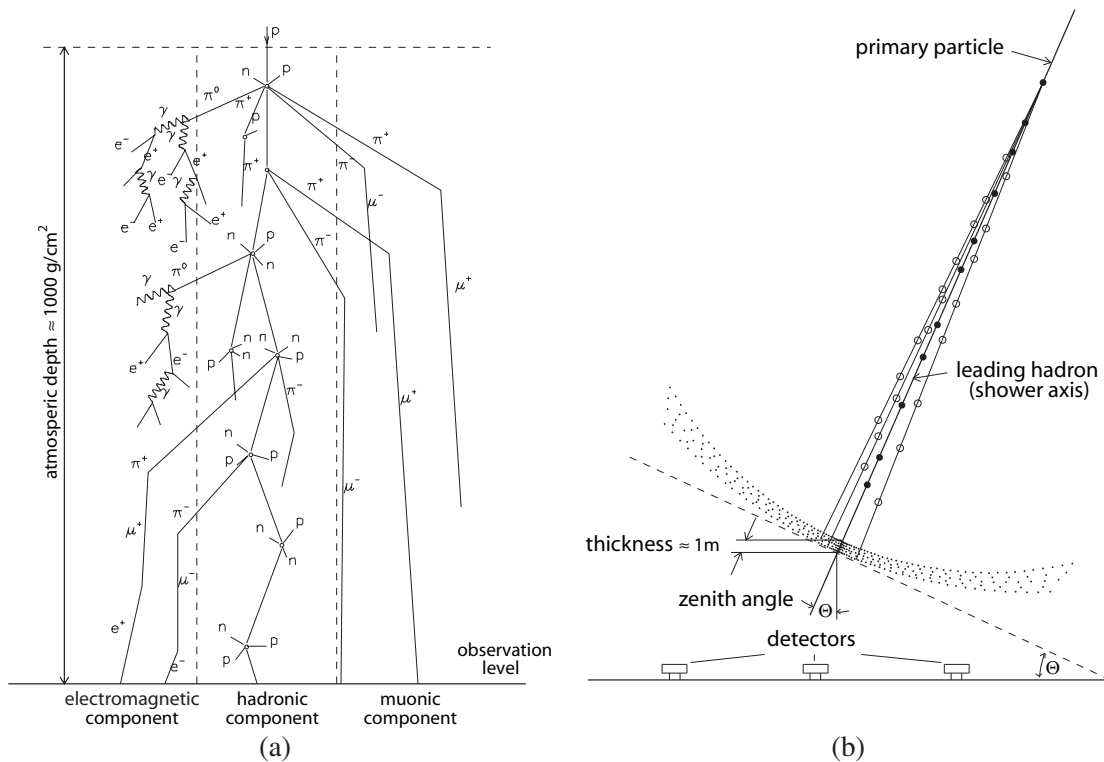


**Figure 2.3:** Schematic view of the development of an extensive air shower. In the *left* figure, the different components and their origin are illustrated. In the *right* figure, the geometry of an extensive air shower is shown. Taken from [Bur06].

### The hadronic component

Only about 1% of the total number of particles in an air shower is due to hadrons. Nevertheless, the hadronic component has a large impact on the shower development, because it feeds the other shower components.

In the initial collision of the primary particle with an air nucleus, the first generation of secondary particles is created in a strong interaction. These secondaries may decay or interact with other air nuclei producing a further generation of secondaries, which in turn may decay or interact again. While the shower propagates towards ground level, these processes occur repeatedly. This leads to a hadronic cascade with an increasing number of hadrons as the atmospheric depth increases. During the development of the cascade, the secondaries of each new generation carry less energy per particle. Thus, it becomes more likely for the hadrons to decay than to interact. Therefore, the number of hadrons in a cascade reaches a maximum, afterwards it decreases exponentially. The atmosphere corresponds to about 11 hadronic interaction lengths, thus, the initial primary particle will not reach sea level.

The secondary hadronic particles consist mainly of neutral and charged pions, followed by kaons, protons and neutrons. The mean transverse momentum of the secondary hadrons is about 400 MeV/c, which is small compared to the overall momentum. Thus, the hadronic component forms a narrow shower with a maximum spread of about 20 m, which propagates along the line of flight of the initial primary particle. This line represents the shower axis. See Fig. 2.3 for an illustration.

For hadrons at low energies ( $E < 10$  GeV), especially neutrons, the transverse momentum can not be neglected in comparison to the longitudinal momenta, which leads to a broad distribution of these particles of up to 1 km.

### The muonic component

The muonic component accounts for 5 % of the total number of particles in an extensive air shower. The muons are mainly generated by the decay of charged pions and kaons:

$$\begin{aligned}\pi^\pm &\longrightarrow \mu^\pm + \nu_\mu(\bar{\nu}_\mu), \\ K^\pm &\longrightarrow \mu^\pm + \nu_\mu(\bar{\nu}_\mu), \\ &\longrightarrow \pi^0 + \mu^\pm + \nu_\mu(\bar{\nu}_\mu).\end{aligned}$$

The density of the atmosphere decreases exponentially with the height. Therefore, the possibility of an interaction of a meson with an air nucleus increases with decreasing height, thus, only at large heights the mesons can decay before they interact. Therefore, most of the muons are generated high in the atmosphere, which in turn means, that they are generated at an early stage of the shower development.

Muons are mainly emitted in the direction of the line of flight of the parent mesons. Therefore, the lateral distribution of the muons is mainly caused by the momenta of these mesons. The contributions of multiple scattering and bremsstrahlung are suppressed by a factor of  $(m_e/m_\mu)^2$  compared to electrons, thus, these processes have only a small effect on the lateral distribution. In addition, muons are not effected by strong interaction and lose energy only by ionization. Therefore, muons travel almost undisturbed and their tracks show back to their point of production.

The lateral distribution of the muonic component can be described similarly to the proposed function in [Lag01]. More details can be found in Chap. 4. In Fig. 2.4, the average longitudinal and lateral density distribution for muons is shown for extensive air showers initiated by two different types of primaries and two different primary energies. The longitudinal development of the muonic component shows an increase of the

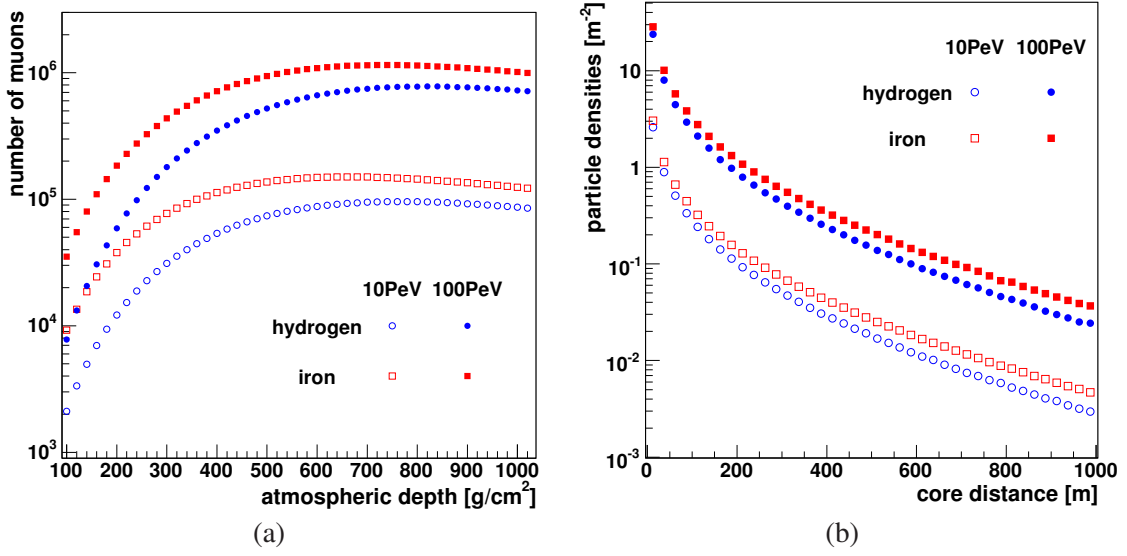
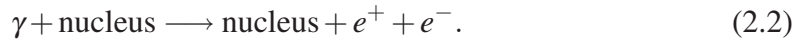


**Figure 2.4:** Average longitudinal (*left*) and lateral distribution (*right*) of muons. In order to obtain these distributions for each primary particle and each primary energy, 50 air showers have been simulated with CORSIKA [Hec98]. Taken from [Bur06].

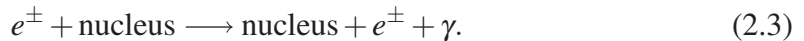
number of muons up to a maximum number. After the maximum, the number of muons decreases only slowly, showing no pronounced maximum but rather a plateau. This is due to the fact, that the muons do not vanish in interactions and the decay is suppressed by the relativistic time dilatation. The lifetime in the laboratory system is prolonged in such a way, that a decay is improbable. It can also be seen, that the maximum depends weakly on the type of the primary particle, but strongly on the energy of the primary particle. Therefore, the number of muons can be used as an energy estimator.

### The electromagnetic component

The electromagnetic component is fed by the hadronic component of the extensive air shower. Neutral pions decay into two photons, each initiating an electromagnetic cascade. The photons generate electron-positron pairs by the reaction:



In turn, the electrons and positrons generate further photons via bremsstrahlung:



Both processes feed each other, which develops to an electromagnetic subcascade of the air shower. Additionally, neutral pions are generated continuously along the shower axis. Each of these pions is the starting point of a new electromagnetic subcascade. The superposition of the subcascades determines the longitudinal development of the number of electromagnetic particles, which multiplies in such a way, that they become the most numerous particles in an air shower. The longitudinal development of a photon-induced shower can be described by [Gre56]:

$$N_e(E_0, t) = \frac{0.31}{\sqrt{\beta_0}} \cdot e^{t(1-1.5 \ln s)}, \quad (2.4)$$

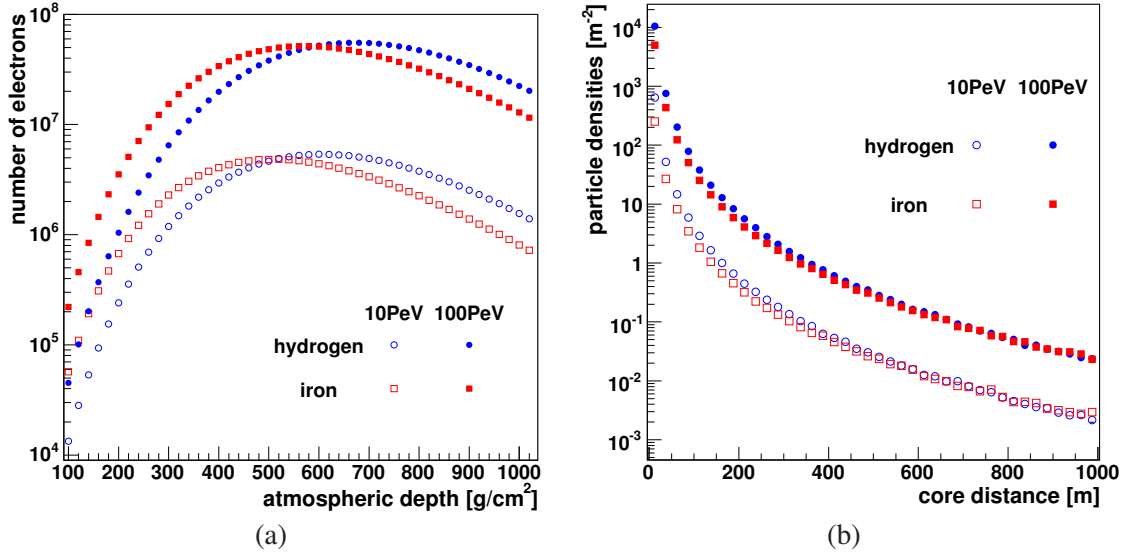


**Figure 2.5:** Average longitudinal (*left*) and lateral distribution (*right*) of electrons. In order to obtain these distributions for each primary particle and each primary energy, 50 air showers have been simulated with CORSIKA [Hec98]. Taken from [Bur06].

with:

$$t = \frac{X}{X_0}, \quad \beta_0 = \ln \frac{E_0}{E_{\text{crit}}}, \quad \text{and} \quad s = \frac{3t}{t + 2\beta_0},$$

where  $i$  is the atmospheric depth measured in units of the radiation length  $X_0$ , which is  $37.15 \text{ g/cm}^2$  in air,  $E_0$  is the energy of the initiating photon, and  $s$  is the so-called (longitudinal) shower age. This age parameter describes the shower development. At the beginning of the shower  $s$  is equal zero and at the maximum of the shower the parameter becomes one. Thus, for  $s > 1$  the number of particles decreases. The critical energy  $E_{\text{crit}}$  defines the energy, at which the energy loss rates due to ionization and due to bremsstrahlung are equal. In air, the critical energy corresponds to  $E_{\text{crit}} = 84.2 \text{ MeV}$ .

The lateral spread of an electromagnetic shower is caused by Coulomb scattering. The lateral distribution can be described by the NKG function, named after J. Nishimura, K. Kamata, and K. Greisen [Gre56, Kam58]:

$$\rho_e(r) = \frac{\Gamma(4.5 - s)}{\Gamma(s)\Gamma(4.5 - 2s)} \cdot \frac{N_e}{2\pi r^2} \cdot \left(\frac{r}{r_M}\right)^{s-2} \left(1 + \frac{r}{r_M}\right)^{s-4.5}, \quad (2.5)$$

with the electron density  $\rho_e$  at the distance  $r$  from the shower axis, the total number of electrons at observation level  $N_e$ , and the Molière radius  $r_M$ , which is  $r_M = 79 \text{ m}$  at sea level.

The NKG function is valid for purely electromagnetic showers. The considered extensive air showers in this section are initiated by hadrons. These showers lead to several electromagnetic subcascades, which superimpose. This means, that the NKG function does not describe such showers. Nevertheless, with different parameters of the NKG function, it can still be used to describe the lateral development of the electromagnetic component of hadronically initiated air showers. In KASCADE-Grande the number

of electrons in an air shower is reconstructed by using a modified NKG function, see Chap. 4.

Fig. 2.5 shows the average longitudinal and lateral density distributions for electrons in an air shower, initiated by primary particles of two different types and two different primary energies. Unlike the longitudinal development of the muonic component, the number of electrons shows a pronounced maximum. This is due to the fact, that electrons interact in the atmosphere, and hence, get lost. This means, that the number of electrons measured at ground depends on the altitude at which the experiment is positioned. The position of the maximum of the number of electrons is called shower maximum  $X_{\max}$  and is measured in units of the atmospheric depth. Furthermore, it can be seen, that the shower maximum depends on the type of the primary particle. Proton induced showers have their maximum deeper in the atmosphere compared to iron induced showers. On the other hand, for a given type of the primary particle, the shower maximum depends only weakly on the primary energy. Therefore, the position of the shower maximum is a measure of the type of the primary particle. This is utilized by the measurement of air showers using fluorescence detectors, like in Auger or Fly's Eye/HiRes.



---

# The KASCADE-Grande experiment

---

The KASCADE-Grande experiment has been built to measure extensive air showers at ground level. The setup is located at the Forschungszentrum Karlsruhe, Germany at 110 m above sea level ( $49^\circ$  N,  $8^\circ$  E) with dedicated detector components to measure the electromagnetic, the muonic and the hadronic parts of extensive air showers. The main purpose of the experiment is the exploration of the chemical composition and the energy spectrum of the primary cosmic radiation.

The KASCADE-Grande experiment has different advantages. Firstly, ambiguities in reconstructing air showers, can be eliminated, with help of several different observables. Secondly, increasing the detector area increases the maximum energy which can be measured, and also the statistics, and hence the precision of the measurement is improved. In order to achieve this, the KASCADE experiment was extended to KASCADE-Grande. Fig. 3.1 shows sketches of the KASCADE-Grande experiment.

KASCADE by itself is divided into three different subdetectors, the central detector, the KASCADE detector array and the muon tracking detector [Ant03b]. This setup allows to measure air showers in the energy range from  $10^{14}$  eV to  $10^{17}$  eV. KASCADE has been taking data since 1996 and the analysis of this data found a knee structure in the energy spectra of the light mass groups [Ant05]. The extrapolation of the measured knee positions led to the expectation, that the knee structures of the heavier mass groups are around  $E = 10^{17}$  eV, which is on the edge of the energy range of KASCADE, causing low statistics of measured air showers and making it impossible to disentangle the knee positions of the heavy components of the cosmic radiation. The extension of KASCADE to KASCADE-Grande helps to this problem. The EAS-TOP experiment [Agl89, Agl93] finished its operation in 2000 and its scintillation detectors were used to enlarge the KASCADE array with 37 detector stations, the Grande array. With this setup, the experiment measures in the range from about  $10^{14}$  eV to  $10^{18}$  eV of the primary particle energy. Additionally, a trigger array (the Piccolo array), providing a common, fast trigger signal for the entire KASCADE-Grande experiment was built, complementing the components of KASCADE-Grande. In the following chapters, an overview of the different experimental components is given.

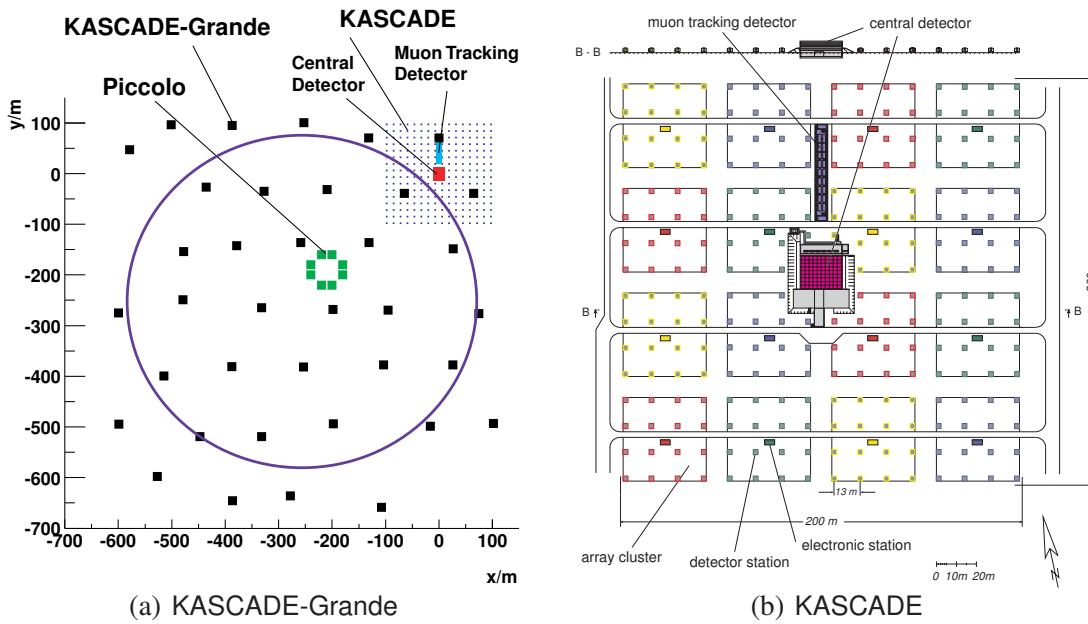


**Figure 3.1:** (a): Sketch of the entire KASCADE-Grande layout. Including the Grande array, the Piccolo array, and the KASCADE experiment [Hau03]. (b): Layout of the KASCADE experiment including the different subdetectors (the central detector, the muon tracking detector and the KASCADE array) [Ant03b].

### 3.1 The KASCADE detector array

The purpose of the KASCADE detector array is the measurement of the electromagnetic and the muonic components of extensive air showers.

A sketch of the array is shown in Fig. 3.1(b). The array consists of 252 detector stations arranged in a grid with a 13 m spacing and a total size of  $200 \times 200 \text{ m}^2$ . These stations are organized in 16 clusters. Every cluster contains 16 detector stations and one electronics station. In order to install the central detector, see Chap. 3.2, one station of each inner cluster had to be removed. Therefore, the four inner clusters contain only 15 stations. Each cluster is an independent unit and can be operated independently [Sch96].

A profile view of a detector station is shown in Fig. 3.2(a). The detector stations of the outer clusters are equipped with two  $e/\gamma$  detectors mounted on an absorber of 10 cm lead and 4 cm iron. Below the absorber a segmented  $\mu$  detector is positioned, see Fig. 3.2(b). The thickness of the absorber material corresponds to about 20 radiation lengths and hence 230 MeV threshold energy for vertical muons [Ant03b]. The stations of the four inner clusters are equipped with four  $e/\gamma$  detectors, but no  $\mu$  detector. For these inner stations, the muonic component is measured by the muon tracking detector and the muon chambers described in Chap. 3.3. In order to obtain a shower reconstruction which is dominated by intrinsic shower fluctuations instead of the sampling statistics, the layout of the array was optimized by means of Monte-Carlo simulations [Ant03b].



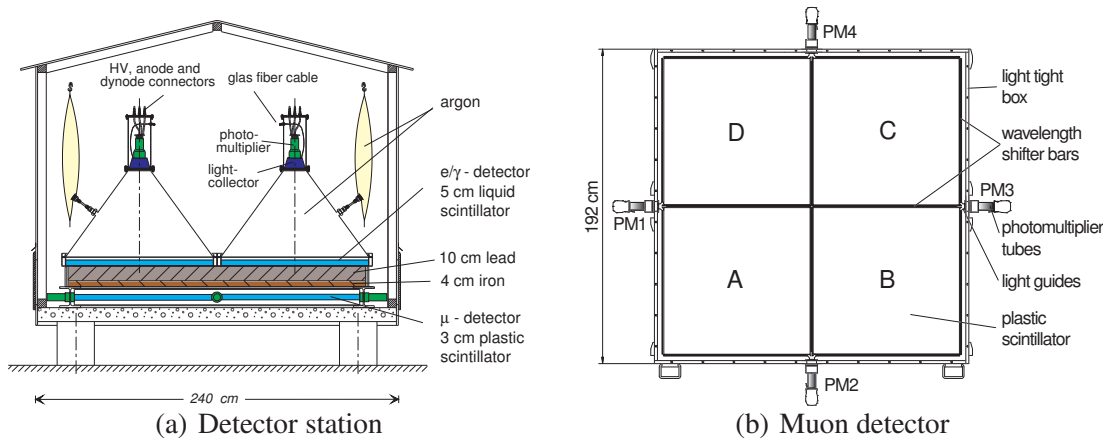


**Figure 3.2:** (a): Schematic view of an array detector station [Ant03b]. (b): Sketch of the  $\mu$  detector [Ant03b].

### 3.1.1 The $e/\gamma$ detector

The  $e/\gamma$  detector (see Fig. 3.2(a)) consists of a circular steel tube of 1 m diameter and 5 cm height. It is vertically mounted on a stainless steel light collection cone. The scintillator material used, PDP, is a mixture of 80 % paraffin and 20 % pseudocumene with 2 g/l of scintillator PMP (1-phenyl-3-mesityl-2-pyranoline). It has a scintillation time of 2.5 ns. The efficiency of light collection is improved by diffusive reflection through a white paint of the cone. Finally, the light is collected by a plexiglass light guide in front of the photomultiplier tube (PMT), which enhances the signal by a factor of 1.8. The 3 inch diameter PMTs (type EMI 9822 or Valvo XP3462) are attached to the light cones.

Two amplifications are used to reach the required dynamic range of about 1 : 8000 [Völ92]. Hence, the signal of the PMT is decoupled at the anode and at the last but two dynode, for the low amplification. The anode signals of the four PMTs are transmitted separately to the data acquisition (DAQ) system. The dynode signals, on the other hand, are summed up and sent then to the DAQ. For the mean energy deposit of a minimum ionizing particle (m.i.p.) at 12 MeV, an energy resolution of 8 % has been reached. The time resolution of the  $e/\gamma$  detector was determined to  $\sigma = 0.77$  ns [Völ92]. With a threshold of 1/4 m.i.p. ( $\approx 3$  MeV) an energy deposit of 2000 m.i.p. can be detected linearly [Ant03b].

### 3.1.2 The $\mu$ detector

A layout of the  $\mu$  detector is shown in Fig. 3.2(b). The quadratic plastic scintillator plate (type Bicron BD-416) is segmented into four 3 cm thick quadratic plates with an edge length of 90 cm. The  $\mu$  detector is shielded by 4 cm of iron and 10 cm of lead. On all four sides the light is read out by a wavelength shifter bar and guided by a plexiglass light guide to the four 1.5 inch PMTs (type EMI 9902 or Valvo XP2081). The individual signals of the four PMTs are sent to the DAQ. The spacial non-uniformity of the sum

signal has been determined to  $\sigma = 2\%$ . The detector reaches an energy resolution of about 10% at 8 MeV, which is the mean energy deposit of a m.i.p., and a time resolution of  $\sigma = 2.9\%$  [Ant03b, Kri92].

### 3.1.3 The FADC system

In cluster 1, the lower left cluster in Fig. 3.1(b), a Flash-ADC (FADC) system is installed. It allows to measure the time structure of individual showers. Together with the separation of the electromagnetic and muonic component it was possible to determine a time cut for the separation of electrons and muons in extensive air showers [Brü07]. More details about the FADC system can also be found in [Hor01].

### 3.1.4 Data acquisition

Every cluster has its own electronics station positioned in the center of the cluster, as can be seen in Fig. 3.1. Each electronics station is equipped with high voltage (HV) control, a clock module, a trigger unit, and KAFE (KASCADE array frontend electronics) modules and is managing the data acquisition, the trigger, and the detector control of the associated detector stations. This way, each cluster acts independently [Sch96].

One KAFE module serves two detector stations belonging to the cluster, i.e. eight KAFE modules are installed in each electronic station. Depending on the configuration of these detector stations, the KAFE modules are processing the four individual anode signals of the  $e/\gamma$  PMTs, the summed dynode signal of the  $e/\gamma$  PMTs, and the four anode signals of the  $\mu$  PMTs. To cancel delays between stations, all signal and HV cables are equal in length. A 5 MHz clock signal pulse, generated by a rubidium high frequency generator, is synchronized with a 1 Hz clock signal coming from a GPS receiver. Both clock signals are distributed to the electronic stations via optical fibers [Ant03b]. These signals are used to determine a common trigger time in order to label each event with a time stamp. At the stage of event building, this allows to relate the data of the individual detector stations with each other.

The KAFE module integrates the anode signal of each station and digitizes it by an 8-bit ADC (analog-to-digital converter). The integration time for PMT signals above discriminator threshold is 200 ns. By means of an energy calibration, the measured charge is converted into the energy deposit of the corresponding station. The discriminator threshold is set to 1/4 of a m.i.p. [Ant03b]. Additionally, each event is marked with the arrival time of the first particle, which is measured with a time-to-digital converter (TDC). The resolution of the TDC is about 270 ps. The whole KASCADE array is triggered by the cluster triggers. A cluster trigger is generated if a certain number of stations in a cluster is above threshold. If one cluster generates such a trigger signal, the remaining clusters are read out by the central DAQ. For outer clusters the number of stations above threshold has to be at least 10, for the inner cluster 20. More details about data acquisition and detector electronics can be found in [Sch96, Ant03b].

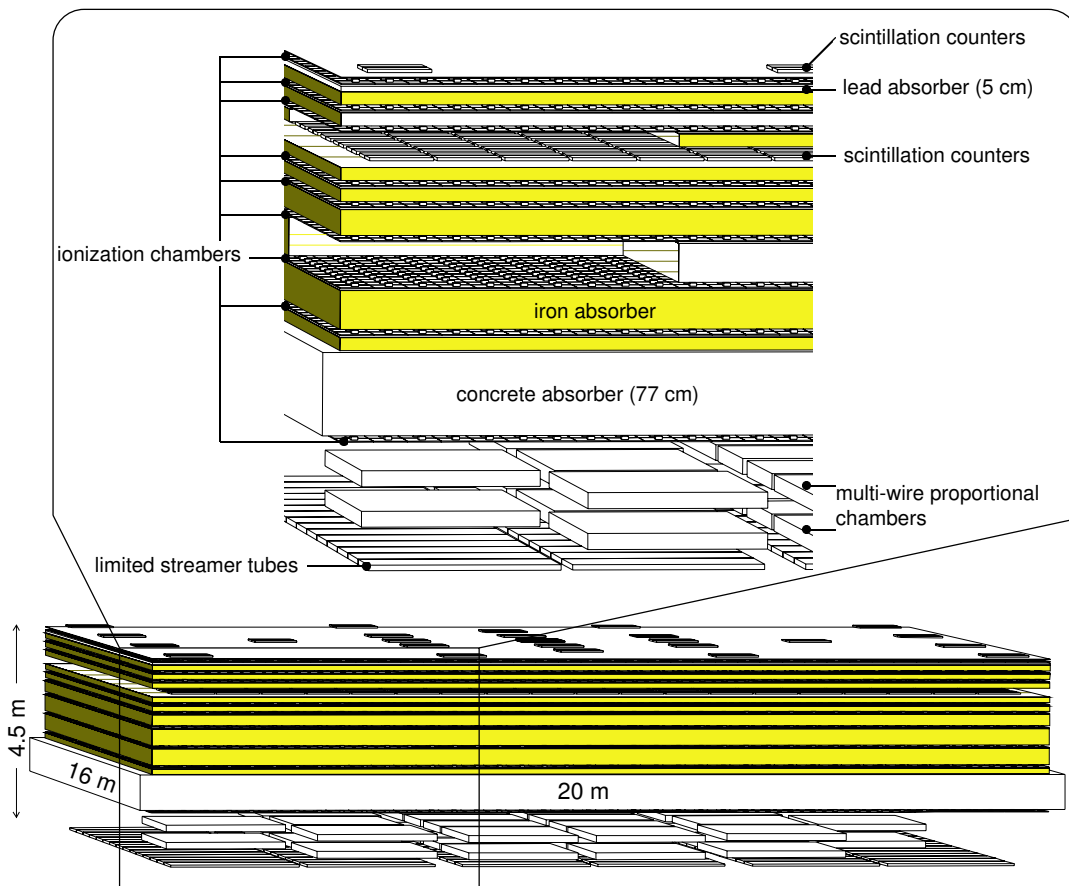


**Figure 3.3:** Schematic view of the central detector and its subdetectors [Ant03b].

## 3.2 The central detector

The central detector is placed in the center of the KASCADE array, as shown in Fig. 3.1(b). Its main purpose is a detailed study of particle densities in the core of the extensive air showers. To achieve this, the central detector is divided into different specialized subdetectors, which can be seen in Fig. 3.3. The combined information of all these subdetectors give a detailed insight into the properties of extensive air showers. The central detector covers an area of about  $320\text{ m}^2$ , ensuring a detection rate of about 100 particles per year at a primary energy of  $10^{16}\text{ eV}$ . The highly segmented hadron sampling calorimeter represents the main part of the detector [Eng99]. It comprises of eight tiers of iron absorber separated by 9 layers of warm-liquid ionization chambers. Above the first lead absorber, the so-called top cluster is mounted. Underneath the third absorber plane, a layer of plastic scintillators serves as timing facility and read out trigger for the other components of the central detector. Finally, in the basement of the central detector, a muon chamber system is installed, consisting of a combination of multi-wire proportional chambers (MWPC), and a layer of limited streamer tubes (LST) [Boz01, Ant03a].

### 3.2.1 Hadron calorimeter

The main task of the hadron calorimeter is the measurement of hadron densities in the shower core and the energies of individual hadrons, hence, the hadron calorimeter is finely segmented. In total it consists of about 11000 ionization chambers, which are filled with purified tetramethylsilane (TMS) or tetramethylpentane (TMP). These liquids were chosen to provide a high dynamic range and long-term stability [Ant03b]. Due to its thickness, corresponding to 11.5 nuclear interaction lengths in the vertical direction, hadrons up to 25 TeV are absorbed. The energy leakage is less than 2.5 %. A detailed description of the calorimeter including operational tests and first results can be found in [Eng99].

### 3.2.2 The muon chamber system and trigger plane

To measure the high energy muons of extensive air showers crossing the calorimeter in correlation with their hadronic components, a muon chamber system was installed at the central detector. The system includes two layers of MWPCs [Boz01], and one layer of LSTs [Ant03a], together with a triggering layer of plastic scintillators.

Two layers of MWPCs with a vertical gap of 38 cm, covering an area of 129 m<sup>2</sup> each, are installed in the basement of the central detector underneath the hadron calorimeter. Thus, the whole absorber consists of 5 cm lead and 172 cm iron absorber of the hadron calorimeter, and 77 cm of concrete. This leads to a threshold of 2.4 GeV for vertical muons. The mean deflection angle for vertical muons is about 1.5 ° [Boz01].

A third layer of LSTs is installed below the MWPCs. It comprises of six rows and 15 modules each. As counting gas pure carbon dioxide (CO<sub>2</sub>) is used. This layer improves the reconstruction of muon tracks. Especially, in showers having their axis close to the central detector, it helps to reduce the ambiguities of the reconstruction [Ant03b].

In addition, there is a layer of 456 scintillation counters (type NE 114) mounted at the third gap of the absorber of the calorimeter (see Fig. 3.3). The absorber above the trigger plane (5 cm lead and 36 cm iron) corresponds to 30 radiation lengths, which corresponds to a threshold energy of 490 MeV for vertical muons. The trigger layer covers 64 % of the calorimeter area [Bre98]. The mean timing resolution was determined to  $\sigma = 1.7$  ns [Ant03b]. The layer is used to trigger the muon chamber system and to get timing information for air showers hitting the central detector. A detailed description of the trigger layer can be found in [Bre98].

### 3.2.3 Top cluster and top layer

On top of the central detector the top cluster and top layer are installed, see Fig. 3.3.

The top cluster covers 7.5 % of the area and fills the gaps of the missing detector station in the center of the KASCADE array. It consists of 25 scintillator counters, which are of the same type as the counters in the trigger layer of the calorimeter (see Chap. 3.2.2). It mainly serves as trigger source for small extensive air showers [Ant03b, Hae96].

The top layer is placed below the top cluster. The top layer consists of chambers which are filled with TMP and covers the entire surface. To achieve a good separation of

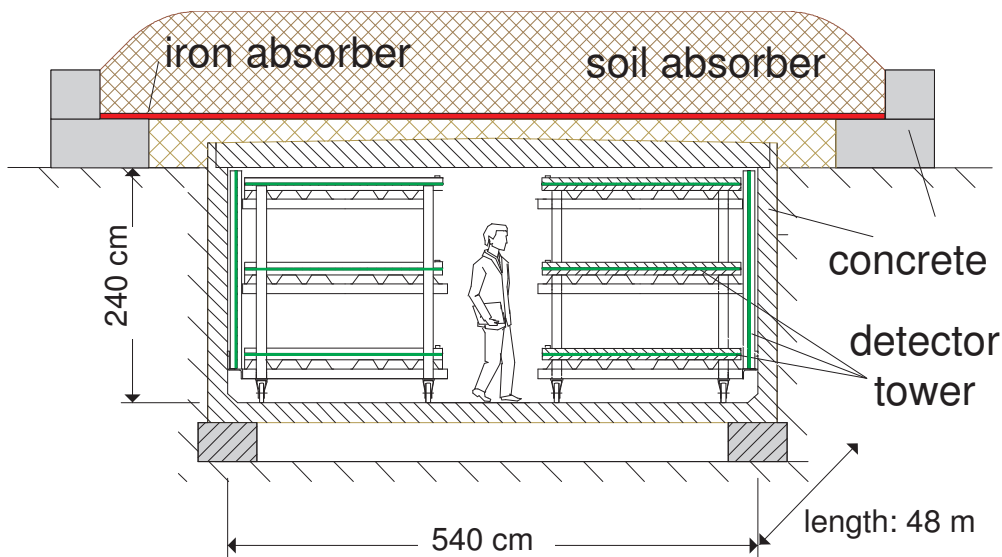


**Figure 3.4:** Side view of the muon tracking detector [Ant03b].

minimal ionizing particles from noise, the chambers are twice as thick as the chambers used in the calorimeter.

For the KASCADE experiment, the central detector was used to determine the shower centers of air showers hitting the central detector. Thereby, the shower centers for small showers could be measured with the top layer, whereas, the centers of large extensive air showers could be determined precisely by the electromagnetic punch-through to the first active layer of ionization chambers of the hadron calorimeter [Ant03b].

### 3.3 The muon tracking detector

In the center of the KASCADE array, to the north of the central detector, the muon tracking detector (MTD) is set up, see Fig. 3.1. The detector is installed in a tunnel ( $5.4 \times 2.4 \times 44 \text{ m}^3$ ) and is shielded with concrete, iron, and soil, resulting in a shielding of 18 radiation lengths thickness and a threshold energy for vertical muons of  $0.8 \text{ GeV}$  [Dol02]. A side view of the configuration can be seen in Fig. 3.4.

The aim of the muon tracking detector is the identification of muons and the reconstruction of their production height in extensive air showers. The production height is sensitive to the primary mass of the cosmic ray particle. Thus, the detector consists of three horizontal levels of LSTs, determining the production height by triangulation. The LSTs are mounted in 16 detector towers with a spacing between the levels of 82 cm. The towers are organized in two rows along the tunnel. With a total length of 32 m, the detector achieves a total detection area of  $128 \text{ m}^2$  for vertical muons. Additionally, one LST is installed vertically on each tower, increasing the acceptance for inclined tracks. The total acceptance is about  $500 \text{ m}^2 \text{ sr}$  [Dol02].

The LSTs are of the same type as those used in the central detector (see Chap. 3.2.2), but using a mixture of isobutane (60%), argon (20%), and  $\text{CO}_2$  (20%) as counting gas. This mixture gives a hit detection probability of 85% and hence a three-hit track

efficiency of 60 % [Ant03b]. The design and dimensions of the muon tracking detector define the geometrical resolution, which is about  $\sigma = 0.35^\circ$  for vertical muons. The true resolution is worse, because of the muons interacting with the shielding and the material of the chambers. The detector geometry is also only known with a finite accuracy. Using a GEANT simulation, the resolution was determined to be  $\sigma = 0.56^\circ$  [Ant03b]. A detailed description of the muon tracking detector and the read-out electronics can be found in [Dol02, Zab02].

### 3.4 The Grande array

The Grande array was installed in order to increase the detector area of the KASCADE experiment to reach higher detectable energies of cosmic radiation. The layout of the experiment can be seen in Fig. 3.1. The array consists of 37 detector stations, distributed over the Forschungszentrum Karlsruhe, Germany. The detector array, with an average grid size of 137 m, provides an effective detector area of more than  $0.5 \text{ km}^2$ . Each detector station consists of 16 scintillation counters (type NE 102A) with an area of  $80 \times 80 \text{ cm}^2$  each, re-used from the former EAS-TOP experiment [Agl89]. These counters, arranged in a square, establish a detector area of  $10 \text{ m}^2$ . Each scintillator is connected to a PMT (type XP3462), whose output signals in turn are passively summed to a high gain signal in the mixer module of the station. The inner four detectors feature an additional second PMT, operating with lower voltage to offer low gain signals. This enables a dynamic range from 0.3 – 30000 charged particles per station. In the center of the Grande array a central DAQ station is positioned. All signals coming out of the mixer module are amplified and shaped with an integration time of  $11 \mu\text{s}$  inside the detector station. Afterwards, the signals are transmitted to the central DAQ station. A peak sensitive ADC in the DAQ station digitizes the received signal [Nav04].

The Grande array is electronically divided into 18 hexagonal clusters. Each of these clusters consist of six outer and one central station, serving as trigger. Two different trigger conditions are implemented. A 4-fold trigger (4/7) demands signals from three outer and the central station. For the 7-fold trigger (7/7), all six outer stations and the central station must have a signal over threshold. The trigger rate of a cluster was measured to about 0.3 Hz and the total rate of Grande to approximately 5.9 Hz [Kam03]. A detailed description of the DAQ system can be found in [Ove04].

### 3.5 The Piccolo array

Between the centers of KASCADE and Grande, a small trigger array (Piccolo) is placed. It provides a fast trigger for the KASCADE muon detection system and the muon tracking detector. In the absence of Piccolo, the multidetector information of KASCADE would only be available for showers above  $10^{17} \text{ eV}$ . With Piccolo the full detection efficiency is reached for about  $E \gtrsim 10^{16} \text{ eV}$  [Kam03].

The Piccolo array comprises of eight scintillator stations arranged in an octagon with a distance of 20 m between the stations. Each station consists of 12 scintillator plates with a total area of  $10 \text{ m}^2$ , re-used from the KARMEN neutrino experiment [Gem90].

Six modules made out of two scintillators are installed in each Piccolo station. Piccolo produces a trigger signal if either a coincidence is detected in four or more out of the 48 modules or in two out of the eight stations. The trigger signal is then sent to KASCADE and Grande.

## 3.6 Central data acquisition

All components of the KASCADE-Grande experiment, the KASCADE detector array, the FADC system, the muon tracking detector, the top cluster, and the top layer, the MWPCs, and the LSTs, the hadron calorimeter, as well as the Grande and the Piccolo arrays are independent components and can be operated independently. In case of failures or maintenance of a component the remaining components can still take data. The data of the different parts can be correlated by the use of common clock signals. All components of the experiment are merged in the central DAQ station, which is housed in the building of the central detector. At the central DAQ the data taking is started and controlled. It accounts for the joint measurement, including the appropriate trigger sources, and hence ensures data consistency [Ant03b].





---

# Reconstruction and simulation of extensive air showers

---

The air showers measured by KASCADE-Grande are reconstructed using the KRETA program, which is an acronym for KASCADE reconstruction for extensive air showers. In the reconstruction the measured TDC and ADC values are used to calculate the properties of extensive air showers like the shower core position, the arrival direction or the number of electrons and the number of muons in the shower. In this work, the number of charged particles  $N_{\text{ch}}$  and the number of muons  $N_{\mu}$  as well as the zenith angle  $\theta$  of an air shower will be used. Part one of this chapter explains the steps performed in the shower reconstruction.

Part two gives an overview of how to simulate extensive air showers in KASCADE-Grande. This is strongly connected with the reconstruction of extensive air showers and it is a crucial tool in the analysis presented in the following chapters.

## 4.1 Reconstruction of extensive air showers in KASCADE-Grande

The analysis in this work is based on showers reconstructed by Grande, i.e. showers triggering the Grande array. Showers detected by the KASCADE array alone or other components of the experiment are not in the scope of this work. Therefore, this chapter focuses on the procedure of reconstructing Grande events. Details about the reconstruction of KASCADE events can be found in [Web99, Ant01, Mai03].

In order to reconstruct Grande showers the KRETA program was extended. Firstly, KRETA has to convert the measured ADC and TDC values per station into energy deposits and time information. This conversion is performed by means of calibration spectra, measured either beforehand or in parallel during data taking. Hence, energy deposits and time information together with the coordinates of each detector station are entering the reconstruction algorithm. The implemented algorithm works in three it-

erative steps, called levels. Each level improves the calculated values of the previous level.

### Level 1

The goal of the first level is to provide starting values of shower observables for the following level. A fast and robust procedure is used in order to assure valid data entering the next level. This is achieved by avoiding minimizing routines, thus, the shower core position is estimated by a center of gravity method. It weights the coordinates of a detector station with the energy deposit measured in this station [Brü07]. This method can just provide shower core positions inside the Grande array.

Two methods are implemented to reconstruct the arrival direction of an extensive air shower within level 1. The first method uses the three stations with the highest energy deposits. A plane shower front is adjusted to the arrival times of these stations in an iterative way, providing a shower direction. The second method, which is used as standard procedure, uses the arrival times of all stations and weights them with locally measured particle densities. An average shower front was determined using simulations and the time differences between the measured data and the expected ones are calculated for every station. The requirement, that the sum of all these differences should be minimal, results in an estimation of the shower front, and hence, of the arrival direction [Brü07]. The advantage of this method is that the average shower front has a curvature. Therefore it is a more realistic shower front than the approximation by a plane, used in the first method. On the other hand, the distance to the shower core has to be known in order to describe the curvature, and accordingly, the method relies on the estimation of the position of the shower core. In case this estimation fails, the first method is used [Bur06, Brü07].

To perform further calculations, it is useful to translate all coordinates into shower disk coordinates (SDC). The shower axis of the air shower is the  $z$ -axis,  $z^{\text{SDC}}$ , in the SDC system. The  $x^{\text{SDC}}-y^{\text{SDC}}$ -plane of the SDC system is perpendicular to the shower axis and represents the shower plane. In this system, shower properties are independent of the arrival direction. For example, the lateral density function:

$$\rho(r) = N_x \cdot f_x(r) \quad (4.1)$$

describes the density of particles of type  $x$  at a distance  $r$  from the shower core in SDC. Here  $N_x$  is the number of particles in the detected air shower and  $f_x(r)$  is the lateral distribution function, also given in SDC, for particles of type  $x$  normalized to 1. Knowing  $f_x(r)$  allows to estimate the number of particles  $N_x^{\text{est}}$  in the shower. The energy deposit is measured in each station  $i$  at distance  $r_i$  from the shower core. The particle density  $\rho_x(r_i)$  is obtained by dividing the energy deposit at distance  $r_i$  by the mean energy deposit of one particle at distance  $r_i$ . The mean energy deposit of one particle is determined using shower simulations. The particle density converts into the number of particles  $n_i^x$  for this station. Summing over all detector stations and correcting the detector area  $A_i$  seen by the shower particles for inclined showers with zenith angle  $\theta$  by factor  $\cos \theta$ :

$$\sum_{i=1}^M n_i^x = \sum_{i=1}^M N_x^{\text{est}} \cdot f_x(r_i) \cdot A_i \cos \theta = N_x^{\text{est}} \cdot \sum_{i=1}^M f_x(r_i) \cdot A_i \cos \theta, \quad (4.2)$$

provides an estimator for the number of particles in the shower [Bur05]:

$$N_x^{\text{est}} = \frac{\sum_{i=1}^M n_i^x}{\sum_{i=1}^M f_x(r_i) \cdot A_i \cos \theta}. \quad (4.3)$$

The Grande detector station can not discriminate between the electromagnetic and the muonic components, i.e. it is measuring all charged particles (see Chap. 3.4). In order to estimate the number of charged particles  $N_{\text{ch}}$  in level 1, the function  $f_{\text{ch}}(r)$  has to be found. Therefore, twenty hydrogen and iron induced air showers were simulated. The primary energy was fixed to  $E_p = 10^{17}$  eV and the zenith angle to  $\theta = 22^\circ$ . The average particle density distribution was fitted to the function:

$$f_{\text{ch}}(r) = \frac{10^{(p_1 r + p_2 r^2 + p_3 r^3)}}{2\pi \cdot C \cdot r_0^2}. \quad (4.4)$$

The parameters were determined to  $C = 4.8267$ ,  $r_0 = 90$  m,  $p_1 = -2.462$ ,  $p_2 = -0.4157$ , and  $p_3 = 0.09863$  [Brü07].

In level 1, the muon number  $N_\mu$  is estimated by using the muon detectors of the KASCADE array (see Chap. 3.1.2) and fitting the measured energy deposit with the lateral density distribution function describing muons:

$$f_\mu(r) = \frac{0.28}{r_0^2} \left(\frac{r}{r_0}\right)^{p_1} \cdot \left(1 + \frac{r}{r_0}\right)^{p_2} \cdot \left(1 + \left(\frac{r}{10 \cdot r_0}\right)^2\right)^{p_3}. \quad (4.5)$$

In order to obtain the parameters of this function, hydrogen and iron initiated air showers in the energy range of  $10^{16}$  eV to  $10^{17}$  eV were simulated and fitted to the lateral density distribution function. Using a scaling factor of  $r_0 = 320$  m, the parameters were determined to be  $p_1 = -0.69$ ,  $p_2 = -2.39$ , and  $p_3 = -1.0$  [Bur05].

The number of electrons  $n_e^i$ , measured with the e/ $\gamma$  detectors in KASCADE, are used to get a first estimate of the electron number  $N_e$  and Eq. (4.4) is used to describe the lateral density distribution function for electrons.

## Level 2

The estimated number of muons  $N_\mu^{\text{est}}$  in level 1 is used to calculate the electron number in level 2. For each station  $i$ , the number of charged particles  $n_i^{\text{ch}}$  is known. The number of estimated muons per station  $n_i^\mu$  can be calculated, using the lateral density distribution function of level 1, Eq. (4.5). The number of electrons  $N_e$  is described by a slightly modified NKG function (see Chap. 2) [Ape06]:

$$f_e(r) = \frac{\Gamma(\beta - s)}{2\pi r_0^2 \Gamma(s - \alpha + 2) \Gamma(\alpha + \beta - 2s - 2)} \left(\frac{r}{r_0}\right)^{s-\alpha} \left(1 + \frac{r}{r_0}\right)^{s-\beta}. \quad (4.6)$$

The parameter  $s$  is the so-called shower age. Performing a CORSIKA air shower simulation (see Chap. 4.2) the parameters were found to be  $\alpha = 1.5$ ,  $\beta = 3.6$ , and  $r_0 = 40$  m [Ape06]. The fit in level 2 has to fulfill the condition that the number of charged particles is the sum of the number of electrons and the number of muons.

Simulated air showers have been used to obtain an average shower front. This shower front was parameterized by a Linsley function [Gla05]:

$$\bar{t}(r) = 2.43 \text{ ns} \cdot \left(1 + \frac{r}{30 \text{ m}}\right)^{1.55} \quad \text{and} \quad \sigma_t(r) = 1.43 \text{ ns} \cdot \left(1 + \frac{r}{30 \text{ m}}\right)^{1.39}. \quad (4.7)$$

It describes the arrival time  $\bar{t}(r)$  and the spread  $\sigma_t(r)$  of the shower particles at distance  $r$  from the shower core. In first order approximation, the arrival time of the first particle out of  $N$  particles in a detector is given by  $\bar{t}_{1\text{st of } N} = \bar{t}/\sqrt{N}$  [Gla05]. Fitting the arrival times of the shower front measured by each Grande detector to the parameterized shower front, improves the estimates of the shower core position and the arrival direction.

Both equations, the lateral density distribution of electrons (Eq. 4.6) and the parameterized average shower front (Eq. 4.7), are linked together by the shower core distance  $r$ . Thus, the fit to the data is done simultaneously in a combined negative-log-likelihood minimization [Gla05]. The global fit has to vary seven free parameters, the core position  $(X_c, Y_c)$ , the shower direction (zenith  $\theta$  and azimuth angle  $\phi$  including a time offset  $\Delta t$ ), the electron number, and the shower age. Unlike in level 1, the resulting shower core position can be outside the Grande array. A new muon number is calculated using the improved shower core position and shower direction. The number of charged particles  $N_{\text{ch}}$ , calculated in this level, will be used in the analysis.

### Level 3

Level 3 uses the improved muon number of level 2 to reconstruct the lateral electron distribution. This improves the determination of the core position, the arrival direction, and the electron number compared to level 2. These enhanced variables are used to fit again the muon lateral distribution, improving the number of muons. The reconstructed parameters of level 3 are the final result of the air shower reconstruction of Grande and are used for all analyses of the KASCADE-Grande data.

## 4.2 Simulation of extensive air showers for KASCADE-Grande

The simulations consist of two main parts. The first part is the simulation of the development of the air shower in the atmosphere down to ground level. The second part simulates the detector response, which is caused by the shower particles in the detector. In the following chapters these simulations are used to determine cuts on the measured data, to estimate systematic errors, and to evaluate the energies of the primary particles.

In KASCADE-Grande the simulation of extensive air showers is accomplished by the CORSIKA (cosmic ray simulation for KASCADE) program [Hec98]. It describes the development of an extensive air shower initiated by high energetic cosmic ray particles with Monte Carlo methods. The initial particle, its energy, and its arrival direction can be chosen. CORSIKA handles muons, electrons, nuclei and photons. Each particle is tracked until it reaches ground level, or until it undergoes a reaction or a decay. If the energy of a particle falls below an adjustable threshold energy, it is not treated furthermore. All decays with branching ratios down to 1 % are considered. The various

Number of sets	Zenith angle range	Energy range [eV]	Passes to CRES	Area enlarged by
4	0° – 42°	$1.0 \cdot 10^{13} - 1.0 \cdot 10^{18}$	10	1
1	0° – 42°	$1.78 \cdot 10^{14} - 1.0 \cdot 10^{18}$	15	1.5
3	0° – 70°	$1.0 \cdot 10^{15} - 1.0 \cdot 10^{18}$	10	1.5
4	0° – 70°	$1.0 \cdot 10^{13} - 1.0 \cdot 10^{18}$	20	2

**Table 4.1:** Simulation sets used in the analysis. See text for the properties in common to all simulation sets.

types of interactions are handled by different programs or modules. The electromagnetic processes are described by EGS4 (Electron Gamma Shower code version 4) [Nel85].

The description of hadronic interactions is divided into two energy regions. One model is responsible for the low energy region, the other one for the high energy region. The choice of the interaction model depends on the energy  $E_{\text{lab}}^n = E_{\text{lab}}/\text{nucleon}$ . The switching between the two models is controlled by an adjustable threshold of this energy [Brü07]. Besides the choice between a low energy and a high energy model, the modular approach allows to use different models and to compare them. This is useful in order to test the models or to estimate the model dependence of an analysis and to study systematic uncertainties.

The detector response is simulated with CRES (cosmic ray event simulation), which is based on GEANT3 [CER94]. It uses the output of CORSIKA to simulate the signals and the energy deposits of all detectors of KASCADE-Grande, caused by the simulated particles at detection level. The simulated air showers are uniformly distributed over an area of  $760 \times 800 \text{ m}^2$ . Because the simulation of extensive air showers is very time consuming, the number of showers which can be simulated in a reasonable time is limited. Therefore, in order to increase the statistics, each simulated shower is used several times with different shower core positions as input for CRES. The output format of CRES and the format of the data obtained by the experiment are the same. This allows to process the simulated and the measured data with the reconstruction program KRETA in an identical way.

CORSIKA 6.307 was used for all simulation sets. In order to describe the hadronic interactions at high energies QGSJET II [Ost06, Ost07] was selected. The low energy part was simulated with FLUKA 2002.4 [Fas03]. The transition energy between these two models was set to 200 GeV. A continuous energy spectrum up to an energy of  $10^{18}$  eV, following a power law  $dI/dE \propto E^\gamma$ , with the flux  $I$  and a spectral index of  $\gamma = -2.0$ , was simulated with five different primary particles: hydrogen, helium, carbon, silicon, and iron. The starting points of the energy spectrum differ for the individual simulation sets, see Tab. 4.1. In total twelve sets were available, consisting of approximately 64,000 simulated air showers each. The detector response was simulated with CRES 1.16/07. Five simulation sets contain air showers in a zenith angle range of 0° – 42°. In four of these five sets each simulated shower was used ten times as CRES input. In one set the showers were used fifteen times with an area that was enlarged by

a factor of 1.5. Seven sets were simulated with zenith angles between  $0^\circ$  and  $70^\circ$ . Three of them were used with an area 1.5 times larger and each shower was re-used ten times. In the remaining four sets the showers were used twenty times with an area enlarged by a factor of 2. Tab. 4.1 summarizes the different simulation sets.

---

# Data sample selection

---

For the analysis, preprocessed data sets are used. Where preprocessed implies two aspects. Firstly, the showers are reconstructed with KRETA, thus all shower properties are available (see Chap. 4.1). Secondly, only those shower events triggered by the (7/7)-coincidence trigger, are selected. At the time of the analysis, data sets from the 2003-12-20 (`run4685`) to the 2007-09-17 (`run6238`), were available, which corresponds to 1367 days of data taking. In this period of time 35,116,785 (7/7)-coincidence events were recorded.

The quality cuts applied to these data are discussed in the first part of this chapter. In the second part, the trigger and reconstruction efficiencies are examined and discussed and additional selection criteria are proposed.

## 5.1 Quality cuts

The reconstructed quantities have uncertainties, which are affecting the quality of the analysis by introducing systematic errors. In order to reduce these errors the uncertainties have to be studied and quality cuts have to be applied on the data. This is possible, because the uncertainties depend on several shower quantities.

Level 3 of the reconstruction procedure provides the most precise values. Therefore, these values have to be used for the analysis. The shower properties are determined by a global fit using a negative-log-likelihood minimization (see Chap. 4.1). This minimization may fail and therefore only events with a successful minimization in level 3 are taken into account. But, even if the global fit works successfully, it is still possible that the determination of shower quantities fails. Thus, this has also to be checked. Especially, three quantities, the number of charged particles  $N_{\text{ch}}$ , the number of muons  $N_{\mu}$ , and the zenith angle  $\theta$ , are of interest, because the analysis is based upon these quantities. Therefore, only shower events with valid entries for these three quantities are selected. Furthermore, since these quantities are important for the analysis, the definition of the quality cuts is based mainly on the examination of these quantities.

In Fig. 5.1 the reconstruction quality of the number of charged particles and the reconstruction accuracy of the zenith angle are examined as a function of the shower core position ( $X_{\text{core}}, Y_{\text{core}}$ ). In order to determine quality cut criteria, the reconstruction accuracy of the shower core position is also shown. All seven simulation sets with a maximum zenith angle of  $70^\circ$  (see Chap. 4.2 and Tab. 4.1) are used to obtain these figures. They show that there is a border effect for the reconstructed values. For

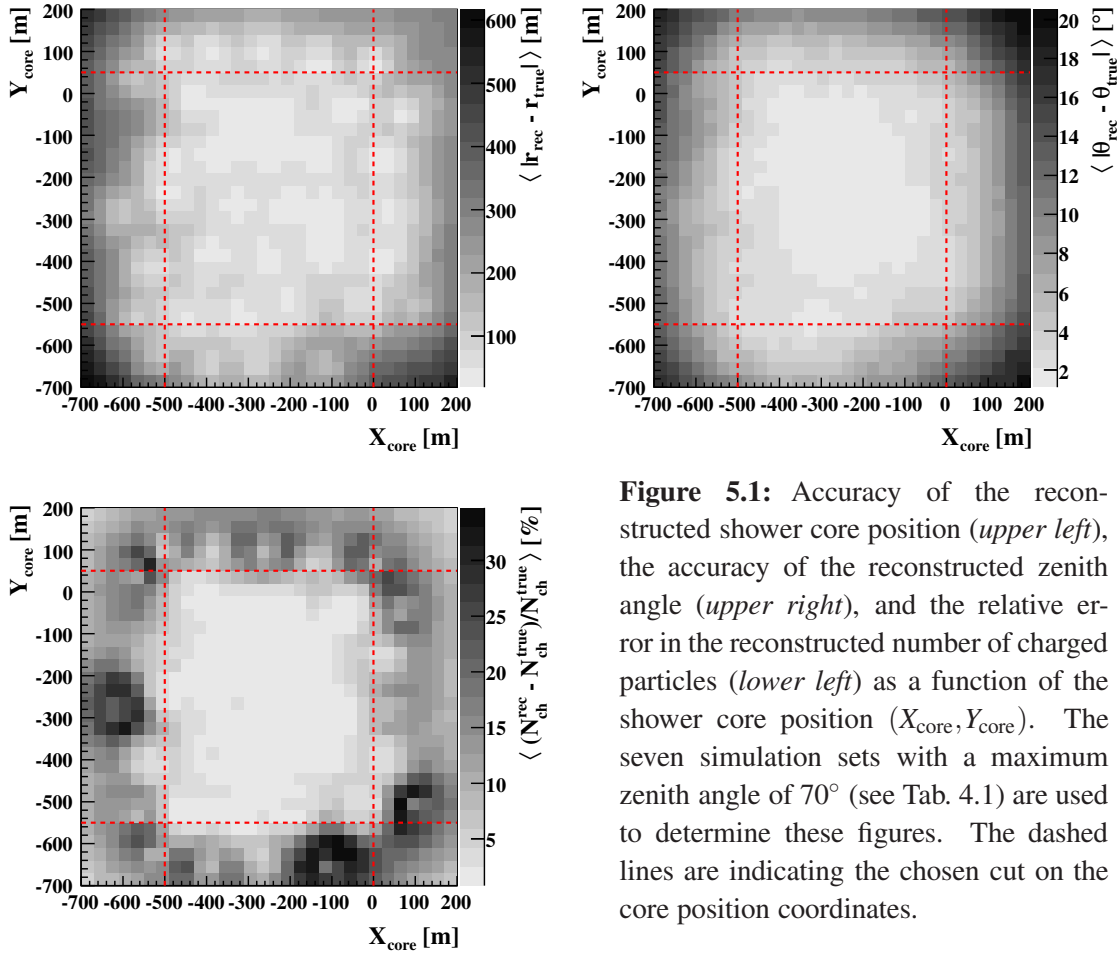


**Figure 5.1:** Accuracy of the reconstructed shower core position (*upper left*), the accuracy of the reconstructed zenith angle (*upper right*), and the relative error in the reconstructed number of charged particles (*lower left*) as a function of the shower core position ( $X_{\text{core}}, Y_{\text{core}}$ ). The seven simulation sets with a maximum zenith angle of  $70^\circ$  (see Tab. 4.1) are used to determine these figures. The dashed lines are indicating the chosen cut on the core position coordinates.

showers at the border or outside of the array, the precision of reconstructed properties decreases significantly compared to showers inside the array. Hence, a cut in the shower core coordinates is applied. Only showers with core positions inside a rectangle defined by:

$$-500 \text{ m} < X_{\text{core}} < 0 \text{ m},$$

$$-550 \text{ m} < Y_{\text{core}} < 50 \text{ m}$$

are selected. This cut is chosen due to the fact that inside this rectangle the reconstruction uncertainties of the considered properties are constant within small variations. The cuts applied are visualized in the figures by the dashed lines.

At the stage of the shower reconstruction, the number of charge particles and the shower age are connected with each other by the particle density distribution function



(see Chap. 4.1). Therefore, the shower age is investigated in order to improve the reconstructed number of charged particles and hence the data quality. Fig. 5.2(a) shows

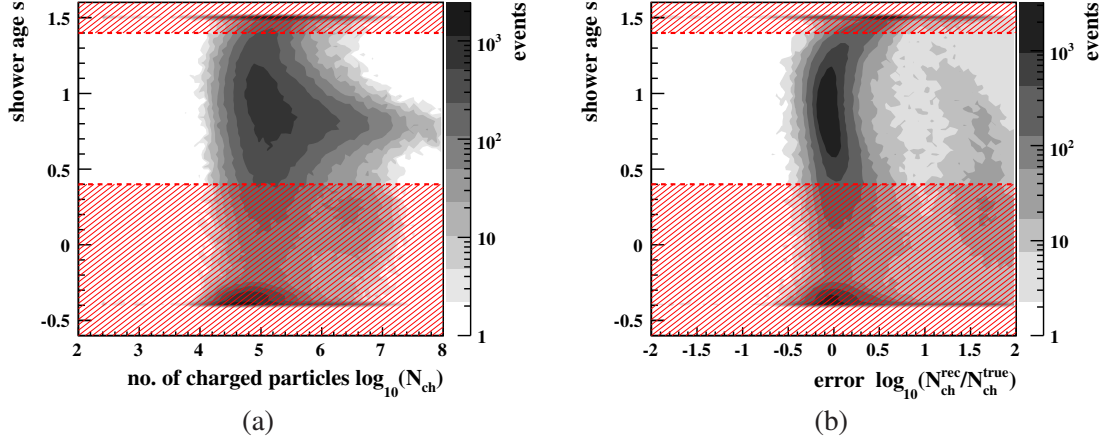


**Figure 5.2:** The shower age of the reconstructed shower versus the number of charged particles  $N_{\text{ch}}$  (*left*) and the shower age as a function of the relative error of the reconstructed number of charged particles (*right*). The cuts on shower age applied are indicated.

the relations between these two shower quantities and Fig. 5.2(b) shows the correlation between the shower age and the reconstruction error. The error is minimal if the reconstructed and the true number of charged particles are equal:

$$N_{\text{ch}}^{\text{rec}} = N_{\text{ch}}^{\text{true}} \quad \Rightarrow \quad \frac{N_{\text{ch}}^{\text{rec}}}{N_{\text{ch}}^{\text{true}}} = 1. \quad (5.1)$$

Therefore, the reconstruction error  $\text{err}_{\text{ch}}$  is minimal, if:

$$\text{err}_{\text{ch}} = \log_{10} \left( \frac{N_{\text{ch}}^{\text{rec}}}{N_{\text{ch}}^{\text{true}}} \right) = 0. \quad (5.2)$$

Most of the events are distributed around the minimum reconstruction error of  $\text{err}_{\text{ch}} = 0$ . For events with a shower age  $s > 1.4$ , the error in the number of charged particles increases. Additionally, bands of events around  $s = 1.5$  and  $s = -0.4$  are seen. These bands are caused by the mathematical limits of the modified NKG functions, see Eq. (4.6). This function is only defined for  $-0.5 < s < 1.55$ . Due to the approximative calculation of the  $\Gamma$ -function, these limits are reduced and hence, events with a shower age  $s > 1.5$  or  $s < -0.4$  are reconstructed with a shower age of  $s = 1.5$  or  $s = -0.4$  leading to the excess of events for both values of  $s$ . Therefore, these regions should be cut away. In addition, an excess of miss-reconstructed shower events around a shower age of  $s = 0.2$  is seen. These events should also be cut away. Therefore, the selection criterion on shower age  $s$  is set to  $0.4 \leq s \leq 1.4$ . With this cut, the uncertainty of the reconstructed number of charged particles is limited to  $-0.5 < \text{err}_{\text{ch}} < 0.5$ . Most of the events are inside this cut range (see Fig. 5.2(a)) and accordingly just a small number of events is cut away. The cut values are visualized by the dashed lines in the figures and the exclusion regions are hatched.

The Grande detector array was designed to extend KASCADE towards higher energies with an overlap region at about  $10^{17}$  eV and it has not been built to detect air showers with a primary energy less than  $10^{16}$  eV effectively. In order to discard these events and to save computing time, an appropriate quality cut has to be applied. Fig. 5.3(a) shows the relation between the number of triggered Grande stations and the primary energy of the air showers detected. A correlation between these two quantities can be seen. Thus, accepting only events, which triggered more than nineteen Grande stations, rejects events with too low energies.

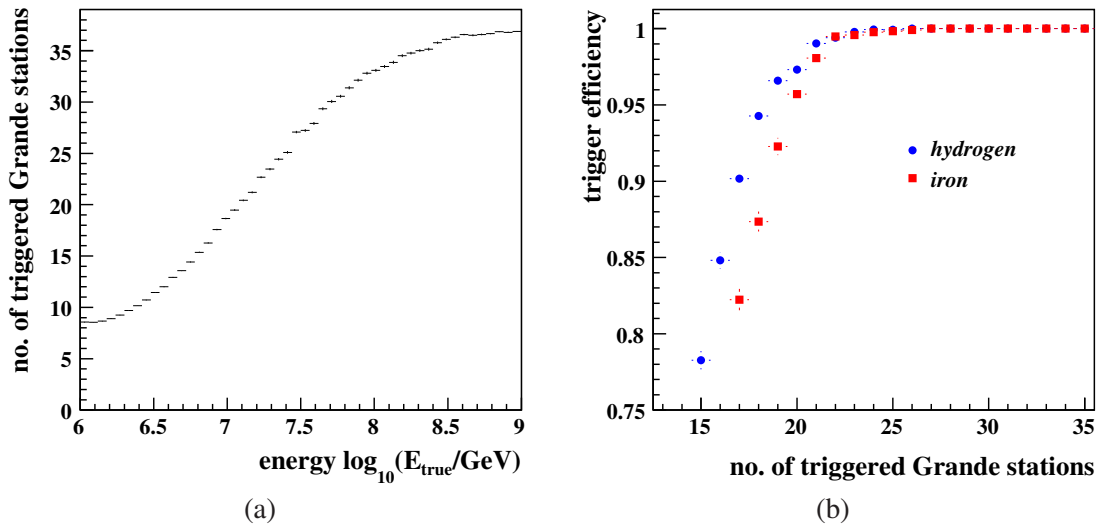


**Figure 5.3:** *Left:* Number of triggered Grande detector stations as a function of the primary energy. At least 20 stations are triggered in average for primary energies above  $10^{16}$  eV. *Right:* Trigger efficiency as a function of the number of triggered Grande detector stations. With 20 or more triggered stations the trigger efficiency is better than 95 %.

This cut should only discard events, which cannot be effectively detected. In order to demonstrate that this is true for events, which are triggered by less than twenty stations, in Fig. 5.3(b) the trigger efficiency is plotted as a function of the number of triggered Grande stations. The trigger efficiency improves with increasing number of triggered stations and with a cut on twenty or more stations, the efficiency is 95 % or better.

Some Grande detector stations are near the ANKA experiment, a synchrotron radiation facility, which can generate fake events in the Grande array. Most of these fake events are caused during the beam injection phase. These phases are recorded in a dedicated database. Events recorded during injection time can be excluded from the analysis by using this database. But also during normal operation, ANKA can generate fake events in Grande. These events were found to have a periodicity. This allows ANKA induced events to be detected by analyzing the time structure of Grande events [Ove07b]. Such events are also excluded from the analysis. In order to determine ANKA induced events, the recorded data has to fulfill additional quality criteria. Thus, events, which do not fulfill these criteria, will also be discarded.

Periods of system maintenance or periods with electronics failures are stored in a run status database [Ove07b]. This allows to select only events where the data quality is not corrupted by hardware failures.

In Tab. 5.1 the quality cut criteria are summarized. Applying all these selection criteria, 2,976,000 events remain of the total recorded (7/7)-coincidence events, which corresponds to 8.5%. Applying a zenith angle cut of  $\theta \leq 40^\circ$ , 2,814,511 events remain, corresponding to 8.0%.

Cut criterion	No. of discarded events (from 35,116,785)	Fraction [%]
> 19 triggered Grande stations	28,236,332	80.4
Core inside fiducial area	14,678,117	41.8
Shower age cut	12,081,430	34.4
Grande status OK	4,499,019	12.8
Successful reconstruction	3,577,723	10.2
Zenith angle $\leq 40^\circ$	2,826,522	8.0
No ANKA induced events	2,637,486	7.5

**Table 5.1:** Summary of the selection criteria applied on the data sets and their effects with respect to the total number of (7/7)-coincidence events.

## 5.2 Trigger and reconstruction efficiency

Shower size spectra are intensity spectra as a function of the shower size, i.e. the number of particles, in our case the number of charged particles  $N_{\text{ch}}$ . In order to calculate the flux, the trigger and reconstruction efficiencies have to be known. Furthermore, in order to apply the constant intensity cut method (see Chap. 6), the trigger and reconstruction efficiency should be almost 100%, otherwise the size spectra could be deformed and the method will not work. Therefore, it is important to evaluate these efficiencies.

The trigger efficiency describes the number of triggered events  $N^{\text{trig}}$  compared to the total number of events  $N^{\text{tot}}$ :

$$\epsilon^{\text{trig}} = \frac{N^{\text{trig}}}{N^{\text{tot}}}. \quad (5.3)$$

Because only events triggered by a (7/7)-coincidence are of interest, only such events are taken into account,  $N^{\text{trig}} = N^{(7/7)}$ . Even if the trigger efficiency  $\epsilon^{(7/7)}$  is 100% and all of the extensive air showers hitting the detector are triggered and recorded, the reconstruction of an event may fail. The reconstruction efficiency  $\epsilon^{\text{rec}}$  accounts for this. Events, that get lost during reconstruction, are deforming the size spectra and the goal is to work in a region with almost 100% reconstruction efficiency. These efficiencies can depend on the shower size, the zenith angle, or the number of triggered Grande stations, which is correlated with the shower size.

Fig. 5.4(a) shows the trigger and reconstruction efficiencies as a function of the shower size or the number of charged particles  $N_{\text{ch}}$ . They are given separately for hydrogen and iron initiated air showers, which are the extreme possibilities. Small showers are not triggered at all, which is reasonable, because these showers do not generate energy deposits over threshold in 7 stations in order to create a (7/7)-coincidence trigger. The distances between these stations are too large compared to the size of the shower disk. With increasing shower size, the efficiency rises and saturates at 100%. This be-

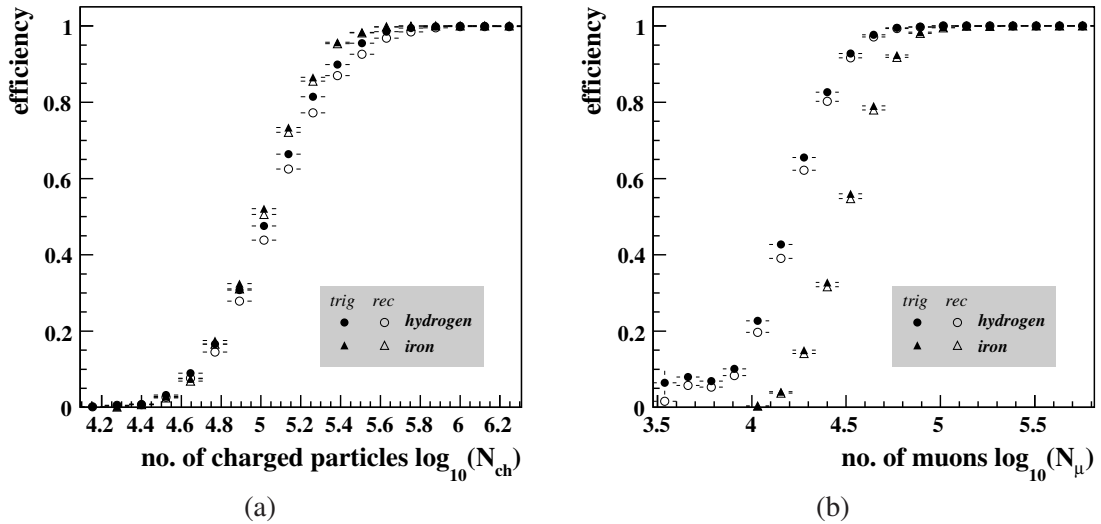


**Figure 5.4:** Trigger and reconstruction efficiency as a function of the number of charged particles (*left*) and the number of muons (*right*).

havior depends on the primary particle and the considered efficiency. As expected, the reconstruction efficiency starts to increase and to reach saturation later than the trigger efficiency. There is a small difference in the efficiencies, comparing hydrogen and iron initiated air showers. Iron initiated showers reach full efficiency at a smaller number of charged particles. This is mainly caused by two effects. Firstly, iron induced showers have a higher energetic  $\gamma$ -component than hydrogen induced showers with the same number of charged particles. This results in higher energy deposits in the Grande detectors, thus the probability to generate a trigger signal increases. Secondly, the shower develops in the atmosphere with an increasing number of particles up to the point of the shower maximum  $X_{\text{max}}$  (see Chap. 2). Beyond this point, the number of electrons decreases, but the number of muons stays almost constant. Additionally, iron initiated air showers start higher in the atmosphere compared to hydrogen initiated showers, having thus, the shower maximum higher in the atmosphere, too. This means that the number of muons is higher for iron initiated showers, for the same number of charged particles, which is the sum of electrons and muons. The full trigger efficiency  $\varepsilon^{(7/7)} = 100\%$  is reached at about  $\log_{10}(N_{\text{ch}}) \approx 5.6$ . A successful reconstruction of showers is guaranteed from  $\log_{10}(N_{\text{ch}}) \approx 5.8$  onwards.

Fig. 5.4(b) shows the efficiency as a function of the number of muons  $N_{\mu}$  in the shower. The trigger and reconstruction efficiencies are shown for hydrogen and iron

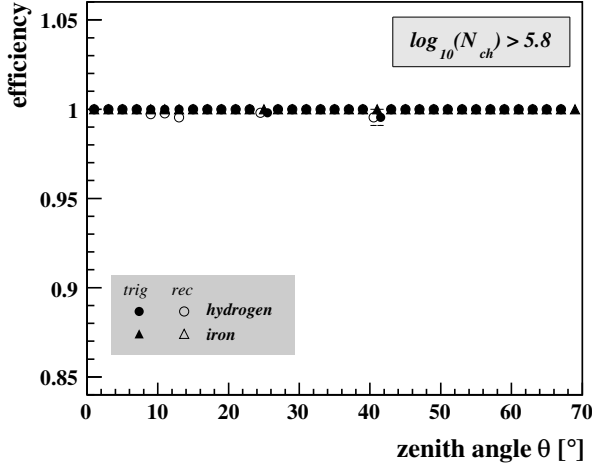


**Figure 5.5:** Trigger and reconstruction efficiencies as a function of the zenith angle. Only showers with  $\log_{10}(N_{ch}) > 5.8$  are used in order to reach full efficiency.

induced showers. The differences between them are more pronounced, but inverted compared to the case of charged particles. This is due to the fact that the energy of the primary particle of an iron induced air shower is on average lower than the primary energy of a hydrogen induced air shower with the same number of muons. The full trigger and reconstruction efficiency are reached at about  $\log_{10}(N_{\mu}) \approx 5.0$ .

In Fig. 5.5 the trigger and reconstruction efficiencies are shown as a function of the zenith angle. In order to eliminate the influence of the number of particles on the efficiencies, only showers with  $\log_{10}(N_{ch}) > 5.8$  are selected. In this case the efficiencies show no dependence on the zenith angle within error bars and they are 100 % over the whole zenith angle range.

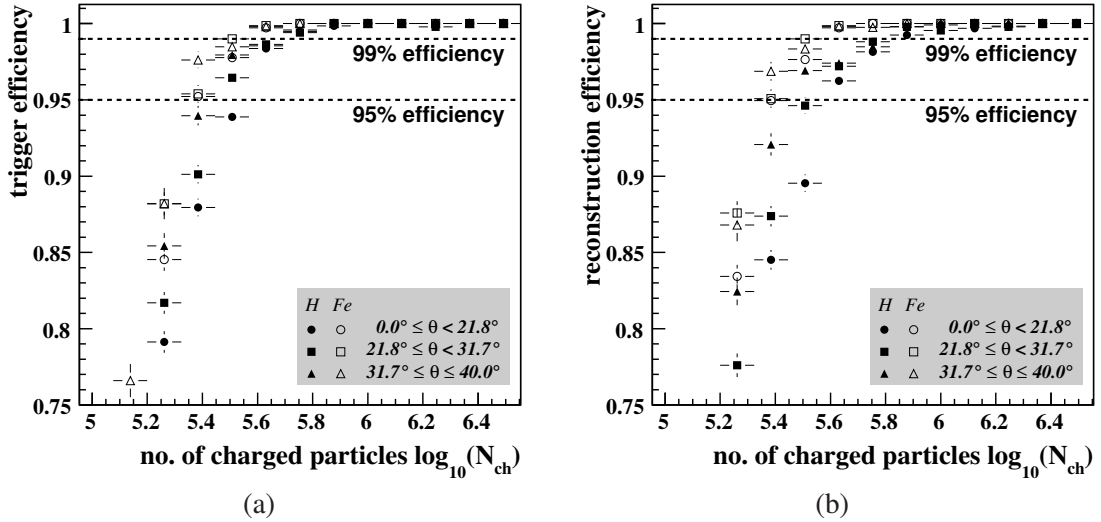


**Figure 5.6:** Trigger and reconstruction efficiencies as a function of the number of charged particles for different zenith angle ranges.

In order to better understand the correlations between the efficiencies, the zenith angle, and the number of charged particles, in Fig. 5.6 the efficiency is plotted as a

function of the number of charged particles, but this time for three different zenith angle bins. Fig. 5.6(a) shows the effect for the trigger efficiency, while the reconstruction efficiency is shown in Fig. 5.6(b). In both cases it is clearly seen that the efficiencies depend slightly on the zenith angle. This effect is predominantly seen for hydrogen induced showers. Dashed lines indicate an efficiency of 99 % and 95 %. With a cut on  $\log_{10}(N_{\text{ch}}) \gtrsim 5.6$  the reconstruction efficiency is higher than 95 % for all zenith angle bins. In order to have a reconstruction efficiency higher than 99 %, the number of charge particles in an air shower has to be  $\log_{10}(N_{\text{ch}}) \gtrsim 5.9$ .

Another possibility to show the correlations between these quantities is seen in Fig. 5.7. In these figures, the efficiency is a function of the zenith angle for different bins of the number of charged particles. For the number of charged particles in the

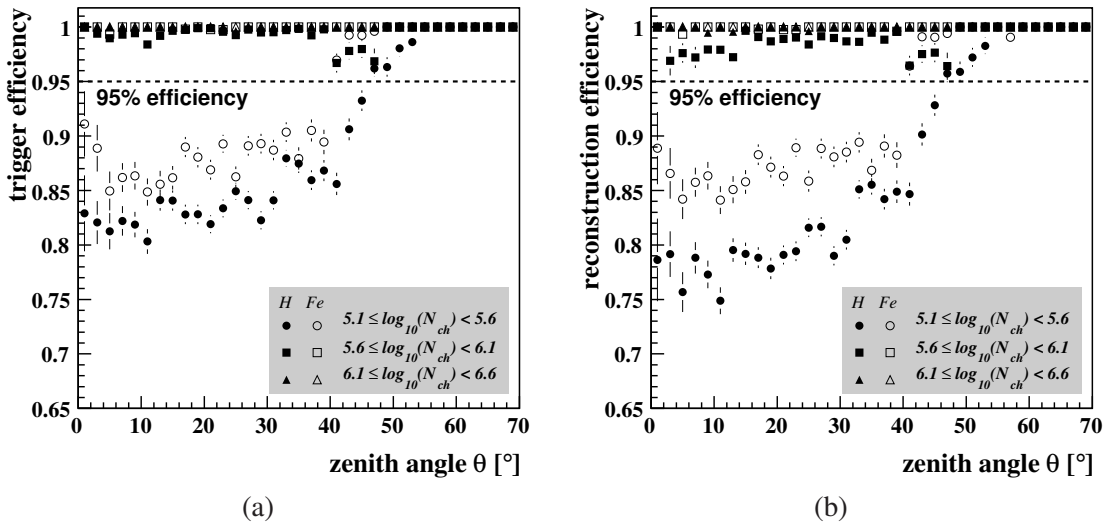


**Figure 5.7:** Trigger and reconstruction efficiencies as a function of the zenith angle for different ranges of the number of charged particles

range of  $5.1 \leq \log_{10}(N_{\text{ch}}) < 5.6$  and zenith angles up to  $40^\circ$ , the efficiencies are always far below 95 %. From about  $40^\circ$  on, the efficiencies increase fast to 100 %. This fast increase is due to the fact, that the number of electrons decreases fast with increasing atmospheric depth, see Chap. 2. The atmospheric depth increases with the zenith angle and for inclined showers ( $\theta > 40^\circ$ ), the curvature of the earth is not negligible, which amplifies the increase of the atmospheric depth. The number of muons reach a maximum and stays almost constant, see Chap. 2. Therefore, a inclined shower is dominated by the number of muons rather than by the number of electrons. The number of charged particles is the sum of the number of muons and the number of electrons. Hence, the number of muons of an inclined shower is much larger compared to a vertical shower with the same number of charged particles. Due to the effect of the curvature of the earth, the transition from electron dominated showers to muon dominated showers goes very fast with increasing zenith angle. In order to get full trigger and reconstruction efficiencies only about  $10^5$  muons are necessary compared to  $10^6$  electrons, see Figs. 5.4. Therefore, for the inclined showers 100 % efficiency is reached very fast with increasing zenith angle. Comparing hydrogen and iron induced showers, it can be seen, that

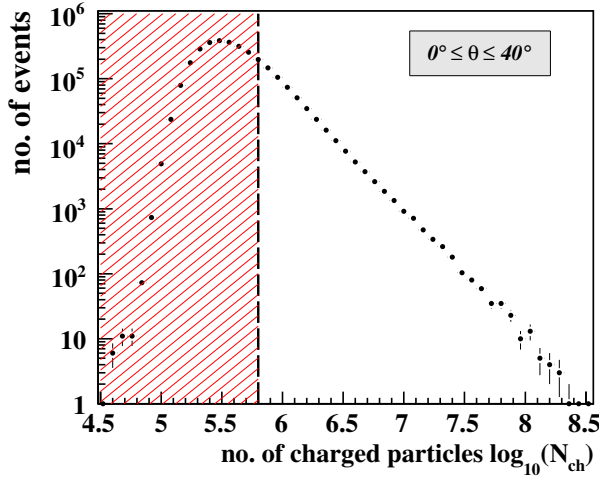


**Figure 5.8:** Number of measured events as a function of the number of charged particles. The diagram contains events in the zenith angle range of  $0^\circ \leq \theta \leq 40^\circ$  with all quality cuts applied. The vertical dashed line indicates the cut in the number of charged particles at  $\log_{10}(N_{\text{ch}}) > 5.8$ .

the efficiencies increase faster for the iron induced showers than for hydrogen induced showers. This is due to the fact, that iron induced showers have their shower maximum  $X_{\text{max}}$  higher in the atmosphere compared to hydrogen induced showers, see Fig. 2.5. Therefore, for hydrogen induced showers, the atmospheric depth from shower maximum to ground level is smaller, and hence, the decrease in the number of electrons is smaller compared to iron induced showers.

In the range of  $5.6 \leq \log_{10}(N_{\text{ch}}) < 6.1$  in Fig. 5.7, the efficiencies are safely above 95 %, which is expected from Figs. 5.4(a) and 5.5. Finally, the last range of  $6.1 \leq \log_{10}(N_{\text{ch}}) < 6.6$  stays at 100 % over the full zenith angle range, which is consistent with Fig. 5.5. Thus, the trigger and reconstruction efficiencies are independent of the zenith angle for showers with a number of charged particles of  $\log_{10}(N_{\text{ch}}) \gtrsim 5.6$ .

Concluding, only showers with a number of muons  $\log_{10}(N_{\mu}) > 5.0$  and a number of charged particles  $\log_{10}(N_{\text{ch}}) > 5.8$  are selected.

### 5.3 Summary

Two kinds of selection criteria were discussed in this chapter. Firstly, quality cuts were introduced in order to ensure reconstructed shower properties with small uncertainties. Applying all these quality criteria 2,976,000 events out of the 35,111,785 (7/7)-coincidence events were selected for further analysis. Secondly, to apply the constant intensity cut (see Chap. 6) it is important that the shapes of the constructed shower size spectra are not modified by efficiency effects. Therefore, the trigger and reconstruction efficiencies were studied and it was shown that the efficiencies are mainly affected by the number of particles in the shower. Thus, cuts on the number of charged particles and the number of muons were proposed. Because the analysis works with the size spectra, these cuts can be applied at the stage of the analysis.

Fig. 5.8 shows a size spectrum, where the number of events is plotted as a function of the number of charged particles. All quality cuts are applied and all resulting events in the zenith angle range of  $0^\circ \leq \theta \leq 40^\circ$  are used.





---

# Constant intensity method and corrected shower size spectra

---

The goal of the analysis presented here is to reconstruct the all particle energy spectrum using the measured KASCADE-Grande data. In order to achieve this, the primary energy of each individual shower has to be determined, which is a non-trivial problem. This has three main reasons. Firstly, the primary energy is not a property of the extensive air shower and hence it is not determined in the reconstruction procedure. Therefore, the primary energy has to be determined indirectly by using the properties of the extensive air shower. Secondly, there are dependencies among the quantities describing the shower properties. For example, the number of charged particles in a shower does not only depend on the primary energy but also on the arrival direction. Thirdly, there are shower fluctuations. This means, that two primary particles of the same type, energy, and arrival direction could lead to two different extensive air showers with different properties like the number of charged particles. Therefore, an appropriate energy estimator has to be found and dependencies and influences of shower fluctuations should be eliminated or at least reduced.

In this chapter, the method of constant intensity is introduced. This method eliminates the dependency on the arrival direction of the observable, and hence, leads to a reference number of charged particles. This new variable is zenith angle independent, but still carries the main features of the number of charged particles, both will be shown in this chapter.

In later chapters, the primary energy will be determined from this attenuation corrected number of charged particles using the number of muons of an extensive air shower and simulations.

## 6.1 Constant intensity method

The constant intensity method [Nag84] can be applied with the assumption, that the flux of cosmic rays is distributed isotropically and that cosmic rays arrive uniformly from all directions. This has to be true on the scale of the angular bins chosen in the analysis. In the considered energy range up to  $10^{18}$  eV, no anisotropy is found, see for example [Bel01, Bir99, Hay99]. Anisotropy studies using data measured with KASCADE-Grande support the assumption of an isotropic distribution [Ove07a]. With this assumption two things follow. Firstly, that the primary energy of a cosmic ray particle corresponds to a certain intensity regardless of its arrival direction. Secondly, that two primaries of the same energy, but different zenith angle, will result in different values of the number of charged particles [Nag84, Wat06].

Diagrams, which show the intensity as a function of the number of charged particles, are called shower size spectra, because the number of charged particles is a measure of the shower size. The constant intensity method uses shower size spectra of different zenith angle bins. Therefore, such diagrams have to be generated in the first step.

### 6.1.1 Shower size spectra

The differential flux as a function of the number of charged particles  $N_{\text{ch}}$  is defined by:

$$\frac{dI(N_{\text{ch}})}{dN_{\text{ch}}} = \frac{1}{A_{\text{eff}} \varepsilon_{\text{trig}} \varepsilon_{\text{rec}} d\Omega} \frac{dn}{dN_{\text{ch}}}, \quad (6.1)$$

with the event rate  $n = dN/dt$ , the effective area  $A_{\text{eff}}$ , the effective trigger  $\varepsilon_{\text{trig}}$  and reconstruction efficiencies  $\varepsilon_{\text{rec}}$ , and the solid angle  $d\Omega$ . The analysis is only applied in regions where  $\varepsilon_{\text{eff}} = \varepsilon_{\text{trig}} \cdot \varepsilon_{\text{rec}} \approx 1$ , see Chap. 5.2. The detection area of inclined showers is reduced by a factor of  $\cos \theta$ , leading to an effective area  $A_{\text{eff}} = A \cos \theta$ , where the detector area  $A = 0.3 \text{ km}^2$  is defined by the fiducial area cut, see Chap. 5.1. The intensity distribution is defined as the integral of the differential flux above a certain shower size  $N_{\text{ch}}^{\text{thresh}}$ :

$$I(> N_{\text{ch}}^{\text{thresh}}) = \int_{N_{\text{ch}}^{\text{thresh}}}^{\infty} \frac{dI(N_{\text{ch}})}{dN_{\text{ch}}} dN_{\text{ch}}, \quad (6.2)$$

which should be constant due to the presumption of the constant intensity method:

$$I(> N_{\text{ch}}^{\text{thresh}}) = \int_{N_{\text{ch}}^{\text{thresh}}}^{\infty} \frac{\partial^2 n(\Omega, N_{\text{ch}})}{A \cos \theta \partial \Omega \partial N_{\text{ch}}} dN_{\text{ch}} = \text{constant}. \quad (6.3)$$

Integrating over the shower size leads to

$$I(> N_{\text{ch}}^{\text{thresh}}) = \frac{1}{A} \cdot \frac{dn(\Omega, > N_{\text{ch}}^{\text{thresh}})}{\cos \theta d\Omega} = \text{constant}. \quad (6.4)$$

Integrating the denominator over the azimuthal angle:

$$\int_0^{2\pi} \cos \theta d\phi \sin \theta d\theta = 2\pi \cdot \cos \theta \sin \theta \frac{d \cos^2 \theta}{2 \sin \theta \cos \theta}, \quad (6.5)$$

results in:

$$\frac{1}{\pi A} \cdot \frac{dn(\cos^2 \theta, > N_{\text{ch}}^{\text{thresh}})}{d\cos^2 \theta} = I(> N_{\text{ch}}^{\text{thresh}}) = \text{constant} \quad (6.6)$$

and hence, in order to fulfill the assumptions of the constant intensity method the zenith angle has to be divided into equidistant bins in  $\cos^2 \theta$ . Events with a reconstructed zenith angle larger than  $40^\circ$  are not considered in the analysis presented here. This is due to the fact that the number of events above  $40^\circ$  is small compared to the total number of events, which leads to low statistics of such events, see Tab. 5.1. The zenith angle range was divided into eight zenith angle bins of equal  $\Delta\cos^2 \theta$ , which are summarized in Tab 6.1.

Zenith angle range [ $^\circ$ ]	Mean [ $^\circ$ ]
0.00 – 13.14	8.61
13.14 – 18.75	16.02
18.75 – 23.18	20.96
23.18 – 27.03	25.08
27.03 – 30.54	28.74
30.54 – 33.83	32.12
33.83 – 36.96	35.32
36.96 – 40.00	38.38

**Table 6.1:** Zenith angle bins. The zenith angle range  $0 \leq \theta \leq 40^\circ$  is divided into 8 bins, which are of equal size in  $\cos^2 \theta$ . The mean is calculated by using the zenith angle distribution of real data, see Chap. 6.1.3.

In the frame of this analysis, the number of charged particles is used to describe the shower size. This choice has two main reasons. Firstly, the Grande detectors do not measure the electromagnetic and the muonic component of the extensive air showers separately, but the sum of both, which is the number of charged particles. The separation is performed due to the reconstruction procedure, see Chap. 4.1. This introduces additional uncertainties to the number of electrons, which do not effect the number of charged particles.

Secondly, the connection between the primary energy and the intensity of the cosmic radiation, when using the constant intensity method, is influenced by the composition of the primary radiation. Assuming only one type of primary particles and the validity of the assumption of isotropically distributed cosmic rays, the correlation between the primary energy and the intensity of the radiation follows immediately. This relation is independent of the type of the primary particle. Therefore, the relation will be valid if either the composition is constant or if the type of the primary particle is known. This would allow to apply the constant intensity method on the different mass groups independently. For real data the mass of the primary particle is not known and the composition is not constant over the whole range [Ant05]. This could lead to a change in the intensity for different zenith angles. Hence, the assumption of isotropy can only

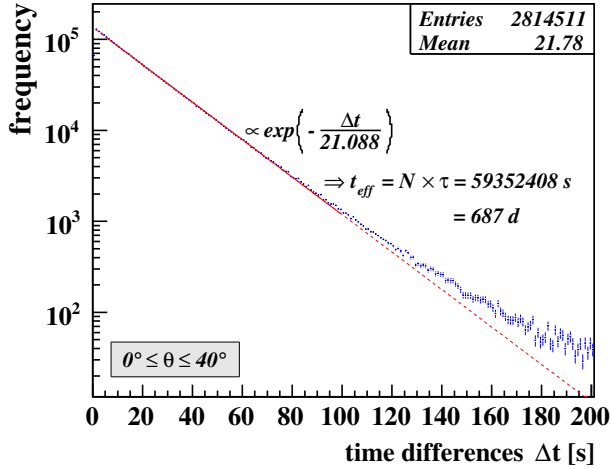


**Figure 6.1:** Distribution of time differences between two successive events. Only events passing the quality cuts and with  $0^\circ \leq \theta \leq 40^\circ$  are selected. The solid line indicates the fit of an exponential function. The dashed line is its prolongation outside the fit range. Using the resulting time constant  $\tau$  the effective measurement time  $t_{\text{eff}}$  can be determined.

be valid locally. But, as [Gla99] suggests, a combination of the number of muons and the number of electrons can reduce the dependence on the type of the primary particle.

The event rate  $n = dN/dt$  in Eq. (6.6) can be substituted by discrete values  $\Delta N/\Delta t$ . In the case of the effective measurement time  $t_{\text{eff}}$ , the variables can be identified by  $\Delta N = N$  and  $\Delta t = t_{\text{eff}}$ , where  $N$  is the total number of events measured in  $t_{\text{eff}}$ , and Eq. (6.6) becomes:

$$I(> N_{\text{ch}}^{\text{thresh}}) = \frac{N(> N_{\text{ch}}^{\text{thresh}})}{\pi A \Delta t_{\text{eff}} \Delta \cos^2 \theta}. \quad (6.7)$$

In order to determine the effective measurement time  $t_{\text{eff}}$ , the time differences between two successive events are calculated for all selected events. This leads to a distribution of time differences, shown in Fig. 6.1. Fitting an exponential function:

$$f(\Delta t) = C \cdot \exp(-\Delta t/\tau) \quad (6.8)$$

to this distribution, the effective measurement time can be determined from:

$$t_{\text{eff}} = N \cdot \tau. \quad (6.9)$$

The distribution is fitted in a range up to a time difference of  $\Delta t = 100$  s, which is indicated by the solid line of the fit function. The dashed line is the prolongation of this fit for values outside the fit range. The fit resulted in a scaling factor of  $C = 11.819 \pm 0.001$  and a time constant of  $\tau = 21.0880 \pm 0.0001$  s. It can be seen, that for time differences above 100 s the distribution does not follow an exponential function. The deviation from an exponential behavior can be caused by periods of maintenances and run starts, which leads to additional time periods without measurements. The number of these periods are small compared to the number of measured events. Also the number of events above  $\Delta t = 100$  s is small compared to the rest, thus the error caused by the deviation of the true time difference distribution from an exponential law is negligible. Furthermore, if the distribution follows an exponential law, the mean of it will be the time constant  $\tau$ . The mean of the distribution (21.78 s) is in good agreement with the determined time constant of the exponential fit, which supports the assumption of an exponential behavior.

In the considered zenith angle range of  $0^\circ \leq \theta \leq 40^\circ$ , in total 2,814,511 events are selected (see Chap. 5.1). Thus, the effective measurement time results to  $t_{\text{eff}} = 59,352,408 \text{ s} = 687 \text{ d}$  from Eq. (6.9), which are effectively more than 2 years of measurement.

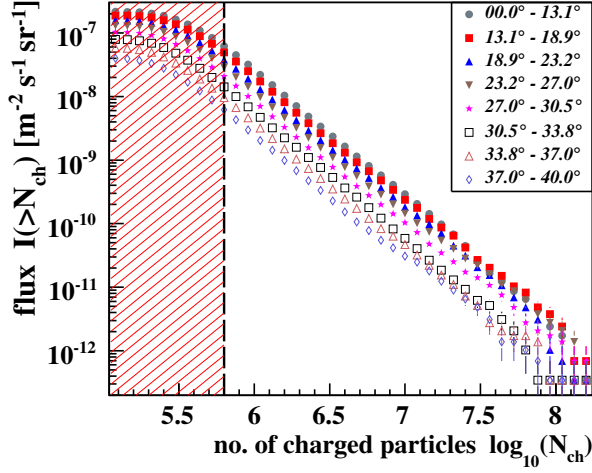


**Figure 6.2:** Measured integral shower size spectra for different zenith angle bins. The dashed line and the hatched area indicating the proposed cut in the number of charged particles in order to get full efficiency.

At this point, all variables of Eq. (6.7) are determined and the integral flux is plotted as a function of the number of charged particles for eight different zenith angle ranges in Fig. 6.2. In the following, the constant intensity method is applied on this diagram.

### 6.1.2 Constant intensity cuts

The number of charged particles  $N_{\text{ch}}$  is calculated for each zenith angle range for different chosen intensities. Fig. 6.3 shows a cut-out of the size spectra plot. The horizontal line illustrates the cut on an arbitrarily chosen intensity  $I_{\text{cut}}$  on the eight shower size spectra. The intersections of the intensity cut with the size spectra, which result in the corresponding shower sizes  $N_{\text{ch,cut}}$ , are indicated by the vertical lines. The intensity cut will most probably not hit the points of the distribution, but will end up between two

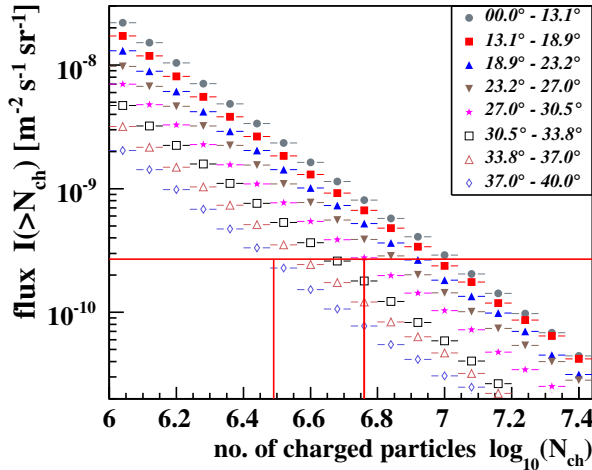


**Figure 6.3:** Cut-out of shower size spectra with illustration of the constant intensity cut. The horizontal line indicates the chosen intensity. Its intersections with the size spectra of different zenith angles are illustrated by vertical lines. For clarity, only two of them are drawn.

points. Therefore, the shower size has to be approximated. It is assumed, that the size spectrum follows a power law at least between two neighboring points [Ant03c], which is in agreement with Fig. 6.2. Furthermore, the power law is a line in a double logarithmic plot and a linear behavior between the two points is the simplest assumption. Nevertheless, it should be avoided to introduce a global assumption about the shape of the size spectrum. Therefore, the approximation should operate only in the region of the intersection points and hence, a local power law between these two points is assumed:

$$N_{\text{ch,cut}} = 10^{\alpha - \beta \cdot \log_{10} I_{\text{cut}}}. \quad (6.10)$$

The point above the intensity cut is connected with the point below by a line in the double logarithmic plot. The intersection of the intensity cut with this line gives the number of charged particles  $N_{\text{ch,cut}}$  for a certain zenith angle range. Thirteen different intensity cut values are chosen:  $I(> N_{\text{ch}}) = \{1.50 \cdot 10^{-8}, 1.2 \cdot 10^{-8}, 1.0 \cdot 10^{-8}, 8.0 \cdot 10^{-9}, 6.5 \cdot 10^{-9}, 5.0 \cdot 10^{-9}, 4.0 \cdot 10^{-9}, 3.0 \cdot 10^{-9}, 2.3 \cdot 10^{-9}, 1.7 \cdot 10^{-9}, 1.2 \cdot 10^{-9}, 7.5 \cdot 10^{-10}, 4.3 \cdot 10^{-10}\} \text{m}^{-2} \text{s}^{-1} \text{sr}^{-1}$ . These values are selected in order to achieve a wide range in intensities, but with small errors. Additionally, the resulting numbers of charged particles within one zenith angle range should not overlap within their errors, see Fig. 6.5.

Details about the error calculation will follow in the next chapter and App. B. The results of the application of the constant intensity method are summarized in Tab. A.1.

### 6.1.3 Attenuation curves

The results of the intensity cuts can be plotted in a different way. For each intensity the number of charged particles is plotted as a function of the zenith angle, which is the mean of an associated zenith angle range. In order to evaluate this zenith angle, the zenith angle distribution of the real data is used. This distribution is divided into the eight different zenith angle bins, see Tab. 6.1. For each bin, the mean in the angle is calculated. This value is used as the reference angle for the bin. In Fig. 6.4 the zenith

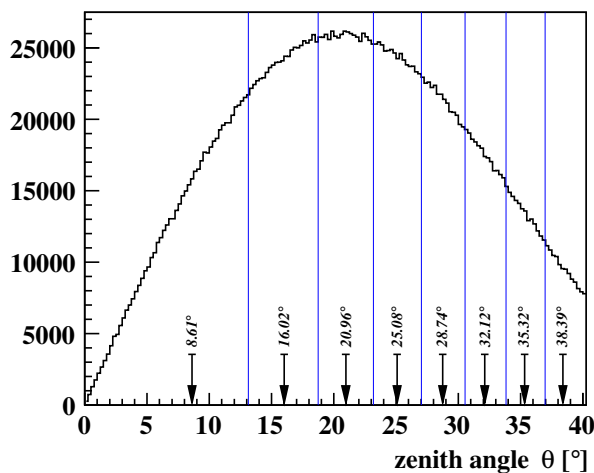


**Figure 6.4:** Measured zenith angle distribution. The vertical lines indicate the boundaries of the zenith angle bins. The arrows point to the calculated mean of the distribution inside each zenith angle bin.

angle distribution up to  $40^\circ$  is shown. The zenith angle ranges are represented by the

vertical lines. The arrows illustrate the calculated mean of the associated bin, which is used as the reference or the mean angle of this bin. The evaluated mean values can be found in Tab. 6.1.

The calculated numbers of charged particles as a function of the zenith angle for the different intensity cuts are shown in Fig. 6.5, these are the so-called attenuation curves. They describe how the particle number is attenuated due to atmospheric depth, which increases with the zenith angle  $\theta$ . The zenith angle is given as the secans of the zenith angle ( $\sec \theta = 1/\cos \theta$ ).

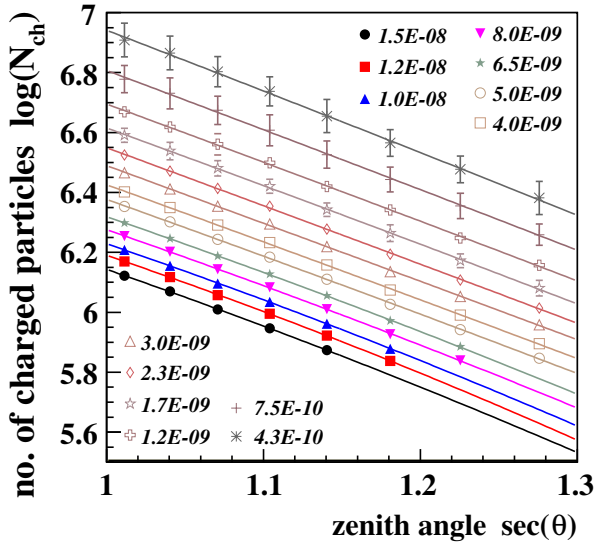


**Figure 6.5:** Attenuation curves. After applying constant intensity cuts to different shower size spectra, the resulting number of charged particles  $N_{\text{ch}}$  is plotted as a function of the zenith angle  $\theta$ . Each curve represents one intensity. Each intensity is fitted with a polynomial of second order.

The errors shown in this figure are the propagated uncertainties of the shower size diagram [Mar07, Bar89]. The cut intensity  $I_{\text{cut}}$  lays between the two neighboring bins:

$$\begin{aligned} \log_{10} N_{\text{ch},0} &= \alpha - \beta \cdot \log_{10} I_0, \\ \log_{10} N_{\text{ch},1} &= \alpha - \beta \cdot \log_{10} I_1, \end{aligned} \quad (6.11)$$

with the integral intensities  $I_0 = i_0$  and  $I_1 = i_0 + i_1$  where  $i_0$  and  $i_1$  are independent. Using Eq. (6.11), the coefficients  $\alpha$  and  $\beta$  can be obtained (for details see App. B). The number of the charged particles  $N_{\text{ch,cut}}$  resulting from the intensity cut  $I_{\text{cut}}$  can then be calculated by:

$$\log_{10} N_{\text{ch,cut}} = \alpha - \beta \cdot \log_{10} I_{\text{cut}}. \quad (6.12)$$

Thus, all uncertainties can be propagated to function (6.10) by constructing the covariance matrix  $V$ :

$$V = \begin{bmatrix} \left(\frac{\partial \alpha}{\partial i_0}\right)^2 \sigma_{i_0}^2 + \left(\frac{\partial \alpha}{\partial i_1}\right)^2 \sigma_{i_1}^2 & \left(\frac{\partial \alpha}{\partial i_0}\right) \left(\frac{\partial \beta}{\partial i_0}\right) \sigma_{i_0}^2 + \left(\frac{\partial \alpha}{\partial i_1}\right) \left(\frac{\partial \beta}{\partial i_1}\right) \sigma_{i_1}^2 \\ \left(\frac{\partial \alpha}{\partial i_0}\right) \left(\frac{\partial \beta}{\partial i_0}\right) \sigma_{i_0}^2 + \left(\frac{\partial \alpha}{\partial i_1}\right) \left(\frac{\partial \beta}{\partial i_1}\right) \sigma_{i_1}^2 & \left(\frac{\partial \beta}{\partial i_0}\right)^2 \sigma_{i_0}^2 + \left(\frac{\partial \beta}{\partial i_1}\right)^2 \sigma_{i_1}^2 \end{bmatrix}. \quad (6.13)$$

Each attenuation curve in Fig. 6.5 is individually fitted with a polynomial of second order:

$$\log_{10} N_{\text{ch}} = \log_{10} N_{\text{ch},21^\circ} \cdot (1 + P_1 \cdot X + P_2 \cdot X^2), \quad (6.14)$$

with:

$$X = X(\theta) = \sec(\theta) - \sec(21^\circ), \quad (6.15)$$

where  $P_1$ ,  $P_2$ , and  $N_{\text{ch},21^\circ}$  are fit parameters. The lines in Fig. 6.5 represent the resulting curves. The detailed results of the fit can be found in Tab. C.1.

The definition of function  $X$  in Eq. (6.15) defines the meaning of the fit parameter  $N_{\text{ch},21^\circ}$ . In this case, the events are referred to a zenith angle of  $21^\circ$  and hence  $N_{\text{ch},21^\circ}$  is the number of charged particles of the shower as if it would arrive from this direction. The reference angle is chosen, because most of the events measured with KASCADE-Grande arrive under a zenith angle of  $21^\circ$ , which can be seen in Fig. 6.6. It shows the zenith angle distribution of the selected measured data with a fit of a Gaussian distribution in order to determine the peak position. The fit results in  $\theta_{\text{ref}} = \theta_{\text{peak}} = 21^\circ$ .

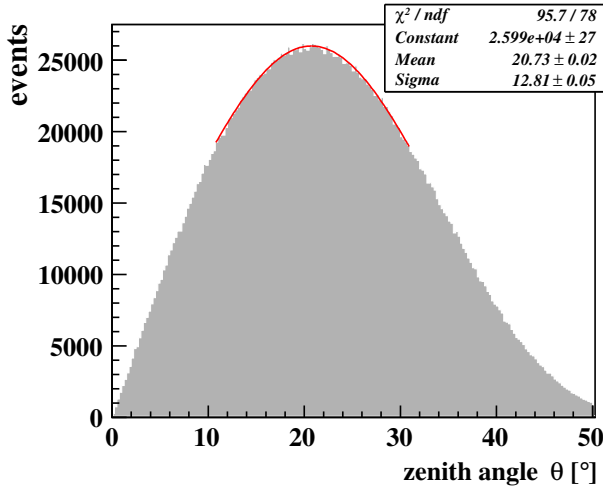


**Figure 6.6:** Measured zenith angle distribution. A Gaussian is fitted to the distribution in order to determine the peak position. The mean of the Gaussian results to  $21^\circ$ , which acts then as the reference angle.

## 6.2 Corrected shower size spectra

Eq. (6.14) can be written as:

$$\log_{10} N_{\text{ch},21^\circ} = \frac{\log_{10} N_{\text{ch}}}{1 + P_1 \cdot X + P_2 \cdot X^2}, \quad (6.16)$$

where  $N_{\text{ch}}$  and  $X$  are known shower properties of the individual event.  $P_1$  and  $P_2$  are determined by the fit of the attenuation curves, see Fig. 6.5 and Tab. C.1. Thus, with Eq. (6.16), a reference number of charged particles  $N_{\text{ch},21^\circ}$  can be determined for each event. An event is represented by a specific point in the parameter space, see Fig. 6.5. Most probably, these points do not hit one of the curves and therefore, the curve nearest to this point is selected. Its parameters are then used to calculate the reference number of charged particles  $N_{\text{ch},21^\circ}$ .

It is also possible to use only one attenuation curve to calculate the reference number of charged particles, like in [Mar07]. This single curve could be an average curve, the mean curve, or the curve with the smallest errors if all curves have within errors the



same shapes. Thus, using only one curve can reduce the uncertainties. But there is an advantage in using several attenuation curves. As mentioned before, the constant intensity method assumes a constant composition of the primary cosmic particles. If the composition changes, the assumption may not be valid anymore. But, if several intensity cut values with the corresponding attenuation curves are used, the composition has only to be constant locally between two cut values, reducing the uncertainties introduced by a change in the composition.

The reference number of charged particles  $N_{\text{ch},21^\circ}$  refers to one zenith angle and hence this variable is a zenith angle independent property of the shower. Therefore, plotting the shower size diagrams for different zenith angles as a function of the reference number of charged particles  $N_{\text{ch},21^\circ}$  instead of the “normal” number of charged particles  $N_{\text{ch}}$  should produce zenith angle independent diagrams. In Fig. 6.7 the fluxes for

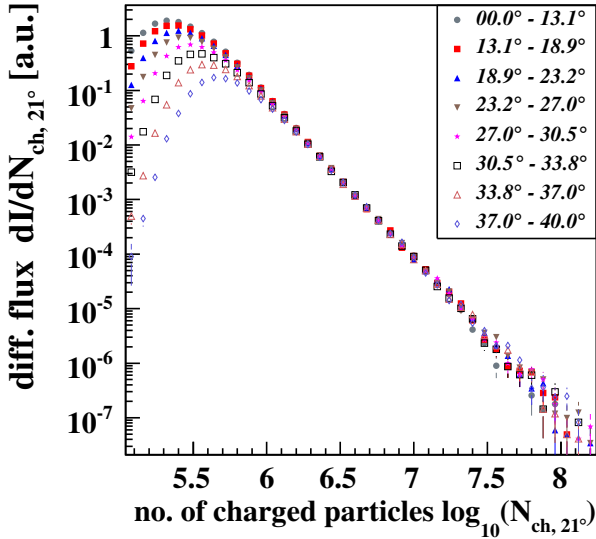


**Figure 6.7:** Shower size spectra. Differential flux as a function of the reference number of charged particles  $N_{\text{ch},21^\circ}$ . Using this variable the shower size spectra for different zenith angle ranges coincide, demonstrating the zenith independence of this variable.

different zenith angle bins are plotted as a function of the reference number of charged particles  $N_{\text{ch},21^\circ}$ . The different diagrams coincide and hence demonstrate that they are zenith angle independent. This allows to determine for each individual air shower event the corresponding intensity.

Additionally, a corrected shower size spectrum, which is the flux plotted as a function of the reference number of charged particles  $N_{\text{ch},21^\circ}$ , can be determined. Fig. 6.8(a) shows the differential flux for events up to a zenith angle of  $40^\circ$ . In Fig. 6.8(b) the differential spectrum is multiplied by  $N_{\text{ch},21^\circ}^3$ , in order to see the structure of the spectrum in more details. The threshold effect described in Chap. 5.2, can be seen in both figures.

The procedure to get a zenith angle independent measure of the shower size, could depend on the choice of the reference angle. In order to evaluate this, the whole procedure was repeated using a reference angle of  $\theta_{\text{ref}} = 0^\circ$ . As expected, the fit parameters are different (see Tab. C.2), but the resulting reference number of charged particles  $N_{\text{ch},0^\circ}$  is still zenith angle independent (see Fig. C.1). In order to see whether the resulting shower size spectra are different, too, the shower size spectra obtained for both reference angles are compared in Fig. 6.9. It shows two spectra with similar structures,

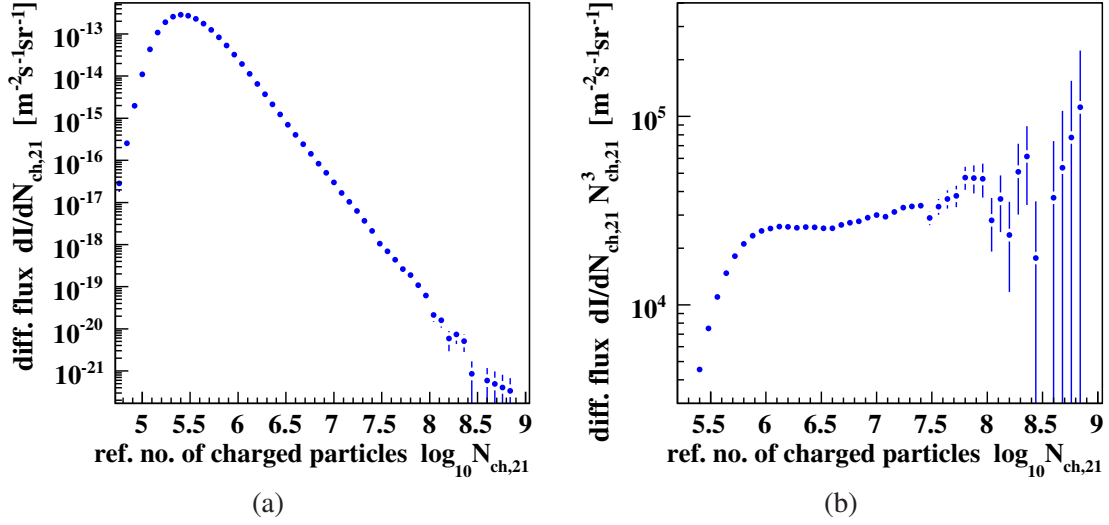


**Figure 6.8:** Corrected shower size spectrum. Differential flux as a function of  $N_{\text{ch},21^\circ}$  (*left*). In the *right* figure, the flux is multiplied by  $N_{\text{ch},21^\circ}^3$  in order to see the structure of the diagram in more detail.

but with a displacement between them. The displacement can be explained by the fact, that the number of charged particles at observation level decreases with increasing zenith angle, i.e. with increasing atmospheric depth, which can be seen in the diagram of the attenuation curves (Fig. 6.5). Thus, the number of charged particles which refer to  $0^\circ$

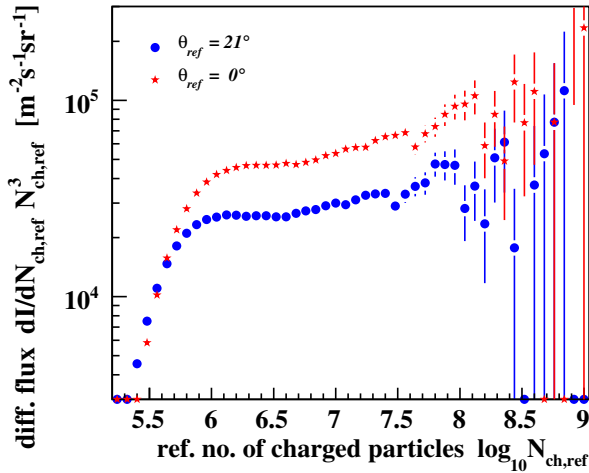


**Figure 6.9:** Shower size spectra as a function of the reference number of charged particles for two different reference angles  $0^\circ$ , and  $21^\circ$ .

is larger compared to the number of charged particles which refer to  $21^\circ$ . Therefore, the shower size spectrum for  $\theta_{\text{ref}} = 0^\circ$  is shifted towards higher values of  $N_{\text{ch}}$ . Because the spectra are shown with a flux that is multiplied by  $N_{\text{ch}}^3$ , the diagram is also shifted to higher flux values. Scaling the spectrum in a way, that both diagrams are coinciding reveals, that they do not deviate from each other and that the choice of the reference angle has no significant influence (see Fig. C.2). To use a reference angle of  $21^\circ$  is justified by the fact, that for real events, most showers come from this direction. This ensures, that

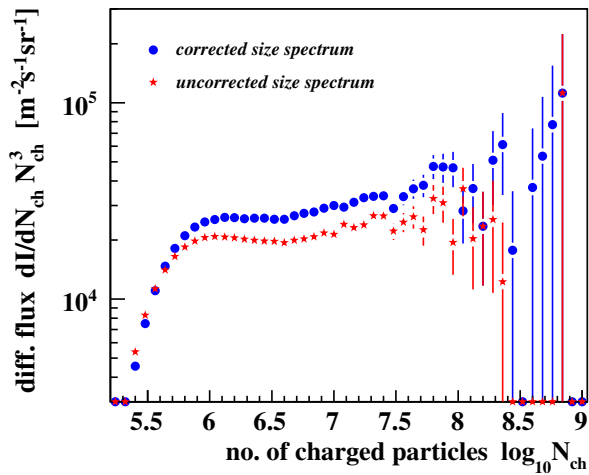


**Figure 6.10:** Comparing the shower size spectrum as a function of reference number of charged particles  $N_{\text{ch},21^\circ}$  to a shower size spectrum as a function of the number of charged particles  $N_{\text{ch}}$ . It shows, that the shape of the spectrum is not changed by using  $N_{\text{ch},21^\circ}$ .

a subsample cut, introduced in the next Chap. 7, is applied in a region with the highest possible statistics of shower events.

Finally, the corrected shower size spectrum can be compared to the uncorrected shower size spectrum, which is a function of the “normal” number of charged particles  $N_{\text{ch}}$  (see also Fig. 5.8). The constant intensity method should not change the features of this diagram. Fig. 6.10 shows both spectra. They are in agreement with each other, except for a shift on the axis, which can be explained in the same way as the shift in Fig. 6.9.

### 6.3 Summary

In this chapter, the method of constant intensity was introduced. This method allows to eliminate the zenith angle dependence of the measured data by using the measured data itself.

In order to apply the constant intensity method, the shower size spectra for different zenith angle bins were determined. Cuts at different intensity values led to attenuation curves, which were fitted with a polynomial of second order. Using these fits the number of charged particles of all events could be referred to a reference angle, which was chosen to be  $\theta_{\text{ref}} = 21^\circ$ . It was shown, that the new variable is zenith angle independent, which allows to calculate an associated intensity for every event.

A corrected shower size spectrum as a function of the new variable could be evaluated. It was shown, that this spectrum agrees with the shower size spectrum as a function of the “normal” number of charged particles  $N_{\text{ch}}$ . Hence, the procedure does not change the features of the size spectrum.

More results and details can be found in App. C.



---

# Subsample selection and energy conversion

---

In this chapter, the conversion relation between the number of muons and the primary energy is determined.

In the first part, the shower fluctuations are investigated in order to motivate the use of the number of muons instead of the number of charged particles as an energy estimator. This is also supported considering composition dependence.

In the second part, the subsample cuts are introduced and motivated. The purpose of these cuts is to minimize the uncertainties of the determination of the energy conversion relation. The relation itself is evaluated in the third part of this chapter.

## 7.1 Shower fluctuations and composition dependence

In extensive air shower experiments shower fluctuations are one source of uncertainty in the determination of the properties of the primary cosmic particles such as the primary energy [AM02]. Two primary cosmic ray particles with the same properties like the energy, the type of the particle, and the arrival direction could lead to showers with a different number of electrons and muons. This is mainly due to two reasons. Firstly, the point of the first interaction is not fixed to a certain height in the atmosphere, which leads to a different starting point of the shower development and thus, to a different number of particles at observation level. Secondly, the process of the shower development is heavily driven by stochastic processes. This leads to different observable numbers, too.

The influence of shower fluctuations on the method of constant intensity is examined in [AM02]. It is concluded that the intrinsic shower fluctuations do not affect the method strongly. In Chap. 8.2, the influence of the shower fluctuations on the determination of the primary energy spectrum is discussed in more details. In this chapter, shower simulations are being used in order to obtain a conversion relation between the number of muons and the primary energy of the extensive air shower. Fluctuations have an influence on the precision of this energy estimator. Thus, the fluctuations are examined

in order to motivate the usage of the number of muons and to estimate the uncertainty introduced by the fluctuations.

All simulation sets available are used, see Tab. 4.1. In order to reduce computing time, each simulated air shower is re-used several times for the simulation of the detector response. In this part, only the fluctuations of the individual showers are examined and hence, the redundant showers are removed from the sets. The remaining showers are divided into several zenith angle and energy ranges. For each section, the number of charged particles and the number of muons are filled in a histogram. Furthermore, the histograms are filled separately for hydrogen and iron induced showers. In Fig. 7.1, the distribution of the number of charged particles and the distribution of the number of muons are shown for iron induced shower for a zenith angle range of  $16^\circ \leq \theta < 24^\circ$  and an energy range of  $7.50 \leq \log_{10} E_p / \text{GeV} \leq 7.75$ .

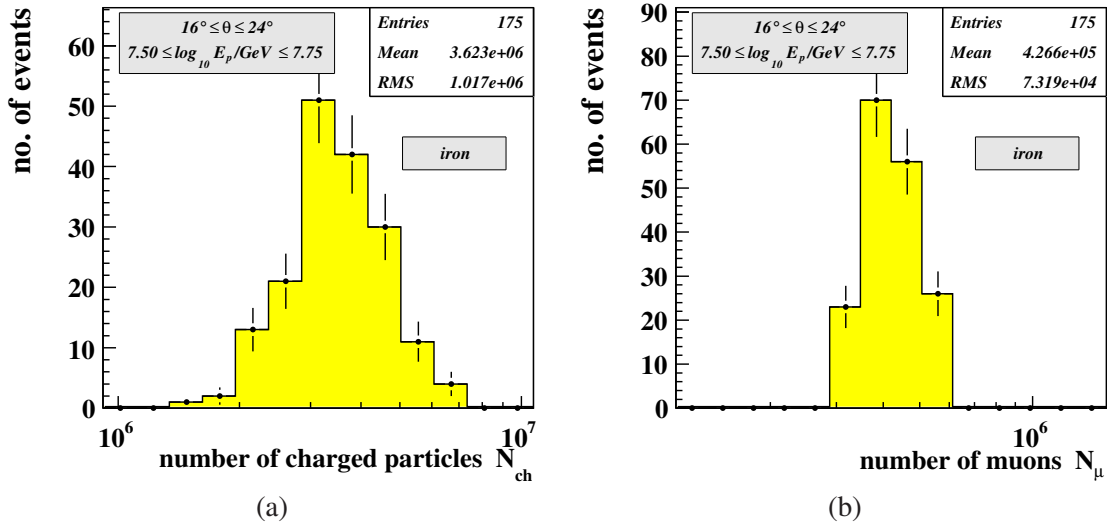


**Figure 7.1:** Shower fluctuations for the number of charged particles (*left*) and the number of muons (*right*). The fluctuation distributions are shown for iron induced showers for the zenith range of  $16^\circ \leq \theta < 24^\circ$  and the energy range of  $7.50 \leq \log_{10} E_p / \text{GeV} \leq 7.75$

The mean of the distribution for muons is  $N_{\text{mean},\mu} = 4.27 \cdot 10^5$  with a RMS of  $\text{RMS}_\mu = 0.73 \cdot 10^5$ . In order to obtain a quantity which can be compared for each bin, the relative fluctuation is calculated:

$$\Delta^{\text{fluc}} = \frac{\text{RMS}}{N_{\text{mean}}}. \quad (7.1)$$

In the case of the number of muons in a bin, the ratio calculates to  $\Delta_\mu^{\text{fluc}} = 17\%$ . For the distribution of the number of charged particles it results in a mean of  $N_{\text{mean,ch}} = 3.62 \cdot 10^6$  and a  $\text{RMS}_{\text{ch}} = 1.02 \cdot 10^6$  and thus, to a ratio of  $\Delta_{\text{ch}}^{\text{fluc}} = 28\%$ . Here the fluctuations of the number of charged particles is significantly larger than the fluctuations for the number of muons. In App. D, results for all bins and for hydrogen induced showers can be found. Fig. 7.2 summarizes the relative fluctuations  $\Delta^{\text{fluc}}$  for each bin of the

distributions. In order to compare the fluctuations of the number of charged particles with those of the number of muons, both diagrams have the same scaling of the fluctuation ratio, i.e. the same color code. The figure shows the relative fluctuations for iron induced showers. The same plots for hydrogen induced showers are found in Fig. D.21

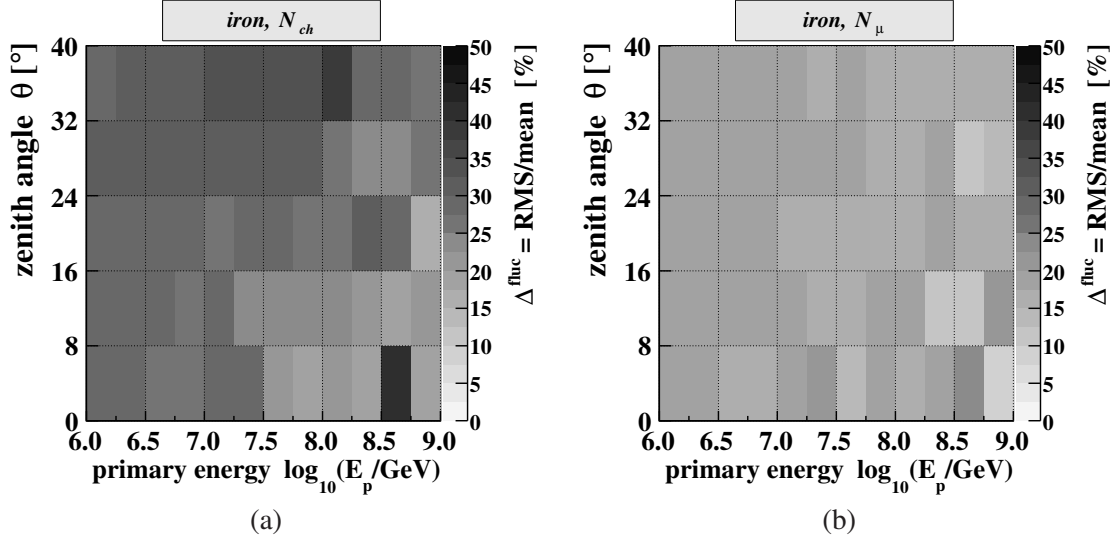


**Figure 7.2:** Relative shower fluctuations of iron induced showers for the number of charged particles (*left*) and the number of muons (*right*). Both diagrams have the same scaling in order to allow their direct comparison.

in App. D. This figure shows, that for hydrogen induced showers, the fluctuations of the number of charged particles are significantly larger than the fluctuations for the number of muons. Thus, in both cases, considering hydrogen and iron initiated showers, it can be seen, that the fluctuations of the number of muons are much smaller compared to the fluctuations of the charged particles.

Besides the shower fluctuations, the composition dependence has to be examined. In contrast to the shower fluctuations, [AM02] found that the composition of the cosmic rays has a strong influence on the determination of the primary energy using the constant intensity method. In order to examine the composition dependence as a function of the number of charged particles compared to the dependence as a function of the number of muons, the same fluctuation diagrams are used (App. D). The relative deviation  $\Delta^{\text{comp}}$  between a hydrogen and an iron induced shower is a measure of the composition dependence of the corresponding bin:

$$\Delta^{\text{comp}} = 2 \frac{|N_{\text{mean,H}} - N_{\text{mean,Fe}}|}{N_{\text{mean,H}} + N_{\text{mean,Fe}}}, \quad (7.2)$$

where  $N_{\text{mean,Fe}}$  is the mean of the fluctuation distribution for iron induced showers and  $N_{\text{mean,H}}$  is the same for hydrogen induced showers. In Fig. 7.3, these relative deviations are shown for each bin for the number of charged particles and for the number of muons. It shows, that the composition dependence as a function of the number of muons is smaller compared to the composition dependence as a function of the number of charged particles.

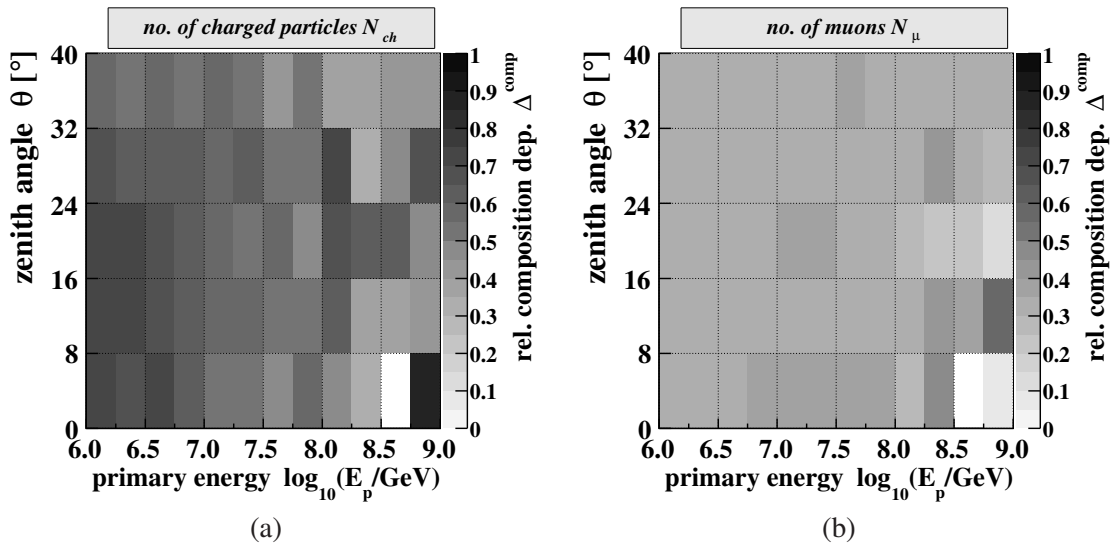


**Figure 7.3:** Relative composition dependence for the number of charged particles (*left*) and the number of muons (*right*).

In order to see the differences between the number of muons and the number of charged particles, the difference between the relative fluctuations for the number of muons and the number of charged particles  $\Delta_\mu^{\text{fluc}} - \Delta_{ch}^{\text{fluc}}$  is calculated for each bin. Hence, a negative value of the difference corresponds to a smaller dependence for the number of muons in the corresponding bin. In Fig. 7.4(a), these differences are plotted for iron induced showers. It shows that the relative fluctuation of the number of muons is always smaller than the relative fluctuations of the number of charged particles. The same is true in the case of hydrogen initiated showers, which can be seen in Fig. D.5. For these showers, only three bins have a difference which is bigger than zero. These are mainly caused by the small statistics of events in these bins, see App. D. Furthermore, these differences are in zenith angle ranges, which are of less interest, because of the subsample cuts introduced later in this chapter.

A similar plot, which shows the differences between the relative composition dependencies, can be seen in Fig. 7.4(b). Both the investigation of the fluctuation dependence and the investigation of the composition dependence, favor the use of the number of muons as the energy estimator.

## 7.2 Subsample cuts

The Grande detector stations can not distinguish between the electromagnetic component and the muonic component, see Chap. 4. In order to calculate the number of muons in an air shower event, the KASCADE detector stations are used. The reconstruction routines determine the lateral density distribution for the muons using those detectors. The extrapolation to distances of the Grande stations leads to an estimation of the muon number for the Grande stations. Thus, it is expected that the accuracy of the muon



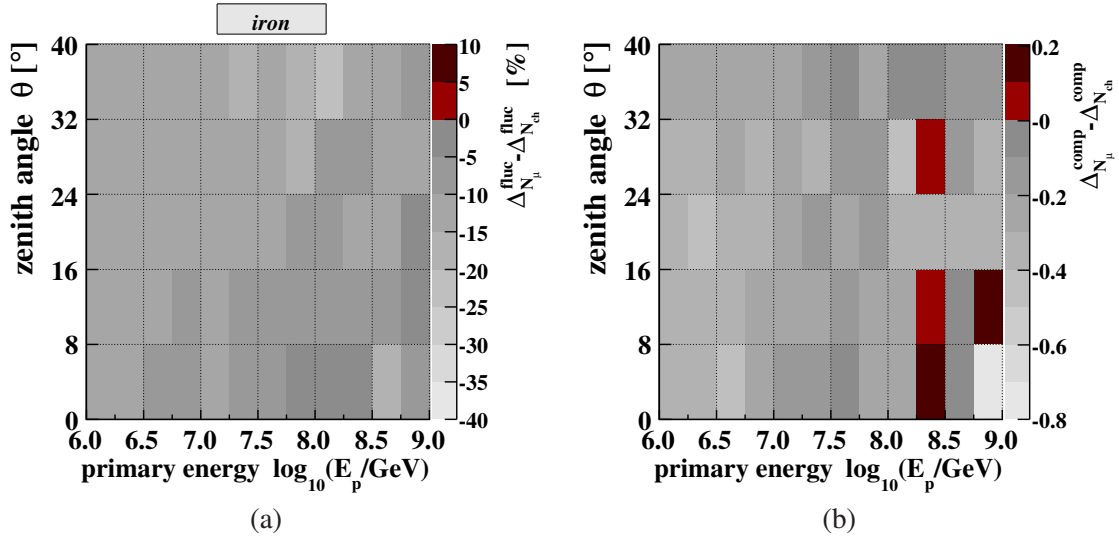


**Figure 7.4:** *Left:* Difference plot between the fluctuations of the number of muons and the number of charged particles for iron induced showers. *Right:* Difference plot between the composition dependencies of the number of muons and the number of charged particles.

number determination depends on the shower core position relative to the KASCADE array.

In order to evaluate this dependence in more detail, the entire simulation sets are used and the accuracy of the reconstruction of the number of muons is calculated:

$$\Delta N_\mu = \frac{N_\mu^{\text{rec}} - N_\mu^{\text{true}}}{N_\mu^{\text{true}}}, \quad (7.3)$$

with the true number of muons  $N_\mu^{\text{true}}$  and the reconstructed number of muons  $N_\mu^{\text{rec}}$ . This reconstruction error is plotted as a function of the distance of the shower core from the KASCADE array  $R_{\text{core}}$  for different ranges of the reconstructed number of muons. In Fig. 7.5, the reconstruction error is shown for four different ranges. The accuracy is determined for hydrogen induced showers, for iron induced showers, and for a mixed composition. The figures show that the reconstruction error of the number of muons depends on the distance of the shower core to the center of the KASCADE array. For the determination of the energy conversion relation, a constant reconstruction error is necessary, otherwise the same number of muons would relate to different primary energies. This also means, that the reconstruction error does not have to be zero. Therefore a core distance cut of  $280\text{m} \leq R_{\text{core}} \leq 400\text{m}$  is proposed in order to ensure that only events with a reliable muon number reconstruction are used for the determination of the energy conversion relation. Using this cut, the reconstruction error stays within an error band of  $\pm 5\%$ .

In Chap. 6, the constant intensity method has been introduced. The application of this method allows to refer the number of charged particles of each event to one defined reference zenith angle. This allows to relate a given number of charged particles to a

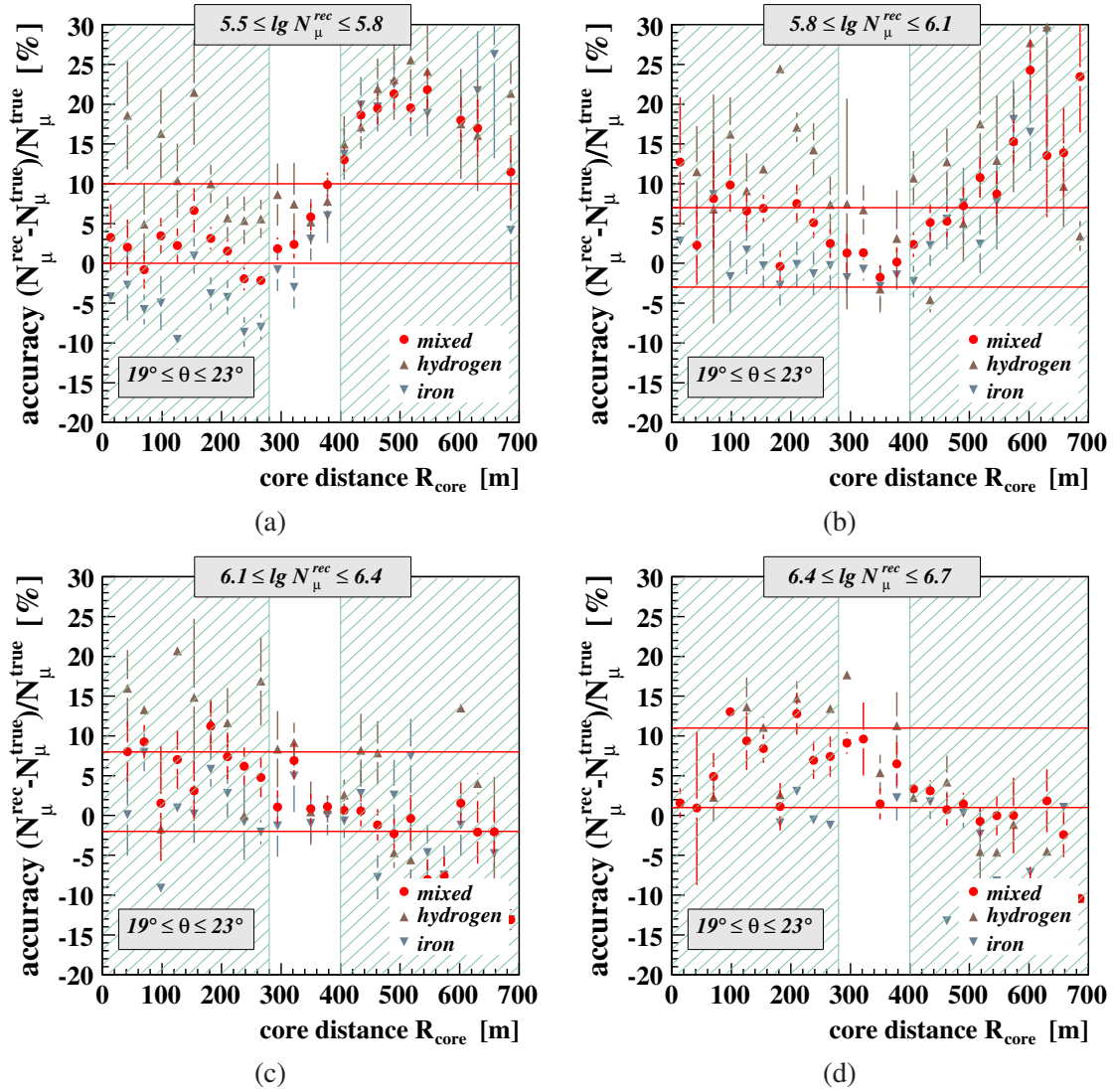


**Figure 7.5:** Reconstruction error of the number of muons as a function of the distance of the shower core to the center of the KASCADE array. In each figure, the reconstruction error is shown for hydrogen and iron induced showers and for the assumption of a mixed composition. The horizontal lines are indicating an error band of  $\pm 5\%$ . A distance cut is applied, which excludes the hatched areas. Each figure shows the reconstruction error for another range of the reconstructed number of muons.

certain intensity. Using a zenith dependent number of charged particles this relation would be ambiguous. This ambiguity is also true for the number of muons. Therefore, a cut in the zenith angle is necessary in addition to the cut in the distance of the shower core. This cut confines the events to a small zenith angle range and thus, the number of muons can be correlated to the primary energy. In order to correlate the number of muons and the reference number of charged particles, the selected zenith angle range should be around the reference angle used in the attenuation curve fit, see Eq. (6.15). The number of simulated air showers available is limited (see Chap. 4.2) and hence, the zenith angle range should be chosen in a range of the highest statistics possible, which is around  $21^\circ$ . Therefore, a zenith angle cut of  $19^\circ \leq \theta \leq 23^\circ$  is applied.

Both selection criteria are applied in addition to the standard quality cuts and are forming the subsample cuts. The cut in the shower core distance results in a ring of selected events inside the fiducial area. This is illustrated in Fig. 7.6, which shows the distribution of the selected events over the Grande array. In order to obtain this figure, the complete sets of simulated air showers have been used.

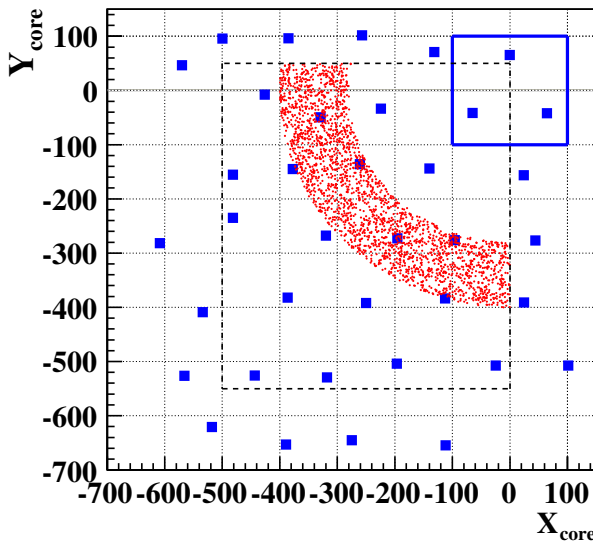


**Figure 7.6:** Schematic view of the KASCADE-Grande experiment, demonstrating the influence of the subsample cuts on the event selection. The shower core position of each selected event is plotted in coordinates of KASCADE-Grande, resulting in a ring structure. The small filled squares illustrate the position of the Grande stations. The KASCADE array is represented by the open square in the top right corner. The dashed lined rectangle indicates the fiducial area cut.

In order to obtain the correlation curve between the reference number of charged particles and the primary energy, these subsample cut criteria will also be used in the next chapter.

## 7.3 Energy conversion

In order to determine the energy conversion between the number of muons and the primary energy, all available sets of simulated air showers are used. In addition to the standard quality cuts, the subsample cuts, introduced above, are applied to these data sets.

The data sets contain air shower events for the five different primary mass groups hydrogen, helium, carbon, silicon, and iron. For a mixed composition, an equal fraction of 20 % for each group is assumed. This mixed composition is used in order to determine

the relation between the number of muons and the primary energy. Fig. 7.7 shows the number of muons as a function of the true primary energy in a two-dimensional histogram using a mixed composition. The color code gives the number of events in the corresponding bin. The width of this distribution is an effect of the fluctuations. In order to determine the energy conversion relation, each selected event is filled in a

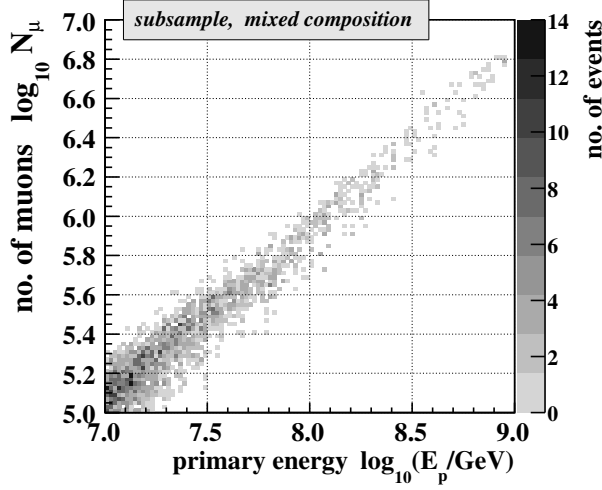


**Figure 7.7:** The number of muons as a function of the true primary energy using a mixed composition and applying the subsample cuts

profile diagram. This diagram is only binned in the number of muons and is bin-free for the primary energy. For each bin, the mean and the spread of the distribution of events corresponding to this bin is calculated. The spread is a measure of the fluctuations inside each bin. Fig. 7.8(a) shows the profile plot of the primary energy as a function of the number of muons for a mixed composition. In order to obtain a general correlation relation between the primary energy and the muon number, a linear function is fitted in the double logarithmic plot:

$$\log_{10} E_p^{\text{true}} = a + b \cdot \log_{10} N_\mu. \quad (7.4)$$

In Chap. 5.2, a cut on the number of muons of  $\log_{10} N_\mu > 5.0$  was proposed, in order to ensure full trigger and reconstruction efficiencies. The highest bin in the diagram contains only one event, therefore, the highest bin should be discarded from the fit. Hence, the fit is performed in the range  $5.0 < \log_{10} N_\mu < 6.8$  and results in:

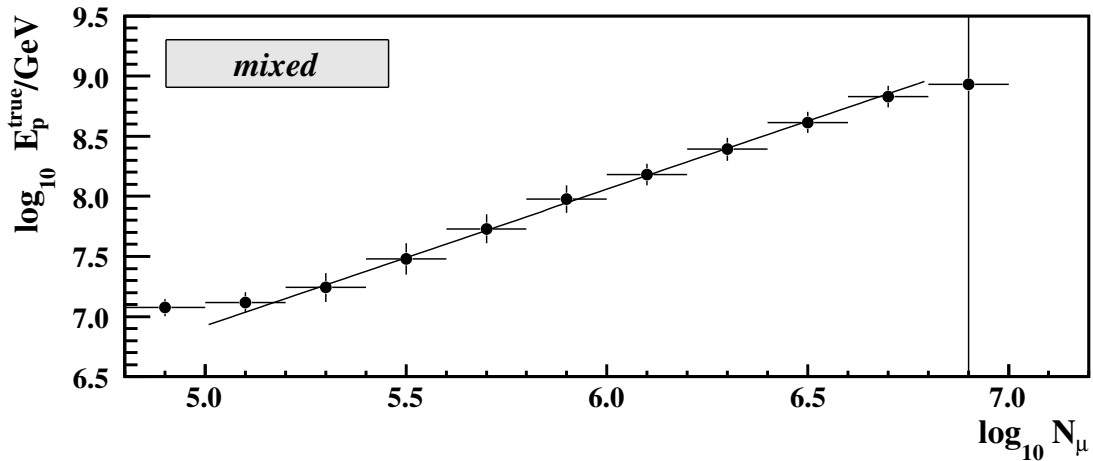
$$a_{\text{mixed}} = 1.24 \pm 0.60, \quad b_{\text{mixed}} = 1.14 \pm 0.10. \quad (7.5)$$

In order to get an estimation of the composition dependence, the same procedures are performed with hydrogen and iron initiated showers, which can be seen in Figs. 7.8(b) and 7.8(c). The fits on these diagrams result in:

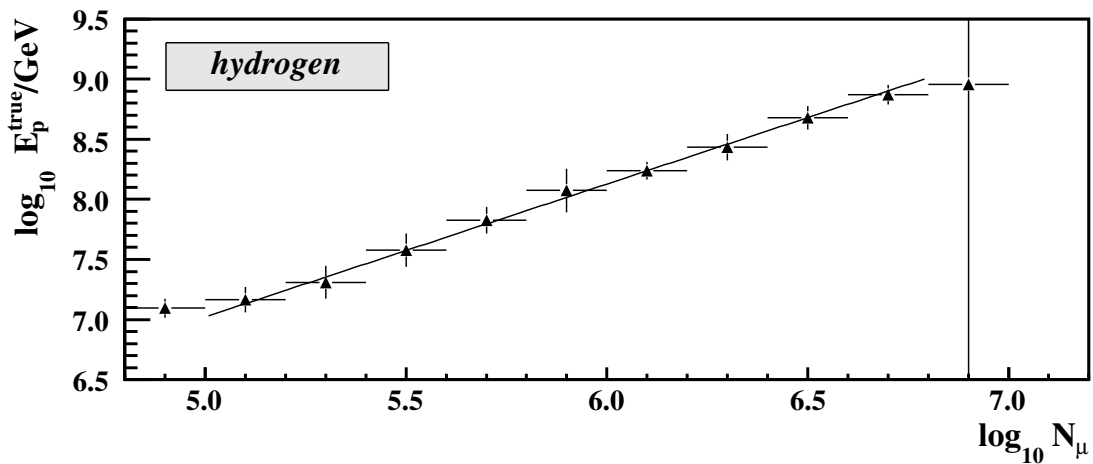
$$a_{\text{H}} = 1.49 \pm 0.67, \quad b_{\text{H}} = 1.11 \pm 0.11, \quad (7.6)$$

$$a_{\text{Fe}} = 1.14 \pm 0.42, \quad b_{\text{Fe}} = 1.15 \pm 0.07. \quad (7.7)$$

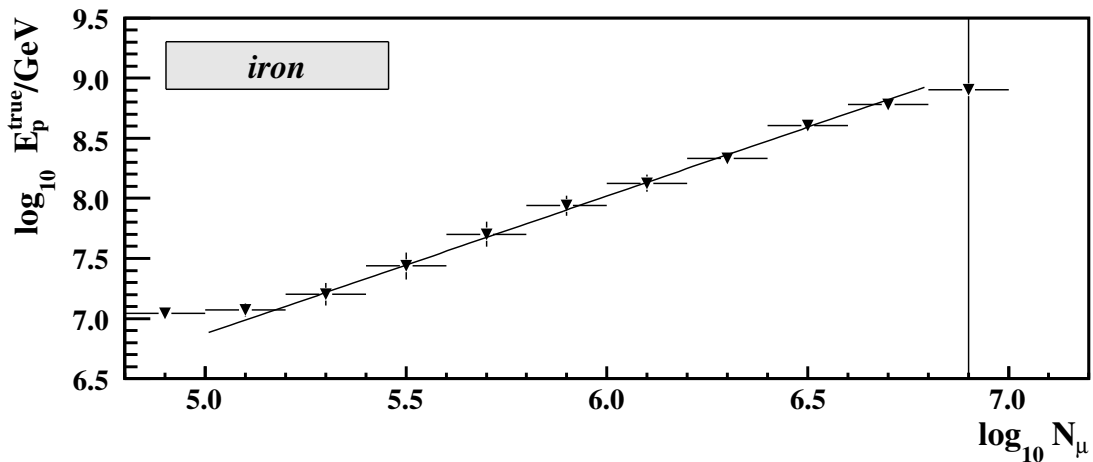
Comparing the errors of these fits it can be seen, that the errors for iron initiated showers are smaller compared to hydrogen initiated showers, which is due to the fact that the fluctuations for iron initiated showers are smaller, see above in Chap. 7.1.



(a) Mixed composition



(b) Hydrogen initiated showers



(c) Iron initiated showers

**Figure 7.8:** Profile diagrams of the primary energy as a function of the number of muons. All simulated shower data sets are used and the subsample cuts are applied. The line is the resulting linear fit to the data points. This fit is used as the energy conversion relation.

The differences between the resulting fit function and each event are calculated, resulting in a distribution centered around zero. This distribution is seen in Fig 7.9(a). In addition, the diagram is scaled in such a way, that the integral over the whole diagram is unity.

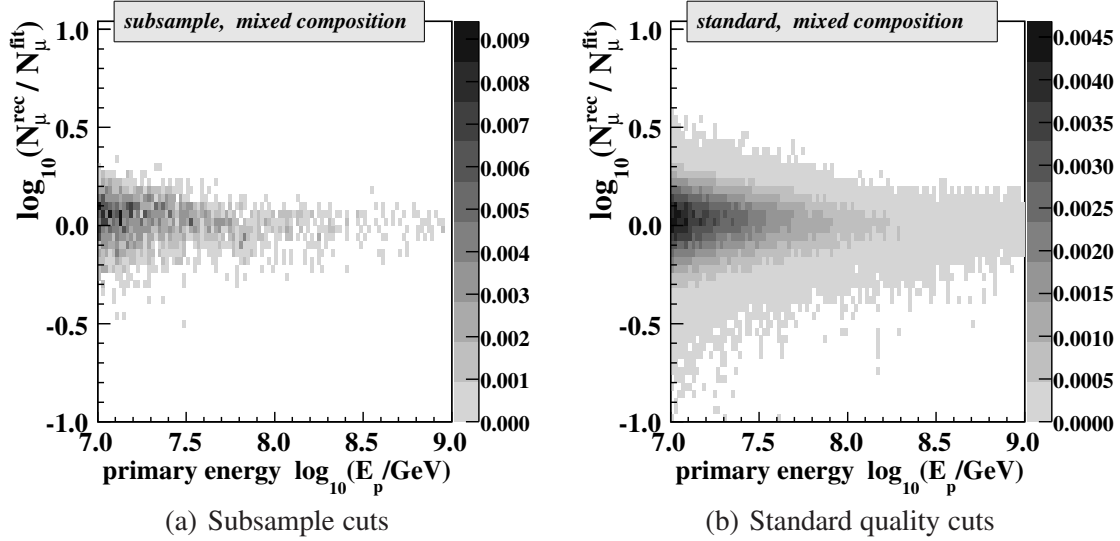


**Figure 7.9:** Difference plots between the energy conversion fit function and the number of muons of an event. A mixed composition is used and the diagrams are scaled in such a way, that the integral over the diagram equals to one. For the *left* figure, the subsample cuts are applied. For the *right* figure only the standard quality cuts are applied.

The whole procedure is repeated only with the application of the standard quality cuts. Detailed results can be found in App. E. The fit for the mixed composition results in:

$$a_{\text{mixed}}^{\text{std}} = 1.23 \pm 0.72, \quad b_{\text{mixed}}^{\text{std}} = 1.14 \pm 0.12. \quad (7.8)$$

Comparing the fit results using standard cut events to those with the additional subsample cuts, e.g. Eqs. (7.5) and (7.8), it can be seen, that the fit values are comparable, but the fit errors are smaller using the subsample cut events.

The difference plot between this fit function and the selected events can be seen in Fig. 7.9(b). The difference plots for the subsample cuts and the standard quality cuts can be compared. It shows, that the distribution is broader for the events where only the standard cuts are applied. In order to investigate this in more detail, both distributions are projected to the y-axis. Due to the fact, that the integrals over both distributions are normalized to one, it is possible to compare them directly. Fig. 7.10 shows both projections. It can be seen, that the distribution, which results from the standard quality cuts, is slightly broader than the distribution resulting from events with the additional subsample cuts applied. In Tab. 7.1, the RMS values of the distributions are summarized. In addition to the assumption of a mixed composition, the values for the assumptions of hydrogen or iron induced showers are included. In Fig. E.7, the results for these two assumptions can be seen. The differences of the RMS of both

Composition	RMS	
	Standard cuts	Subsample cuts
mixed	$0.14 \pm 0.09$	$0.11 \pm 0.07$
hydrogen	$0.15 \pm 0.10$	$0.12 \pm 0.08$
iron	$0.11 \pm 0.08$	$0.08 \pm 0.05$

**Table 7.1:** Comparison of the standard cuts with the subsample cuts using the distribution of the number of muons.

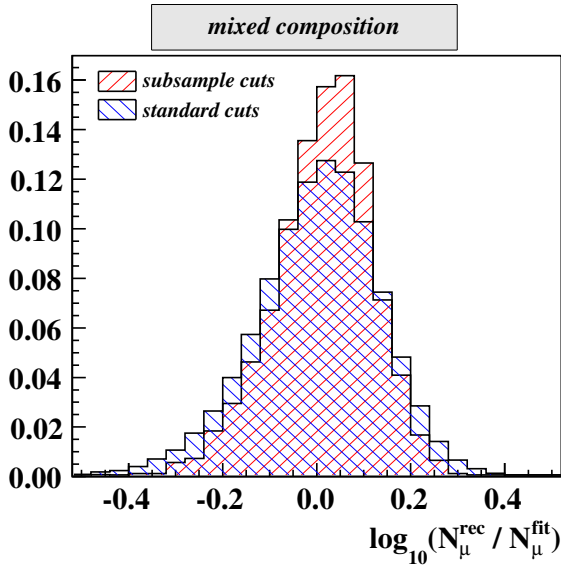


**Figure 7.10:** Comparing the standard quality cuts with the additional subsample cuts for the number of muons. Projection of the difference distribution of Fig. 7.9 to the y-axis. A mixed composition is used.

samples are small and within error bars, they are compatible with each other.

## 7.4 Summary

In this chapter the shower fluctuations were examined. It was shown, that the number of muons is less sensitive to the shower fluctuations and the composition dependence of the primary radiation than the number of charged particles. Therefore, the number of muons was used as the energy estimator.

Additionally, the subsample cuts were introduced. The reasons for that were twofold. Firstly, the reconstruction of the number of muons depends on the distance of the shower core to the KASCADE array. In order to have a stable reconstructed number of muons with small variations, a cut in the core distance was introduced. Secondly, the zenith angle should be confined to the reference angle introduced in the previous chapter in order to reduce the uncertainties introduced by different arrival directions. Therefore, the following subsample cuts were introduced:

$$\begin{aligned}
 280 \text{ m} &\leq R_{\text{core}} \leq 400 \text{ m}, \\
 19^\circ &\leq \theta \leq 23^\circ.
 \end{aligned}
 \tag{7.9}$$

A relation between the number of muons and the primary energy was determined. In order to obtain this relation, several simulation sets were used. Applying the subsample cuts and plotting the primary energy as a function of the number of muons allowed to fit a linear function to the resulting diagrams. This was performed for a mixed composition with an equal fraction of all five primary mass groups, for hydrogen induced showers, and for iron induced showers. The result for the mixed composition will be used as an energy estimation. The both resulting functions for hydrogen and iron induced showers will be used as an estimator for the composition dependence of the energy estimation.

Finally, the fit results were used in order to evaluate the influence of the subsample cuts. It was shown, that distributions for the subsample cut events are more narrow and more confined.



---

# All particle primary energy spectrum

---

In the first part of this chapter, the calibration function, which converts the reference number of charged particles into the primary energy, is determined. This relation is obtained from measured data. This calibration function allows to determine the energy spectrum.

In the second part, the various sources of systematic uncertainties, are studied. Monte-Carlo simulations are used in order to study the shower fluctuations and their influence on the determination of the energy spectrum in more detail. Finally, the reconstructed energy spectrum including the systematic uncertainties is given.

## 8.1 Energy calibration function

In Chap. 7, the conversion relation between the number of muons and the primary energy is determined. This conversion relation is deduced using shower simulations. Although each successfully reconstructed real event has a reconstructed number of muons, the determined conversion relation can not be applied directly to the data. This has two reasons. Firstly, in order to determine the conversion relation, a cut in the shower core distance to the KASCADE array is applied. This selection guarantees, that the variation of the reconstruction uncertainties in the number of muons is confined within an error band of  $\pm 5\%$ . Otherwise, it is possible, that a certain primary energy corresponds to different numbers of muons. This will also happen if the conversion relation is used for real data directly. This means, that the validity of the conversion relation is not given for shower core distances outside the selection range.

Secondly, in Chap. 6, it was shown, that the number of charged particles and the intensity are not directly connected. The intensity also depends on the zenith angle. Using the constant intensity method, the zenith angle dependence can be eliminated and therefore the reference number of charged particles can be correlated to the intensity. The same is true for the number of muons, where the relation between the primary energy and the number of muons depends on the zenith angle. In order to determine the conversion relation a zenith angle cut has been applied (see previous chapter).

Hence, in order to determine the energy calibration function, the following procedure is performed using measured data. Firstly, the reference number of charged particles is zenith angle independent. Thus, the primary energy should be a function of the reference number of charged particles. Secondly, besides the reference number of charged particles the number of muons is determined for each event. Using the conversion relation, this number of muons can be converted into the primary energy. Therefore, for each event the reference number of charged particles and their primary energy are determined. In order to guarantee, that the number of muons is inside the parameters used for the determination of the conversion relation, the measured events have to fulfill the subsample cut criteria. Thus, the whole procedure leads to a relation between the primary energy and the reference number of charged particles, which is valid for all events fulfilling the quality cut criteria.

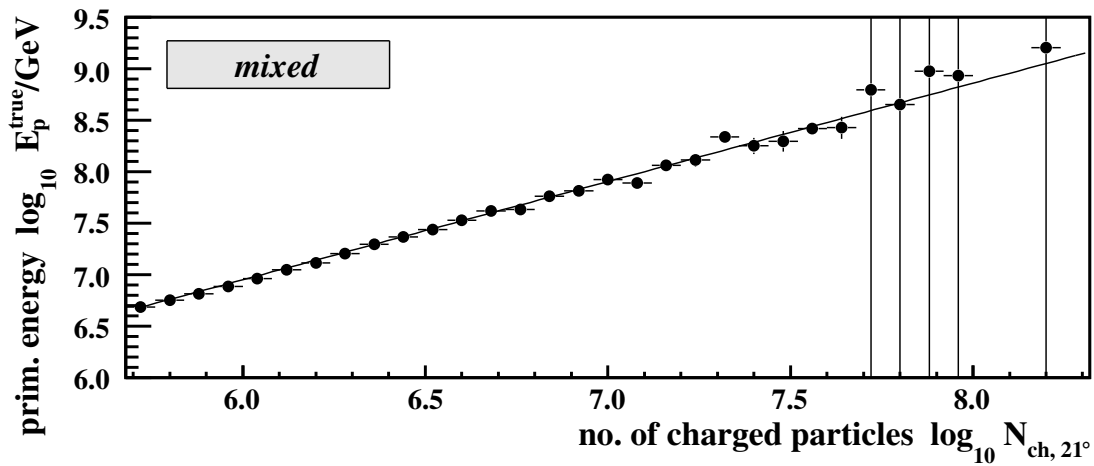
The subsample cuts, Eq. (7.9), are applied for every measured shower event and the reference number of charged particles is calculated using Eq. (6.16). The primary energy of the selected events is determined with the conversion relation, Eq. (7.4), using the reconstructed number of muons. The calculated primary energy  $E_p$  is then plotted as a function of the reference number of charged particles  $N_{\text{ch},21^\circ}$ , using a profile plot. This is seen in Fig. 8.1(a). The calibration relation is shown in a double logarithmic plot and the points follow a linear behavior. Therefore, in order to determine the calibration function a linear function is fitted to the points, which corresponds to a power law in the double linear plot:

$$\log_{10} E_p = \zeta + \xi \cdot \log_{10} N_{\text{ch},21^\circ}. \quad (8.1)$$

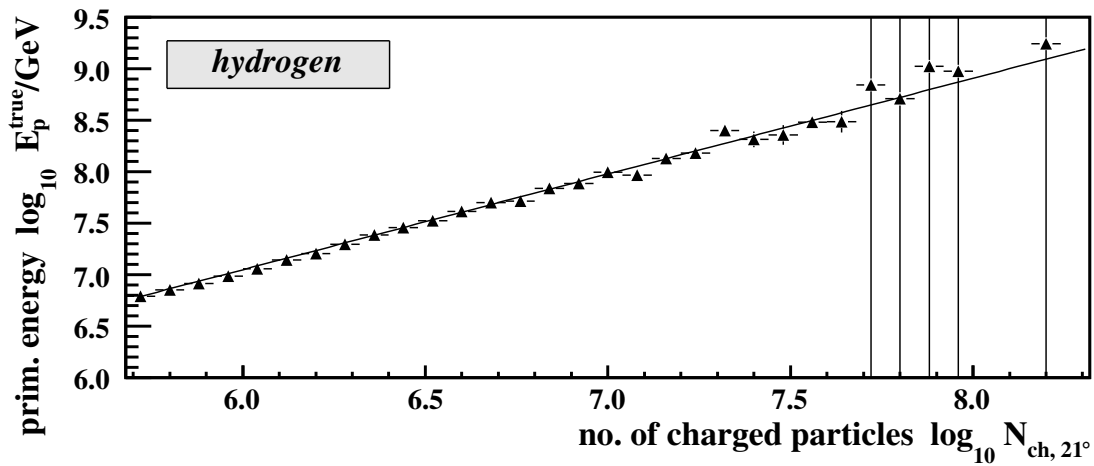
If  $S$  is the spread of the values inside a bin and  $n$  its number of entries, then the error for the bin is calculated by  $S/\sqrt{n}$ . If the bin contains only one entry, then the error of this bin is 100 %. This is true for all bins with  $\log_{10} N_{\text{ch},21^\circ} > 7.7$ . Hence, these bins are discarded in the fit. In Chap. 5.2, a cut on the number of charged particles of  $\log_{10} N_{\text{ch}} > 5.8$  was proposed, in order to ensure full trigger and reconstruction efficiencies. Therefore, the fit is performed in the range  $5.8 < \log_{10} N_{\text{ch},21^\circ} < 7.7$ . The result of this fit is summarized in Tab. 8.1.

Additionally, in the previous chapter the conversion relation is determined for the assumptions of a pure hydrogen and a pure iron composition. Using these relations, two calibration curves can be determined, representing these two primary assumptions. These extreme cases are used to estimate the composition dependence. In Figs. 8.1(b) and (c), these two relations together with the resulting fit functions are shown. The fit results are summarized in Tab. 8.1. The three relations, describing the conversion for the mixed, the pure hydrogen, and the pure iron composition, are linear equations. All three functions are applied to the same data set, thus, the resulting profile diagrams are only shifted to each other. Therefore, the  $\chi^2$  is the same for all fits.

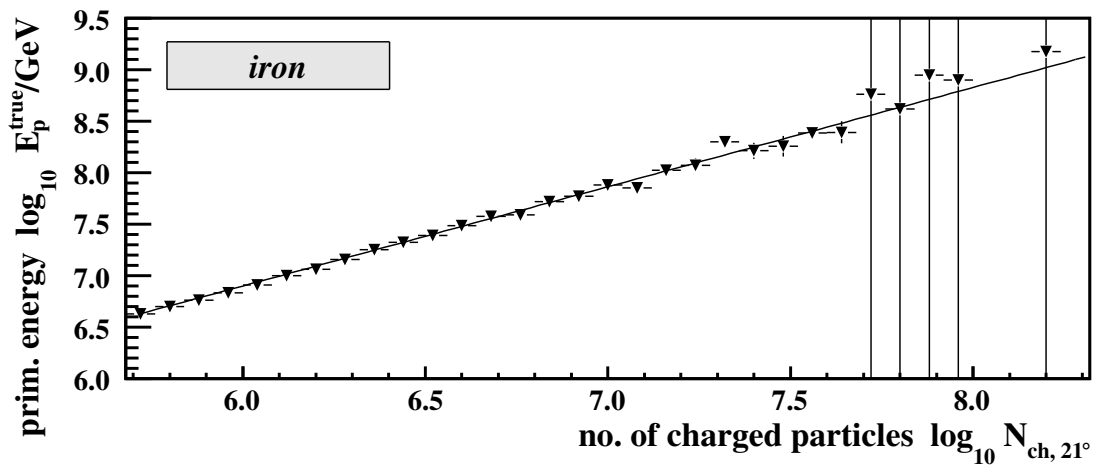
The resulting fit functions are used to determine the energy spectrum for every event fulfilling the quality cut criteria of the full sample. In Fig. 8.2, the resulting energy spectrum for the assumption of a mixed composition is seen. The errors drawn in this figure are only statistical. The spectrum is scaled in the same way as described in Chap. 6, in order to obtain a differential flux spectrum.



(a) Mixed composition



(b) Hydrogen initiated showers



(c) Iron initiated showers

**Figure 8.1:** Profile diagrams of the primary energy as a function of the reference number of charged particles  $N_{\text{ch},21^\circ}$ . Measured air shower events are used, which are fulfilling the subsample cut criteria. The line is the resulting linear fit to the data points. This fit is used as the energy calibration function. The bins for  $\log_{10} N_{\text{ch},21^\circ} > 7.7$  are containing only one event, causing an error of 100 %.

Composition	$\zeta$	$\xi$	$\chi^2/\text{dof}$
mixed	$1.23 \pm 0.14$	$0.95 \pm 0.02$	19.3/14
hydrogen	$1.48 \pm 0.13$	$0.93 \pm 0.02$	19.3/14
iron	$1.12 \pm 0.14$	$0.96 \pm 0.03$	19.3/14

**Table 8.1:** Results of the calibration fit.

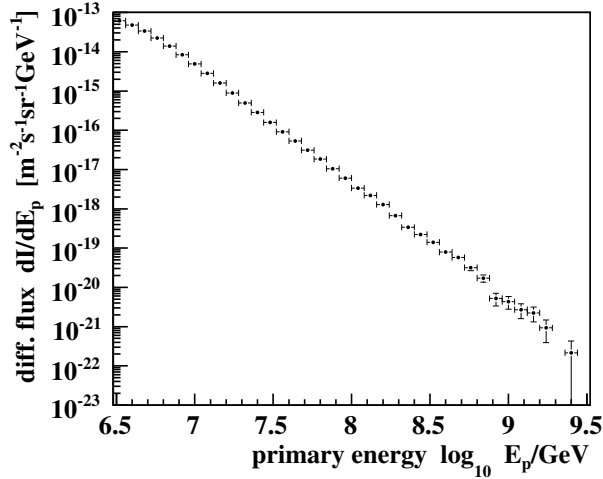


**Figure 8.2:** Differential flux of the cosmic rays as a function of the primary energy. The energy is determined using the calibration function on a single event basis for all measured events fulfilling the standard cut criteria. Only statistical errors are shown.

## 8.2 Study of systematic uncertainties

In this section, the systematic uncertainties of the determined energy spectrum are studied. There are three groups of sources of systematic uncertainties. Firstly, there are systematic uncertainties introduced by the finite resolution of the detector and errors introduced by the shower reconstruction procedure. These lead to uncertainties in the measured quantities used in the analysis. Secondly, there are uncertainties introduced by the analysis methods, e.g. the uncertainties of the various fits have an influence on the energy spectrum. Finally, there are uncertainties introduced by the physical nature of the cosmic rays and the extensive air showers, such as the shower fluctuations and the fact, that cosmic rays are a composition of different primary particles.

### 8.2.1 Influence of the uncertainty in the shower core position reconstruction

The shower core position is determined in the reconstruction software by a global fit, see Chap. 4.1. The uncertainty in the calculation of the core position leads to an erroneous event selection. Only events inside the fiducial area are selected, which is defined by the quality cut criteria, see Chap. 5.1. Due to the uncertainties in the determination of the core position, events, which are inside the fiducial area, could be reconstructed outside of this area and events from outside could end up inside the fiducial area. This leads to a wrong number of events in the bins of the shower size spectra, see Fig. 6.2. This affects the method of constant intensity, because it is applied to these spectra.

In order to determine the amount of events that are mis-selected, simulated air showers are used. The true core position  $(X_{\text{core}}^{\text{true}}, Y_{\text{core}}^{\text{true}})$  and the reconstructed core position  $(X_{\text{core}}^{\text{rec}}, Y_{\text{core}}^{\text{rec}})$  of each simulated event are known. For the entire simulation sets the number of events inside the fiducial area  $N_{\text{inside}}^{\text{true}}$ , the number of events inside the fiducial area, but reconstructed outside  $N_{\text{outside}}^{\text{mis-rec}}$ , and the number of events outside the fiducial area, but reconstructed inside  $N_{\text{inside}}^{\text{mis-rec}}$ , are determined, see Tab. 8.2. These numbers are determined for different ranges of the number of charged particles.

The calculation of the number of events, which are reconstructed outside although they are inside the fiducial area, can be accomplished straightforwardly. On the other hand, the calculation of the number of events, which are mis-reconstructed inside the fiducial area is more difficult, because the simulated core positions are limited to the simulated area. Hence, there could be events outside the simulated area, which would be reconstructed inside the array, that are not seen.

In [Gla05], the uncertainty of the reconstruction of the shower core position is estimated using showers simulated with CORSIKA and CRES, see Chap. 4. These simulations are used to calculate the deviation between the reconstructed and the true shower core positions. This accuracy of the determination of the core position is determined as a function of the number of electrons and it shows, that the accuracy increases with increasing number of electrons. For events with trigger and reconstruction efficiencies of 100 %, the resolution of the core position is better than 12 m and nearly independent of the type of the primary particle. In [DP07] the core position resolution is determined by using measured data and the known reconstruction resolution of the KASCADE array. Only showers with a core position inside the KASCADE array are used. This allows to compare the core position determined with the Grande reconstruction and core position determined with the KASCADE reconstruction. With the known accuracy of the KASCADE reconstruction, an overall core position resolution of 6.4 m was determined.

The shortest distance of the edge of the fiducial area to the KASCADE-Grande detection area is 50 m, see Chap. 4.2 and Fig. E.1. In all simulation sets the showers are distributed over the full Grande array. In some sets the shower are evenly distributed over an enlarged area. Depending on the simulation set the area is 1.5 or 2 times larger than the Grande detection area, see 4.1. This means that the distance between the border of the fiducial area and the border of the simulated area is more than  $3\sigma$  of the core position resolution. This is sufficient to determine the number of mis-reconstructed events.

	$N_{\text{inside}}^{\text{true}}$	$N_{\text{outside}}^{\text{mis-rec}}$	$N_{\text{inside}}^{\text{mis-rec}}$	$\Delta_{\text{N}}^{\text{outside}}$	$\Delta_{\text{N}}^{\text{inside}}$
$\log_{10} N_{\text{ch}} < 6.0$	31094	1713	548	0.055	0.018
$6.0 \leq \log_{10} N_{\text{ch}} < 6.5$	38703	1291	614	0.033	0.016
$6.5 \leq \log_{10} N_{\text{ch}} < 7.0$	17384	348	285	0.020	0.016
$7.0 \leq \log_{10} N_{\text{ch}} < 7.5$	5915	117	130	0.020	0.023
$7.5 \leq \log_{10} N_{\text{ch}} < 8.0$	2131	47	43	0.022	0.020
$8.0 \leq \log_{10} N_{\text{ch}}$	447	9	14	0.020	0.031

**Table 8.2:** Effect of the mis-reconstructed shower core positions on the number of selected events.

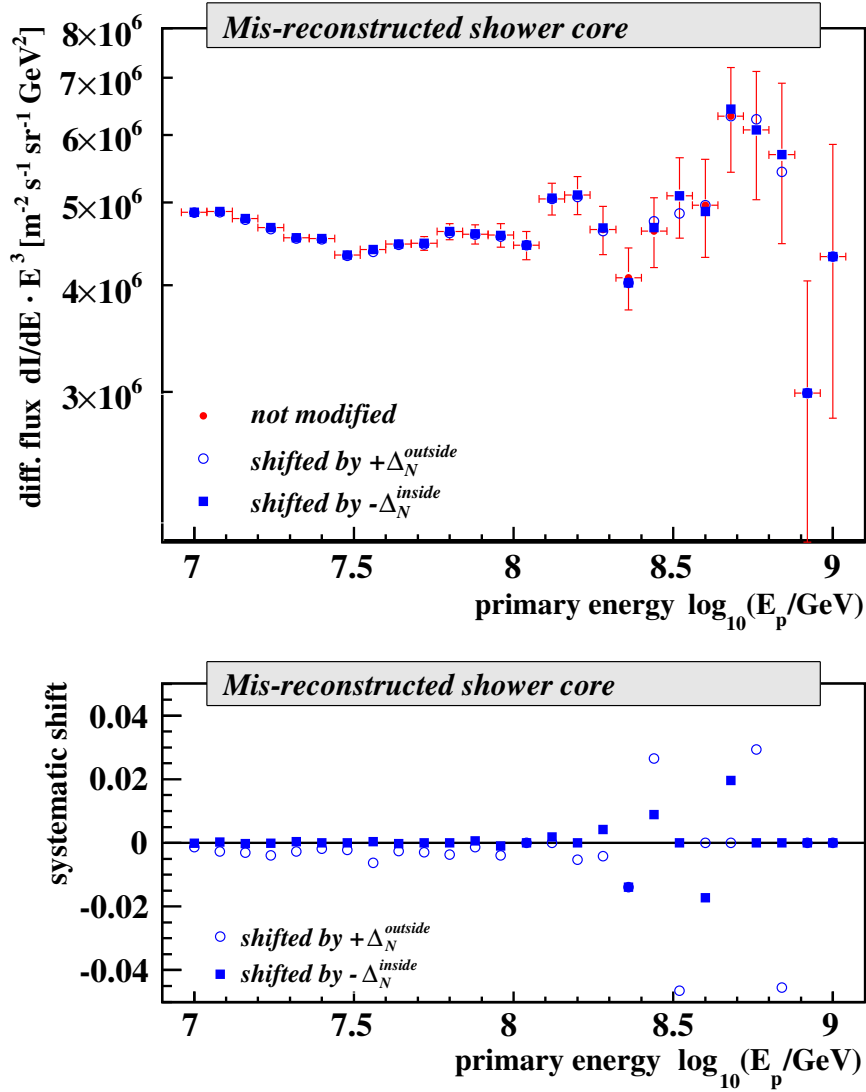


**Figure 8.3:** Study of the influence of the mis-reconstructed shower core positions on the determination of the energy spectrum. The *top* panel shows the resulting energy spectra in comparison to the unchanged spectrum. In the *bottom* panel, the relative systematic shift of the two changed spectra to the unchanged one is shown.

The relative deviation of the reconstructed events can be calculated from the determined number of reconstructed and mis-reconstructed shower core positions:

$$\begin{aligned} \Delta_N^{\text{outside}}(N_{\text{ch}}) &= N_{\text{outside}}^{\text{mis-rec}} / N_{\text{inside}}^{\text{true}}, \\ \Delta_N^{\text{inside}}(N_{\text{ch}}) &= N_{\text{inside}}^{\text{mis-rec}} / N_{\text{inside}}^{\text{true}}. \end{aligned} \quad (8.2)$$

These deviations depend on the number of charged particles. In order to evaluate the influence of these effects on the energy flux spectrum, the whole analysis is repeated with shower size spectra, which are appropriately shifted with respect to the number of events per bin. This is performed in two ways. For the first run, the calculated number

of events per bin  $N$  is increased by:

$$N_{\text{shifted}} = (1 + \Delta_N^{\text{outside}})N.$$

In the other run the number is decreased by:

$$N_{\text{shifted}} = (1 - \Delta_N^{\text{inside}})N.$$

The resulting energy spectra are shown in the upper panel of Fig. 8.3. The relative differences between the determined spectrum and the shifted spectra are calculated for each bin. This results in the estimation of the relative systematic shift, which can be seen in the lower panel of the figure.

### 8.2.2 Influence of the precision in the arrival direction reconstruction

Another quantity of an extensive air shower, that plays an important role in the determination of the energy spectrum, is the arrival direction, i.e. the zenith angle  $\theta$ . In [Gla05], the angular resolution is determined. It shows, that the angular resolution for events with 100 % efficiency is better than  $0.6^\circ$  with only a slight dependence on the type of the primary particle. Using real measured data [DP07] and the known resolution of the KASCADE experiment, the resolution is determined to be  $0.6^\circ$  for the complete set of events with 100 % efficiency. Therefore, in the following a variation of the zenith angle of  $\pm 0.6^\circ$  is applied.

The accuracy of the reconstruction of the arrival direction has two effects on the final energy spectrum. Firstly, the shower size spectrum has to be scaled correctly in order to obtain a flux spectrum. Because the scaling factor depends on the zenith angle, see Eq. (6.7), a variation in the zenith angle of  $\sigma_\theta = \pm 0.6^\circ$  leads to a constant shift of the energy spectrum, which can be seen in Fig. 8.4.

Secondly, there is an impact on the shower size spectra for different zenith angle ranges, see Fig. 6.2. Due to a mis-reconstructed zenith angle, an event could end up in the wrong zenith angle bin. This could affect the result of the constant intensity cut. In order to determine the change in the energy spectrum, the zenith angle of each event is shifted by  $\sigma_\theta$  and new shower size spectra are generated. This is performed separately for a positive and a negative shift. In Fig. 8.5 these energy spectra are shown together with the relative difference of the shifted spectra to the unchanged spectrum. The negative shift results in a systematic shift of the energy spectrum in order of 0.5 %, whereas the effect of a positive shift in  $\theta$  results in a deviation of about 0.1 %.

### 8.2.3 Influence of the precision of the reconstructed number of charged particles

The uncertainties of the reconstruction of the number of charged particles have a direct impact on the determination of the shower size spectra.

The uncertainty of the number of charged particles should be smaller than the uncertainties of the numbers of electrons and muons, because the latter are derived from

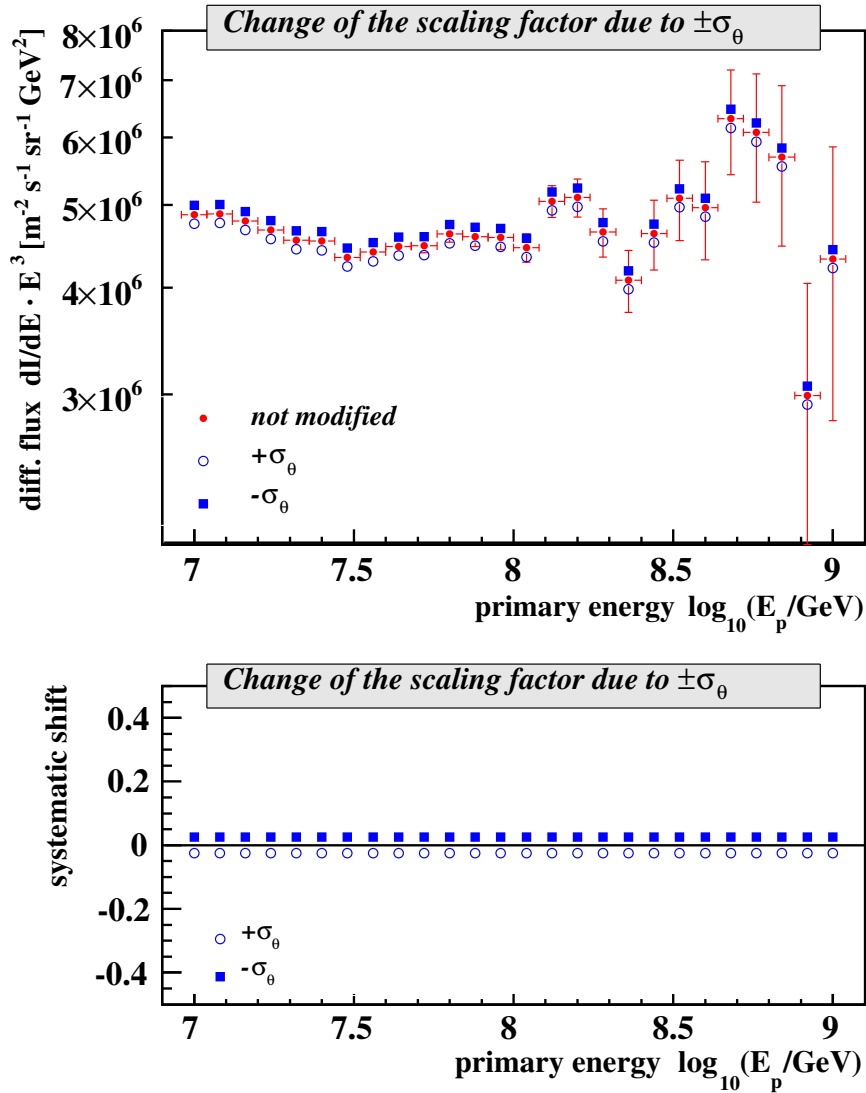


**Figure 8.4:** Study of the influence of the angular resolution on the determination of the energy spectrum. The scaling factor, which is used in order to obtain a flux spectrum, is shifted due to the resolution of the zenith angle. The *top* panel shows the resulting energy spectra in comparison to the unchanged spectrum. In the *bottom* panel, the relative systematic shifts of the changed spectra to the unchanged one are shown.



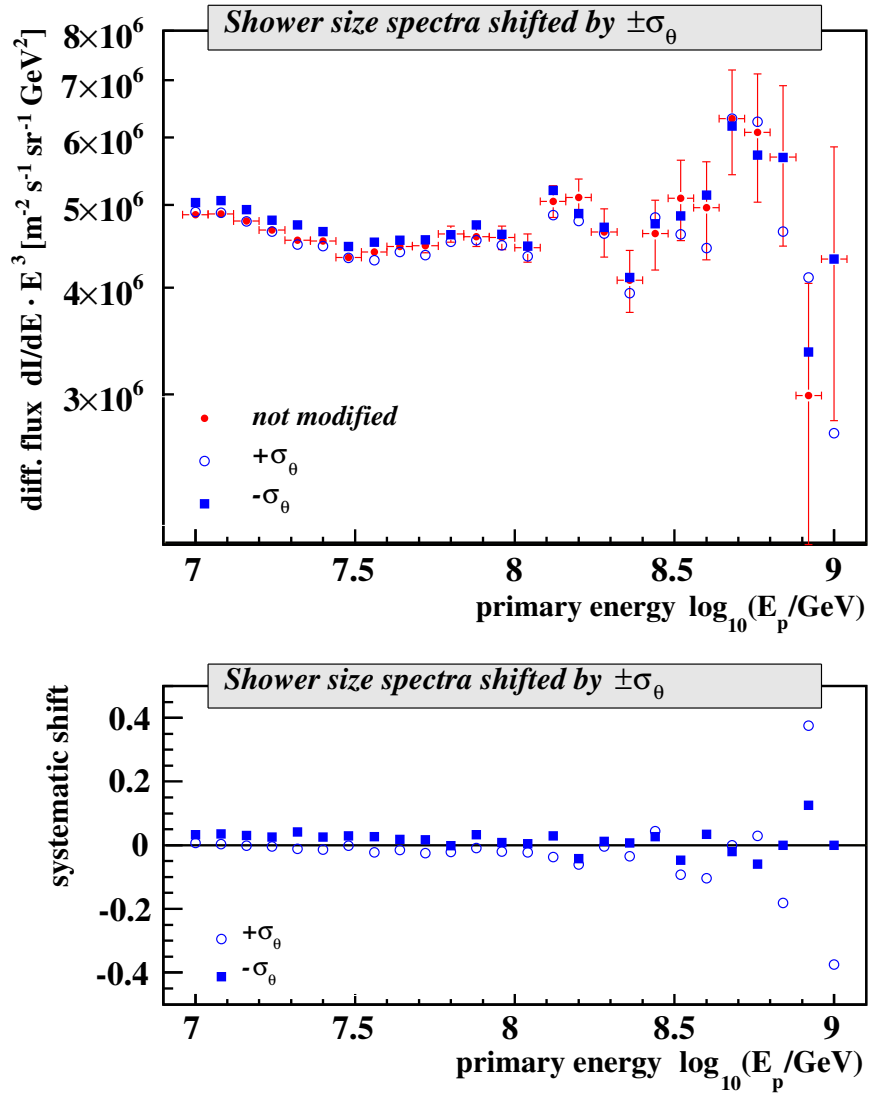


**Figure 8.5:** Study of the influence of the angular resolution on the determination of the energy spectrum. Each event is shifted by the angular resolution, which leads to new shower size spectra. The *top* panel shows the resulting energy spectra in comparison to the unchanged spectrum. In the *bottom* panel, the relative systematic shifts of the changed spectra to the unchanged one are shown.

the number of charged particles. The resolution of the electron number is estimated to be in the order of 15 % and for the number of muons it is in the order of 25 % [Hau07]. The resolution of the number of charged particles is estimated to be in the order of about 15 % using measured data [DP07]. This value contains contributions from both, statistical accuracy and a small systematic bias in estimating the number of charge particles. Thus, the number of charged particles for every event is shifted by  $\pm 15\%$  in order to calculate the shower size spectra. The positive and the negative shifts are performed separately. In Fig. 8.6, the resulting energy spectrum is shown in the upper panel.

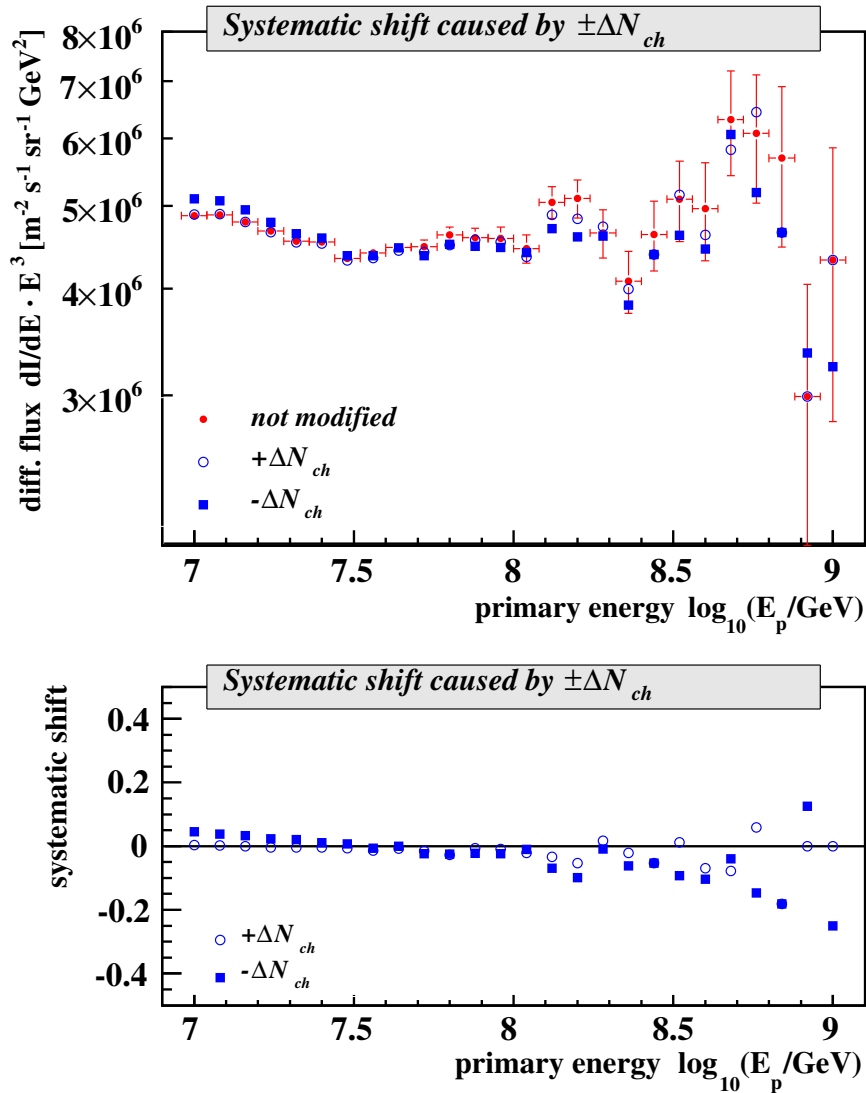


**Figure 8.6:** Study of the influence of the mis-reconstruction of the number of charged particles on the determination of the energy spectrum. The *top* panel shows the resulting energy spectra in comparison to the unchanged spectrum. In the *bottom* panel, the relative systematic shift of the two changed spectra to the unchanged one, is shown.

The relative systematic shift, which results from the variation of the number of charged particles is shown in the lower panel of the same figure. It is seen, that the slope of the

energy spectrum is changed. For both cases a steepening of the spectrum is observed, but the effect of the positive shift is smaller.

### 8.2.4 Influence of the uncertainties of the various applied fits

Besides the uncertainties of the properties of extensive air showers, which have a direct impact on the shower size spectra, and hence, on the precision of the resulting energy spectrum, there are uncertainties introduced by the methods and procedures, which are applied in order to determine the energy spectrum. In particular, each fit results in parameters with uncertainties. These error sources are discussed in the following.

In general, the parameters in each fit are determined with a certain precision, i.e. each parameter has an associated error. These errors lead to different resulting fit functions. These alternative fit functions are used in order to determine the effect of the uncertainties of the fit on the final energy spectrum.

#### Fit of the attenuation curves

The constant intensity cuts are applied after the determination of the shower size spectra. These lead to several attenuation diagrams, see Chap. 6 and Fig. 6.5. The fits of these diagrams result in the attenuation curves, that are used in order to determine a zenith angle independent number of charged particles, see Eq. (6.16). The errors of the fitting parameters  $\sigma_{P_1}$  and  $\sigma_{P_2}$  result in uncertainties in the determination of the reference number of charged particles  $N_{\text{ch},21^\circ}$ . Therefore, each attenuation curve is varied within its errors, using a combination with opposite signs, i.e.  $(+\sigma_{P_1}, -\sigma_{P_2})$  and  $(-\sigma_{P_1}, +\sigma_{P_2})$ . Other combinations lead to an overestimation of the uncertainty. The whole analysis is repeated using both variations separately. In Fig. 8.7 the resulting energy spectra are compared to the unchanged energy spectrum. The resulting systematic shift is shown in the lower panel of this figure.

#### Fit of the conversion relation

In the next step of the analysis, the conversion relation is determined. This is accomplished by a fit on the profile plot of the true primary energy as a function of the number of muons, see Eq. (7.4), which have uncertainties due to the reconstruction of the number of muons, the fluctuations of the muon number, and the assumed energy distribution in the simulations. The errors of the fit parameters are used as first order approximation of the total uncertainties of the conversion relation and are combined with opposite sign  $(+\sigma_a, -\sigma_b)$  and  $(-\sigma_a, +\sigma_b)$ . For both combinations, the energy spectrum is determined. In the upper left panel of Fig. 8.8, the resulting energy spectra are compared to the unchanged spectrum, the systematic shift can be seen in the lower left panel.

The systematic shift is much bigger compared to the systematic shifts considered up to here. This is mainly caused by the shower fluctuations. In order to account for these fluctuations and to estimate the uncertainties caused by them, the errors in the profile diagram describe the spreading inside each bin. This is a measure of the uncertainties caused by the shower fluctuations. Therefore, the systematic uncertainties, which are

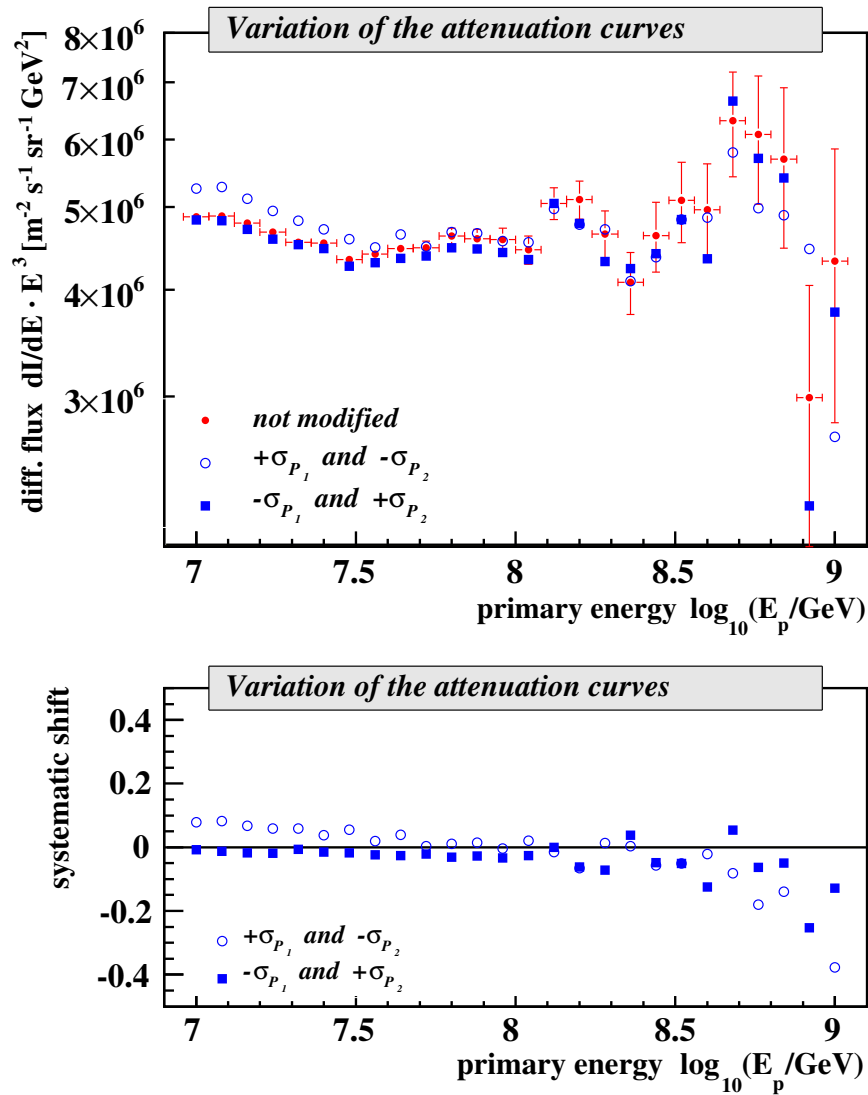


**Figure 8.7:** Study of the influence of the variations of the fitted attenuation curves on the energy spectrum. The attenuation curves could be modified according to the error of the fit parameters, which results in different energy spectra. The *top* panel shows the resulting energy spectra in comparison to the unchanged spectrum. In the *bottom* panel, the relative systematic shift of the two changed spectra to the unchanged one, is shown.

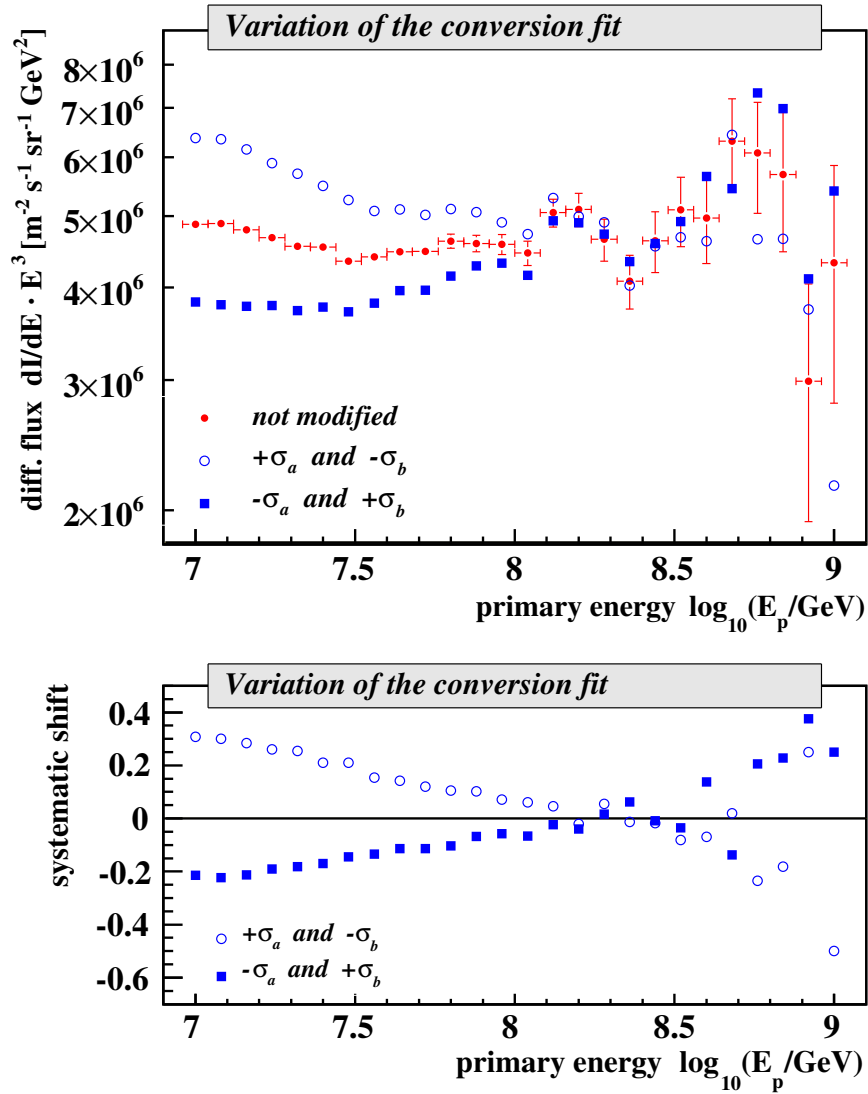


**Figure 8.8:** Study of the influence of the variations of the fitted conversion curve on the determination of the energy spectrum. The fit lead to fit parameters and associated errors. These errors are used to modify the resulting curves in order to determine the systematic effect on the resulting energy spectrum. The *top* panel shows the resulting energy spectra in comparison to the unchanged spectrum. In the *bottom* panel, the relative systematic shifts of the changed spectra to the unchanged one, are shown.

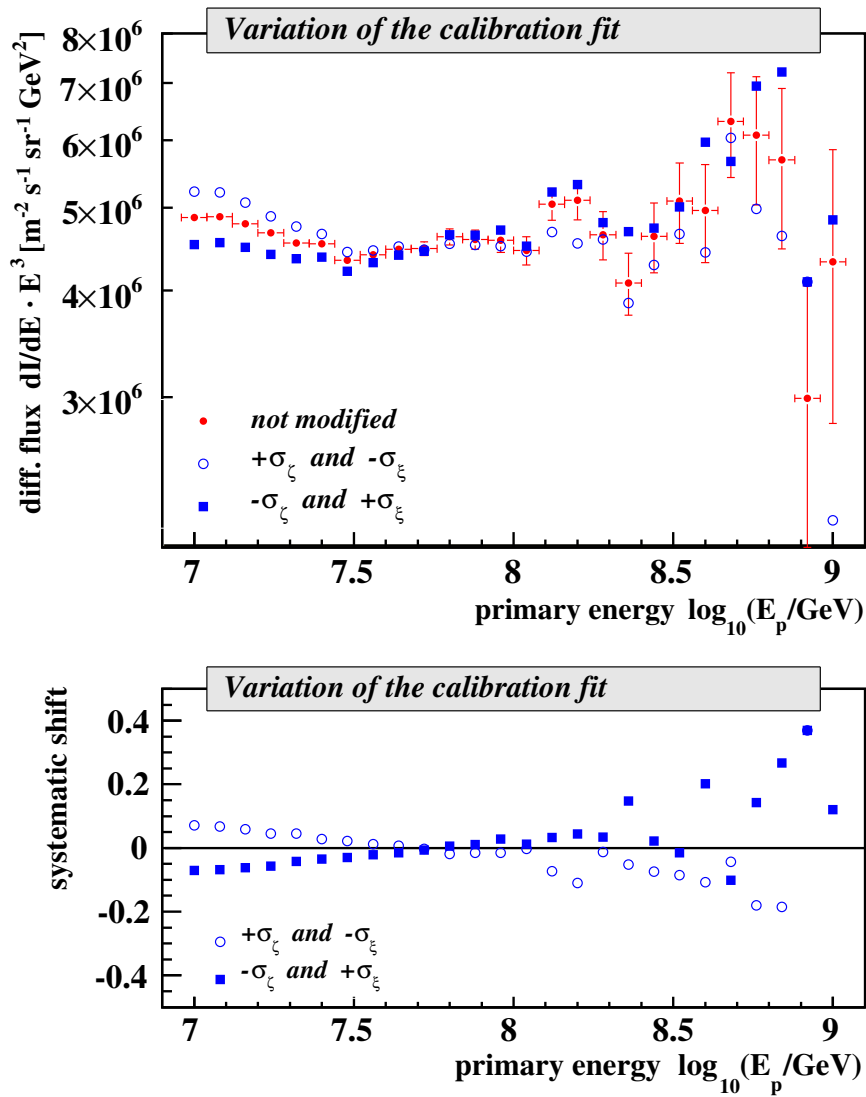


**Figure 8.9:** Study of the influence of the variations of the fitted calibration curve on the determination of the energy spectrum. The fit leads to fit parameters and associated errors. These errors are used to modify the resulting curves in order to determine the systematic effect on the resulting energy spectrum. The *top* panel shows the resulting energy spectra in comparison to the unchanged spectrum. In the *bottom* panel, the relative systematic shifts of the changed spectra to the unchanged one, are shown.

determined in this step, are also an estimate of the uncertainties caused by the shower fluctuations.

### Fit of the calibration curve

In the final step of the analysis, the calibration curve is determined. This is explained in the first part of this chapter. The two opposing combinations of the errors of the fit parameters,  $(\pm\sigma_\zeta, \mp\sigma_\xi)$ , are used to determine the energy spectra. These can be seen in the upper right panel of Fig. 8.9. The systematic shift is calculated like in the previous sections and is shown in the lower right panel of the figure.

## 8.2.5 Influence of the primary composition

The composition of the primary cosmic radiation is one source of uncertainties, which is caused by the nature of the cosmic rays itself. The systematic uncertainties are estimated by the different assumptions of the primary composition for the determination of the conversion and the calibration curve. For the mean energy spectrum, a composition of equal fractions of hydrogen, helium, carbon, silicon, and iron is assumed. The assumptions of pure hydrogen and pure iron initiated showers are used to estimate the extremes of the composition dependence. All three energy spectra resulting from the various assumptions are shown in the upper panel of Fig. 8.10. In the lower panel of this figure the systematic shift is shown.

## 8.2.6 Influence of the shower fluctuations

Another source for systematic uncertainties, that is connected with the nature of the development of extensive air showers, are the shower fluctuations. These fluctuations lead to different measured properties of two air showers, which are caused by two primary particles with the same quantities, i.e. with the same energy, arrival direction, and type of the primary particle. The influence of the fluctuations on the resulting energy spectrum is investigated by using a Monte-Carlo simulation. Instead of simulating the whole shower development and detector response, only those aspects, which are important for the analysis of shower fluctuations, are simulated (“toy Monte-Carlo”). In the following, the individual steps are described.

### Step 1

Firstly, cosmic ray particles with their main properties are generated. In order to determine the energy of a particle, an energy spectrum following a power law is simulated. In order to get sufficient statistics for high energies, the spectral index of the energy spectrum is set to  $\gamma = -2.5$ . This distribution is used to generate random energy values following the power law. The measured zenith angle distribution, see Fig. 6.6, is used in the same way in order to generate zenith angles following their true distribution. Additionally, the type of the primary particle is randomly chosen in such a way, that the number of hydrogen initiated showers and the number of iron initiated showers are equal. This leads to pairs of the primary energy  $E_p^{\text{true}}$ , the arrival direction  $\theta^{\text{true}}$ , and the

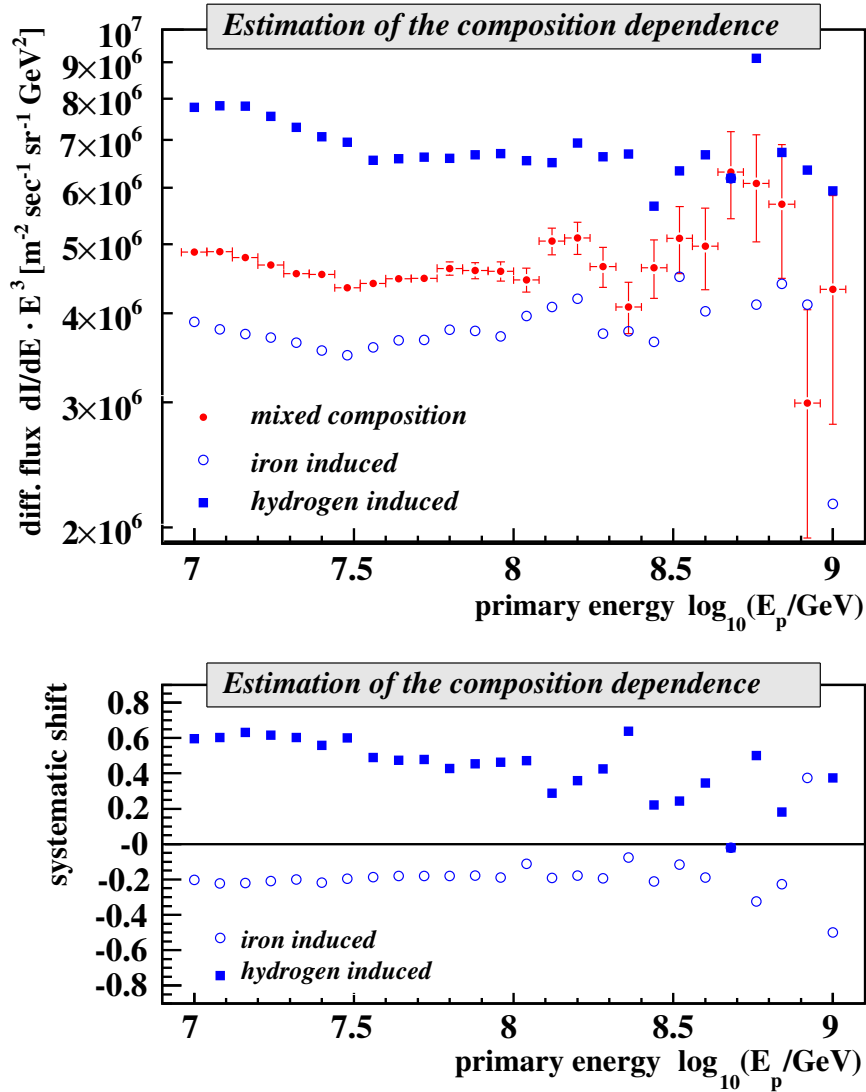


**Figure 8.10:** Study of the influence of the composition of the cosmic rays on the energy spectrum. The conversion function is determined for the assumptions of a mixed composition, for pure hydrogen initiated showers, and pure iron initiated showers. The assumption of a mixed composition is used for the determination of the primary spectrum, whereas the other assumptions are used as an estimate of the composition dependence. The *top* panel shows the comparison of the reconstructed energy spectrum with the two extreme assumptions. In the *bottom* panel, the relative systematic shift is shown.



type of the primary particle, describing the primary cosmic rays. In total,  $5 \cdot 10^7$  such primary particles in an energy of  $10^6$  GeV to  $5 \cdot 10^9$  GeV are simulated.

### Step 2

In this step, the primary energy  $E_p^{\text{true}}$  is converted into a number of charged particles,  $N_{\text{ch}}^{\text{true}}$ . In order to obtain the number of charged particles, a conversion relation is necessary, which relates the simulated primary energy to the number of charged particles. This relation does not need to include all physical implications like composition dependence or shower fluctuations, it should only relate these two quantities in a simple way in the order of the right magnitude. Therefore, the sets of fully simulated air shower events are used. The number of charged particles is plotted as a function of the primary energy and the resulting profile diagram is fitted with a power law, which corresponds to a linear relation in the double logarithmic plot, see Fig. 8.11. This relation is used to estimate the number of charge particles  $N_{\text{ch}}^{\text{true}}$  for each event.

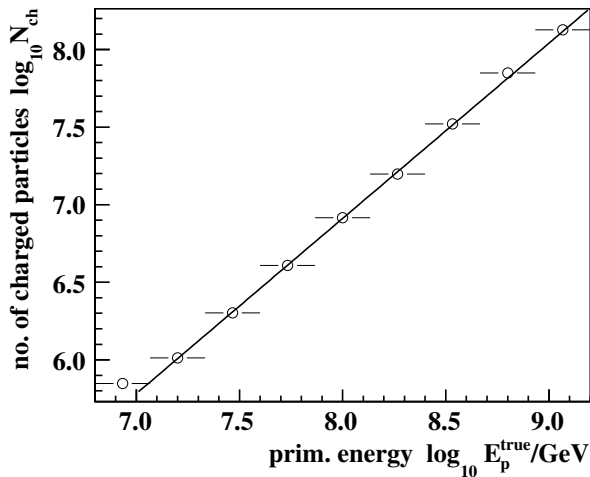


**Figure 8.11:** The number of charged particles as a function of the primary energy. The fit on this distribution leads to a simplified conversion relation between the number of charged particles and the primary energy.

### Step 3

In step 3, the fluctuations are applied to each event. The shower fluctuations are due to a statistical process and the main source of these fluctuations is the variation of the production height of the extensive air shower, see Chap. 2. In Chap. 7.1, the fluctuations of the number of charged particles for different zenith angle and energy ranges are determined. They are determined for hydrogen and iron induced showers. For each of these fluctuation diagrams, see e.g. Fig. 7.1(a), the RMS and the mean of the distributions are calculated. In Figs. 7.2(a) and D.21(a), the relative fluctuations  $\Delta^{\text{fluc}} = \text{RMS}/N_{\text{mean}}$  are shown as a function of the zenith angle and the primary energy. In order to obtain a functional correlation between these quantities the following function is fitted on these diagrams, see [Mar07]:

$$\frac{\text{RMS}}{N_{\text{mean}}} = A \cdot E_p^B, \quad (8.3)$$

with  $A$  and  $B$  linear in  $\cos \theta$ :

$$\begin{aligned} A &= \alpha + \beta \cdot \cos \theta, \\ B &= \gamma + \delta \cdot \cos \theta. \end{aligned} \quad (8.4)$$

For hydrogen induced showers the computed parameters are ( $\chi^2/\text{dof} = 47.6/56$ ):

$$\alpha_{\text{H}} = -826 \pm 73, \quad \beta_{\text{H}} = 1421 \pm 102, \quad \gamma_{\text{H}} = 0.205 \pm 0.013, \quad \delta_{\text{H}} = -0.234 \pm 0.011, \quad (8.5)$$

and for iron induced showers the fit results in ( $\chi^2/\text{dof} = 24.8/56$ ):

$$\alpha_{\text{Fe}} = -75 \pm 12, \quad \beta_{\text{Fe}} = 144 \pm 17, \quad \gamma_{\text{Fe}} = 0.174 \pm 0.017, \quad \delta_{\text{Fe}} = -0.235 \pm 0.015. \quad (8.6)$$

In Fig. 8.12, the resulting fit functions are shown for both assumptions of primary particles.

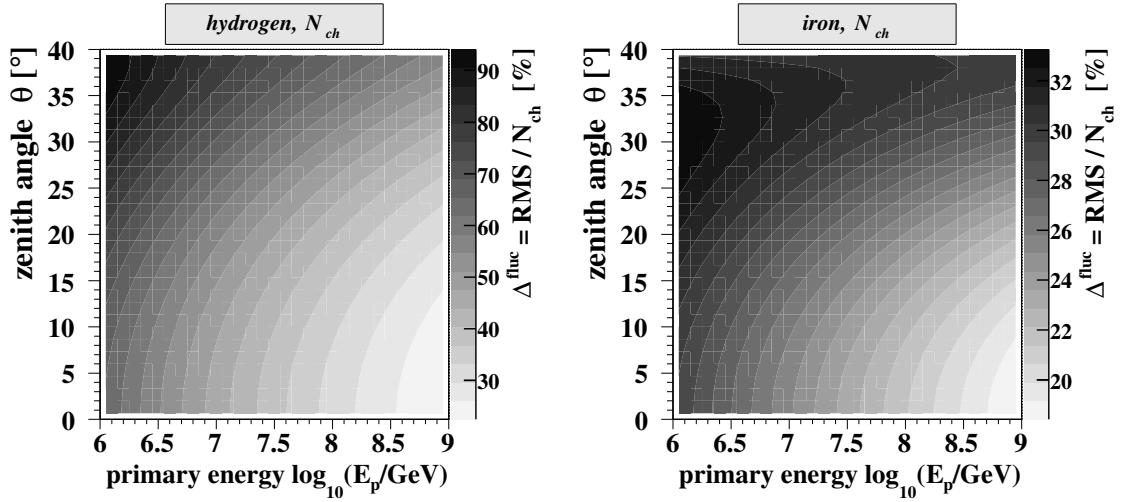


**Figure 8.12:** Fit of the relative shower fluctuation. The determined relative shower fluctuations, see Figs. 7.2(a) and D.21(a), are fitted with a two dimensional function. The resulting functions for hydrogen (*left*) and iron initiated showers (*right*) are shown.

Using the simulated type of the primary particle and the number of charged particles together with these fit functions, the RMS of the fluctuations can be evaluated. In logarithmic scale, the fluctuation diagrams, see e.g. Fig. 7.1(a), nearly follow a Gaussian distribution. Thus, the determined number of charged particle and the RMS are used to define the mean and the deviation of a Gaussian distribution, which is used to get a single random number from it. This single random number is the fluctuated number of charged particles  $N_{\text{ch}}^{\text{fluc}}$  of this simulated event.

Hence, at the end of step 3, the true number of charged particles  $N_{\text{ch}}^{\text{true}}$  and the fluctuated number of charged particles  $N_{\text{ch}}^{\text{fluc}}$  are determined for each simulated event. The calculations in the following steps are performed for both numbers of charged particles, separately.

#### Step 4

In order to determine the reference number of charged particles, the procedures described in Chap. 6 are similarly repeated for the simulated events. Therefore, shower size spectra for different zenith angle bins are determined and a constant intensity cut is

performed on these spectra. This leads to an attenuation curve. In contrast to the procedure performed on the measured data, only one constant intensity cut is applied and hence only one attenuation curve is obtained. This is justified by the facts, that, firstly, the generated energy spectrum has a constant composition over the whole range. Therefore, the method is valid over the full range and one curve is sufficient, see Chap. 6.1.3. Secondly, only the concept of the constant intensity method and the influence of the shower fluctuations on the determination of the energy spectrum should be evaluated in this chapter. The attenuation curve is fitted with Eq. (6.14) and hence the reference number of charged particles can be determined, see Eq. (6.16).

### Step 5

The conversion relation between the primary energy and the number of charged particles, which was determined in step 2, is used to obtain the primary energy from the reference number of the charged particles for each simulated event. Thus, the energy spectrum can be determined.

In Fig. 8.13, the simulated true energy spectrum, the determined energy spectrum without applied fluctuations, and the determined energy spectrum with fluctuations applied are shown in comparison.

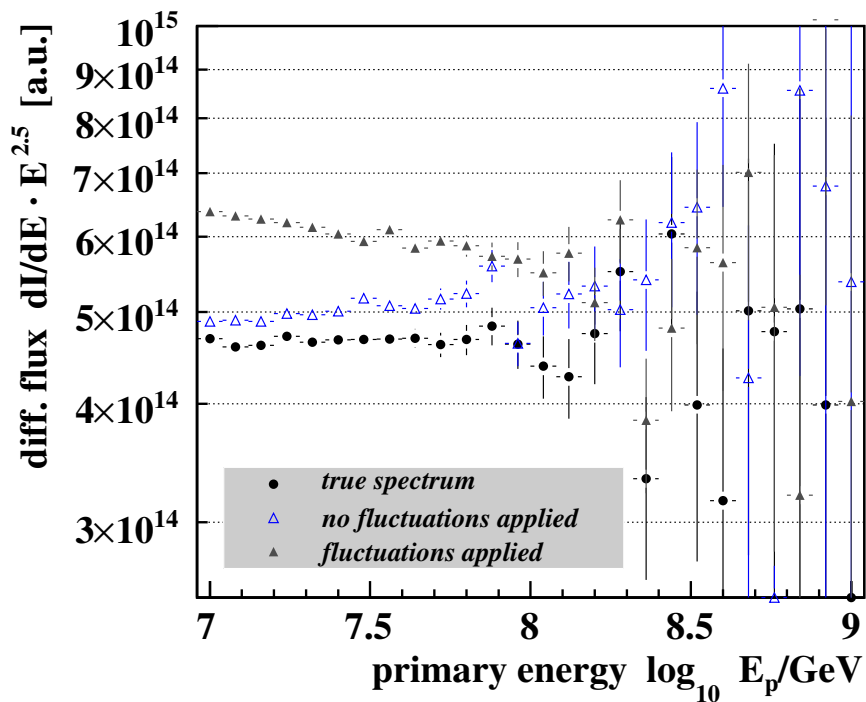


**Figure 8.13:** Study of the influence of the shower fluctuations on the determination of the energy spectrum. The diagram is determined by the use of a Monte-Carlo simulations (“toy MC”) of air shower events. The energy spectrum is reconstructed for events with and without applied fluctuations. These spectra are compared to the simulated true energy spectrum.

Firstly, the true energy spectrum and determined spectrum without applied fluctuations are in good agreement with each other. A small change in the slope can be seen, but it is within the error bars. The reconstructed spectrum is slightly higher in amplitude, which can be explained by an overestimation of the reconstructed energy. Nevertheless, the comparison shows, that the reconstruction of the energy spectrum using the constant intensity method works well.

Secondly, comparing the reconstructed energy spectrum, where the shower fluctuations are applied, shows more pronounced deviations. The reconstructed energy spectrum is steeper and the flux for each bin is higher compared to the true spectrum. This means that events are moved to higher energy bins. Furthermore, more events with low energies are moved towards higher bins than events at high energies are moved towards higher bins, which leads to the steepening of the energy spectrum.

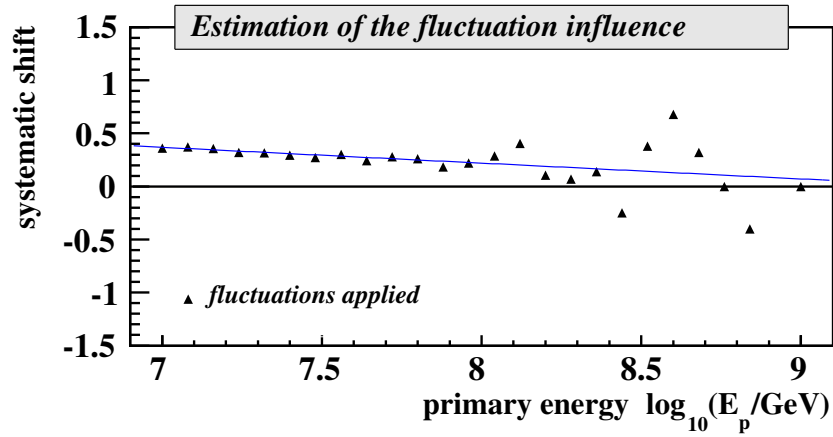


**Figure 8.14:** Systematic deviations caused by shower fluctuations. The relative systematic shift is calculated using Fig. 8.13. The line is a linear fit on the relative deviation, see text.

In Fig. 8.14, the systematic deviation of the reconstructed energy spectrum with applied fluctuations from the true input energy spectrum is shown. In Fig. 8.13, it is seen, that for energies  $\log_{10} E_p/\text{GeV} > 8.3$  the statistical error dominates in comparison to the systematic deviations. Therefore, the relative systematic deviations are fitted with a linear function in the energy range of  $7.0 \leq \log_{10} E_p/\text{GeV} \leq 8.3$  and prolonged towards higher energies.

## 8.2.7 Overall systematic error

In the previous sections, the various sources of systematic uncertainties have been studied. The results of these studies are summarized in Tab. 8.3. In order to get an overall systematic error the various systematic uncertainties  $\sigma_{\text{sys}}^i$  are added quadratically:

$$\sigma_{\text{sys}} = \sqrt{\sum_i (\sigma_{\text{sys}}^i)^2}. \quad (8.7)$$

Source of uncertainty	Systematic shift	
	lower energies ( $\approx 10^7$ GeV)	higher energies ( $\approx 10^{8.8}$ GeV)
mis-reconstruction of core position	$\approx 0.5\%$	$\approx 4\%$
arrival direction effecting the:		
- scaling factor	$\approx 2.5\%$	$\approx 2.5\%$
- shower size spectra	$\approx 4\%$	$\approx 10\%$
reconstr. number of charged particles	$\approx 5\%$	$\approx 10\%$
uncertainties in fit parameters:		
- attenuations curves	$\approx 8\%$	$\approx 15\%$
- conversion relation	$\approx 30\%$	$\approx 25\%$
- calibration relation	$\approx 8\%$	$\approx 15\%$
primary composition	$\approx 60\%$	$\approx 50\%$
shower fluctuations	$\approx 40\%$	$\approx 15\%$

**Table 8.3:** Summary of the systematic uncertainties.

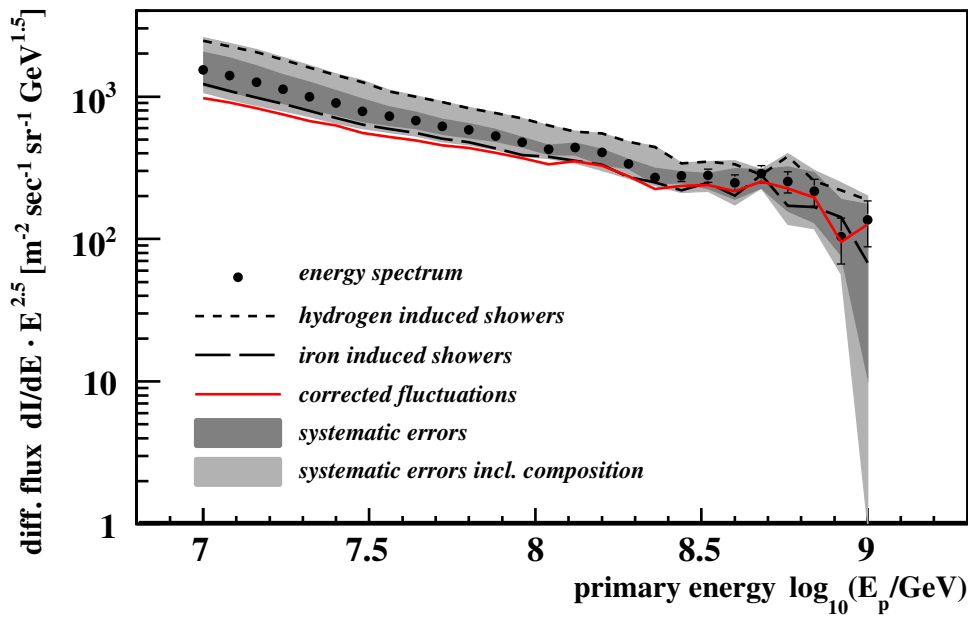


**Figure 8.15:** Determined energy spectrum including systematic uncertainties. The points forming the reconstructed energy spectrum. The statistical errors are shown together with the data points. The broader error band is the overall systematic error. The narrower band is the systematic error without the uncertainties caused by the composition of the cosmic rays. The estimates of the extreme cases of the composition dependence are shown as dashed lines. The solid line shows the energy spectrum with applied correction of shift, caused by shower fluctuations.

The uncertainties caused by the shower fluctuations are included by the systematic variations of the fit of the conversion relation. Therefore, the estimation of the effect of the shower fluctuations is not included in the overall systematic error.

The overall error can be displayed as an error band. This is seen in Fig. 8.15. In order to see the dependence of the composition in more detail, two kinds of error bands are shown. The narrower error band includes all systematic uncertainties except for the uncertainty caused by the composition dependence. In the broader error band this uncertainty is included. The two extreme estimation of the compositions are shown as dashed lines above and below the energy spectrum. The solid line shows the energy spectrum corrected for the fluctuation shift. This is obtained by subtracting the systematic shift, see Fig. 8.14, from the determined energy spectrum.

There are two main parts of the systematic uncertainties. Firstly, the uncertainty, which is caused by the fit of the conversion relation. This uncertainty are mainly caused by the fluctuations of the showers and the low statistics of the simulated shower events, which can not be changed significantly due to heavy time consumption of these simulations. Secondly, the systematic uncertainty of the composition dependence causes another main part of the overall systematic uncertainty.

The overall error is dominated by the systematic uncertainty, but the statistical error increases with increasing energy due to the decreasing number of events caused by the steep energy spectrum. In the Tab. F.1 the values for the energy spectrum together with the various uncertainties can be found.

### 8.3 Summary

In this chapter, the conversion function determined in the previous chapter was used in order to obtain the calibration relation, which converts the reference number of charged particles  $N_{\text{ch},21^\circ}$  into the primary energy. This relation was established by the use of events fulfilling the additional subsample cuts. This relation was then applied to all events passing the standard quality cuts, and finally, the primary energy spectrum could be determined.

In the second part of this chapter, the various sources of systematic uncertainties and their impact on the determination of the energy spectrum were studied. It was found, that the uncertainty caused by the unknown composition of the primary radiation leads to a main fraction of the overall systematic error. Another main part is caused by the uncertainty in the determination of the conversion relation.

Furthermore, it was shown, that the constant intensity method is a tool to determine the primary energy. But it was also shown, that this method is limited by the unavoidable shower fluctuations. The influence of the shower fluctuations was estimated by using a Monte-Carlo simulation of air shower events. Firstly, due to the shower fluctuations the energy, and hence, the total flux is overestimated compared to the true flux. Secondly, the slope of the resulting energy spectrum is changed. The true slope is flatter than the slope of the determined spectrum.

---

# Summary and conclusions

---

In this thesis, the all particle energy spectrum of the primary cosmic rays was determined in the energy range of  $10^{16}$  eV –  $10^{18}$  eV by using data, which were measured with the KASCADE-Grande experiment. More precisely, the data of the Grande detector array were analyzed. Nevertheless, the measurements of the entire KASCADE-Grande experiment were necessary for the reconstruction of the air showers, especially for the separation of the number of electrons and the number of muons.

The data were selected by various quality cut criteria in order to ensure high quality data. In particular, a successful reconstruction of the number of charged particles and the number of muons had to be ensured, because these properties of an air shower are crucial for the analysis. Data sets from December 2003 to September 2007 were analyzed.

In order to determine the energy spectrum, the constant intensity method was used to eliminate the zenith angle dependence of the number of charged particles. This was necessary in order to correlate the number of charged particles to the intensity of the cosmic rays and, thus, to their primary energy. It was shown, that the number of muons can be used as an energy estimator. Subsample cuts were applied in order to improve the quality of the conversion relation between the primary energy and the number of muons. The correlation with the primary energy was then established by using Monte-Carlo simulations.

Extensive air showers were simulated using the program CORSIKA with QGSJET II and FLUKA as hadron interaction models. The detector response was simulated by internal KASCADE-Grande program CRES, which is based on GEANT3. Besides using these simulations in order to establish the correlation function, they were also used to study the shower fluctuations and the impact of the composition of the primary cosmic rays on the determination of the primary energy spectrum. Among the systematic uncertainties studied, the shower fluctuations and the uncertainty of the composition were found to have the largest impact.

In Fig. 9.1, the measured energy spectrum is shown in comparison with the results from other experiments. In order to see the structure of the spectrum in more detail, the flux is multiplied by  $E^{2.5}$ .

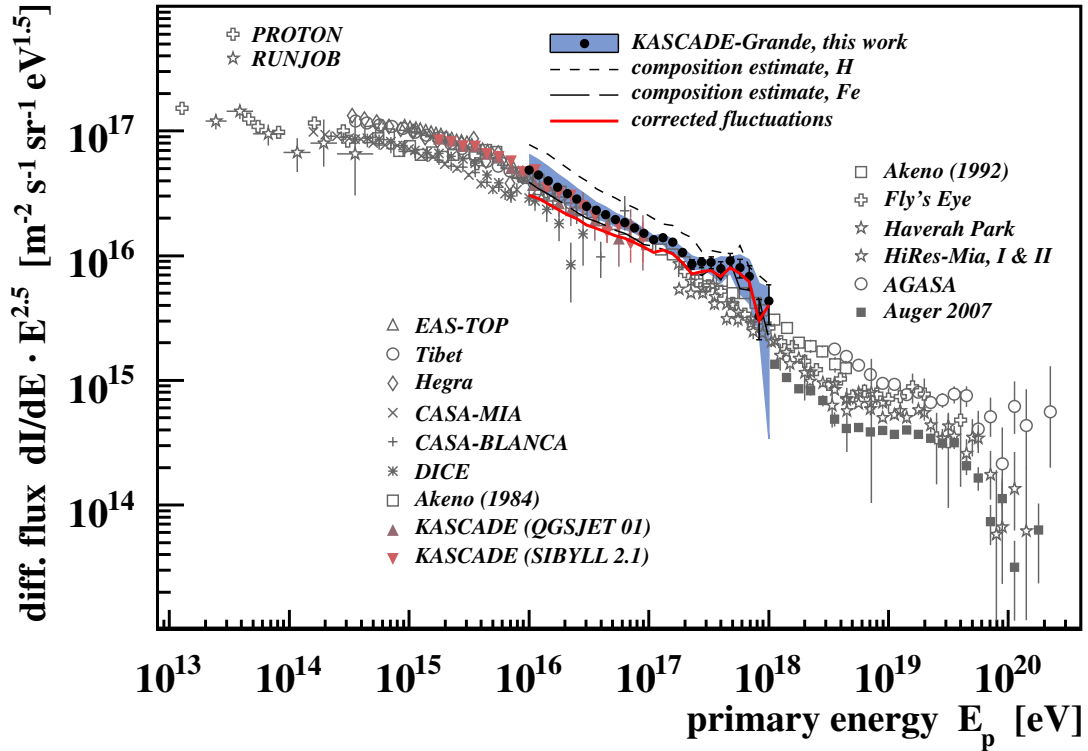


**Figure 9.1:** All particle energy spectrum in comparison with results from PROTON [Gri70], RUNJOB [Apa01], EAS-TOP [Agl99], Tibet [Ame95], Hegra [Arq00], CASA-MIA [Gla99], CASA-BLANCA [Fow01], DICE [Swo00], KASCADE [Ant05], Akeno [Nag84, Nag92], Fly’s Eye [Bir94], Haverah Park [Ave03], HiRes [AZ01, Abb08], AGASA [Tak03], and Auger [Rot07, Per07, FSL07]. For the energy spectrum determined in this thesis, the error band of the systematics without the estimation of the composition dependence is shown. In addition, the two extremes for pure hydrogen and pure iron induced showers are shown, in order to give an estimate on the effect of the composition of the cosmic ray. The solid line represents the corrected spectrum due to the study of shower fluctuations, see text in Chap. 8.2.

It can be seen, that the energy spectrum, which was determined in this thesis, is in good agreement with the measurements of the other experiments. For the KASCADE experiment, the energy spectrum was determined using unfolding techniques [Ant05], with two different hadron interaction models. In the energy range of  $10^{16}$  eV to  $10^{17}$  eV, the results of KASCADE overlap with the results of this work. The measurements of KASCADE-Grande and KASCADE are in good agreement in this energy range. Furthermore, it shows, that the measurable energy range of KASCADE could be successfully extended to energies up to  $10^{18}$  eV, closing the gap in energy to experiments like Fly’s Eye/HiRes, AGASA, and Auger, which measure at the highest energies.



For the highest energy bins, the statistical errors are in the order of 35 % and the systematic errors are in the order of 95 %. Due to the ongoing data taking, the statistical errors will decrease in future. Reducing the systematic errors is harder to achieve. Recently, a review of the reconstruction procedures was started. It is one aim, that an improved reconstruction leads to reduced systematic uncertainties. Additionally, other procedures to determine the energy spectrum are studied, like using the  $S(500)$ , i.e. the density of charged particles at a distance of 500 m from the shower core, as an energy estimator [Tom07]. These methods may lead to smaller systematic errors. Moreover, using unfolding techniques, like for KASCADE data, could lead to energy spectra for different mass groups.



---

# Number of charged particles determined by applying the constant intensity method

---

In Chap. 6.1.2 the constant intensity method is applied to eight shower size spectra with different zenith angle ranges. This leads to a number of charged particles  $N_{\text{ch}}$  for each intensity and zenith angle range. It was used for 13 different intensity cut values. The trigger and reconstruction efficiencies were examined in Chap. 5.2. It was concluded, that only showers with a number of charged particles  $\log_{10}(N_{\text{ch}}) \geq 5.8$  should be used in the analysis. The following table summarizes the intensity cut values  $I_{\text{cut}}$  and the resulting number of charged particles  $N_{\text{ch,cut}}$ .

Intensity $\log_{10}\left(\frac{I(>N_{ch})}{m^{-2}s^{-1}sr^{-1}}\right)$	Number of charged particles $\log_{10}(N_{ch})$ in zenith angle range [°] (mean of range [°])									
	0.0 – 13.1 (8.6)	13.1 – 18.9 (16.0)	18.9 – 23.2 (21.0)	23.2 – 27.0 (25.1)	27.0 – 30.5 (28.7)	30.5 – 33.8 (32.1)	33.8 – 37.0 (35.3)	37.0 – 40.0 (38.4)		
-7.82	6.12±0.01	6.07±0.01	6.01±0.01	5.95±0.01	5.87±0.01	(5.79±0.01)	(5.70±0.01)	(5.59±0.01)		
-7.92	6.17±0.01	6.12±0.01	6.06±0.01	6.00±0.01	5.92±0.01	5.84±0.01	(5.75±0.01)	(5.65±0.01)		
-8.00	6.21±0.01	6.16±0.01	6.10±0.01	6.03±0.01	5.96±0.01	5.88±0.01	(5.79±0.01)	(5.69±0.01)		
-8.10	6.25±0.01	6.20±0.01	6.14±0.01	6.08±0.01	6.01±0.01	5.93±0.01	5.84±0.01	(5.74±0.01)		
-8.19	6.30±0.01	6.25±0.01	6.19±0.01	6.13±0.01	6.06±0.01	5.97±0.01	5.88±0.01	(5.79±0.01)		
-8.30	6.35±0.01	6.30±0.01	6.24±0.01	6.18±0.01	6.11±0.01	6.03±0.01	5.94±0.01	5.85±0.01		
-8.40	6.40±0.02	6.35±0.01	6.29±0.02	6.23±0.02	6.16±0.01	6.07±0.01	5.99±0.02	5.90±0.02		
-8.52	6.47±0.02	6.41±0.02	6.35±0.02	6.30±0.02	6.22±0.02	6.14±0.02	6.05±0.02	5.96±0.02		
-8.64	6.52±0.02	6.47±0.02	6.41±0.02	6.35±0.02	6.28±0.02	6.19±0.02	6.11±0.02	6.01±0.02		
-8.77	6.59±0.02	6.54±0.03	6.48±0.03	6.42±0.02	6.34±0.02	6.26±0.03	6.17±0.02	6.08±0.03		
-8.92	6.67±0.03	6.62±0.03	6.56±0.04	6.50±0.03	6.42±0.03	6.34±0.03	6.25±0.03	6.16±0.03		
-9.12	6.78±0.05	6.73±0.05	6.67±0.05	6.61±0.05	6.53±0.05	6.44±0.04	6.36±0.04	6.26±0.04		
-9.37	6.91±0.06	6.87±0.06	6.80±0.05	6.74±0.05	6.66±0.06	6.57±0.04	6.48±0.04	6.38±0.06		

**Table A.1:** The number of charged particles  $\log_{10}N_{ch}$  determined by applying cuts at different intensities  $\log_{10}I(>N_{ch})$  on the shower size spectra for different zenith angle ranges. The mean of each angle range is given in brackets in the header of the table. If the number of charged particles  $\log_{10}N_{ch}$  is below 5.8, which is required for full efficiency, it will be given in brackets. These values are listed just for completeness and will not be used in the further steps of the analysis presented here.

---

# Error propagation when using the constant intensity method

---

In Chap. 6.1 the constant intensity method is applied to shower size spectra with different zenith angle ranges. The uncertainties in the intensity of the different shower size spectra can be propagated to the number of charged particles  $N_{\text{ch}}$  in order to obtain the attenuation curve diagrams (Fig. 6.5). The error propagation is explained in detail in this appendix (see also [Mar07, Bar89]).

The constant intensity cut is applied to integral size spectra. The size spectrum between the two neighboring points to the cut intensity  $I_{\text{cut}}$  is approximated by a local power law, which corresponds to a linear relation in a double logarithmic plot. Thus, the number of charged particles for the cut is calculated by:

$$\log_{10} N_{\text{ch,cut}} = \alpha - \beta \cdot \log_{10} I_{\text{cut}}. \quad (\text{B.1})$$

The coefficients  $\alpha$  and  $\beta$  can be determined by the equation system:

$$\begin{aligned} \log_{10} N_{\text{ch},0} &= \alpha - \beta \cdot \log_{10} I_0, \\ \log_{10} N_{\text{ch},1} &= \alpha - \beta \cdot \log_{10} I_1, \end{aligned} \quad (\text{B.2})$$

where  $N_{\text{ch},0}$  and  $N_{\text{ch},1}$  are the numbers of charged particles of the neighboring points. The intensities  $I_0 = i_0$  and  $I_1 = i_0 + i_1$  of these points are described by the independent variables  $i_0$  and  $i_1$ . Thus, for the coefficients it follows:

$$\alpha = \log_{10} N_{\text{ch},0} + \beta \log_{10} i_0, \quad (\text{B.3})$$

$$\beta = \log_{10} \frac{N_{\text{ch},0}}{N_{\text{ch},1}} \left( \log_{10} \frac{i_0 + i_1}{i_0} \right)^{-1}. \quad (\text{B.4})$$

Thus, the covariance matrix

$$V = \begin{bmatrix} \sigma_{\alpha}^2 & \text{cov}(\alpha, \beta) \\ \text{cov}(\alpha, \beta) & \sigma_{\beta}^2 \end{bmatrix}, \quad (\text{B.5})$$

can be constructed:

$$\sigma_{\alpha}^2 = \left( \frac{\partial \alpha}{\partial i_0} \right)^2 \sigma_{i_0}^2 + \left( \frac{\partial \alpha}{\partial i_1} \right)^2 \sigma_{i_1}^2, \quad (\text{B.6})$$

$$\sigma_{\beta}^2 = \left( \frac{\partial \beta}{\partial i_0} \right)^2 \sigma_{i_0}^2 + \left( \frac{\partial \beta}{\partial i_1} \right)^2 \sigma_{i_1}^2, \quad (\text{B.7})$$

$$\text{cov}(\alpha, \beta) = \left( \frac{\partial \alpha}{\partial i_0} \right) \left( \frac{\partial \beta}{\partial i_0} \right) \sigma_{i_0}^2 + \left( \frac{\partial \alpha}{\partial i_1} \right) \left( \frac{\partial \beta}{\partial i_1} \right) \sigma_{i_1}^2. \quad (\text{B.8})$$

The derivatives are resulting in

$$\frac{\partial \alpha}{\partial i_0} = \log_{10} \frac{N_{\text{ch},0}}{N_{\text{ch},1}} \left[ \frac{i_1 \ln i_0 + (i_0 + i_1) \ln \frac{i_0 + i_1}{i_0}}{i_0(i_0 + i_1) \left( \ln \frac{i_0 + i_1}{i_0} \right)^2} \right], \quad (\text{B.9})$$

$$\frac{\partial \alpha}{\partial i_1} = \log_{10} \frac{N_{\text{ch},0}}{N_{\text{ch},1}} \left[ \frac{-\ln i_0}{(i_0 + i_1) \left( \ln \frac{i_0 + i_1}{i_0} \right)^2} \right], \quad (\text{B.10})$$

$$\frac{\partial \beta}{\partial i_0} = \ln \frac{N_{\text{ch},0}}{N_{\text{ch},1}} \left[ \frac{i_1}{i_0(i_0 + i_1) \left( \ln \frac{i_0 + i_1}{i_0} \right)^2} \right], \quad (\text{B.11})$$

$$\frac{\partial \beta}{\partial i_1} = \ln \frac{N_{\text{ch},0}}{N_{\text{ch},1}} \left[ \frac{-1}{i_0(i_0 + i_1) \left( \ln \frac{i_0 + i_1}{i_0} \right)^2} \right]. \quad (\text{B.12})$$

Hence, using Eq. (B.1) the error of the size spectra can be propagated to the attenuation diagrams by calculating the variance  $V(\log_{10} N_{\text{ch},\text{cut}})$  of the resulting number of charged particles  $N_{\text{ch},\text{cut}}$

$$V(\log_{10} N_{\text{ch},\text{cut}}) = \sigma_\alpha^2 + (\log_{10} I_{\text{cut}})^2 \sigma_\beta^2 - 2 \log_{10} I_{\text{cut}} \text{cov}(\alpha, \beta). \quad (\text{B.13})$$





---

# Result of the application of the constant intensity method

---

This appendix contains tables of the fits of the attenuation curves described in Chap. 6.1.3 and the application of the resulting reference number of charged particles  $N_{\text{ch},21^\circ}$ .

In App. C.1 the results of the polynomial fits to the different attenuation curves (see Fig. 6.5) are summarized. Depending on the chosen reference angle (see Eq. (6.15)) the fit parameters result in different values, which are listed in the two tables.

App. C.2 shows the shower size spectra for different zenith angle ranges as a function of the reference number of charged particles  $N_{\text{ch},0^\circ}$ , when using  $0^\circ$  as reference. It shows, that the resulting number of charged particles is zenith angle independent and the procedure works independent of the choice of the reference angle.

In App. C.3 a comparison between two corrected shower size spectra for reference angles  $0^\circ$  and  $21^\circ$  is shown. In contrast to Fig. 6.9, both diagrams are shifted towards each other in order to better see the differences. No significant differences can be seen, which indicates, that the choice of the reference angle has no influence.

In App. C.4 different corrected shower size spectra as a function of the reference number of charged particles  $N_{\text{ch},21^\circ}$  are shown.

## C.1 Results of the attenuation curve fits

Reference angle $\theta_{\text{ref}} = 21^\circ$			
Intensity	Fit parameter		
$\log_{10} \left( \frac{I(>N_{\text{ch}})}{[\text{m}^{-2}\text{s}^{-1}\text{sr}^{-1}]} \right)$	$\log_{10} N_{\text{ch},21^\circ}$	$P_1$	$P_2$
-7.82	$6.010 \pm 0.005$	$-0.320 \pm 0.014$	$-0.12 \pm 0.35$
-7.92	$6.059 \pm 0.005$	$-0.316 \pm 0.014$	$-0.15 \pm 0.22$
-8.00	$6.097 \pm 0.005$	$-0.312 \pm 0.016$	$-0.13 \pm 0.23$
-8.10	$6.144 \pm 0.005$	$-0.308 \pm 0.016$	$-0.09 \pm 0.15$
-8.19	$6.188 \pm 0.006$	$-0.305 \pm 0.018$	$-0.09 \pm 0.17$
-8.30	$6.243 \pm 0.006$	$-0.305 \pm 0.018$	$-0.03 \pm 0.11$
-8.40	$6.290 \pm 0.007$	$-0.304 \pm 0.021$	$-0.02 \pm 0.13$
-8.52	$6.353 \pm 0.008$	$-0.303 \pm 0.026$	$-0.01 \pm 0.16$
-8.64	$6.412 \pm 0.010$	$-0.302 \pm 0.029$	$-0.01 \pm 0.17$
-8.77	$6.479 \pm 0.011$	$-0.298 \pm 0.033$	$-0.03 \pm 0.20$
-8.92	$6.557 \pm 0.014$	$-0.297 \pm 0.040$	$-0.02 \pm 0.24$
-9.12	$6.667 \pm 0.021$	$-0.297 \pm 0.059$	$-0.02 \pm 0.34$
-9.37	$6.798 \pm 0.024$	$-0.299 \pm 0.068$	$-0.02 \pm 0.42$

**Table C.1:** Attenuation fit results for the reference angle of  $21^\circ$ .

Reference angle $\theta_{\text{ref}} = 0^\circ$			
Intensity	Fit parameter		
$\log_{10} \left( \frac{I(>N_{\text{ch}})}{[\text{m}^{-2}\text{s}^{-1}\text{sr}^{-1}]} \right)$	$\log_{10} N_{\text{ch},0^\circ}$	$P_1$	$P_2$
-7.82	$6.143 \pm 0.010$	$-0.296 \pm 0.053$	$-0.12 \pm 0.34$
-7.92	$6.190 \pm 0.010$	$-0.289 \pm 0.040$	$-0.15 \pm 0.21$
-8.00	$6.229 \pm 0.011$	$-0.288 \pm 0.043$	$-0.13 \pm 0.22$
-8.10	$6.276 \pm 0.010$	$-0.289 \pm 0.034$	$-0.09 \pm 0.15$
-8.19	$6.319 \pm 0.012$	$-0.286 \pm 0.039$	$-0.09 \pm 0.17$
-8.30	$6.377 \pm 0.012$	$-0.294 \pm 0.032$	$-0.03 \pm 0.11$
-8.40	$6.426 \pm 0.014$	$-0.295 \pm 0.038$	$-0.02 \pm 0.13$
-8.52	$6.490 \pm 0.018$	$-0.296 \pm 0.046$	$-0.01 \pm 0.16$
-8.64	$6.549 \pm 0.021$	$-0.294 \pm 0.050$	$-0.01 \pm 0.17$
-8.77	$6.615 \pm 0.023$	$-0.288 \pm 0.058$	$-0.03 \pm 0.20$
-8.92	$6.695 \pm 0.029$	$-0.288 \pm 0.070$	$-0.02 \pm 0.24$
-9.12	$6.807 \pm 0.043$	$-0.289 \pm 0.101$	$-0.02 \pm 0.34$
-9.37	$6.941 \pm 0.052$	$-0.290 \pm 0.120$	$-0.02 \pm 0.42$

**Table C.2:** Attenuation fit results for the reference angle of  $0^\circ$ .

## C.2 Resulting shower size spectra using reference angle $0^\circ$

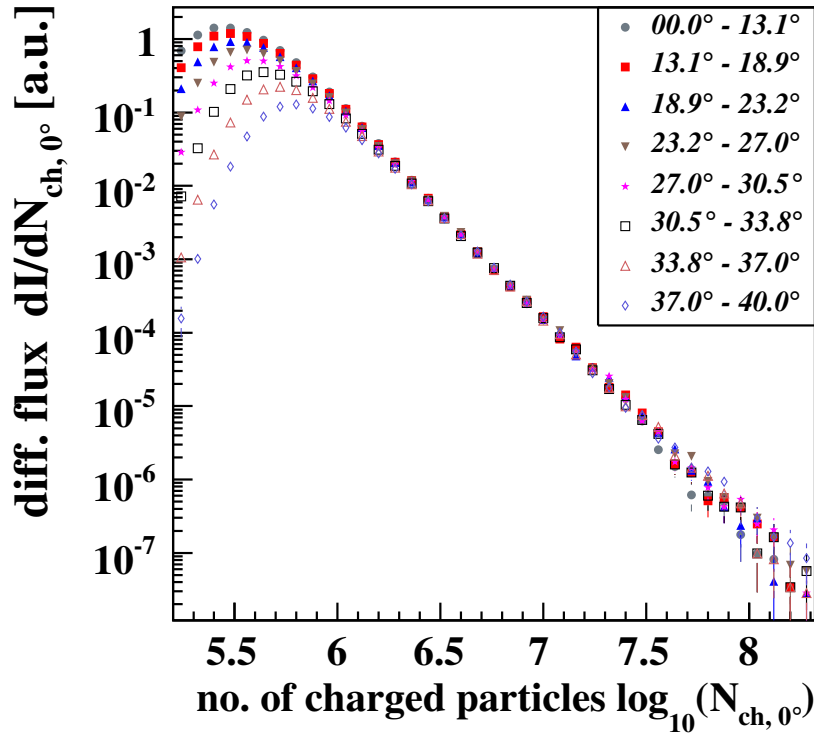


**Figure C.1:** Shower size spectra as a function of the number of charged particles referred to  $0^\circ$  for different zenith angle ranges. Using this reference angle results in a zenith angle independent measure of the number of charged particles.

### C.3 Comparing the corrected shower size spectra for the reference angles $0^\circ$ and $21^\circ$

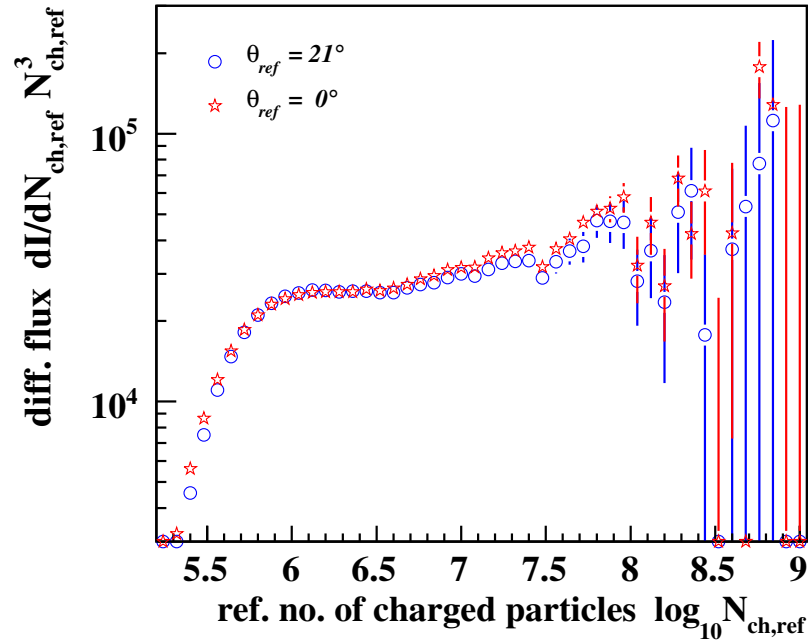


Figure C.2: Comparing shower size spectra for two different reference angles. The displacement of the spectra has been compensated.

## C.4 Corrected shower size spectra

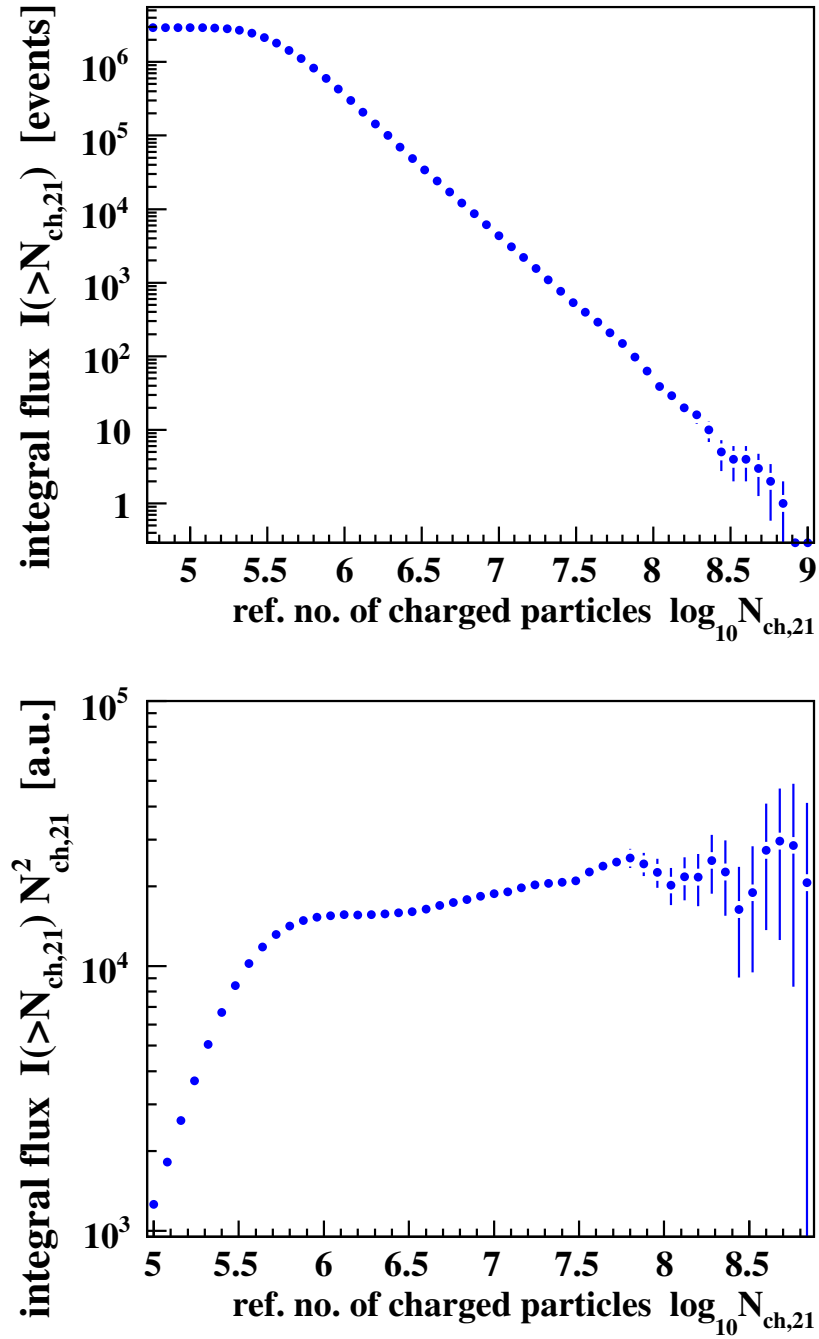


Figure C.3: *Top:* Integral shower size spectra as a function of the reference number of charged particles  $N_{\text{ch},21}$ . *Bottom:* Integral flux multiplied by  $N_{\text{ch},21}^2$ .



---

# Examination of the shower fluctuations

---

This appendix contains the results of the examination of the shower fluctuations described in Chap. 7.1. The distributions of the number of charged particles and the number of muons are determined for different ranges of the zenith angle and of the primary energy. These distributions are evaluated for hydrogen and iron induced showers separately.

In Apps. D.1 to D.4, the distributions for all different ranges are shown. In addition, the values for the mean and the RMS of each distribution are summarized in a table at the beginning of each chapter. The distribution for the number of charged particles are shown in Apps. D.1 (hydrogen induced) and D.2 (iron induced). In Apps. D.3 (hydrogen induced) and D.4 (iron induced), the results for the number of muons are shown.

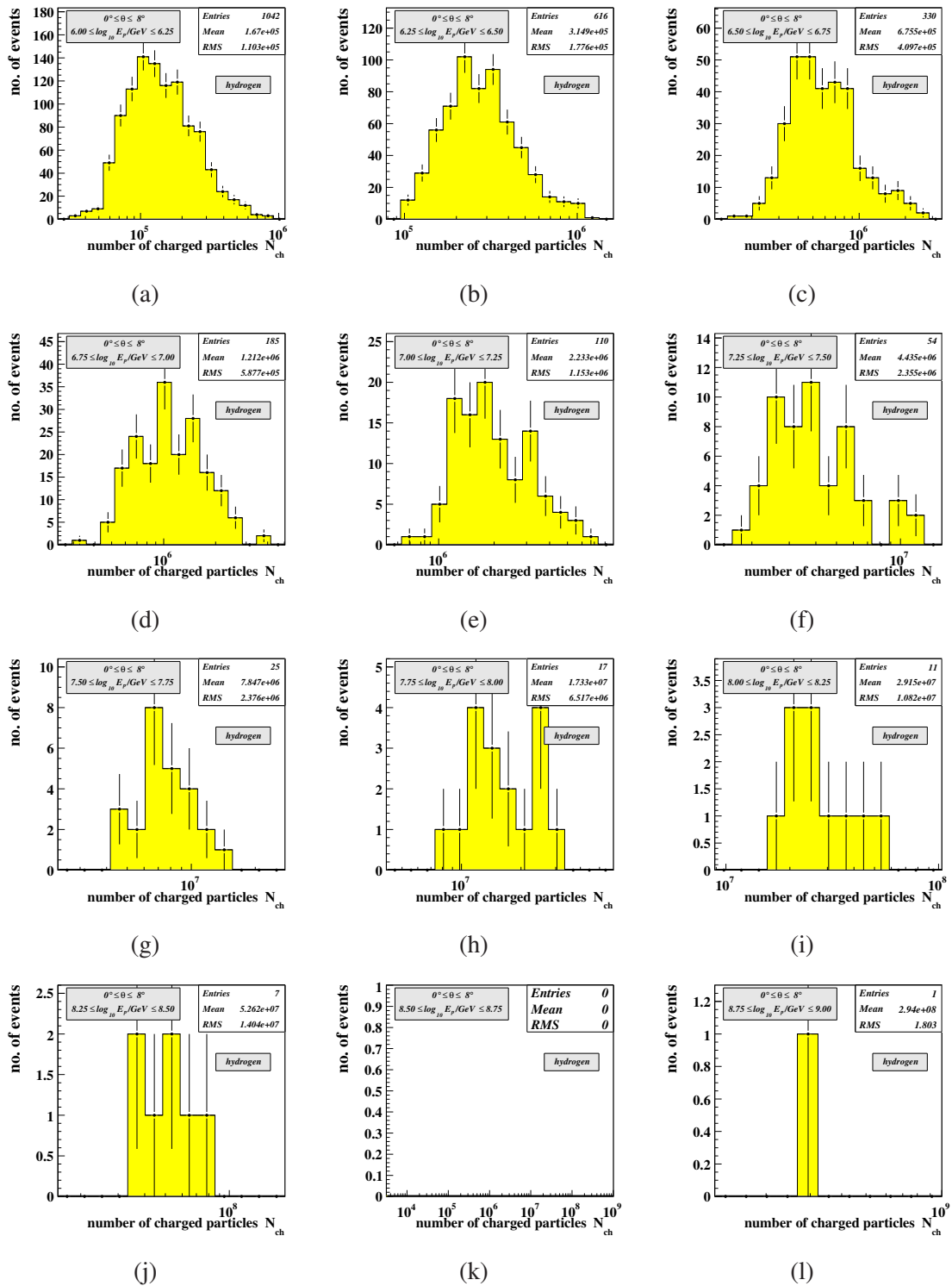
App. D.5 shows the summary plots of the relative fluctuation (see Eq. (7.1)) for hydrogen induced showers. The plots for iron induced shower can be found in Chap. 7.1. Finally, a difference plot of these two diagrams is shown, which can be compared it with Fig. 7.4(a).

## D.1 Fluctuations of the number of charged particles for hydrogen induced showers

$\log_{10} E_p/\text{GeV}$	$0^\circ-8^\circ$		$8^\circ-16^\circ$		$16^\circ-24^\circ$		$24^\circ-32^\circ$		$32^\circ-40^\circ$	
	MEAN	RMS	MEAN	RMS	MEAN	RMS	MEAN	RMS	MEAN	RMS
6.00 – 6.25	$1.67 \cdot 10^5$	$1.10 \cdot 10^5$	$1.50 \cdot 10^5$	$0.95 \cdot 10^5$	$1.22 \cdot 10^5$	$0.84 \cdot 10^5$	$8.61 \cdot 10^4$	$6.86 \cdot 10^4$	$5.15 \cdot 10^4$	$4.90 \cdot 10^4$
6.25 – 6.50	$3.15 \cdot 10^5$	$1.78 \cdot 10^5$	$2.99 \cdot 10^5$	$1.81 \cdot 10^5$	$2.44 \cdot 10^5$	$1.67 \cdot 10^5$	$1.64 \cdot 10^5$	$1.22 \cdot 10^5$	$9.77 \cdot 10^4$	$8.61 \cdot 10^4$
6.50 – 6.75	$6.75 \cdot 10^5$	$4.10 \cdot 10^5$	$5.71 \cdot 10^5$	$3.39 \cdot 10^5$	$4.67 \cdot 10^5$	$2.91 \cdot 10^5$	$3.16 \cdot 10^5$	$2.11 \cdot 10^5$	$1.89 \cdot 10^5$	$1.51 \cdot 10^5$
6.75 – 7.00	$1.21 \cdot 10^6$	$0.59 \cdot 10^6$	$1.08 \cdot 10^6$	$0.56 \cdot 10^6$	$8.82 \cdot 10^5$	$4.80 \cdot 10^5$	$6.46 \cdot 10^5$	$4.25 \cdot 10^5$	$3.59 \cdot 10^5$	$2.93 \cdot 10^5$
7.00 – 7.25	$2.23 \cdot 10^6$	$1.15 \cdot 10^6$	$2.01 \cdot 10^6$	$0.96 \cdot 10^6$	$1.67 \cdot 10^6$	$0.88 \cdot 10^6$	$1.18 \cdot 10^6$	$0.75 \cdot 10^6$	$7.30 \cdot 10^5$	$5.27 \cdot 10^5$
7.25 – 7.50	$4.43 \cdot 10^6$	$2.36 \cdot 10^6$	$4.02 \cdot 10^6$	$1.72 \cdot 10^6$	$3.12 \cdot 10^6$	$1.54 \cdot 10^6$	$2.41 \cdot 10^6$	$1.50 \cdot 10^6$	$1.33 \cdot 10^6$	$0.98 \cdot 10^6$
7.50 – 7.75	$7.85 \cdot 10^6$	$2.38 \cdot 10^6$	$7.36 \cdot 10^6$	$3.09 \cdot 10^6$	$6.65 \cdot 10^6$	$3.22 \cdot 10^6$	$4.31 \cdot 10^6$	$2.17 \cdot 10^6$	$2.37 \cdot 10^6$	$1.36 \cdot 10^6$
7.75 – 8.00	$1.73 \cdot 10^7$	$0.65 \cdot 10^7$	$1.47 \cdot 10^7$	$0.71 \cdot 10^7$	$1.12 \cdot 10^7$	$0.41 \cdot 10^7$	$8.23 \cdot 10^6$	$4.38 \cdot 10^6$	$4.96 \cdot 10^6$	$4.04 \cdot 10^6$
8.00 – 8.25	$2.91 \cdot 10^7$	$1.08 \cdot 10^7$	$3.11 \cdot 10^7$	$1.45 \cdot 10^7$	$2.59 \cdot 10^7$	$1.18 \cdot 10^7$	$1.99 \cdot 10^7$	$1.10 \cdot 10^7$	$8.31 \cdot 10^6$	$4.66 \cdot 10^6$
8.25 – 8.50	$5.26 \cdot 10^7$	$1.40 \cdot 10^7$	$5.00 \cdot 10^7$	$1.38 \cdot 10^7$	$4.67 \cdot 10^7$	$2.00 \cdot 10^7$	$2.69 \cdot 10^7$	$1.07 \cdot 10^7$	$1.62 \cdot 10^7$	$0.99 \cdot 10^7$
8.50 – 8.75	–	–	$9.84 \cdot 10^7$	$3.86 \cdot 10^7$	$9.62 \cdot 10^7$	$4.61 \cdot 10^7$	$5.94 \cdot 10^7$	$1.95 \cdot 10^7$	$3.23 \cdot 10^7$	$1.85 \cdot 10^7$
8.75 – 9.00	$2.94 \cdot 10^8$	–	$1.92 \cdot 10^8$	$0.40 \cdot 10^8$	$1.58 \cdot 10^8$	$0.56 \cdot 10^8$	$1.33 \cdot 10^8$	$0.61 \cdot 10^8$	$6.00 \cdot 10^7$	$3.16 \cdot 10^7$

**Table D.1:** Summary of the fluctuation distributions of the number of charged particles for hydrogen induced showers. Each distribution covers a certain energy and zenith angle range. For each distribution the mean and the RMS is given. There are certain ranges where the distribution contains no event (neither the mean nor the RMS can be calculated) or only one event (the RMS cannot be calculated), these are indicated by a “–” in the table.



Figure D.1: Fluctuation diagrams for  $N_{ch}$ , hydrogen, and  $0^\circ \leq \theta < 8^\circ$

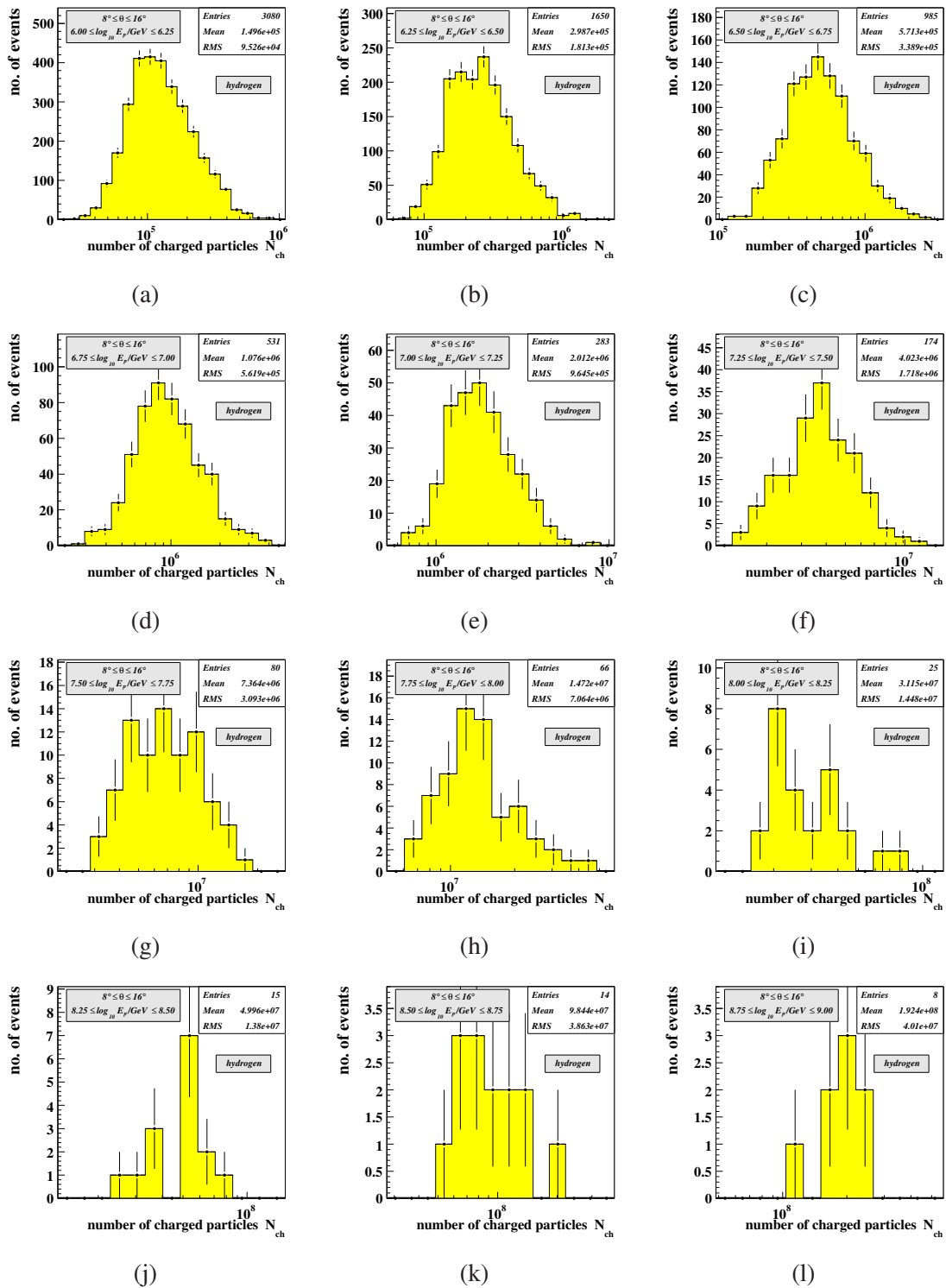
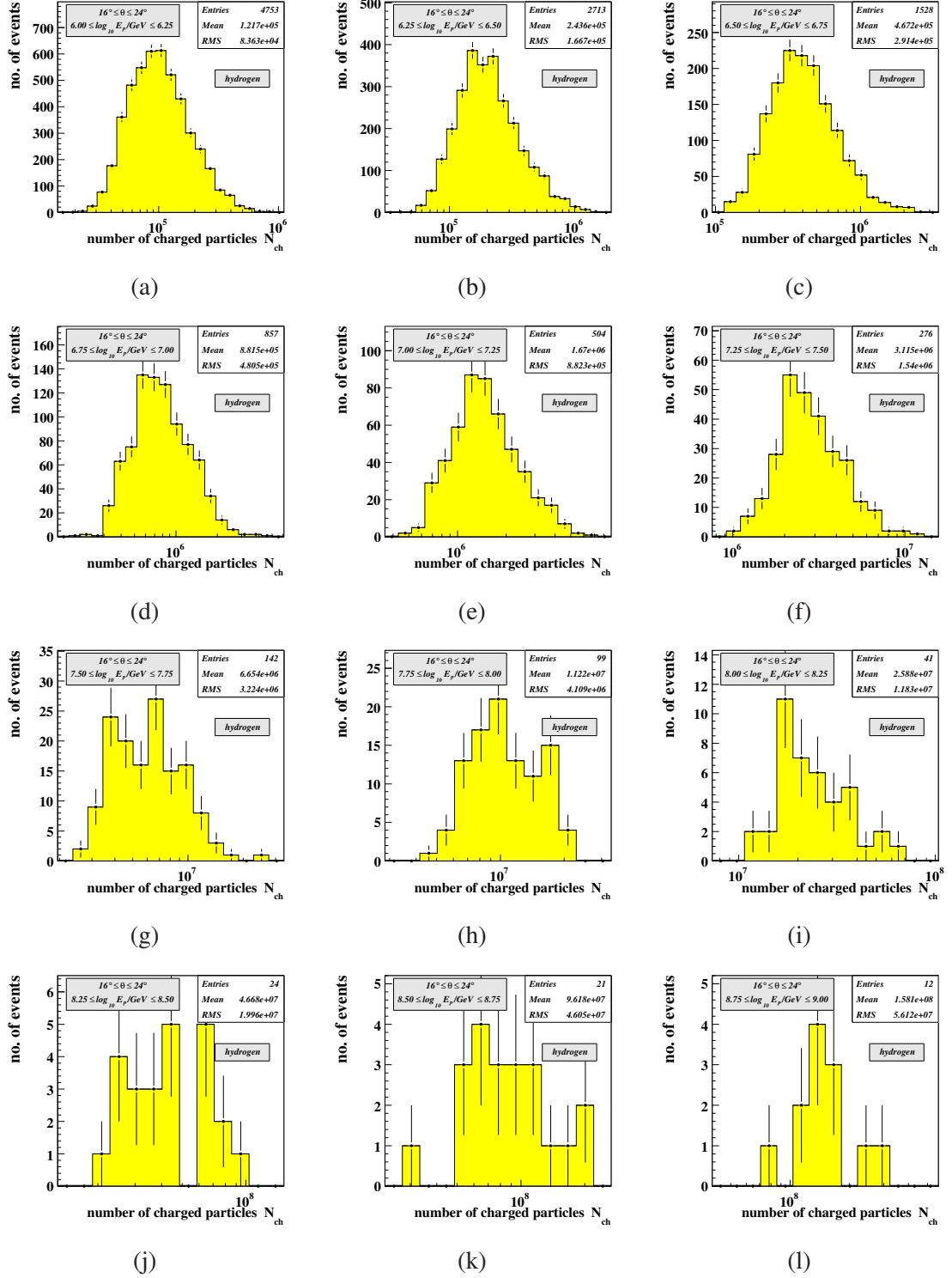


Figure D.2: Fluctuation diagrams for  $N_{\text{ch}}$ , hydrogen, and  $8^\circ \leq \theta < 16^\circ$

Figure D.3: Fluctuation diagrams for  $N_{ch}$ , hydrogen, and  $16^\circ \leq \theta < 24^\circ$

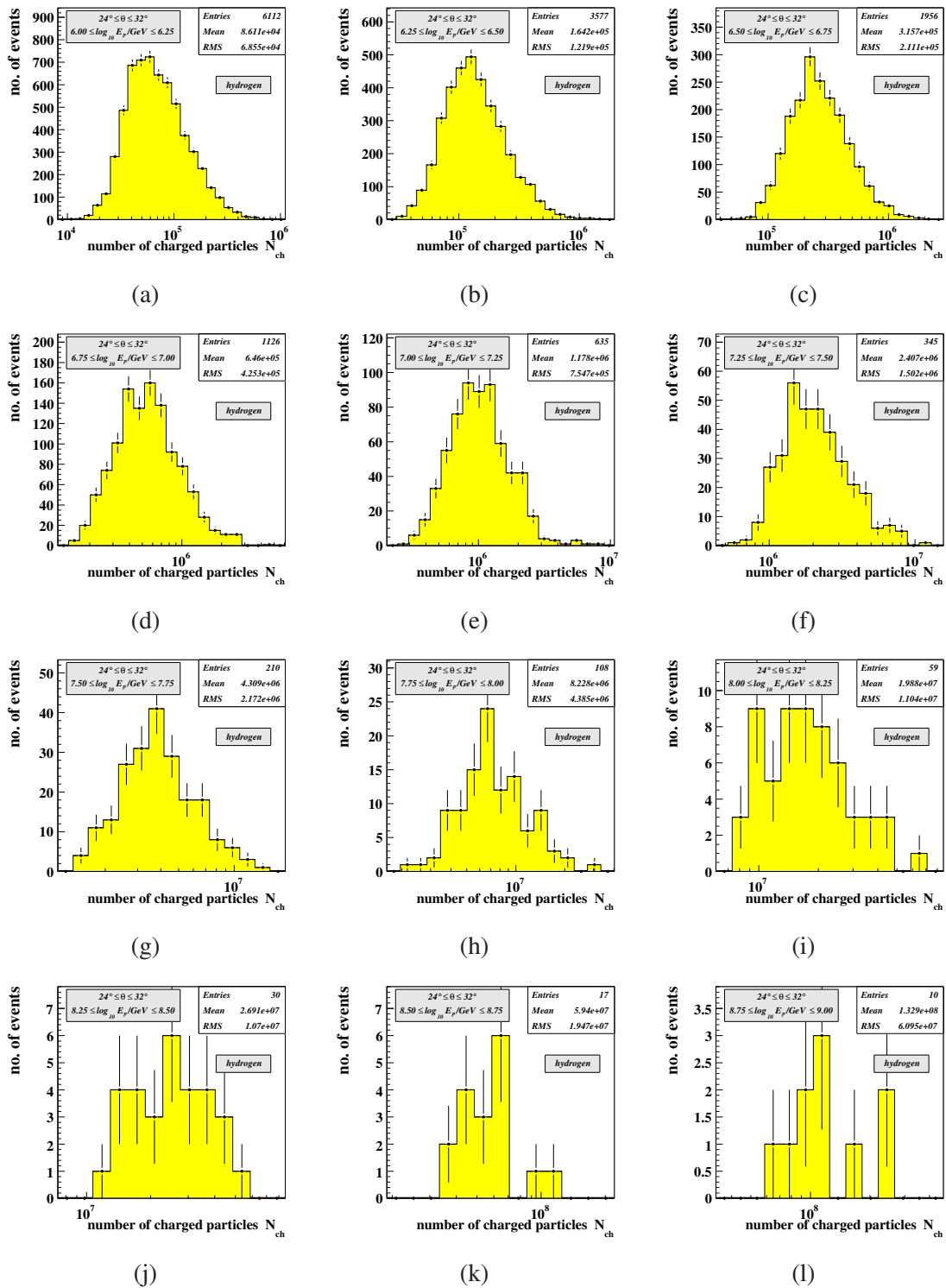
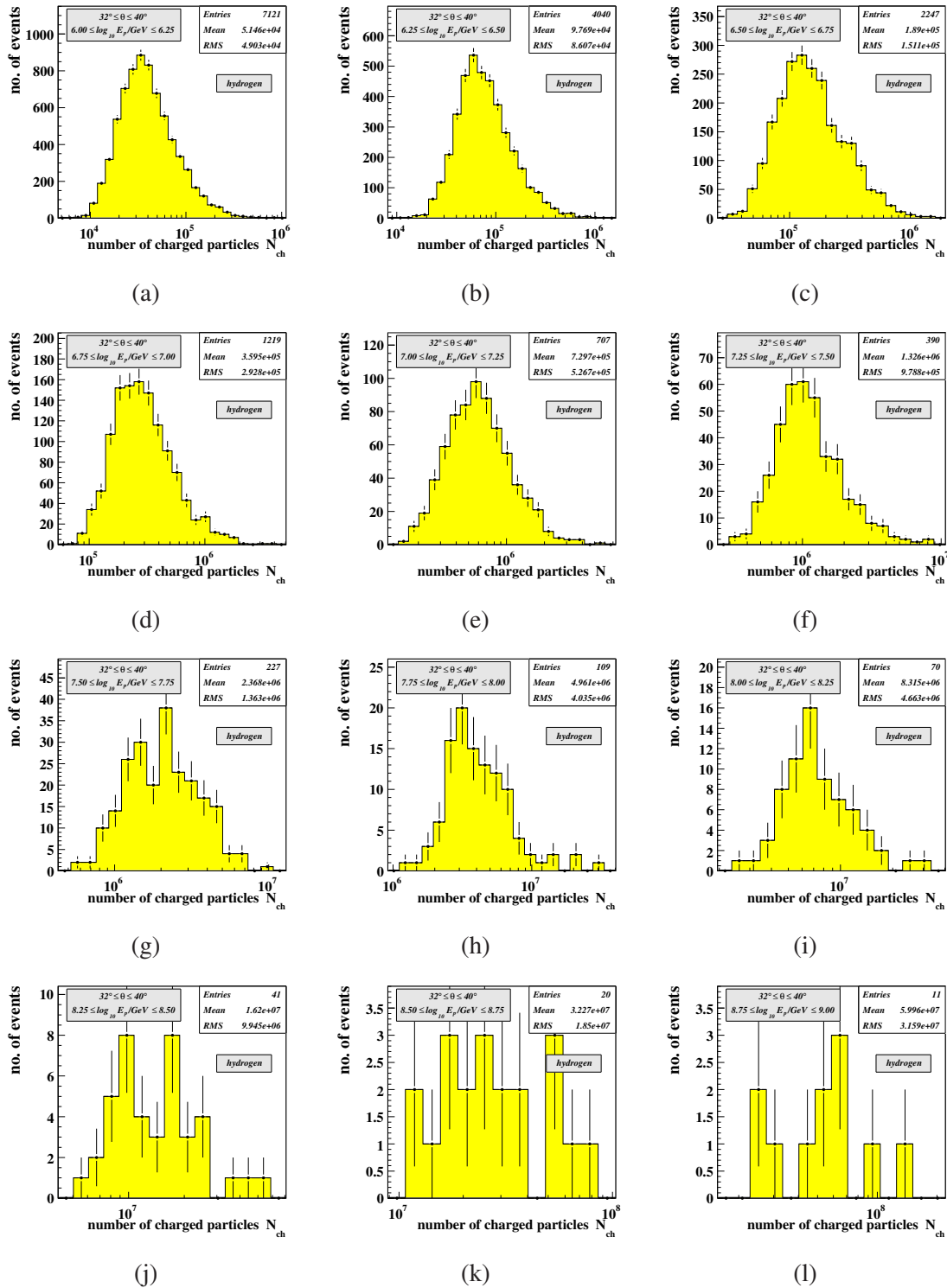


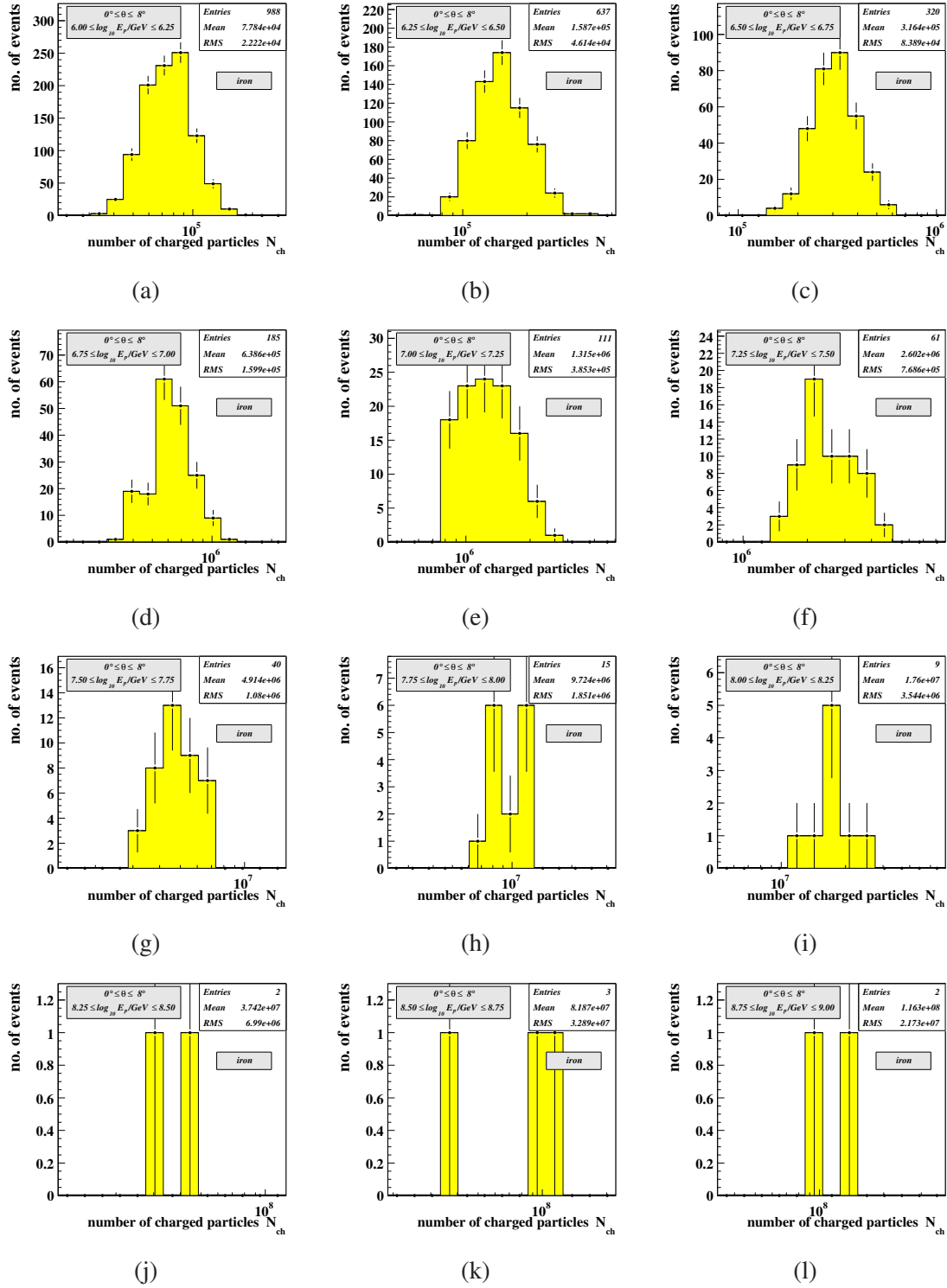
Figure D.4: Fluctuation diagrams for  $N_{ch}$ , hydrogen, and  $24^\circ \leq \theta < 32^\circ$

Figure D.5: Fluctuation diagrams for  $N_{ch}$ , hydrogen, and  $32^\circ \leq \theta \leq 40^\circ$

## D.2 Fluctuations of the number of charged particles for iron induced showers

$\log_{10} E_p / \text{GeV}$	$0^\circ-8^\circ$		$8^\circ-16^\circ$		$16^\circ-24^\circ$		$24^\circ-32^\circ$		$32^\circ-40^\circ$	
	MEAN	RMS	MEAN	RMS	MEAN	RMS	MEAN	RMS	MEAN	RMS
6.00 – 6.25	$7.78 \cdot 10^4$	$2.22 \cdot 10^4$	$7.04 \cdot 10^4$	$2.04 \cdot 10^4$	$5.81 \cdot 10^4$	$1.70 \cdot 10^4$	$4.30 \cdot 10^4$	$1.32 \cdot 10^4$	$2.92 \cdot 10^4$	$0.87 \cdot 10^4$
6.25 – 6.50	$1.59 \cdot 10^5$	$0.46 \cdot 10^5$	$1.43 \cdot 10^5$	$0.41 \cdot 10^5$	$1.15 \cdot 10^5$	$0.34 \cdot 10^5$	$8.44 \cdot 10^4$	$2.58 \cdot 10^4$	$5.58 \cdot 10^4$	$1.71 \cdot 10^4$
6.50 – 6.75	$3.16 \cdot 10^5$	$0.84 \cdot 10^5$	$2.87 \cdot 10^5$	$0.80 \cdot 10^5$	$2.29 \cdot 10^5$	$0.68 \cdot 10^5$	$1.66 \cdot 10^5$	$0.51 \cdot 10^5$	$1.07 \cdot 10^5$	$0.34 \cdot 10^5$
6.75 – 7.00	$6.39 \cdot 10^5$	$1.60 \cdot 10^5$	$5.76 \cdot 10^5$	$1.55 \cdot 10^5$	$4.63 \cdot 10^5$	$1.36 \cdot 10^5$	$3.34 \cdot 10^5$	$1.05 \cdot 10^5$	$2.07 \cdot 10^5$	$0.65 \cdot 10^5$
7.00 – 7.25	$1.31 \cdot 10^6$	$0.39 \cdot 10^6$	$1.13 \cdot 10^6$	$0.32 \cdot 10^6$	$9.24 \cdot 10^5$	$2.54 \cdot 10^5$	$6.53 \cdot 10^5$	$2.05 \cdot 10^5$	$4.06 \cdot 10^5$	$1.33 \cdot 10^5$
7.25 – 7.50	$2.60 \cdot 10^6$	$0.77 \cdot 10^6$	$2.27 \cdot 10^6$	$0.53 \cdot 10^6$	$1.87 \cdot 10^6$	$0.54 \cdot 10^6$	$1.28 \cdot 10^6$	$0.41 \cdot 10^6$	$7.95 \cdot 10^5$	$2.69 \cdot 10^5$
7.50 – 7.75	$4.91 \cdot 10^6$	$1.08 \cdot 10^6$	$4.39 \cdot 10^6$	$1.05 \cdot 10^6$	$3.62 \cdot 10^6$	$1.02 \cdot 10^6$	$2.50 \cdot 10^6$	$0.77 \cdot 10^6$	$1.56 \cdot 10^6$	$0.51 \cdot 10^6$
7.75 – 8.00	$9.72 \cdot 10^6$	$1.85 \cdot 10^6$	$8.41 \cdot 10^6$	$2.06 \cdot 10^6$	$6.91 \cdot 10^6$	$1.86 \cdot 10^6$	$4.78 \cdot 10^6$	$1.54 \cdot 10^6$	$2.84 \cdot 10^6$	$0.93 \cdot 10^6$
8.00 – 8.25	$1.76 \cdot 10^7$	$0.35 \cdot 10^7$	$1.67 \cdot 10^7$	$0.41 \cdot 10^7$	$1.32 \cdot 10^7$	$0.35 \cdot 10^7$	$9.56 \cdot 10^6$	$2.39 \cdot 10^6$	$5.65 \cdot 10^6$	$2.16 \cdot 10^6$
8.25 – 8.50	$3.74 \cdot 10^7$	$0.70 \cdot 10^7$	$3.35 \cdot 10^7$	$0.71 \cdot 10^7$	$2.48 \cdot 10^7$	$0.75 \cdot 10^7$	$1.96 \cdot 10^7$	$0.49 \cdot 10^7$	$1.11 \cdot 10^7$	$0.31 \cdot 10^7$
8.50 – 8.75	$8.19 \cdot 10^7$	$3.29 \cdot 10^7$	$6.58 \cdot 10^7$	$1.16 \cdot 10^7$	$5.03 \cdot 10^7$	$1.46 \cdot 10^7$	$3.64 \cdot 10^7$	$0.83 \cdot 10^7$	$2.10 \cdot 10^7$	$0.62 \cdot 10^7$
8.75 – 9.00	$1.16 \cdot 10^8$	$0.22 \cdot 10^8$	$1.26 \cdot 10^8$	$0.28 \cdot 10^8$	$9.59 \cdot 10^7$	$1.56 \cdot 10^7$	$6.71 \cdot 10^7$	$1.77 \cdot 10^7$	$3.90 \cdot 10^7$	$1.03 \cdot 10^7$

**Table D.2:** Summary of the fluctuation distributions of the number of charged particles for iron induced showers. Each distribution covers a certain energy and zenith angle range. For each distribution the mean and the RMS is given.

Figure D.6: Fluctuation diagrams for  $N_{ch}$ , iron, and  $0^\circ \leq \theta < 8^\circ$

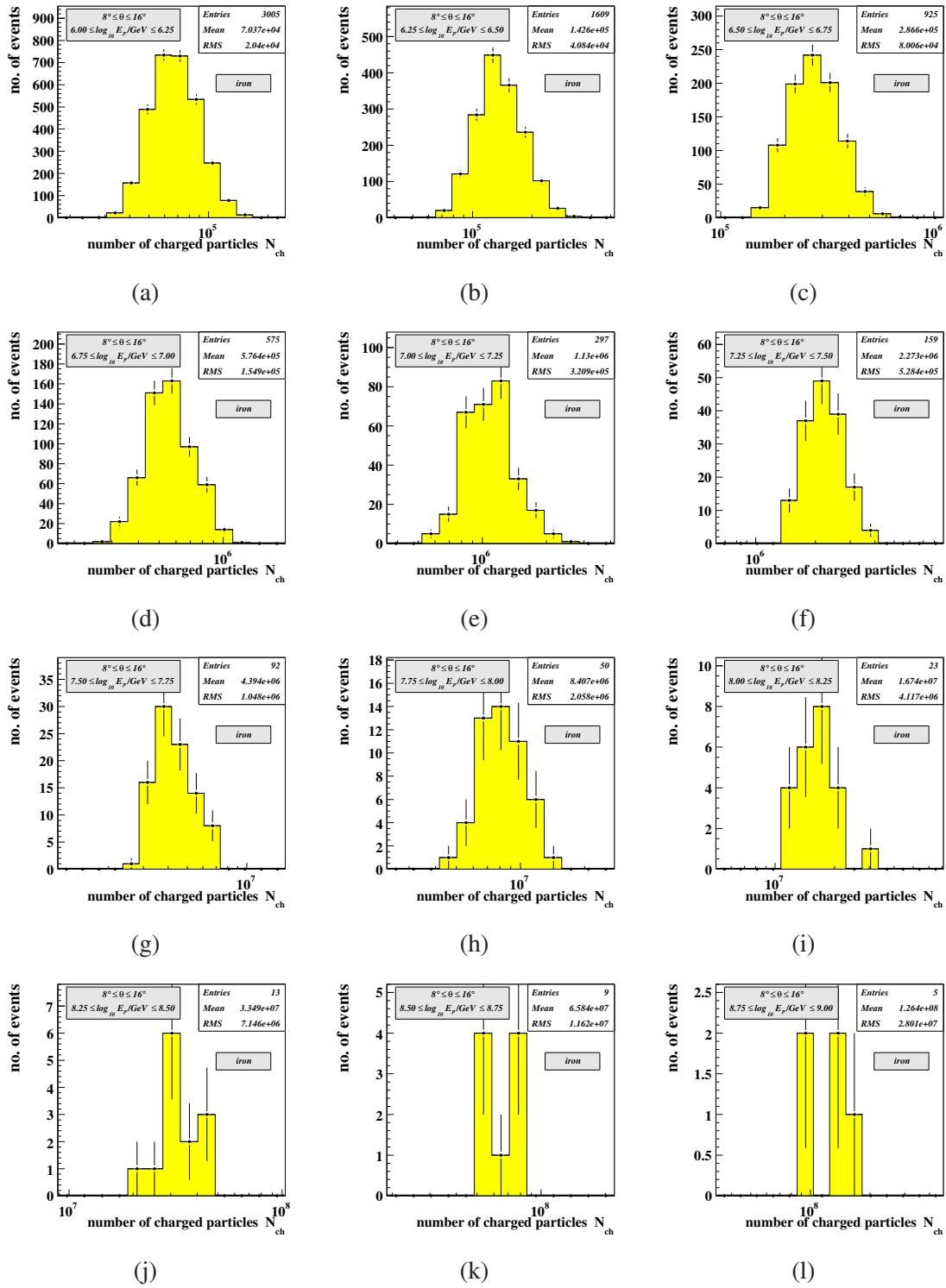


Figure D.7: Fluctuation diagrams for  $N_{ch}$ , iron, and  $8^\circ \leq \theta < 16^\circ$



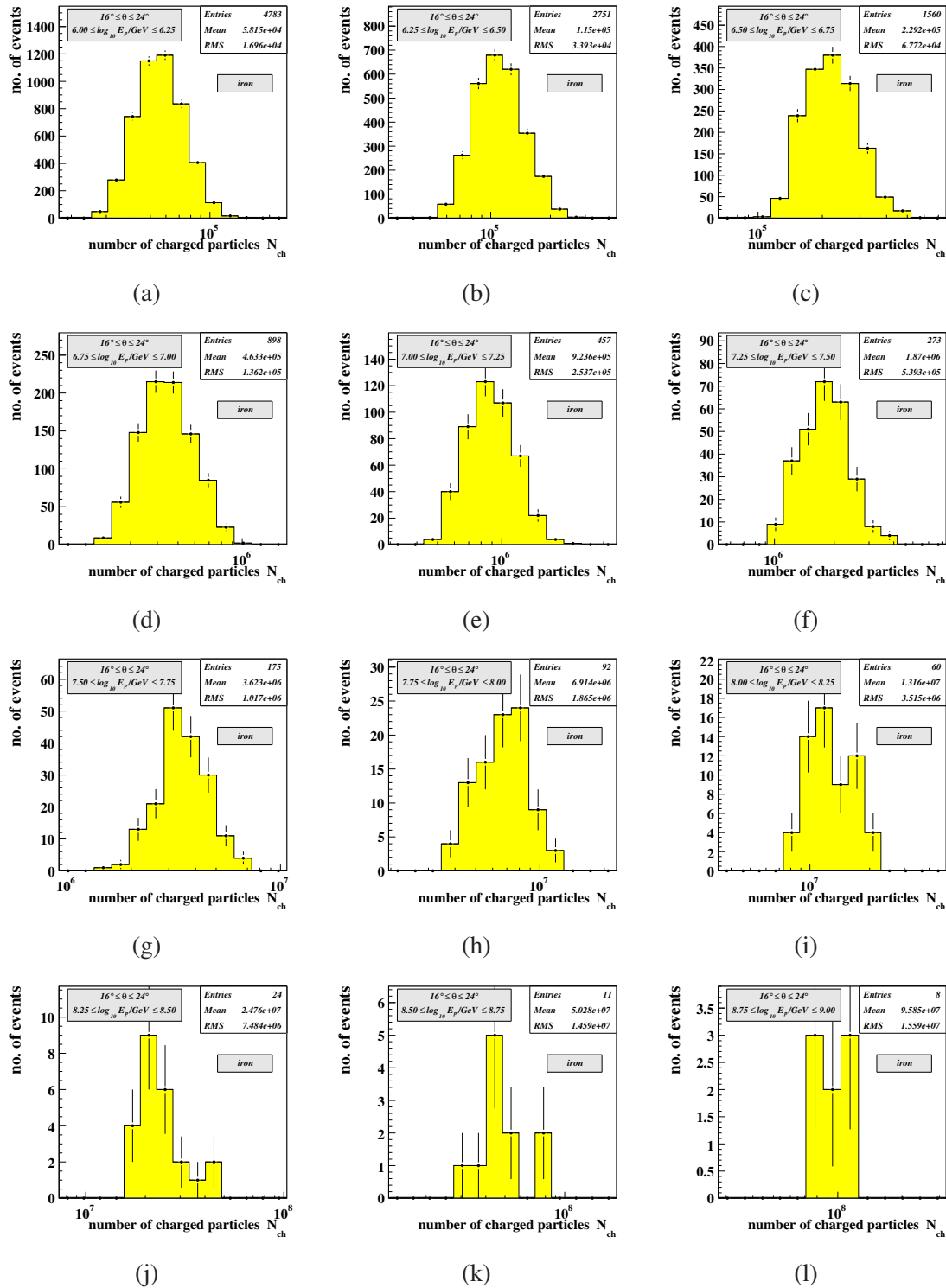


Figure D.8: Fluctuation diagrams for  $N_{ch}$ , iron, and  $16^\circ \leq \theta < 24^\circ$

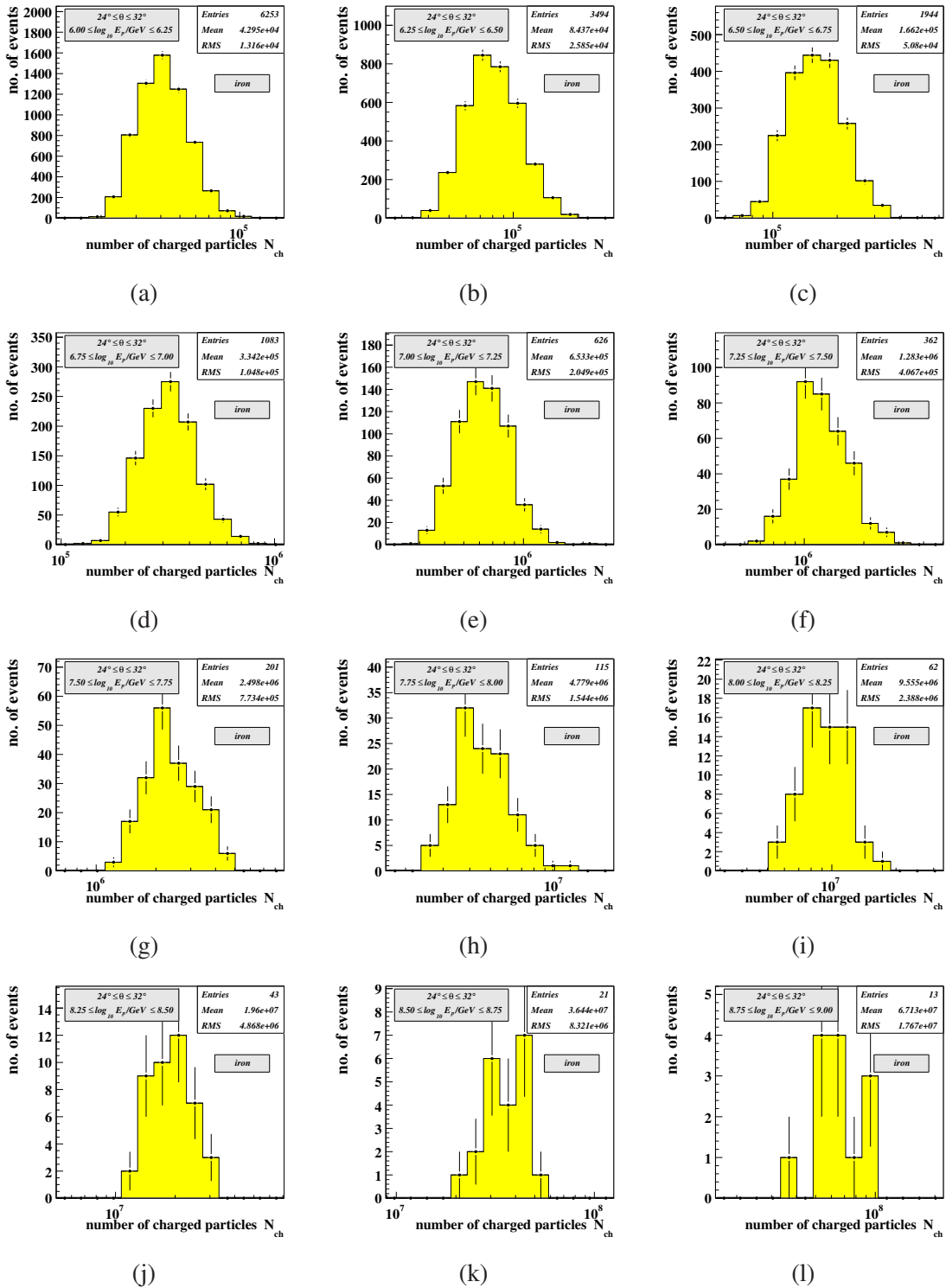
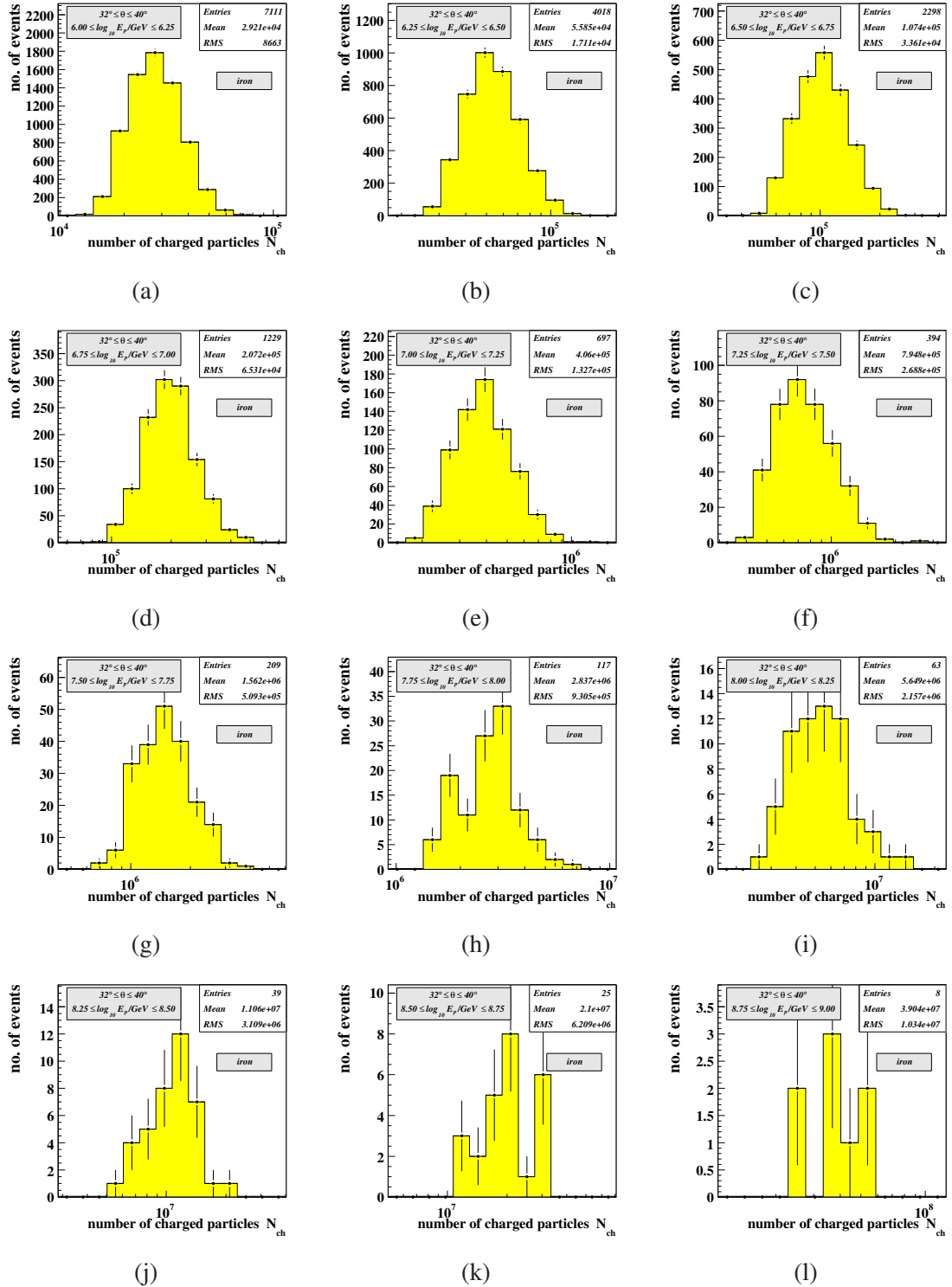


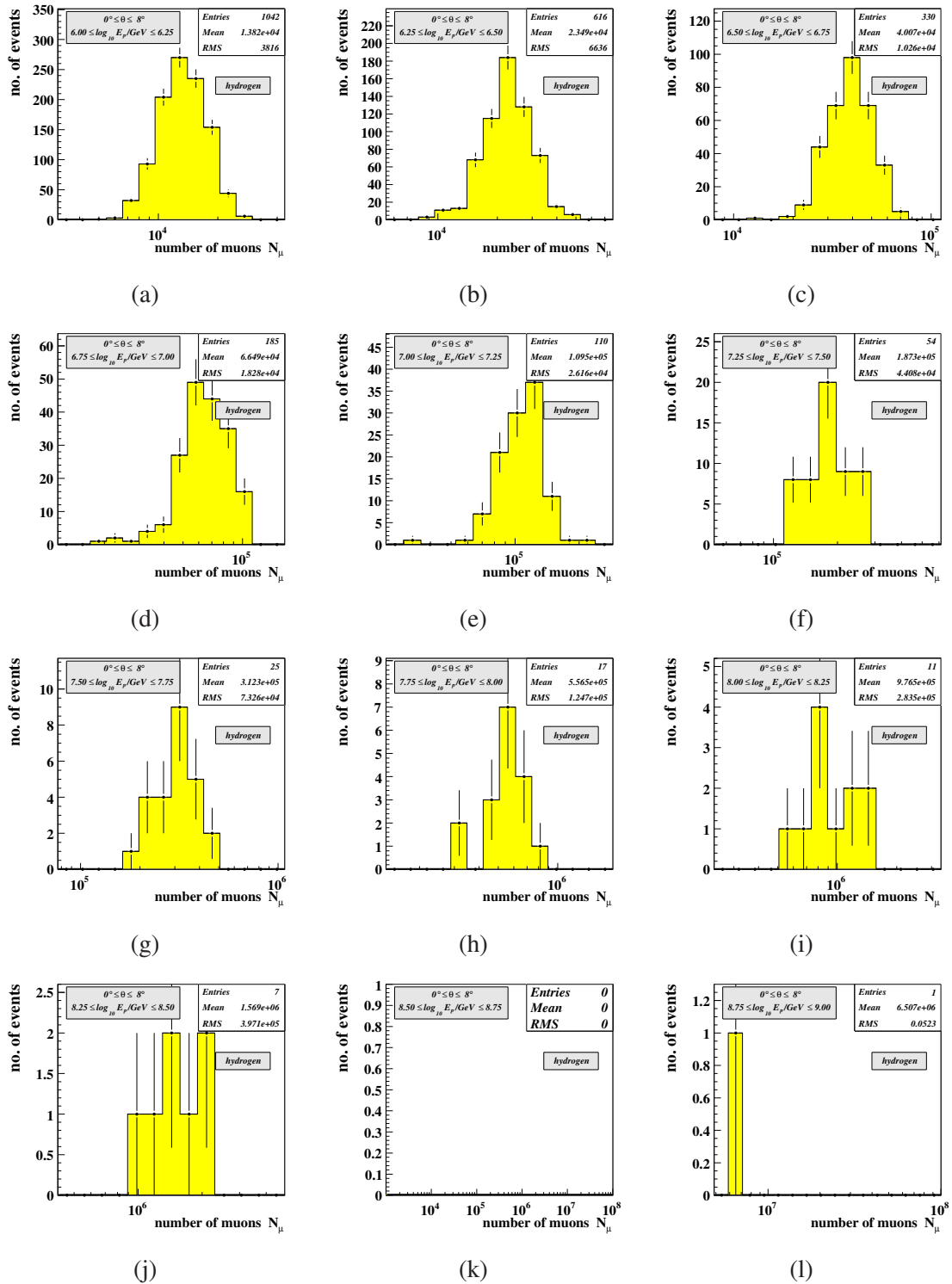
Figure D.9: Fluctuation diagrams for  $N_{ch}$ , iron, and  $24^\circ \leq \theta < 32^\circ$

Figure D.10: Fluctuation diagrams for  $N_{ch}$ , iron, and  $32^\circ \leq \theta \leq 40^\circ$

### D.3 Fluctuations of the number of muons for hydrogen induced showers

$\log_{10} E_p/\text{GeV}$	$0^\circ-8^\circ$		$8^\circ-16^\circ$		$16^\circ-24^\circ$		$24^\circ-32^\circ$		$32^\circ-40^\circ$	
	MEAN	RMS	MEAN	RMS	MEAN	RMS	MEAN	RMS	MEAN	RMS
6.00 – 6.25	$1.38 \cdot 10^4$	$0.38 \cdot 10^4$	$1.34 \cdot 10^4$	$0.38 \cdot 10^4$	$1.29 \cdot 10^4$	$0.37 \cdot 10^4$	$1.17 \cdot 10^4$	$0.35 \cdot 10^4$	$1.04 \cdot 10^4$	$0.31 \cdot 10^4$
6.25 – 6.50	$2.35 \cdot 10^4$	$0.66 \cdot 10^4$	$2.30 \cdot 10^4$	$0.62 \cdot 10^4$	$2.19 \cdot 10^4$	$0.62 \cdot 10^4$	$1.98 \cdot 10^4$	$0.56 \cdot 10^4$	$1.77 \cdot 10^4$	$0.51 \cdot 10^4$
6.50 – 6.75	$4.01 \cdot 10^4$	$1.03 \cdot 10^4$	$3.89 \cdot 10^4$	$1.06 \cdot 10^4$	$3.71 \cdot 10^4$	$0.98 \cdot 10^4$	$3.38 \cdot 10^4$	$0.93 \cdot 10^4$	$2.96 \cdot 10^4$	$0.84 \cdot 10^4$
6.75 – 7.00	$6.65 \cdot 10^4$	$1.83 \cdot 10^4$	$6.55 \cdot 10^4$	$1.67 \cdot 10^4$	$6.32 \cdot 10^4$	$1.60 \cdot 10^4$	$5.83 \cdot 10^4$	$1.54 \cdot 10^4$	$5.05 \cdot 10^4$	$1.41 \cdot 10^4$
7.00 – 7.25	$1.10 \cdot 10^5$	$0.26 \cdot 10^5$	$1.09 \cdot 10^5$	$0.29 \cdot 10^5$	$1.03 \cdot 10^5$	$0.26 \cdot 10^5$	$9.64 \cdot 10^4$	$2.57 \cdot 10^4$	$8.72 \cdot 10^4$	$2.38 \cdot 10^4$
7.25 – 7.50	$1.87 \cdot 10^5$	$0.44 \cdot 10^5$	$1.89 \cdot 10^5$	$0.43 \cdot 10^5$	$1.74 \cdot 10^5$	$0.42 \cdot 10^5$	$1.68 \cdot 10^5$	$0.46 \cdot 10^5$	$1.47 \cdot 10^5$	$0.38 \cdot 10^5$
7.50 – 7.75	$3.12 \cdot 10^5$	$0.73 \cdot 10^5$	$3.13 \cdot 10^5$	$0.79 \cdot 10^5$	$3.01 \cdot 10^5$	$0.63 \cdot 10^5$	$2.77 \cdot 10^5$	$0.70 \cdot 10^5$	$2.43 \cdot 10^5$	$0.63 \cdot 10^5$
7.75 – 8.00	$5.57 \cdot 10^5$	$1.25 \cdot 10^5$	$5.30 \cdot 10^5$	$1.44 \cdot 10^5$	$5.07 \cdot 10^5$	$1.17 \cdot 10^5$	$4.63 \cdot 10^5$	$0.96 \cdot 10^5$	$4.11 \cdot 10^5$	$0.97 \cdot 10^5$
8.00 – 8.25	$9.77 \cdot 10^5$	$2.84 \cdot 10^5$	$9.12 \cdot 10^5$	$2.12 \cdot 10^5$	$8.97 \cdot 10^5$	$2.21 \cdot 10^5$	$8.35 \cdot 10^5$	$1.75 \cdot 10^5$	$7.05 \cdot 10^5$	$1.57 \cdot 10^5$
8.25 – 8.50	$1.57 \cdot 10^6$	$0.40 \cdot 10^6$	$1.42 \cdot 10^6$	$0.31 \cdot 10^6$	$1.55 \cdot 10^6$	$0.37 \cdot 10^6$	$1.32 \cdot 10^6$	$0.29 \cdot 10^6$	$1.21 \cdot 10^6$	$0.28 \cdot 10^6$
8.50 – 8.75	–	–	$2.71 \cdot 10^6$	$0.60 \cdot 10^6$	$2.68 \cdot 10^6$	$0.70 \cdot 10^6$	$2.40 \cdot 10^6$	$0.62 \cdot 10^6$	$2.08 \cdot 10^6$	$0.41 \cdot 10^6$
8.75 – 9.00	$6.51 \cdot 10^6$	–	$3.52 \cdot 10^6$	$1.02 \cdot 10^6$	$5.12 \cdot 10^6$	$1.15 \cdot 10^6$	$4.05 \cdot 10^6$	$1.08 \cdot 10^6$	$3.48 \cdot 10^6$	$0.83 \cdot 10^6$

**Table D.3:** Summary of the fluctuation distributions of the number of muons for hydrogen induced showers. Each distribution covers a certain energy and zenith angle range. For each distribution the mean and the RMS is given. There are certain ranges where the distribution contains no event (neither the mean nor the RMS can be calculated) or only one event (the RMS cannot be calculated), these are indicated by a “–” in the table.

Figure D.11: Fluctuation diagrams for  $N_\mu$ , hydrogen, and  $0^\circ \leq \theta < 8^\circ$

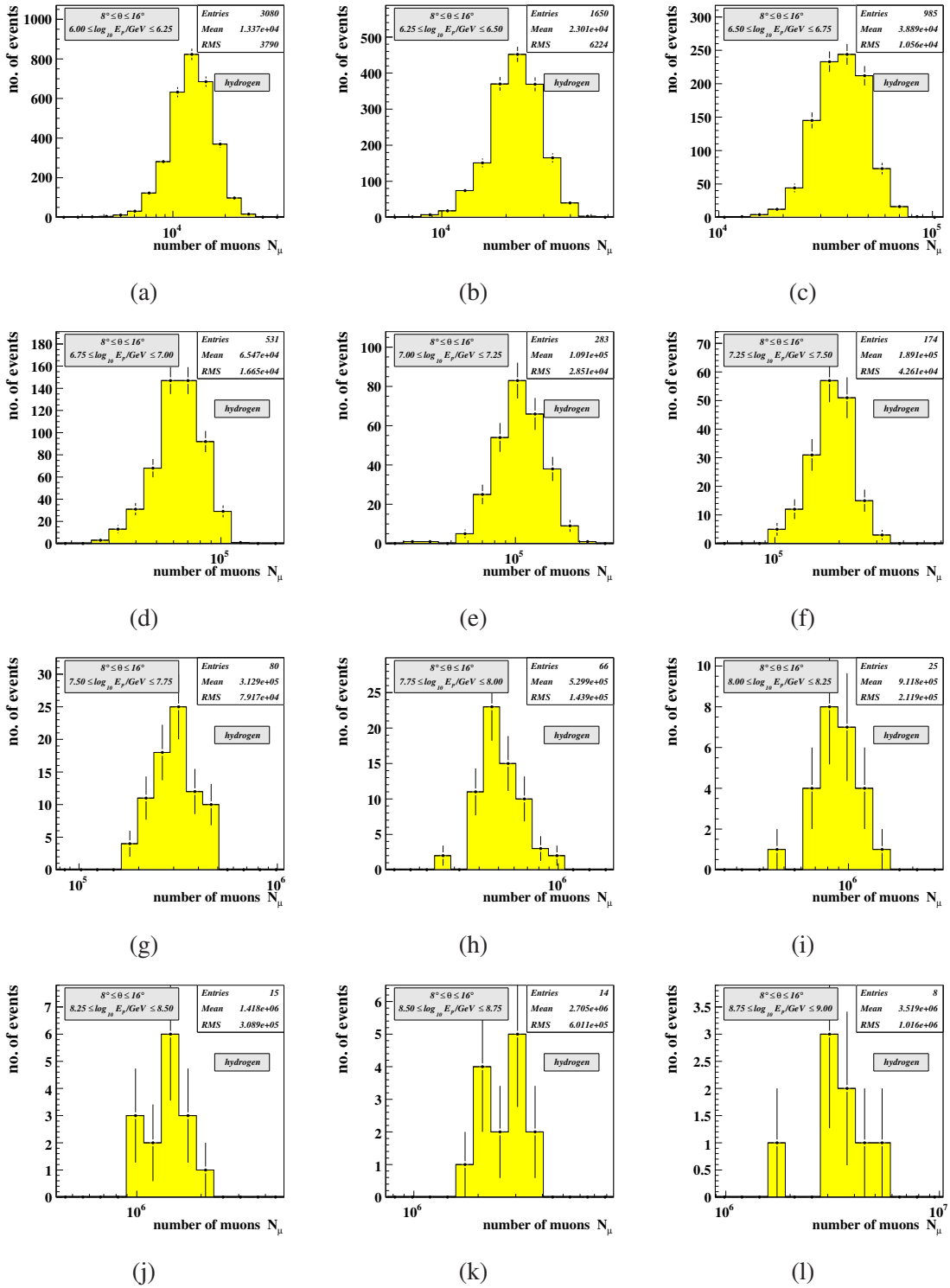
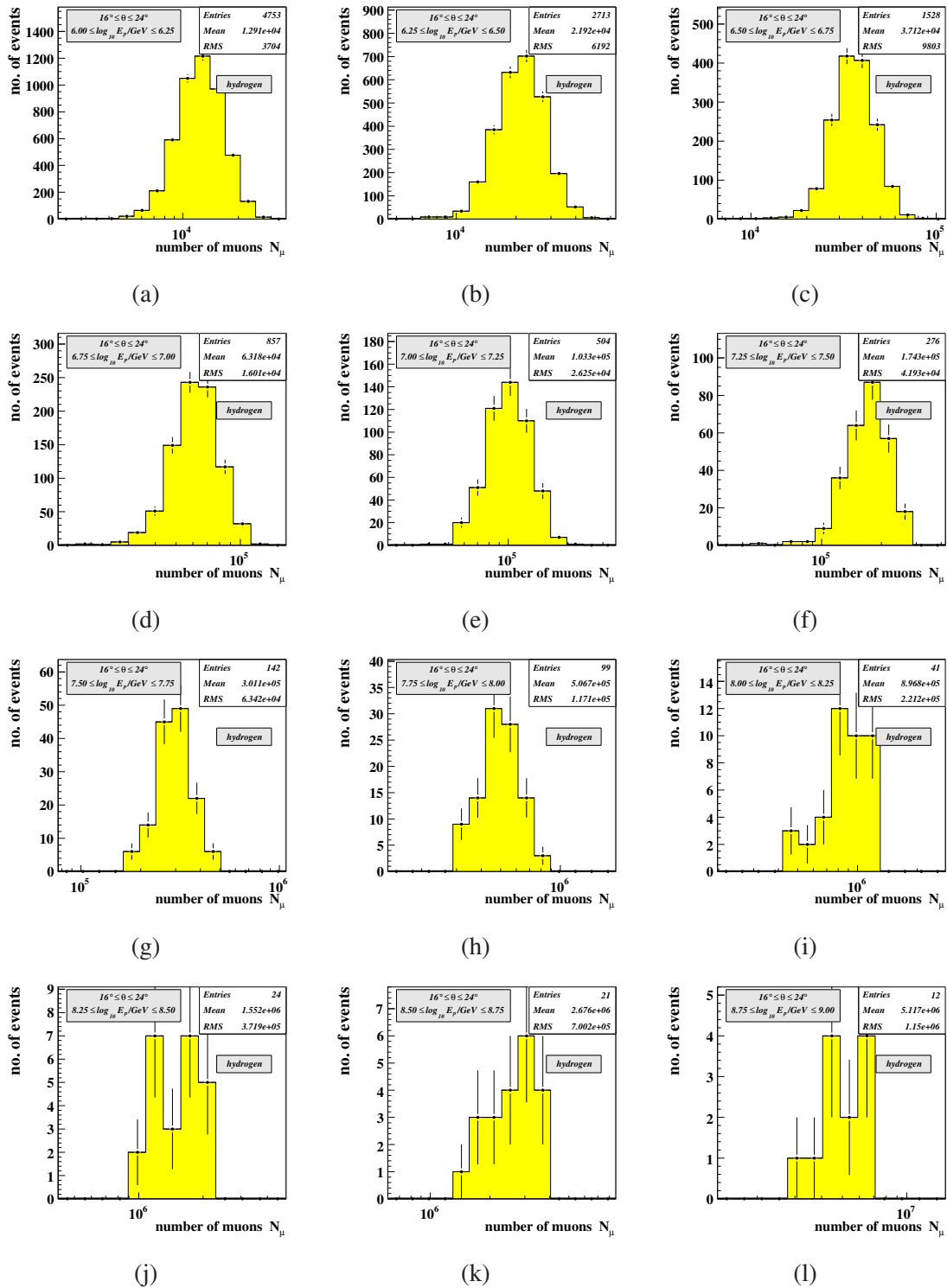


Figure D.12: Fluctuation diagrams for  $N_\mu$ , hydrogen, and  $8^\circ \leq \theta < 16^\circ$

Figure D.13: Fluctuation diagrams for  $N_\mu$ , hydrogen, and  $16^\circ \leq \theta < 24^\circ$

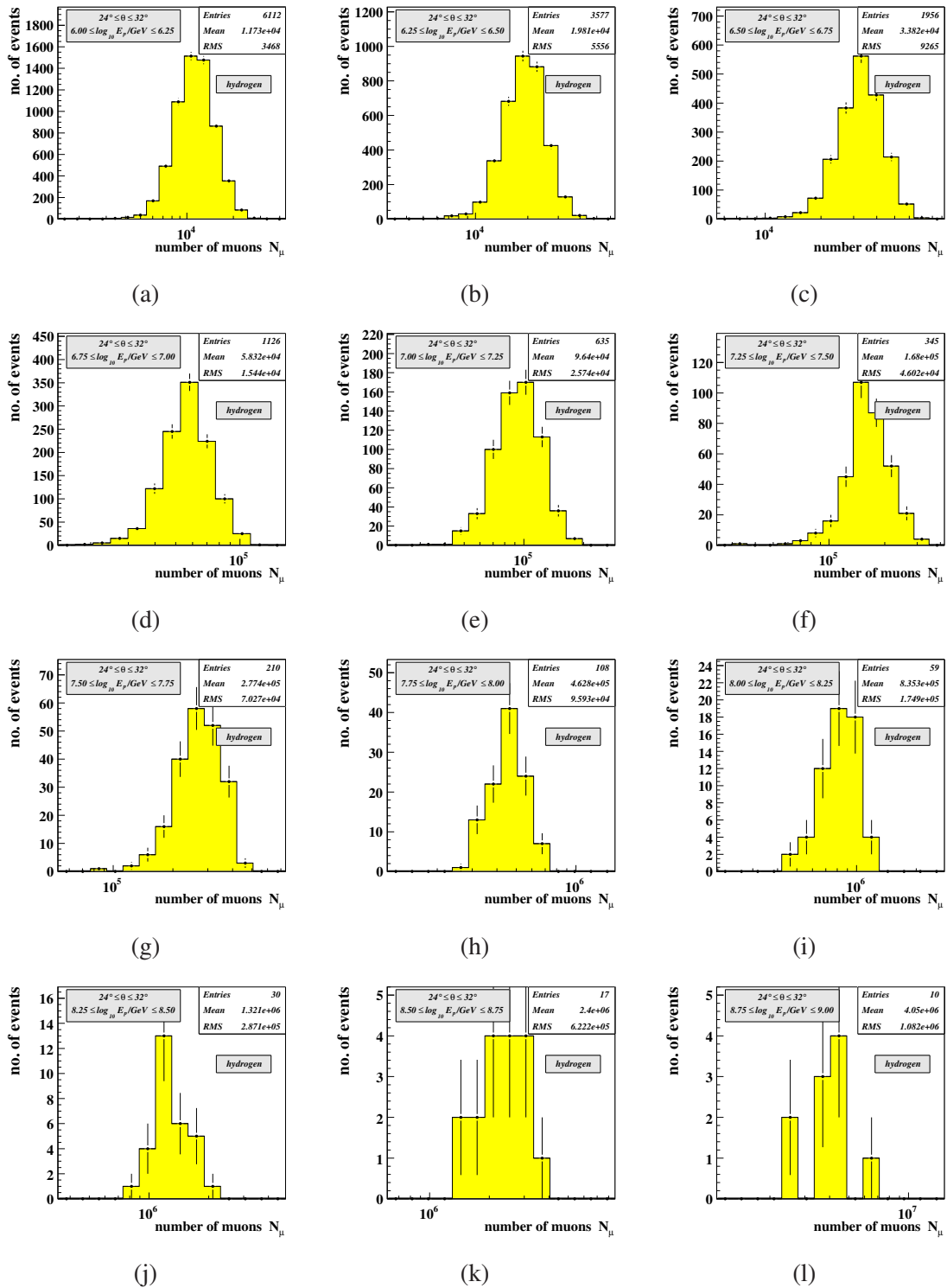
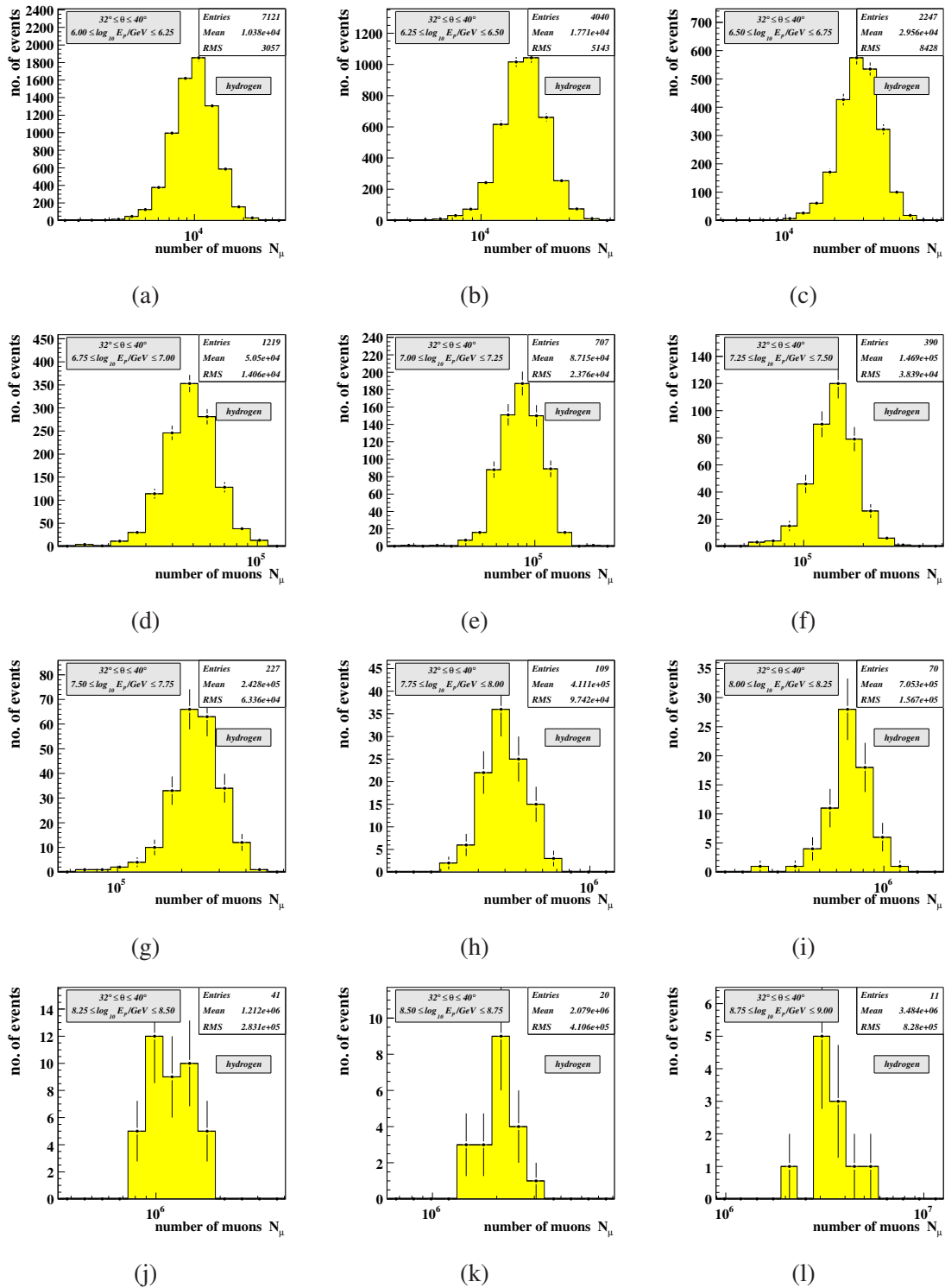


Figure D.14: Fluctuation diagrams for  $N_\mu$ , hydrogen, and  $24^\circ \leq \theta < 32^\circ$



Figure D.15: Fluctuation diagrams for  $N_\mu$ , hydrogen, and  $32^\circ \leq \theta \leq 40^\circ$

## D.4 Fluctuations of the number of muons for iron induced showers

$\log_{10} E_p / \text{GeV}$	$0^\circ-8^\circ$		$8^\circ-16^\circ$		$16^\circ-24^\circ$		$24^\circ-32^\circ$		$32^\circ-40^\circ$	
	MEAN	RMS	MEAN	RMS	MEAN	RMS	MEAN	RMS	MEAN	RMS
6.00 – 6.25	$1.94 \cdot 10^4$	$0.34 \cdot 10^4$	$1.89 \cdot 10^4$	$0.34 \cdot 10^4$	$1.79 \cdot 10^4$	$0.31 \cdot 10^4$	$1.64 \cdot 10^4$	$0.30 \cdot 10^4$	$1.45 \cdot 10^4$	$0.27 \cdot 10^4$
6.25 – 6.50	$3.32 \cdot 10^4$	$0.59 \cdot 10^4$	$3.20 \cdot 10^4$	$0.57 \cdot 10^4$	$3.01 \cdot 10^4$	$0.53 \cdot 10^4$	$2.76 \cdot 10^4$	$0.50 \cdot 10^4$	$2.46 \cdot 10^4$	$0.44 \cdot 10^4$
6.50 – 6.75	$5.53 \cdot 10^4$	$0.92 \cdot 10^4$	$5.48 \cdot 10^4$	$0.98 \cdot 10^4$	$5.11 \cdot 10^4$	$0.91 \cdot 10^4$	$4.71 \cdot 10^4$	$0.84 \cdot 10^4$	$4.16 \cdot 10^4$	$0.75 \cdot 10^4$
6.75 – 7.00	$9.47 \cdot 10^4$	$1.55 \cdot 10^4$	$9.25 \cdot 10^4$	$1.62 \cdot 10^4$	$8.70 \cdot 10^4$	$1.55 \cdot 10^4$	$8.04 \cdot 10^4$	$1.42 \cdot 10^4$	$7.06 \cdot 10^4$	$1.27 \cdot 10^4$
7.00 – 7.25	$1.64 \cdot 10^5$	$0.31 \cdot 10^5$	$1.55 \cdot 10^5$	$0.27 \cdot 10^5$	$1.49 \cdot 10^5$	$0.25 \cdot 10^5$	$1.36 \cdot 10^5$	$0.24 \cdot 10^5$	$1.20 \cdot 10^5$	$0.21 \cdot 10^5$
7.25 – 7.50	$2.75 \cdot 10^5$	$0.56 \cdot 10^5$	$2.66 \cdot 10^5$	$0.41 \cdot 10^5$	$2.53 \cdot 10^5$	$0.44 \cdot 10^5$	$2.29 \cdot 10^5$	$0.42 \cdot 10^5$	$2.04 \cdot 10^5$	$0.36 \cdot 10^5$
7.50 – 7.75	$4.57 \cdot 10^5$	$0.67 \cdot 10^5$	$4.38 \cdot 10^5$	$0.70 \cdot 10^5$	$4.27 \cdot 10^5$	$0.73 \cdot 10^5$	$3.90 \cdot 10^5$	$0.71 \cdot 10^5$	$3.49 \cdot 10^5$	$0.64 \cdot 10^5$
7.75 – 8.00	$7.98 \cdot 10^5$	$1.41 \cdot 10^5$	$7.27 \cdot 10^5$	$1.36 \cdot 10^5$	$7.19 \cdot 10^5$	$1.25 \cdot 10^5$	$6.54 \cdot 10^5$	$1.10 \cdot 10^5$	$5.78 \cdot 10^5$	$1.01 \cdot 10^5$
8.00 – 8.25	$1.26 \cdot 10^6$	$0.20 \cdot 10^6$	$1.26 \cdot 10^6$	$0.23 \cdot 10^6$	$1.19 \cdot 10^6$	$0.20 \cdot 10^6$	$1.13 \cdot 10^6$	$0.19 \cdot 10^6$	$9.97 \cdot 10^5$	$1.72 \cdot 10^5$
8.25 – 8.50	$2.58 \cdot 10^6$	$0.48 \cdot 10^6$	$2.18 \cdot 10^6$	$0.27 \cdot 10^6$	$1.98 \cdot 10^6$	$0.36 \cdot 10^6$	$2.00 \cdot 10^6$	$0.35 \cdot 10^6$	$1.68 \cdot 10^6$	$0.27 \cdot 10^6$
8.50 – 8.75	$3.82 \cdot 10^6$	$0.91 \cdot 10^6$	$3.88 \cdot 10^6$	$0.45 \cdot 10^6$	$3.37 \cdot 10^6$	$0.54 \cdot 10^6$	$3.28 \cdot 10^6$	$0.39 \cdot 10^6$	$2.88 \cdot 10^6$	$0.49 \cdot 10^6$
8.75 – 9.00	$5.95 \cdot 10^6$	$0.56 \cdot 10^6$	$6.42 \cdot 10^6$	$1.35 \cdot 10^6$	$5.72 \cdot 10^6$	$0.86 \cdot 10^6$	$5.37 \cdot 10^6$	$0.80 \cdot 10^6$	$4.74 \cdot 10^6$	$0.79 \cdot 10^6$

**Table D.4:** Summary of the fluctuation distributions of the number of muons for iron induced showers. Each distribution covers a certain energy and zenith angle range. For each distribution the mean and the RMS is given.

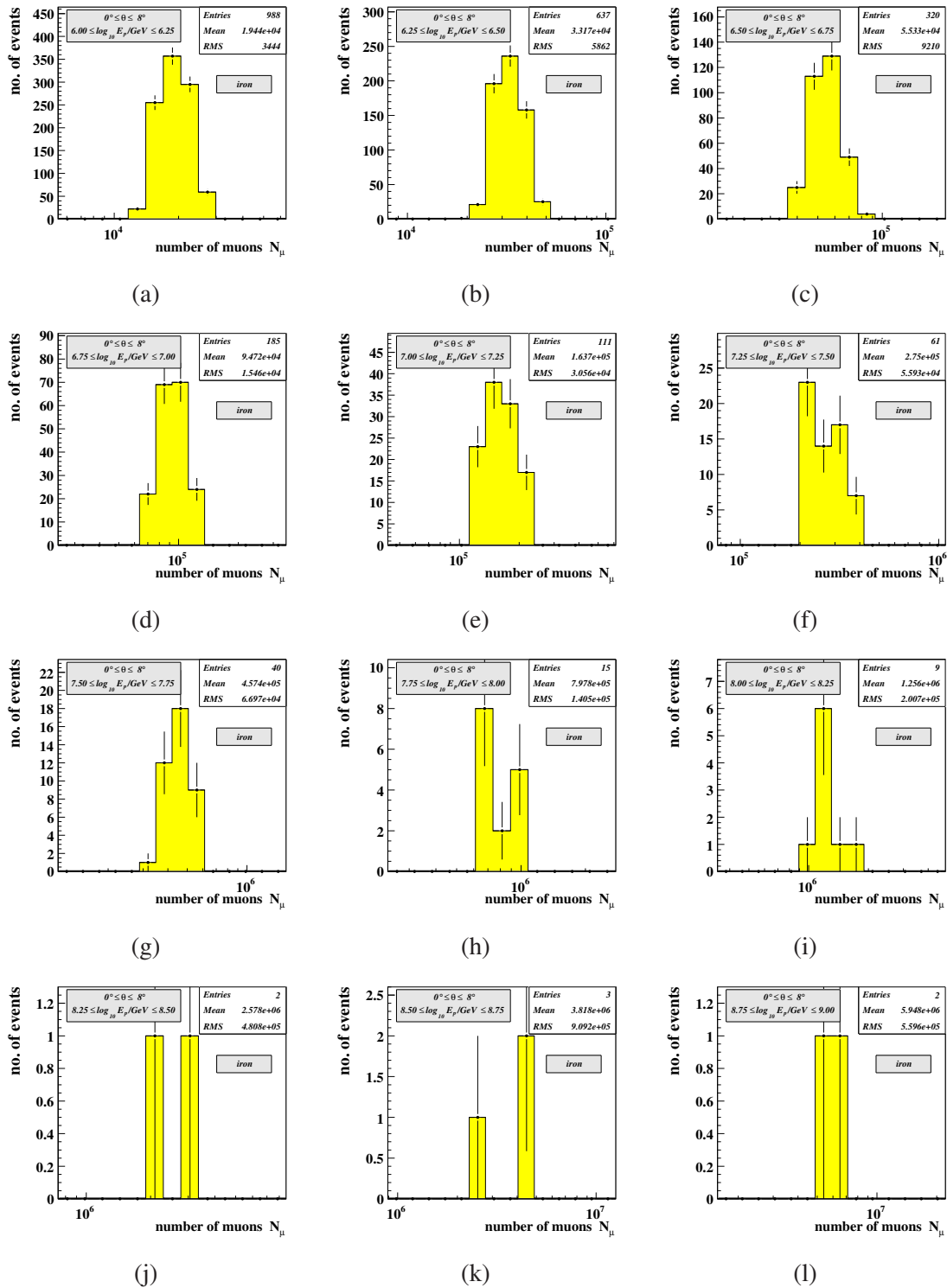


Figure D.16: Fluctuation diagrams for  $N_\mu$ , iron, and  $0^\circ \leq \theta < 8^\circ$

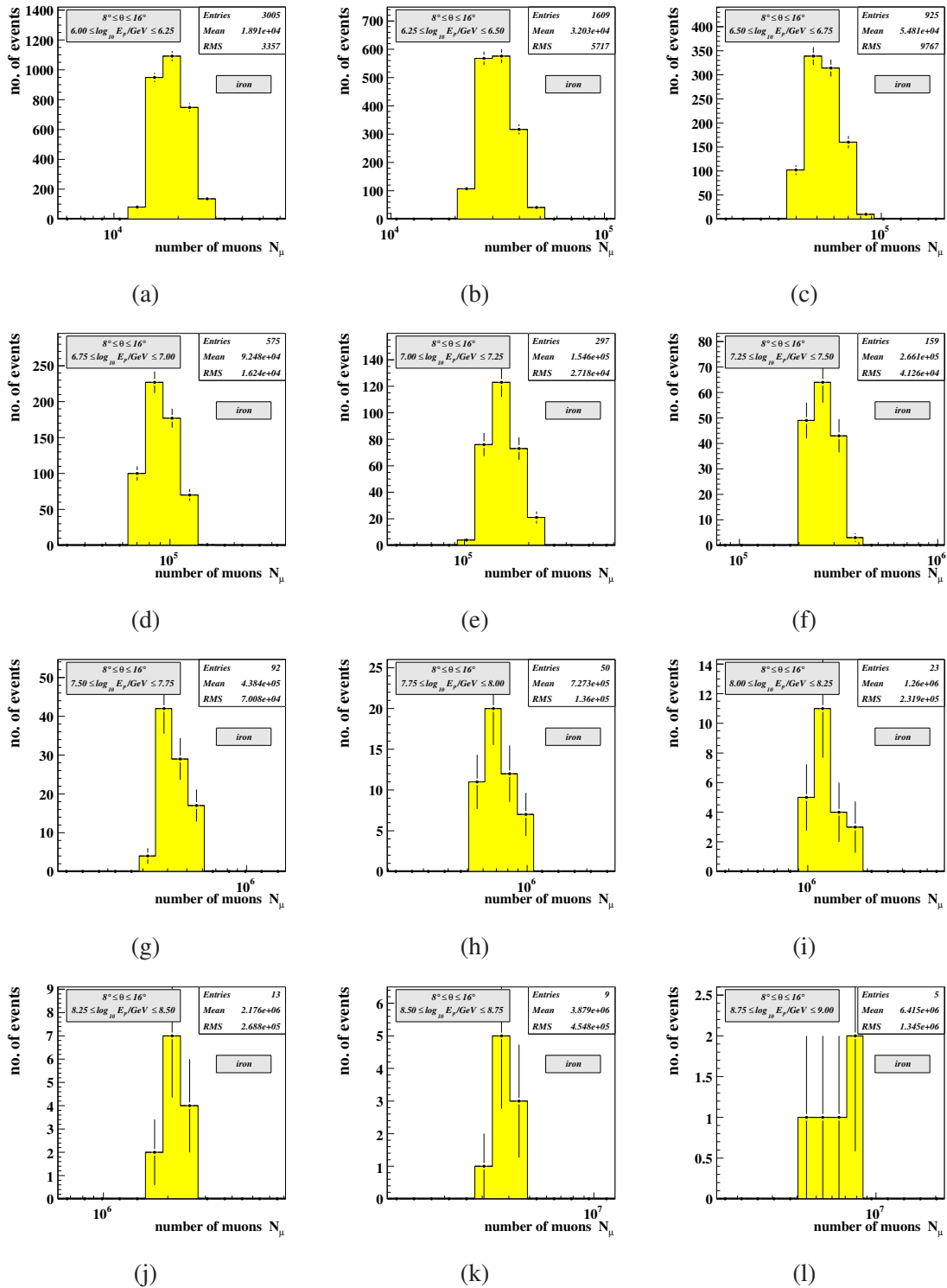


Figure D.17: Fluctuation diagrams for  $N_\mu$ , iron, and  $8^\circ \leq \theta < 16^\circ$

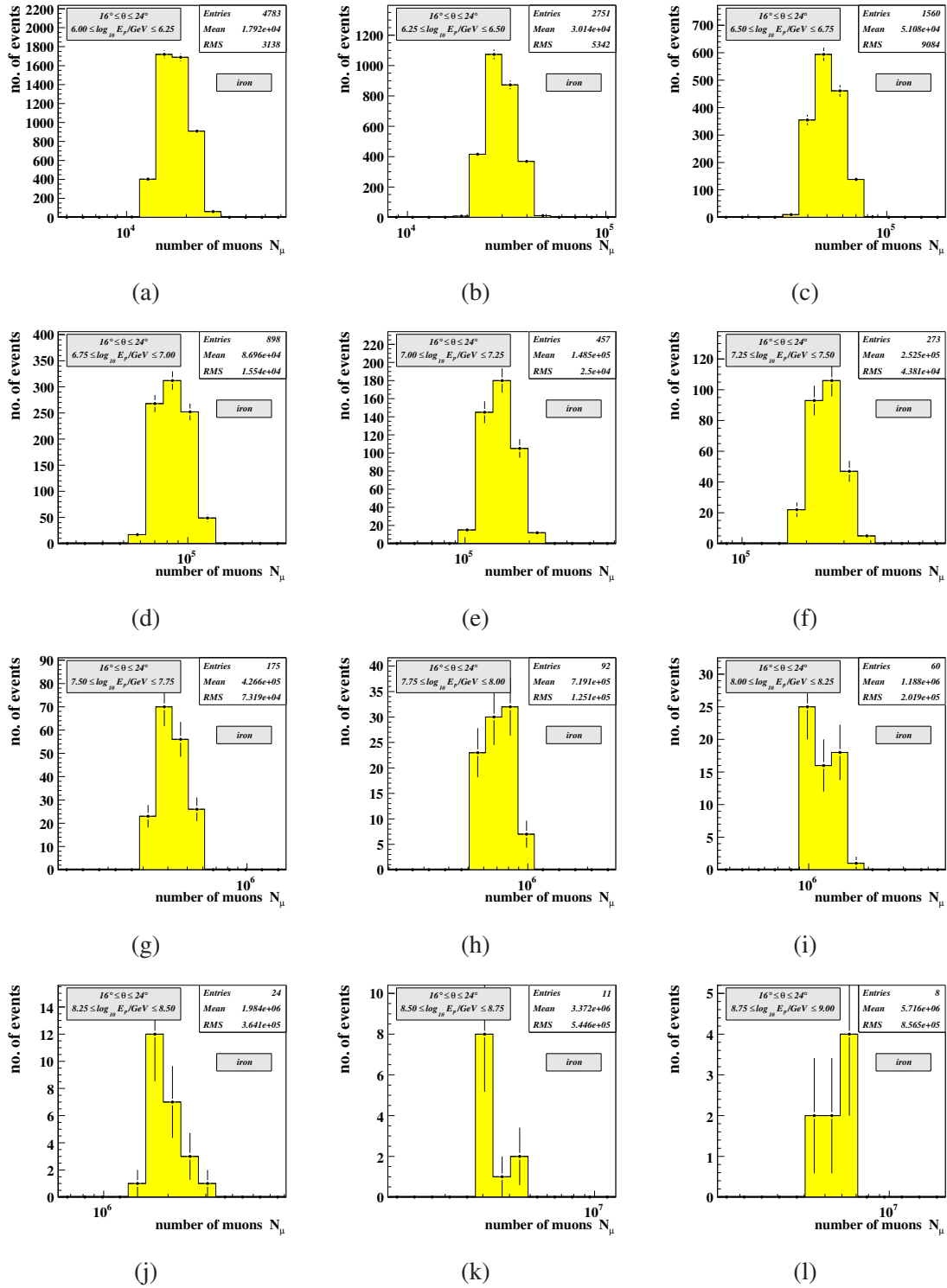


Figure D.18: Fluctuation diagrams for  $N_\mu$ , iron, and  $16^\circ \leq \theta < 24^\circ$

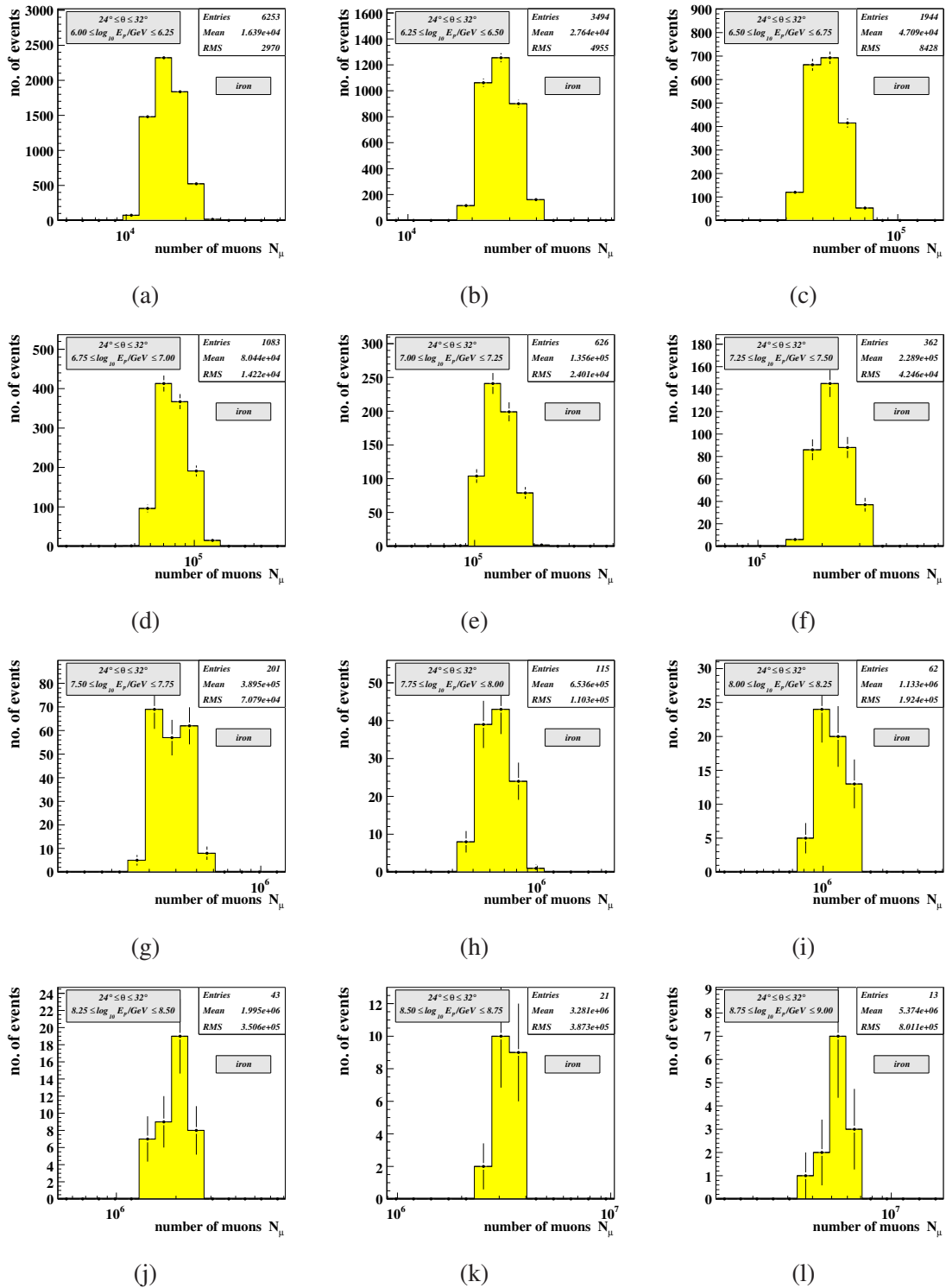
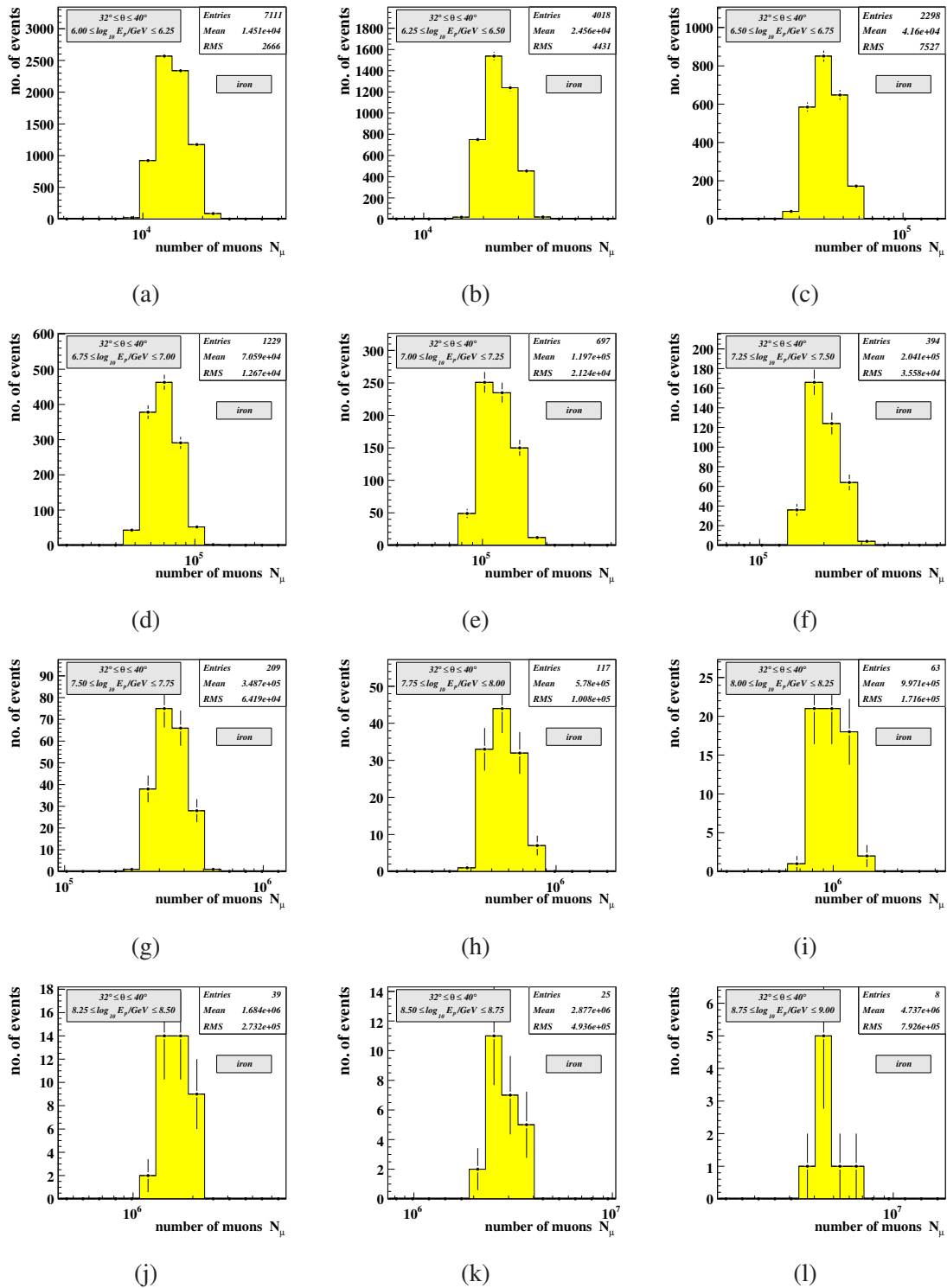
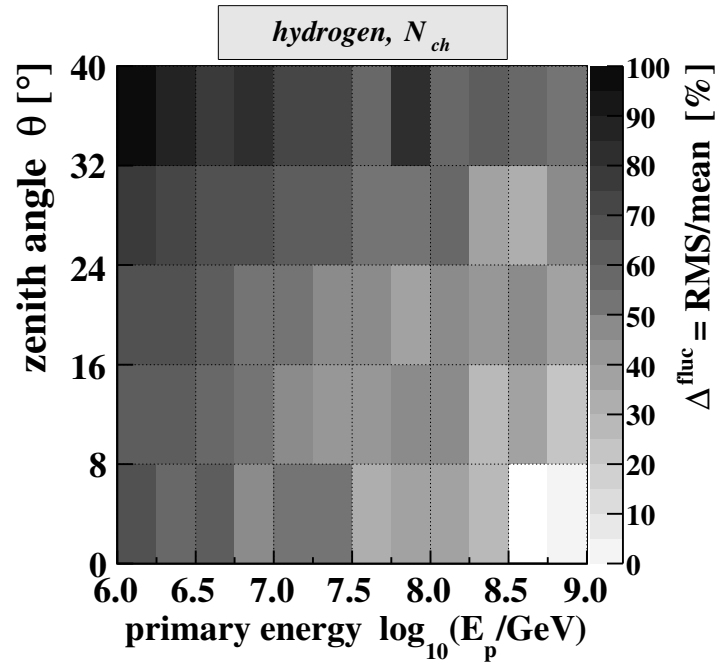


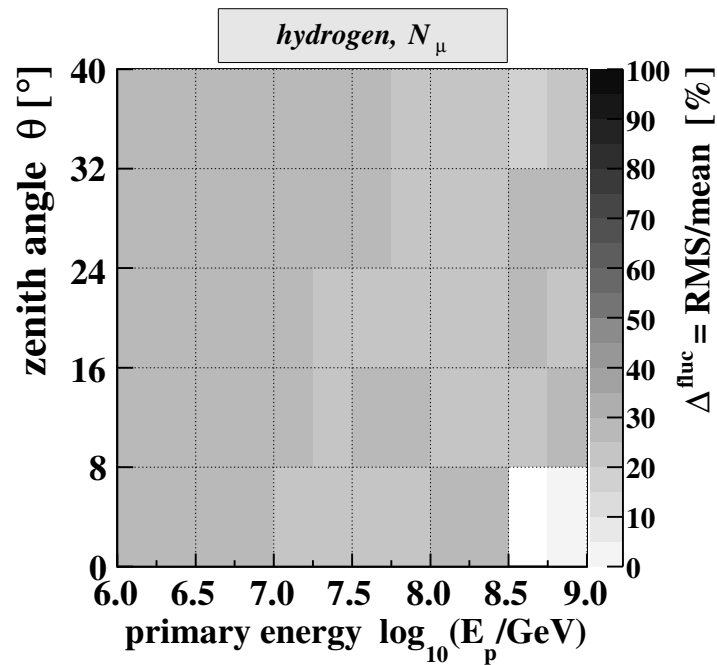
Figure D.19: Fluctuation diagrams for  $N_\mu$ , iron, and  $24^\circ \leq \theta < 32^\circ$

Figure D.20: Fluctuation diagrams for  $N_\mu$ , iron, and  $32^\circ \leq \theta \leq 40^\circ$

## D.5 Summary of the fluctuations for hydrogen induced showers



(a)



(b)

**Figure D.21:** Summarizing shower fluctuations for hydrogen induced showers.



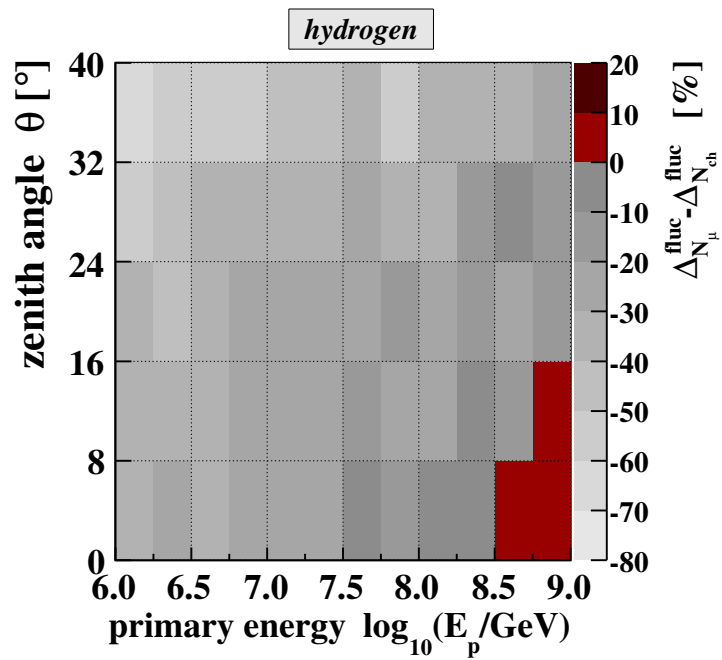


Figure D.22: Difference plot between  $N_{\mu}$  and  $N_{\text{ch}}$  for hydrogen induced showers



---

# Examination of the energy conversion

---

This appendix contains results of the examination and determination of the energy conversion, see Chap. 7.3.

In addition to the illustration of the influence of the subsample cuts on the event selection (see Fig. 7.6) in App. E.1 the event distribution for the KASCADE-Grande array is shown for the application of the standard cuts.

In App. E.2 the distributions of the number of muons as a function of the true primary energy are shown. The distributions are plotted for hydrogen and iron induced showers using the standard as well as the subsample cuts. For the standard cuts, the distribution of a mixed composition is shown, too. This can be compared with Fig 7.7, which shows the distribution for a mixed composition using the subsample cuts.

In App. E.3 the profile plots of the primary energy as a function of the number of muons using the standard quality cuts are shown, in addition to the profile plots using the subsample cuts, see Fig. 7.8.

Finally, in App. E.4 the difference plots between the corresponding fit function and the number of muons for each event is shown for hydrogen and iron induced showers, independently (see also Chap. 7.1 and Fig. 7.9). Additionally, the profile plots of these two distributions are shown.

## E.1 Influence of standard quality cuts on the event distribution over the KASCADE-Grande array

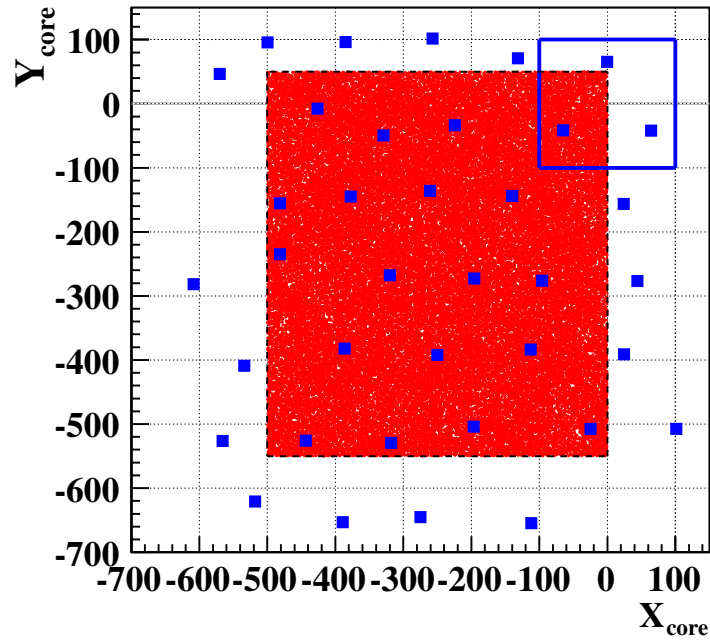
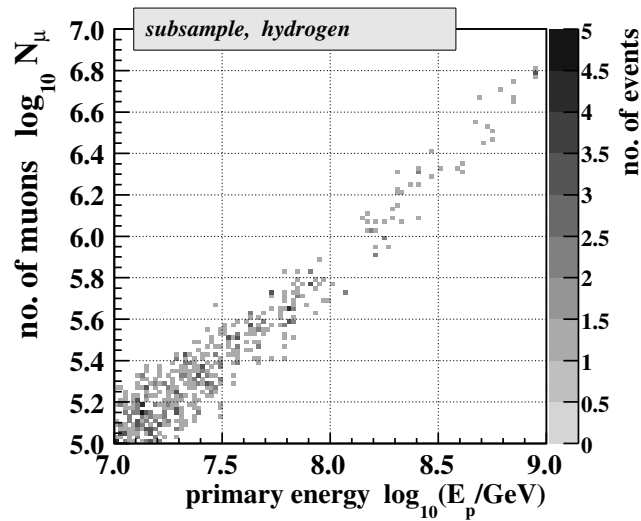
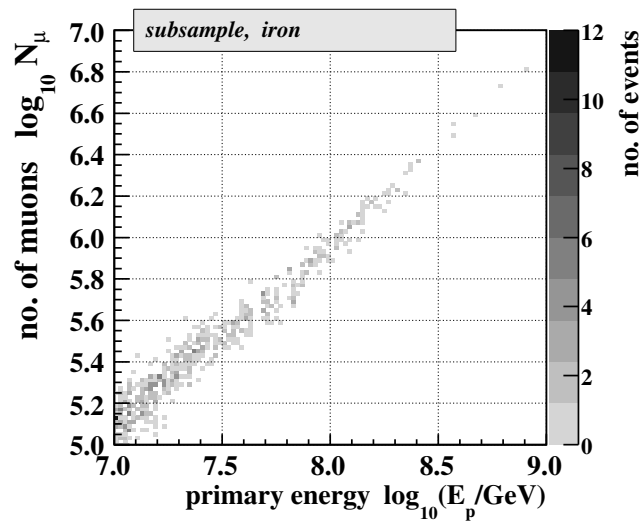


**Figure E.1:** Schematic view of the KASCADE-Grande experiment, demonstrating the influence of the standard cuts on the event selection. The shower core position of each selected event is plotted in coordinates of KASCADE-Grande. The small filled squares illustrate the position of the Grande stations. The KASCADE array is represented by the open square in the top right corner. The dashed lined rectangle indicates the fiducial area cut.

## E.2 Distributions of the muon number as a function of the primary energy

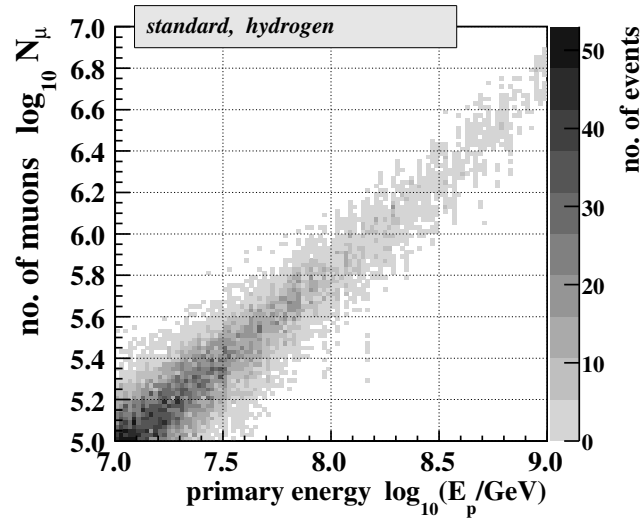


(a)

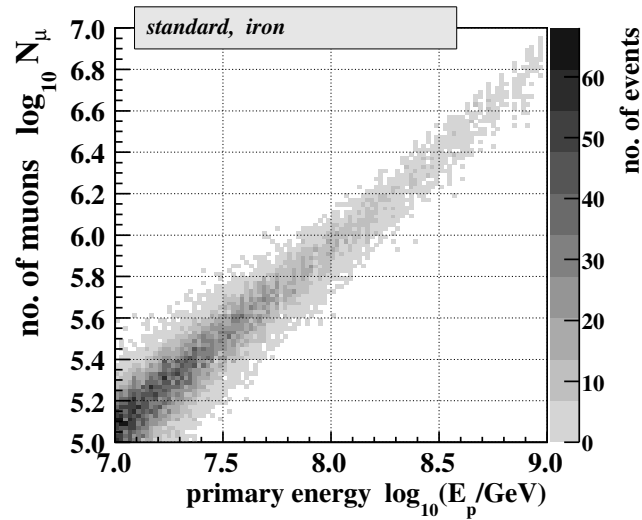


(b)

**Figure E.2:** The number of muons as a function of the true primary energy for hydrogen (*top*) and iron induced showers (*bottom*). All sets of simulated air showers are used and the subsample cuts are applied.



(a)



(b)

**Figure E.3:** The number of muons as a function of the true primary energy for hydrogen (*top*) and iron induced showers (*bottom*). All sets of simulated air showers are used and the standard quality cuts are applied.

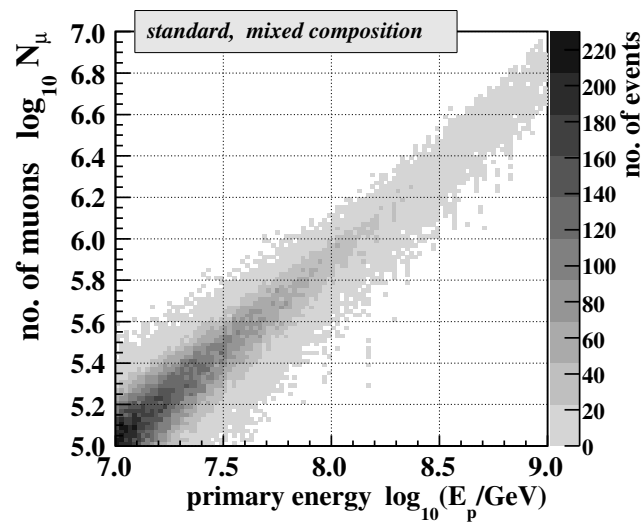
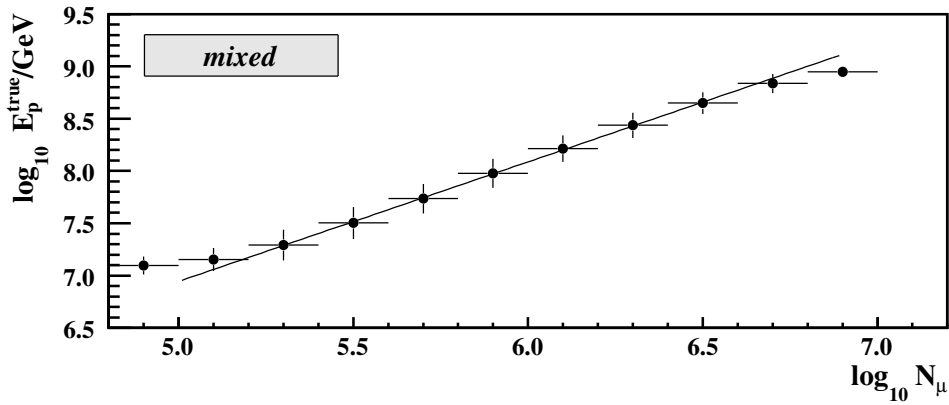
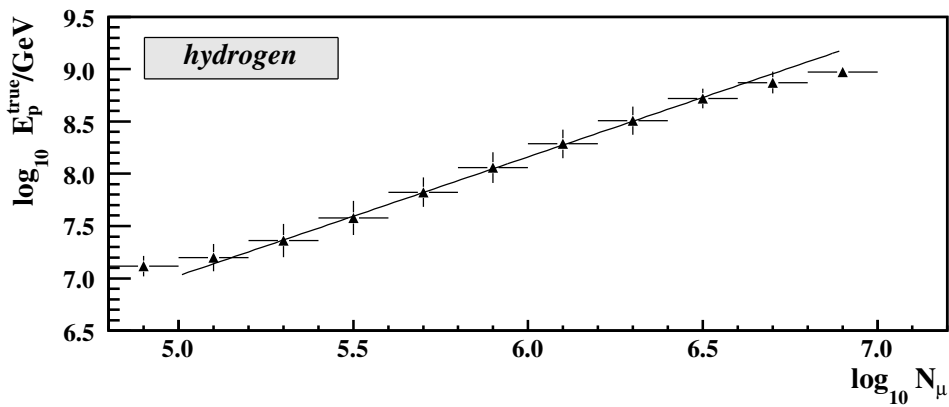


**Figure E.4:** The number of muons as a function of the true primary energy for the assumption of a mixed composition. All sets of simulated air showers are used and the standard quality cuts are applied.

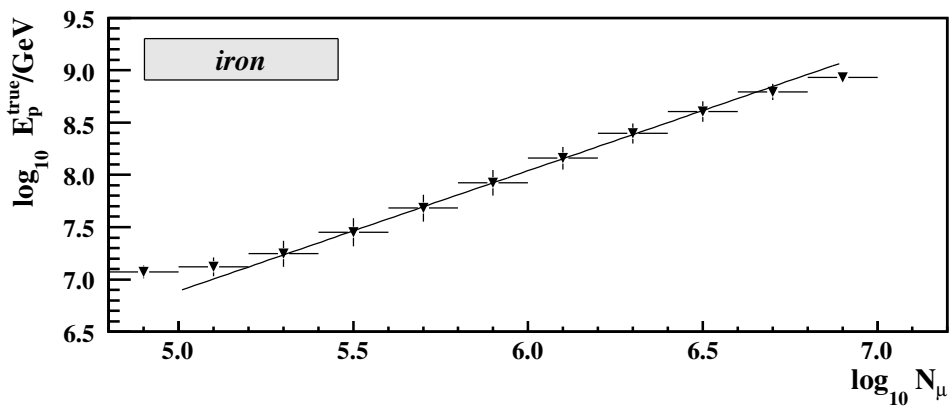
### E.3 Profile plots for the energy conversion using standard cuts



(a) Mixed composition



(b) Hydrogen initiated showers



(c) Iron initiated showers

**Figure E.5:** Profile diagrams of the primary energy as a function of the number of muons. All simulated shower data sets are used and the standard quality cuts are applied. The line is the resulting linear fit to the data points.



## E.4 Comparing results using subsample cuts with results using standard quality cuts

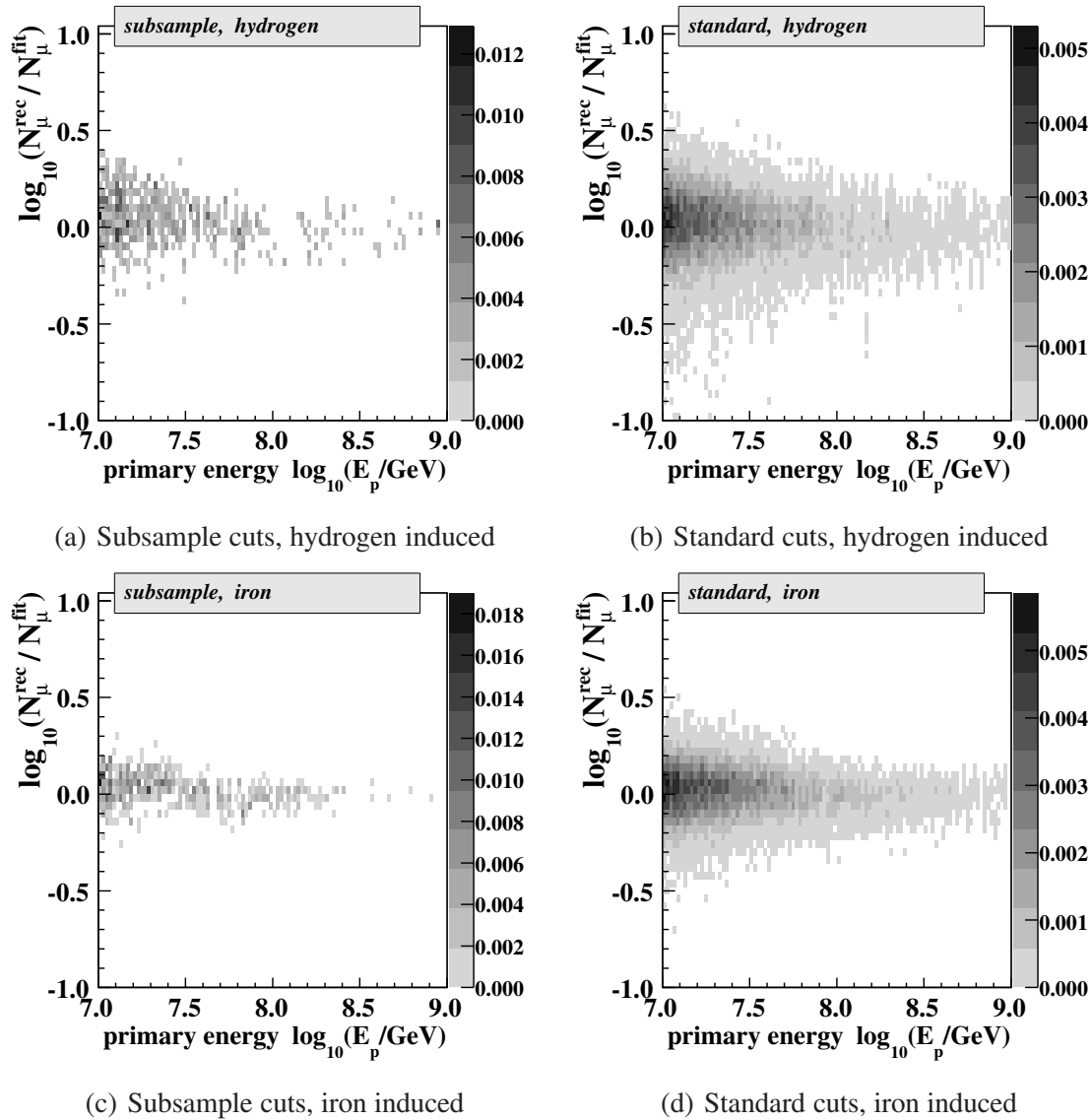
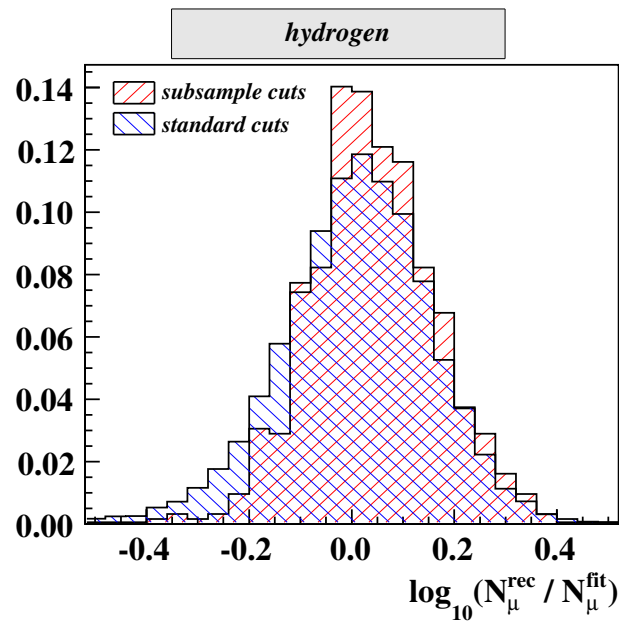
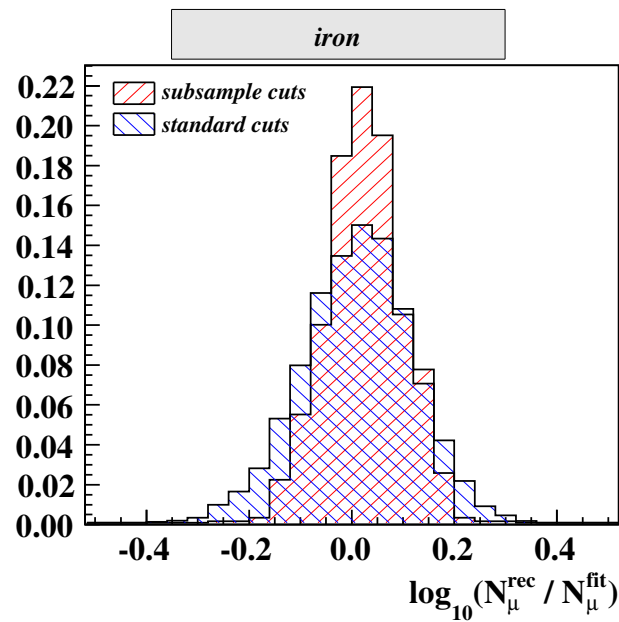


**Figure E.6:** Difference plots between energy conversion fit function and the number of muons of an event. Plotted for hydrogen (*top* figures) and iron induced shower events (*bottom* figures). The diagrams are scaled in such a way, that the integral over each diagram equals to one. For the figures on the *left*, the subsample cuts are applied. For the figures on the *right*, only the standard quality cuts are applied.



(a) Hydrogen induced showers



(b) Iron induced showers

**Figure E.7:** Comparing the standard quality cuts with additional subsample cuts for the number of muons. Projection of the difference distribution of Fig. E.6 to the y-axis. Hydrogen and iron induced shower events are used.

---

# Energy spectrum with systematics

---

In Chap. 8, the energy spectrum is determined together with its systematic errors. In Tab. F.1, the differential flux with its statistical and systematic errors is given for each energy bin. The systematic error contains all systematic uncertainties except for the systematic shift caused by the composition dependence. The composition dependence is given as the differential fluxes for the two extreme assumption, i.e. for hydrogen and iron induced showers. The shower fluctuations are studied, too. The resulting systematic shift leads to a new energy spectrum with a different flux and a different spectral index. The resulting spectrum is also given. More details can be found in Chap. 8.

Energy $\log_{10}(E/\text{GeV})$	Flux $\frac{dI}{dE}/(\text{m}^{-2}\text{s}^{-1}\text{sr}^{-1}\text{GeV}^{-1})$			
		Hydrogen	Iron	Fluctuations
7.00	$(4.87 \pm 0.02^{+1.76}_{-1.11}) \cdot 10^{-15}$	$7.78 \cdot 10^{-15}$	$3.89 \cdot 10^{-15}$	$3.07 \cdot 10^{-15}$
7.08	$(2.81 \pm 0.01^{+0.98}_{-0.66}) \cdot 10^{-15}$	$4.50 \cdot 10^{-15}$	$2.18 \cdot 10^{-15}$	$1.81 \cdot 10^{-15}$
7.16	$(1.59 \pm 0.01^{+0.51}_{-0.35}) \cdot 10^{-15}$	$2.59 \cdot 10^{-15}$	$1.24 \cdot 10^{-15}$	$1.04 \cdot 10^{-15}$
7.24	$(8.91 \pm 0.05^{+2.58}_{-1.79}) \cdot 10^{-16}$	$14.39 \cdot 10^{-16}$	$7.04 \cdot 10^{-16}$	$5.94 \cdot 10^{-16}$
7.32	$(4.99 \pm 0.04^{+1.40}_{-0.94}) \cdot 10^{-16}$	$7.99 \cdot 10^{-16}$	$3.98 \cdot 10^{-16}$	$3.38 \cdot 10^{-16}$
7.40	$(2.86 \pm 0.02^{+0.65}_{-0.50}) \cdot 10^{-16}$	$4.46 \cdot 10^{-16}$	$2.24 \cdot 10^{-16}$	$1.98 \cdot 10^{-16}$
7.48	$(1.58 \pm 0.02^{+0.35}_{-0.24}) \cdot 10^{-16}$	$2.52 \cdot 10^{-16}$	$1.27 \cdot 10^{-16}$	$1.11 \cdot 10^{-16}$
7.56	$(9.20 \pm 0.12^{+1.47}_{-1.29}) \cdot 10^{-17}$	$13.70 \cdot 10^{-17}$	$7.48 \cdot 10^{-17}$	$6.57 \cdot 10^{-17}$
7.64	$(5.37 \pm 0.08^{+0.81}_{-0.65}) \cdot 10^{-17}$	$7.92 \cdot 10^{-17}$	$4.40 \cdot 10^{-17}$	$3.90 \cdot 10^{-17}$
7.72	$(3.10 \pm 0.06^{+0.38}_{-0.38}) \cdot 10^{-17}$	$4.58 \cdot 10^{-17}$	$2.54 \cdot 10^{-17}$	$2.29 \cdot 10^{-17}$
7.80	$(1.84 \pm 0.04^{+0.20}_{-0.22}) \cdot 10^{-17}$	$2.63 \cdot 10^{-17}$	$1.51 \cdot 10^{-17}$	$1.38 \cdot 10^{-17}$
7.88	$(1.05 \pm 0.03^{+0.11}_{-0.09}) \cdot 10^{-17}$	$1.53 \cdot 10^{-17}$	$0.87 \cdot 10^{-17}$	$0.80 \cdot 10^{-17}$
7.96	$(6.03 \pm 0.19^{+0.48}_{-0.64}) \cdot 10^{-18}$	$8.83 \cdot 10^{-18}$	$4.89 \cdot 10^{-18}$	$4.67 \cdot 10^{-18}$
8.04	$(3.38 \pm 0.13^{+0.24}_{-0.28}) \cdot 10^{-18}$	$4.97 \cdot 10^{-18}$	$3.00 \cdot 10^{-18}$	$2.66 \cdot 10^{-18}$
8.12	$(2.20 \pm 0.10^{+0.14}_{-0.34}) \cdot 10^{-18}$	$2.84 \cdot 10^{-18}$	$1.78 \cdot 10^{-18}$	$1.76 \cdot 10^{-18}$
8.20	$(1.28 \pm 0.07^{+0.06}_{-0.28}) \cdot 10^{-18}$	$1.74 \cdot 10^{-18}$	$1.05 \cdot 10^{-18}$	$1.04 \cdot 10^{-18}$
8.28	$(6.72 \pm 0.44^{+0.49}_{-1.35}) \cdot 10^{-19}$	$9.58 \cdot 10^{-19}$	$5.41 \cdot 10^{-19}$	$5.52 \cdot 10^{-19}$
8.36	$(3.39 \pm 0.28^{+0.57}_{-0.32}) \cdot 10^{-19}$	$5.56 \cdot 10^{-19}$	$3.14 \cdot 10^{-19}$	$2.83 \cdot 10^{-19}$
8.44	$(2.22 \pm 0.21^{+0.10}_{-0.39}) \cdot 10^{-19}$	$2.71 \cdot 10^{-19}$	$1.75 \cdot 10^{-19}$	$1.87 \cdot 10^{-19}$
8.52	$(1.40 \pm 0.15^{+0.04}_{-0.32}) \cdot 10^{-19}$	$1.75 \cdot 10^{-19}$	$1.24 \cdot 10^{-19}$	$1.20 \cdot 10^{-19}$
8.60	$(7.9 \pm 1.0^{+1.9}_{-1.8}) \cdot 10^{-20}$	$10.6 \cdot 10^{-20}$	$6.4 \cdot 10^{-20}$	$6.8 \cdot 10^{-20}$
8.68	$(5.75 \pm 0.81^{+0.38}_{-1.65}) \cdot 10^{-20}$	$5.87 \cdot 10^{-20}$	$5.64 \cdot 10^{-20}$	$5.07 \cdot 10^{-20}$
8.76	$(3.19 \pm 0.55^{+0.83}_{-1.42}) \cdot 10^{-20}$	$4.79 \cdot 10^{-20}$	$2.16 \cdot 10^{-20}$	$2.85 \cdot 10^{-20}$
8.84	$(1.72 \pm 0.37^{+0.60}_{-1.25}) \cdot 10^{-20}$	$2.03 \cdot 10^{-20}$	$1.33 \cdot 10^{-20}$	$1.55 \cdot 10^{-20}$
8.92	$(5.2 \pm 1.8^{+3.9}_{-1.3}) \cdot 10^{-21}$	$11.0 \cdot 10^{-21}$	$3.2 \cdot 10^{-21}$	$4.8 \cdot 10^{-21}$
9.00	$(4.3 \pm 1.5^{+1.2}_{-4.0}) \cdot 10^{-21}$	$5.9 \cdot 10^{-21}$	$2.2 \cdot 10^{-21}$	$4.0 \cdot 10^{-21}$

**Table F.1:** Resulting energy spectrum with statistical and the overall systematic errors. The overall systematic error does not contain estimations of the composition dependence, which is given as the differential flux for hydrogen (*third column*) and iron induced showers (*fourth column*). The *fifth column* gives the values for the flux with the corrected fluctuations.

# List of Figures

2.1	Energy spectrum of the cosmic radiation . . . . .	4
2.2	Comparison of the relative elemental abundance in the solar system and the cosmic radiation . . . . .	5
2.3	Schematic view of the development of an extensive air shower . . . . .	9
2.4	Average longitudinal and lateral distribution of muons . . . . .	11
2.5	Average longitudinal and lateral distribution of electrons . . . . .	12
3.1	KASCADE-Grande detector layout . . . . .	16
3.2	KASCADE detector station and $\mu$ detector . . . . .	17
3.3	Schematic view of the central detector . . . . .	19
3.4	Muon tracking detector . . . . .	21
5.1	Accuracy of the reconstruction of the shower core position, the zenith angle, and the number of charged particles as a function of the shower core position . . . . .	32
5.2	Reconstructed shower age $s$ . . . . .	33
5.3	Correlations between the number of triggered Grande detector stations, the primary energy, and the trigger efficiency . . . . .	34
5.4	Trigger and reconstruction efficiency as a function of the number of charged particles and the number of muons . . . . .	36
5.5	Efficiency as a function of the zenith angle . . . . .	37
5.6	Trigger and reconstruction efficiencies as a function of the number of charged particles for different zenith angle ranges . . . . .	37
5.7	Trigger and reconstruction efficiencies as a function of the zenith angle for different ranges of the number of charged particles . . . . .	38
5.8	Shower size spectra: Number of events as a function of the number of charged particles . . . . .	39
6.1	Distribution of time differences between two successive events . . . . .	44
6.2	Measured integral shower size spectra for different zenith angle bins . . . . .	45
6.3	Cut-out of shower size spectra with illustration of the constant intensity cut . . . . .	45
6.4	Measured zenith angle distribution showing bin sizes and the mean of the zenith bin . . . . .	46
6.5	Attenuation curves . . . . .	47
6.6	Measured zenith angle distribution with a fit of a Gaussian distribution . . . . .	48

6.7	Shower size spectra as a function of $N_{\text{ch},21^\circ}$ for different zenith angle ranges . . . . .	49
6.8	Corrected shower size spectrum as a function of $N_{\text{ch},21^\circ}$ . . . . .	50
6.9	Comparing shower size spectra using different reference angles . . . . .	50
6.10	Comparing the shower size spectrum as a function of $N_{\text{ch},21^\circ}$ with a spectrum which is a function of $N_{\text{ch}}$ . . . . .	51
7.1	Example of shower fluctuations for the number charged particles and the number of muons . . . . .	54
7.2	Relative shower fluctuations of iron induced showers . . . . .	55
7.3	Relative composition dependence for the number of charged particles and the number of muons . . . . .	56
7.4	Difference plots between the number of muons and the number of charged particles for the fluctuation and composition dependence . . . . .	57
7.5	Reconstruction error of the number of muons as a function of the shower core distance for different ranges of the reconstructed muon number $\log_{10} N_{\mu}^{\text{rec}}$ . . . . .	58
7.6	Influence of the subsample cuts on the event selection . . . . .	59
7.7	The number of muons as a function of the true primary energy using a mixed composition and applying the subsample cuts . . . . .	60
7.8	Profile diagrams of the primary energy as a function of the number of muons, applying the subsample cuts . . . . .	61
7.9	Difference plots between the energy conversion fit function and the number of muons for each event using a mixed composition . . . . .	62
7.10	Comparing the standard quality cuts with the additional subsample cuts for the number of muons using a mixed composition . . . . .	63
8.1	Energy calibration function . . . . .	67
8.2	Primary energy flux spectrum . . . . .	68
8.3	Study of the influence of the mis-reconstructed shower core positions on the determination of the energy spectrum . . . . .	70
8.4	Study of the influence of changing the scaling factor due to the angular resolution on the determination of the energy spectrum. . . . .	72
8.5	Study of the influence of the angular resolution on the determination of the energy spectrum . . . . .	73
8.6	Study of the influence of the mis-reconstruction of the number of charged particles on the determination of the energy spectrum . . . . .	74
8.7	Study of the influence of the variations of the fitted attenuation curves on the determination of the energy spectrum . . . . .	76
8.8	Study of the influence of the variations of the fitted conversion curve on the determination of the energy spectrum . . . . .	77
8.9	Study of the influence of the variations of the fitted calibration curve on the determination of the energy spectrum . . . . .	78
8.10	Study of the influence of the composition of the cosmic rays on the determination of the energy spectrum . . . . .	80
8.11	The number of charged particles as a function of the primary energy . . . . .	81
8.12	Fit of the relative shower fluctuation . . . . .	82

8.13	Study of the influence of the shower fluctuations on the determination of the energy spectrum . . . . .	83
8.14	Systematic deviations caused by shower fluctuations . . . . .	84
8.15	Determined energy spectrum including systematic uncertainties . . . . .	85
9.1	All particle energy spectrum in comparison with results from other measurements . . . . .	88
C.1	Shower size spectra as a function of $N_{\text{ch},0^\circ}$ for different zenith angle ranges. . . . .	99
C.2	Comparing shower size spectra for two different reference angles with the shift compensated. . . . .	100
C.3	Integral shower size spectra as a function of the reference number of charged particles $N_{\text{ch},21^\circ}$ . . . . .	101
D.1	Fluctuation diagrams for $N_{\text{ch}}$ , hydrogen, and $0^\circ \leq \theta < 8^\circ$ . . . . .	105
D.2	Fluctuation diagrams for $N_{\text{ch}}$ , hydrogen, and $8^\circ \leq \theta < 16^\circ$ . . . . .	106
D.3	Fluctuation diagrams for $N_{\text{ch}}$ , hydrogen, and $16^\circ \leq \theta < 24^\circ$ . . . . .	107
D.4	Fluctuation diagrams for $N_{\text{ch}}$ , hydrogen, and $24^\circ \leq \theta < 32^\circ$ . . . . .	108
D.5	Fluctuation diagrams for $N_{\text{ch}}$ , hydrogen, and $32^\circ \leq \theta \leq 40^\circ$ . . . . .	109
D.6	Fluctuation diagrams for $N_{\text{ch}}$ , iron, and $0^\circ \leq \theta < 8^\circ$ . . . . .	111
D.7	Fluctuation diagrams for $N_{\text{ch}}$ , iron, and $8^\circ \leq \theta < 16^\circ$ . . . . .	112
D.8	Fluctuation diagrams for $N_{\text{ch}}$ , iron, and $16^\circ \leq \theta < 24^\circ$ . . . . .	113
D.9	Fluctuation diagrams for $N_{\text{ch}}$ , iron, and $24^\circ \leq \theta < 32^\circ$ . . . . .	114
D.10	Fluctuation diagrams for $N_{\text{ch}}$ , iron, and $32^\circ \leq \theta \leq 40^\circ$ . . . . .	115
D.11	Fluctuation diagrams for $N_\mu$ , hydrogen, and $0^\circ \leq \theta < 8^\circ$ . . . . .	117
D.12	Fluctuation diagrams for $N_\mu$ , hydrogen, and $8^\circ \leq \theta < 16^\circ$ . . . . .	118
D.13	Fluctuation diagrams for $N_\mu$ , hydrogen, and $16^\circ \leq \theta < 24^\circ$ . . . . .	119
D.14	Fluctuation diagrams for $N_\mu$ , hydrogen, and $24^\circ \leq \theta < 32^\circ$ . . . . .	120
D.15	Fluctuation diagrams for $N_\mu$ , hydrogen, and $32^\circ \leq \theta \leq 40^\circ$ . . . . .	121
D.16	Fluctuation diagrams for $N_\mu$ , iron, and $0^\circ \leq \theta < 8^\circ$ . . . . .	123
D.17	Fluctuation diagrams for $N_\mu$ , iron, and $8^\circ \leq \theta < 16^\circ$ . . . . .	124
D.18	Fluctuation diagrams for $N_\mu$ , iron, and $16^\circ \leq \theta < 24^\circ$ . . . . .	125
D.19	Fluctuation diagrams for $N_\mu$ , iron, and $24^\circ \leq \theta < 32^\circ$ . . . . .	126
D.20	Fluctuation diagrams for $N_\mu$ , iron, and $32^\circ \leq \theta \leq 40^\circ$ . . . . .	127
D.21	Summarizing shower fluctuations for hydrogen induced showers . . . . .	128
D.22	Difference plot between $N_\mu$ and $N_{\text{ch}}$ for hydrogen induced showers . . . . .	129
E.1	Influence of the standard cuts on the event selection. . . . .	132
E.2	The number of muons as a function of the true primary energy for hydrogen and iron induced showers using subsample cuts . . . . .	133
E.3	The number of muons as a function of the true primary energy for hydrogen and iron induced showers using subsample cuts . . . . .	134
E.4	The number of muons as a function of the true primary energy for a mixed composition using standard cuts . . . . .	135
E.5	Profile diagrams of the primary energy as a function of the number of muons, applying the standard cuts. . . . .	136
E.6	Difference plots between energy conversion fit function and the number of muons for each event using hydrogen and iron induced showers . . . . .	137

- E.7 Comparing the standard quality cuts with additional subsample cuts for the number of muons for hydrogen and iron induced showers. . . . . 138



# List of Tables

4.1	Simulation sets used in the analysis . . . . .	29
5.1	Summary of the selection criteria applied to the data sets and their effects	35
6.1	Zenith angle bins . . . . .	43
7.1	Comparison of the standard cuts with the subsample cuts using the distribution of the number of muons . . . . .	63
8.1	Results of the calibration fit . . . . .	68
8.2	Effect of the mis-reconstructed shower core positions . . . . .	69
8.3	Summary of the systematic uncertainties . . . . .	85
A.1	Number of charged particles determined by applying the constant intensity method . . . . .	92
C.1	Attenuation fit results for the reference angle of $21^\circ$ . . . . .	98
C.2	Attenuation fit results for the reference angle of $0^\circ$ . . . . .	98
D.1	Summary of the fluctuation distributions of $N_{\text{ch}}$ and hydrogen induced showers . . . . .	104
D.2	Summary of the fluctuation distributions of $N_{\text{ch}}$ and iron induced showers	110
D.3	Summary of the fluctuation distributions of $N_\mu$ and hydrogen induced showers . . . . .	116
D.4	Summary of the fluctuation distributions of $N_\mu$ and iron induced showers	122
F.1	Resulting energy spectrum with systematics . . . . .	140



# List of Acronyms

Acronym	Explanation
ADC	analog-to-digital converter
AGASA	Akeno giant air shower array
AGN	active galactic nucleus
ANKA	Angströmquelle Karlsruhe
CASA	Chicago air shower array
-BLANCA	broad lateral non-imaging Cherenkov array
-MIA	Michigan array
CORSIKA	cosmic ray simulation for KASCADE
CRES	cosmic ray event simulation
DAQ	data acquisition
DICE	dual imaging Cherenkov experiment
EAS	extensive air shower
EGS4	electron gamma shower code version 4
FADC	flash analog-to-digital converter
FLUKA	fluktuierende Kaskade
GEANT	for geometry and tracking
GPS	global positioning system
GZK	Greisen Zatsepin Kuzmin
HV	high voltage
HiRes	high resolution Fly's Eye
KAFE	KASCADE array frontend electronics
KASCADE	Karlsruhe shower core and array detector
KRETA	KASCADE reconstruction for extensive air showers
LST	limited streamer tubes
MC	Monte Carlo
m.i.p.	minimum ionizing particle
MTD	muon tracking detector
MWPC	multi-wire proportional chamber
NKG	J. Nishimura, K. Kamata, and K. Greisen
QGSJET	quark-gluon string model with minijet production

*continued on next page*

*continued from previous page*

---

<b>Acronym</b>	<b>Explanation</b>
PMT	photomultiplier tube
RMS	root mean square
SDC	shower disk coordinates
TDC	time-to-digital converter
TMP	tetramethylpentane
TMS	tetramethylsilane

---

# Bibliography

- [Abb08] R. Abbasi et al. (HiRes Collaboration), *Observation of the GZK cutoff by the HiRes experiment*, Phys. Rev. Lett. **100** (2008), 101101, astro-ph/0703099.
- [Agl89] M. Aglietta et al., *The EAS TOP array at  $E(0) = 10^{14}\text{eV} - 10^{16}\text{eV}$ : Stability and resolutions*, Nucl. Instrum. Meth. **A277** (1989), 23–28.
- [Agl93] M. Aglietta et al. (EAS-TOP Collaboration), *UHE cosmic ray event reconstruction by the electromagnetic detector of EAS-TOP*, Nucl. Instrum. Meth. **A336** (1993), 310–321.
- [Agl99] M. Aglietta et al. (EAS-TOP and LVD Collaboration), *Study of the c.r. composition and interaction at  $E_0 = 10\text{-TeV}$  to  $100\text{-TeV}$  from the observation of H.E. muons and atmospheric Cherenkov light in EAS*, Nucl. Phys. Proc. Suppl. **75A** (1999), 259–261.
- [Aha04] F. A. Aharonian et al. (The HESS Collaboration), *High-energy particle acceleration in the shell of a supernova remnant*, Nature. **432** (2004), 75–77, astro-ph/0411533.
- [AM02] J. Alvarez-Muniz, R. Engel, T. K. Gaisser, J. A. Ortiz, and T. Stanev, *Atmospheric shower fluctuations and the constant intensity cut method*, Phys. Rev. **D66** (2002), 123004, astro-ph/0209117.
- [Ame95] M. Amenomori et al. (Tibet AS gamma Collaboration), *The Cosmic ray energy spectrum between  $10^{14.5}\text{eV}$  and  $10^{16.3}\text{eV}$  covering the 'knee' region*, Astrophys. J. **461** (1995), 408–414.
- [Ant01] T. Antoni et al. (KASCADE Collaboration), *Electron, muon, and hadron lateral distributions measured in air-showers by the KASCADE experiment*, Astropart. Phys. **14** (2001), 245–260, astro-ph/0004233.
- [Ant03a] T. Antoni, *Nachweis hochenergetischer Myonen in ausgedehnten Luftschauern bei KASCADE*, Ph.D. thesis, Universität Heidelberg, Germany, 2003.
- [Ant03b] T. Antoni et al. (KASCADE Collaboration), *The Cosmic ray experiment KASCADE*, Nucl. Instrum. Meth. **A513** (2003), 490–510.

- [Ant03c] T. Antoni et al. (the KASCADE Collaboration), *Measurements of attenuation and absorption lengths with the KASCADE experiment*, *Astropart. Phys.* **19** (2003), 703–714, astro-ph/0303036.
- [Ant05] T. Antoni et al. (The KASCADE Collaboration), *KASCADE measurements of energy spectra for elemental groups of cosmic rays: Results and open problems*, *Astropart. Phys.* **24** (2005), 1–25, astro-ph/0505413.
- [Apa01] A. V. Apanasenko et al. (RUNJOB Collaboration), *Composition and energy spectra of cosmic-ray primaries in the energy range  $10^{13}$  eV/particle to approx.  $10^{15}$  eV/particle observed by Japanese-Russian joint balloon experiment*, *Astropart. Phys.* **16** (2001), 13–46.
- [Ape06] W. D. Apel et al. (KASCADE Collaboration), *Comparison of measured and simulated lateral distributions for electrons and muons with KASCADE*, *Astropart. Phys.* **24** (2006), 467–483, astro-ph/0510810.
- [Arq00] F. Arqueros et al. (HEGRA Collaboration), *Energy spectrum and chemical composition of cosmic rays between 0.3-PeV and 10-PeV determined from the Cherenkov- light and charged-particle distributions in air showers*, *Astron. Astrophys.* **359** (2000), 682–694, astro-ph/9908202.
- [Aug39] P. Auger, P. Ehrenfest, R. Maze, J. Daudin, and A. F. Robley, *Extensive cosmic-ray showers*, *Rev. Mod. Phys.* **11** (1939), 288–291.
- [Ave03] M. Ave et al., *Mass composition of cosmic rays in the range  $2 \times 10^{17}$  -  $3 \times 10^{18}$  measured with the Haverah Park Array*, *Astropart. Phys.* **19** (2003), 61–75, astro-ph/0203150.
- [AZ01] T. Abu-Zayyad et al. (HiRes-MIA Collaboration), *Measurement of the cosmic ray energy spectrum and composition from  $10^{17}$  eV to  $10^{18.3}$  eV using a hybrid fluorescence technique*, *Astrophys. J.* **557** (2001), 686–699, astro-ph/0010652.
- [Bar89] R. J. Barlow, *A Guide to the Use of Statistical Methods in the Physical Science*.
- [Bel01] J. A. Bellido, R. W. Clay, B. R. Dawson, and M. Johnston-Hollitt, *Southern hemisphere observations of a  $10^{18}$  eV cosmic ray source near the direction of the galactic centre*, *Astropart. Phys.* **15** (2001), 167–175, astro-ph/0009039.
- [Ber99] E. G. Berezhko and L. T. Ksenofontov, *Composition of cosmic rays accelerated in supernova remnants*, *J. Exp. Theor. Phys.* **89** (1999), 391–403.
- [Bir94] D. J. Bird et al. (HIRES Collaboration), *The Cosmic ray energy spectrum observed by the Fly's Eye*, *Astrophys. J.* **424** (1994), 491–502.
- [Bir99] D. Bird et al., *Study of Broad-Scale anisotropy of Cosmic-Ray arrival directions from  $2 \times 10^{17}$  eV to  $10^{20}$  eV from Fly's Eye data*, *Astrophys. J.* **511** (1999), 739–749, astro-ph/9806096.

- [Boz01] H. Bozdog et al., *The detector system for measurement of multiple cosmic muons in the central detector of KASCADE*, Nucl. Instrum. Meth. **A465** (2001), 455–471.
- [Bre98] M. Brendle and U. Raidt, *The triggering and timing electronics of the KASCADE central detector*, Nucl. Instrum. Meth. **A412** (1998), 420–424.
- [Brü07] M. Brüggemann, *Determination of an arrival time cut for the separation of electrons and muons in extensive air showers*, Ph.D. thesis, Universität Siegen, Germany, 2007.
- [Bur05] J. v. Buren et al., *Muon Size Spectrum measured by KASCADE-Grande*, Proc. of the 29<sup>th</sup> Int. Cosmic Ray Conf., Pune **6** (2005), 301–304.
- [Bur06] J. v. Buren, *Investigations of the Muon Component of Extensive Air Showers Measured by KASCADE-Grande*, Ph.D. thesis, Universität Karlsruhe, Germany, 2006.
- [Can02] J. Candia, E. Roulet, and L. N. Epele, *Turbulent diffusion and drift in galactic magnetic fields and the explanation of the knee in the cosmic ray spectrum*, JHEP **12** (2002), 033, astro-ph/0206336.
- [CER94] CERN, *GEANT 3.21 detector description and simulation tool*, CERN Library Long Writeup W5013, CERN, Genève, 1994.
- [Ces83] C. J. Cesarsky and T. Montmerle, *Gamma rays from active regions in the galaxy - The possible contribution of stellar winds*, Space Sci. Revs. **36** (1983), 173–193.
- [Che86] K. S. Cheng, C. Ho, and M. Ruderman, *Energetic radiation from rapidly spinning pulsars. I - Outer magnetosphere gaps. II - VELA and Crab*, Astrophys. J. **300** (1986), 500–539.
- [Dol02] P. Doll et al., *Muon tracking detector for the air shower experiment KASCADE*, Nucl. Instrum. Meth. **A488** (2002), 517–535.
- [DP07] F. Di Pierro et al., *Shower size spectrum reconstructed with KASCADE-Grande*, Prepared for 30th International Cosmic Ray Conference (ICRC 2007), Merida, Yucatan, Mexico, 3-11 Jul 2007.
- [Dru83] L. O. Drury, *An introduction to the theory of diffusive shock acceleration of energetic particles in tenuous plasmas*, Reports of Progress in Physics **46** (1983), 973–1027.
- [Eng99] J. Engler et al., *A warm-liquid calorimeter for cosmic-ray hadrons*, Nucl. Instrum. Meth. **A427** (1999), 528–542.
- [Eno02] R. Enomoto et al., *The Acceleration of cosmic ray protons in the supernova remnant RX J1713.7-3946*, Nature **416** (2002), 823–826.

- [Erl97] A. D. Erlykin and A. W. Wolfendale, *A single source of cosmic rays in the range  $10^{15}$  eV to  $10^{16}$  eV*, J. Phys. **G23** (1997), 979–989.
- [Fas03] A. Fasso et al., *The physics models of FLUKA: Status and recent development*, hep-ph/0306267.
- [Fer49] E. Fermi, *On the Origin of the Cosmic Radiation*, Phys. Rev. **75** (1949), 1169–1174.
- [Fow01] J. W. Fowler et al., *A measurement of the cosmic ray spectrum and composition at the knee*, Astropart. Phys. **15** (2001), 49–64, astro-ph/0003190.
- [FSL07] P. Facal San Luis (Pierre Auger Collaboration), *Measurement of the UHECR spectrum above 10 EeV at the Pierre Auger Observatory using showers with zenith angles greater than 60 degrees*, 0706.4322.
- [Gem90] H. Gemmeke et al., *The High resolution neutrino calorimeter KARMEN*, Nucl. Instrum. Meth. **A289** (1990), 490–495.
- [Gla99] M. A. K. Glasmacher et al., *The cosmic ray energy spectrum between  $10^{14}$  eV and  $10^{16}$  eV*, Astropart. Phys. **10** (1999), 291–302.
- [Gla05] R. Glasstetter et al., *Shower Size Reconstruction at KASCADE-Grande*, Proc. of the 29<sup>th</sup> Int. Cosmic Ray Conf., Pune **6** (2005), 293–296.
- [Gre56] K. Greisen, *The Extensive Air Showers*, Prog. Cosmic Ray Phys. **III** (1956), 1–141.
- [Gre66] K. Greisen, *End to the cosmic ray spectrum?*, Phys. Rev. Lett. **16** (1966), 748–750.
- [Gri70] N. L. Grigorov et al., *Study of the energy spectrum of high- an ultrahigh-energy primary cosmic rays on board “Proton” spacecraft*, Sov. J. Nucl. Phys. **11** (1970), 1058–1069.
- [Hae96] R. Haeusler, *Aufbau und erste Messungen des Top-Clusters von KASCADE*, Diploma thesis, Universität Karlsruhe, Germany, 1996.
- [Har90] A. K. Harding and T. K. Gaisser, *Acceleration by pulsar winds in binary systems*, Astrophys. J. **358** (1990), 561–574.
- [Hau03] A. Haungs et al., *The KASCADE-Grande experiment*, Proc. of the 28<sup>th</sup> Int. Cosmic Ray Conf., Tsukuba **2** (2003), 985–988.
- [Hau07] A. Haungs et al., *The KASCADE-Grande experiment*, Prepared for 30th International Cosmic Ray Conference (ICRC 2007), Merida, Yucatan, Mexico, 3-11 Jul 2007.
- [Hay99] N. Hayashida et al. (AGASA Collaboration), *The anisotropy of cosmic ray arrival direction around  $10^{18}$  eV*, Astropart. Phys. **10** (1999), 303–311, astro-ph/9906056.



- [Hec98] D. Heck, G. Schatz, T. Thouw, J. Knapp, and J. N. Capdevielle, *CORSIKA: A Monte Carlo code to simulate extensive air showers*, Report **FZKA-6019** (1998).
- [Hes12] V. Hess, *Über Beobachtungen der durchdringenden Strahlung bei sieben Freiballonfahrten*, Phys. Zeitsch. **13** (1912), 1084–1091.
- [Hor01] A. Horneffer, *Aufbau eines Flash-ADC Systems und Messung der Zeitstruktur ausgedehnter Luftschauer mit dem KASCADE-Experiment*, Diploma thesis, Universität Karlsruhe, Germany, 2001.
- [Jok87] J. R. Jokipii and G. Morfill, *Ultra-high-energy cosmic rays in a galactic wind and its termination shock*, Astrophys. J. **312** (1987), 170–177.
- [Kam58] K. Kamata and J. Nishimura, *The Lateral and the Angular Structure Functions of Electron Showers*, Prog. of Theo. Phys. Suppl. **6** (1958), 93–155.
- [Kam03] K.-H. Kampert et al., *Status of the KASCADE-Grande experiment*, Nucl. Phys. Proc. Suppl. **122** (2003), 422–426, astro-ph/0212347.
- [Kaz01] D. Kazanas and A. Nicolaidis, *Cosmic ray 'knee': A herald of new physics?*, astro-ph/0103147.
- [Knu06] S. P. Knurenko et al., *Characteristics of EAS and primary particle mass composition in the energy region of  $10^{17}$  eV –  $3 \times 10^{19}$  eV by Yakutsk data*, Nucl. Phys. Proc. Suppl. **151** (2006), 92–95, astro-ph/0411483.
- [Kob02] K. Kobayakawa, Y. Sato, and T. Samura, *Acceleration of particles by oblique shocks and cosmic ray spectra around the knee region*, Phys. Rev. **D66** (2002), 083004, astro-ph/0008209.
- [Kri92] W. Kriegleder, *Ein Detektorsystem zum Nachweis von Myonen in ausgedehnten Luftschauern für das KASCADE-Projekt*, Ph.D. thesis, Universität Karlsruhe, Germany, 1992, KfK 5023.
- [Kul58] G. Kulikov and G. Kristiansen, *On the size spectrum of extensive air showers*, Journal of Experimental and Theoretical Physics **35** (1958), 441–444.
- [Lag01] A. A. Lagutin and R. I. Raikin, *Lateral distribution of electrons in EAS at superhigh energies: predictions and experimental data*, Nucl. Phys. Proc. Suppl. **97** (2001), 274–277.
- [Mai03] G. Maier, *Suche nach Anisotropie in der kosmischen Strahlung mit dem KASCADE-Experiment*, Ph.D. thesis, Universität Karlsruhe, Germany, 2003.
- [Mar07] C. I. Mariş, J. Blümer, M. Roth, T. Schmidt, and M. Unger, *Comparison of Two Methods to Infer the Cosmic Ray Spectrum at Highest Energies*, GAP **2007-044** (2007), internal report of the Pierre Auger Experiment; privat communication.

- [Nag84] M. Nagano et al., *Energy spectrum of primary cosmic rays between  $10^{14.5}$  eV and  $10^{18}$  eV*, J. Phys. **G10** (1984), 1295.
- [Nag92] M. Nagano et al., *Energy spectrum of primary cosmic rays above  $10^{17}$  eV determined from the extensive air shower experiment at Akeno*, J. Phys. **G18** (1992), 423–442.
- [Nav04] G. Navarra et al., *KASCADE-Grande: A large acceptance, high-resolution cosmic-ray detector up to  $10^{18}$  eV*, Nucl. Instrum. Meth. **A518** (2004), 207–209.
- [Nel85] W. R. Nelson, H. Hirayama, and D. W. O. Rogers, *The EGS4 code system*, Report **SLAC-0265** (1985), Stanford Linear Accelerator Center.
- [Ost06] S. Ostapchenko, *Non-linear screening effects in high energy hadronic interactions*, Phys. Rev. **D74** (2006), 014026, hep-ph/0505259.
- [Ost07] S. Ostapchenko, *Status of QGSJET*, AIP Conf. Proc. **928** (2007), 118–125, arXiv:0706.3784 [hep-ph].
- [Ove04] S. Over, *Development and commissioning of data acquisition systems for the KASCADE-Grande experiment*, Diploma thesis, Universität Siegen, Germany, 2004.
- [Ove07a] S. Over et al., *Search for anisotropy and point sources of cosmic rays with the KASCADE-Grande experiment*, Prepared for 30th International Cosmic Ray Conference (ICRC 2007), Merida, Yucatan, Mexico, 3-11 Jul 2007.
- [Ove07b] S. Over, *The Grande Data Quality database*, 2007, Internal report.
- [Per07] L. Perrone (Pierre Auger Collaboration), *Measurement of the UHECR energy spectrum from hybrid data of the Pierre Auger Observatory*, 0706.2643.
- [Ptu93] V. S. Ptuskin, S. I. Rogovaya, V. N. Zirakashvili, L. G. Chuvilgin, G. B. Khristiansen, E. G. Klepach, and G. V. Kulikov, *Diffusion and drift of very high energy cosmic rays in galactic magnetic fields*, Astron. Astrophys. **268** (1993), 726–735.
- [Rac93] J. P. Rachen and P. L. Biermann, *Extragalactic ultrahigh-energy cosmic rays. I. Contribution from hot spots in FR-II radio galaxies*, Astron. Astrophys. **272** (1993), 161–175, astro-ph/9301010.
- [Rot07] M. Roth (Pierre Auger Collaboration), *Measurement of the UHECR energy spectrum using data from the Surface Detector of the Pierre Auger Observatory*, arXiv:0706.2096 [astro-ph].
- [Sch96] H. Schieler, *Konzeption, Entwicklung und Test des lokalen Datenerfassungssystems für das strukturierte Detektor-Array von KASCADE*, Ph.D. thesis, Universität Karlsruhe, Germany, 1996.

- [Sig03] G. Sigl, *The enigma of the highest energy particles of nature*, Ann. Phys. **303** (2003), 117–141, astro-ph/0210049.
- [Sim83] J. A. Simpson, *Elemental and isotopic composition of the galactic cosmic rays*, Ann. Rev. Nucl. Part. Sci. **33** (1983), 323–382.
- [Sta93] T. Stanev, P. L. Biermann, and T. K. Gaisser, *Cosmic rays. 4. The Spectrum and chemical composition above  $10^{*4}$ -GeV*, Astron. Astrophys. **274** (1993), 902–908, astro-ph/9303006.
- [Swo00] S. P. Swordy and D. B. Kieda, *Elemental composition of cosmic rays near the knee by multiparameter measurements of air showers*, Astropart. Phys. **13** (2000), 137–150, astro-ph/9909381.
- [Tak03] M. Takeda et al., *Energy determination in the Akeno Giant Air Shower Array experiment*, Astropart. Phys. **19** (2003), 447–462, astro-ph/0209422.
- [Tom07] G. Toma et al., *Features of the S(500) distribution for large air showers detected with the KASCADE-Grande array*, Prepared for 30th International Cosmic Ray Conference (ICRC 2007), Merida, Yucatan, Mexico, 3-11 Jul 2007.
- [Uch07] Y. Uchiyama, F. A. Aharonian, T. Tanaka, T. Takahashi, and Y. Maeda, *Extremely fast acceleration of cosmic rays in a supernova remnant*, Nature **449** (2007), 576–578.
- [Völ92] G. Völker, *Ein Detektorsystem zum Nachweis der e/ $\gamma$ -Komponente großer Luftschauer im UHE-Bereich*, Ph.D. thesis, Universität Karlsruhe, Germany, 1992.
- [Wat06] A. A. Watson, *Observations of ultra-high energy cosmic rays*, J. Phys. Conf. Ser. **39** (2006), 365–371, astro-ph/0511800.
- [Web99] J. Weber, *Untersuchung der elektromagnetischen und myonischen Komponente ausgedehnter Luftschauer und Bestimmung der Elementzusammensetzung der kosmischen Strahlung*, Ph.D. thesis, Universität Karlsruhe, Germany, 1999.
- [Wef91] F. Wefel, *Cosmic rays, supernovae and the interstellar medium*, NATO ASIC Series 337 **337C** (1991), 29.
- [Wig00] R. Wigmans, *On big bang relics, the neutrino mass and the spectrum of cosmic rays*, Nucl. Phys. Proc. Suppl. **85** (2000), 305–310, hep-ph/0107263.
- [WS98] B. Wiebel-Sooth, P. L. Biermann, and H. Meyer, *Cosmic Rays VII. Individual element spectra: prediction and data*, Astron. Astrophys. **330** (1998), 389–398, astro-ph/9709253.
- [Zab02] J. Zabierowski and P. Doll, *Front-end readout boards for streamer tube muon tracking detector in the KASCADE EAS Experiment*, Nucl. Instrum. Meth. **A484** (2002), 528–532.

- [Zat66] G. T. Zatsepin and V. A. Kuzmin, *Upper limit of the spectrum of cosmic rays*, JETP Lett. **4** (1966), 78–80.

# Danksagung

An dieser Stelle möchte ich mich bei all jenen bedanken, ohne die diese Arbeit nicht möglich gewesen wäre.

An erster Stelle möchte ich mich sehr herzlich bei meinem Doktorvater Prof. Dr. Peter Buchholz für die interessante und lehrreiche Zeit, die ich in seiner Arbeitsgruppe verbringen durfte, bedanken. Ich möchte mich dafür bedanken, dass er es mir ermöglichte in einer internationalen Kollaboration mitzuarbeiten und dabei viele nützliche Erfahrungen zu sammeln.

Ich bedanke mich sehr herzlich bei Prof. Dr. Claus Grupen für die Bereitschaft diese Arbeit als Zweitgutachter zu bewerten. Ebenso einen herzlichen Dank für seine freundliche Art mir bei Fragen zu helfen und für die anregenden Diskussionen.

Bei der gesamten Siegener Arbeitsgruppe bedanke ich mich für die Zusammenarbeit und die angenehme Arbeitsatmosphäre. Ich danke meinen Kollegen Thomas Bäcker und Sven Over und meinem ehemaligen Kollegen Dr. Marc Brüggemann für die angenehme Zeit in Siegen und Karlsruhe und für die stets angenehme Atmosphäre im gemeinsamen Büro.

Ich danke den Mitgliedern der KASCADE-Grande-Kollaboration für die gute Zusammenarbeit und die freundliche Unterstützung, die diese Arbeit erst ermöglichten. Mein besonderer Dank gilt Dr. Andreas Haungs für die fachliche Unterstützung und seine stete Bereitschaft und Geduld auf meine Fragen einzugehen.

Ich danke den Kollegen Thomas Bäcker und Valentin Sipica, dass sie freiwillig Zeit geopfert haben, um diese Arbeit Korrektur zu lesen.

Mein größter Dank gilt meiner gesamten Familie. Ich danke insbesondere meinen Eltern, die mich stets unterstützt haben. Ganz besonders danke ich meiner Frau Corinna für ihr stetes Vertrauen und Unterstützung und für ihre aufgebrachte Geduld, vor allem während der Abfassung dieser Arbeit.